AN ABSTRACT OF THE THESIS OF

Zoran Jovanovic for the degree of Doctor of Philosophy in Chemical Engineering presented on August 30, 1994.

Title: Kinetic Study on the Production of Silicon Nitride by Direct Nitridation of Silicon in a Fluidized Bed: Experiment and Modeling

Abstract approved: _____

Dr. Shoichi Kimura

Direct nitridation of porous silicon pellets (d_p ~ 400 μm) composed of fine grains ($d_{g,m}$ ~ 2 μm) was performed in a fluidized bed reactor (55 mm ID) using nitrogen (30-90%) - hydrogen (5-50%) - argon mixtures as the nitriding gas in the temperature range 1200-1390°C. The effects of reaction temperature, hydrogen, nitrogen and pretreatment of raw materials on the nitridation of silicon and the yields of α- and β-form were investigated. It was shown that a high silicon conversion (99%) and a high α/β ratio (~10) in the produced silicon nitride can be achieved by controlling the reaction temperature and the content of nitriding atmosphere.

Nitridation is initiated after an induction period which becomes shorter with an increase in reaction temperature and/or nitrogen concentration, but is unaffected by hydrogen. Both the final conversion of silicon and α/β ratio

increase with an increase in reaction temperature and/or with a decrease in nitrogen concentration, but remain essentially unaffected by hydrogen.

The mechanism of nitridation remains unclear. The most reasonable assumption for it, based on TEM photos of reacting pellets, is that the process is controlled by the nitrogen transport through the crackling, polycrystalline nitride layer, with nitride crystallites detaching from the silicon surface after reaching a critical thickness, so fresh silicon surface is exposed.
A mathematical model developed on the basis of this assumption, applied to the conversion of a single grain, predicted the critical nitride layer thickness in agreement with experimental observations.

Modeling was also applied to nitridation of grains having a wide size distribution, in which case the effective silicon surface area was shown to reasonably linearly decrease with an increase in the overall conversion. The assumption of a constant average silicon consumption rate per this area led to a correlation which predicts the progress of nitridation in a wide range of experimental conditions. The results show that the average nitridation rate per the effective surface area obeys a first order rate law with respect to nitrogen and that the process has an apparent activation energy of ~340 kJ/mol in the temperature range 1200-1300°C.

Kinetic Study on the Production of Silicon Nitride by Direct Nitridation of Silicon in a Fluidized Bed: Experiment and Modeling

by

Zoran R. Jovanovic

A THESIS

submitted to

Oregon State University

in partial fulfillment of
the requirements for the
degree of

Doctor of Philosophy

Completed August 30, 1994
Commencement June 1995

Doctor of Philosophy thesis of Zoran R. Jovanovic presented on August 30, 1994

APPROVED:

Redacted for Privacy

Major Professor, representing Chemical Engineering

Redacted for Privacy

Head of Department of Chemical Engineering

Redacted for Privacy

Dean of Graduate School

I understand that my thesis will become part of the permanent collection of Oregon State University Libraries. My signature below authorizes release of my thesis to any reader upon request.

Redacted for Privacy

Zoran R. Jovanovic, Author

ACKNOWLEDGMENT

I would like to express my gratitude to **Dr. Shoichi Kimura** for a number of useful suggestions, and for unselfishly sharing his knowledge and experience with me along this project.

Special thanks to **Nick Wannenmacher** for his support, advice and encouragement. He was always ready to help and to teach me everything he knew: from welding and sophisticated electronics, to english writing and grammar. Finally, thank you Nick for being such a wonderful friend.

During this project, as well as my overall graduate program, I had the privilege to be close to **Dr. Octave Levenspiel** and to discuss chemical engineering and general science with him. This was a great experience which unlocked my mind, and which will definitely benefit me in my future career.

The advice and professional help of many scientists from different fields, friends, and my fellow graduate students, were pertinent for the success in this project. Special thanks to: **Dr. Jun Koike** (transmission electron microscopy), **Pat Woodward** (X-ray diffraction), **Khavinet Lourvanij** (porosimetry measurements), **Yao-Dian Liu, Tsai-Cheng Wang, Dah-Cheng Lin, Hardeepak (Happy) Gill** (all helping me in doing experiments). I also enjoyed discussions of my work with **Dr. Milo Koretsky** and **Dr. John Wager**.

Finally, I am grateful to **NSF** for funding this project (grant CTS9241320) and providing financial support for me, and to **Shin-Etsu Chemical Company, Ltd.** for providing raw materials.

TABLE OF CONTENTS

TABLE OF CONTENTS (continued)

LIST OF FIGURES

LIST OF FIGURES (continued)

LIST OF FIGURES (continued)

LIST OF FIGURES (continued)

LIST OF FIGURES (continued)

LIST OF TABLES

LIST OF APPENDICES

LIST OF APPENDIX FIGURES

LIST OF APPENDIX TABLES

LIST OF APPENDIX TABLES (continued)

NOTATION

a	parameter defined by Equation 47 (s/m^2)
a_i	mass fraction of α-silicon nitride in silicon nitride standard #i
a_{rs}	approximated overall decrease rate in the effective surface area of silicon due to both reaction and structural factors (m^2)
A	constant defined by Equation B33 (-)
b	stoichiometric coefficient defined by Equation 21
b_i	mass fraction of β-silicon nitride in silicon nitride standard #i
B	constant defined by Equation B33 (-)
C_A	molar concentration of species A ($kmol/m^3$)
$\overline{C}$	dimensionless concentration
C	constant defined by Equation B34 (-)
d	crystallite size evaluated by XRD measurements (Å)
$d_{g,m}$	initial grain diameter of the grains that participate with w_m percent by mass in the total distribution (μm)
$d_{g,mean}$	statistical mean of a grain size distribution (μm)
d_p	mean diameter of raw silicon pellet (μm)
D	effective diffusion coefficient (m^2/s)
D	constant defined by Equation B34 (-)
D_{CM}	apparent diffusion coefficient in Equations 38 and 39 (m^2/s)
D_{eff}	apparent diffusion coefficient (m^2/s)
E_{app}	apparent activation energy of the process (kJ/mol)
f_{rs}	dimensionless factor defined by Equation 72

NOTATION (continued)

F	Faraday's constant (96,487 C/equiv.)
ΔG^o	Standard Gibbs energy of a reaction (kJ/mol)
H	partition coefficient that relates gas bulk concentration of a species with concentration of the species at gas-solid interface (-)
ΔH	heat of a reaction (kJ/mol)
$I_\gamma\ (hkl)$	integrated intensity of a X-rays beam diffracted from reflection (*hkl*) of crystalline phase γ
J_i	molar flux of species i (mol/m^2 s)
k_0	apparent coefficient of the nitrogen transport through the product layer toward the silicon/silicon nitride interface (m/s)
k_s	constant of a first order reaction occurring at the solid surface, based on the bulk gas concentration of a gaseous reactant (m/s)
k^*	parameter defined by Equation 59 (m^2/s)
k^{**}	universal scaling parameter defined by Equations 62 and 63 (s^{-1}).
K	parameter defined by Equation 27 (s^{-1})
K^o	parameter defined by Equation 80 (hr^{-1})
$K_{\delta/\gamma}$	calibration constant which relates intensity ratio of diffracted X-rays from reflections of two phases in a mixture with a mass fraction ratio of these phases
$K^o_{i,\delta}$	constant defined by Equation B1
m_i	mass of silicon nitride standard **#i** (g)
m_3	mass of silicon standard **#3**, **#3a** or **#3b** (g)
M	integer which determines the maximum possible number of peeling product shell occurrences for a particular conversion (-)

NOTATION (continued)

M_B	molar mass of species B (kg/kmol)
N_i	number of moles of species i (mol)
N_m	number of grains in a fraction of a size distribution which has a mean initial radius $R_{0,m}$ (-)
r_c	radius of unreacted core of a spherical grain (μm)
r''_{Si}	process rate defined per unit effective surface area of silicon (mol/m^2 s)
r''_0	"intrinsic process rate", i.e. the average nitridation rate per the effective surface area (mol/m^2 s)
ΔP_{bed}	pressure drop through a fluidized bed (mm water)
R	universal gas constant (8.314 J/mol K)
R_0	initial grain radius (μm)
R_i	radius of unreacted silicon grain at a moment of i^{th} product shell peeling occurrence (μm)
R_M	radius of unreacted silicon grain at a moment of the last possible product shell peeling occurrence (μm)
R^*	outer radius of a swelling spherical grain, reacting according to the SIM model (μm)
S	unreacted silicon surface area (m^2)
S_0	initial surface area of a grains having a wide size distribution (m^2)
S_{eff}	effective silicon surface area that reasonably contribute to the reaction (m^2)
S_m	total surface of a fraction of grains in a size distribution which have a mean initial radius $R_{0,m}$ (-)

NOTATION (continued)

S_w	specific surface area of silicon pellets or original silicon grains (m^2/g)
S^*	portion of unreacted silicon surface area occupied by large grains in a particular size distribution that negligible affects overall process rate (m^2)
t	reaction time (hr or s)
t_i	moment of the i^{th} product shell peeling occurrence (s)
t_*	arbitrary scale parameter for time (s)
t^*	parameter that corrects reaction time scale for an induction period and an initial reaction stage (hr)
$\bar{t}$	dimensionless time
T	absolute temperature (K)
u	superficial gas fluidizing velocity (cm/s)
u_0	set point superficial gas fluidizing velocity (cm/s)
u_i	mobility of charged species (m^2/mol J s)
w_m	distribution mass (volume) fraction of grains having an initial radius $R_{0,m}$ (%)
W_α'	mass fraction of the α-silicon nitride in silicon-silicon nitride mixtures on silicon free basis (-)
W_β'	mass fraction of the β-silicon nitride in silicon-silicon nitride mixtures on silicon free basis (-)
W_γ	mass fraction of phase γ in a mixture (-)
x_i	fractional conversion defined by Equation 48
X	overall conversion of silicon (% or dimensionless)

NOTATION (continued)

X_1	constant defined by Equation B32 (-)
X_2	constant defined by Equation B32 (-)
X_m	conversion of a fraction of grains in a size distribution which have a mean initial radius $R_{0,m}$ (-)
X_f	asymptotic overall conversion (%) defined by Equation 77
X^j	overall silicon conversion determined in the sample sampled at discrete reaction time t^j (-)
X_i	overall conversion of silicon at a moment of i^{th} product shell peeling occurrence (% or dimensionless)
X_α	yield of α-silicon nitride (%, or dimensionless)
X_β	yield of β-silicon nitride (%, or dimensionless)
y_*	arbitrary scale parameter for length (m)
$\overline{y}$	dimensionless distance
Y	function defined by Equation 60 (m^2)
Y_1	constant defined by Equation B31 (-)
Y_2	constant defined by Equation B31 (-)
V_0	total initial volume of grains in a given size distribution (m^3)
V_m	volume of a fraction grains in a size distribution which have a mean initial radius $R_{0,m}$ (-)
z	number of proton charges carried by a charged species

NOTATION (continued)

Greek Letters

δ	thickness (μm)
δ^*	critical silicon nitride layer thickness at which nitride breaks and peals from the surface (nm)
δ_{max}	maximum film thickness that corresponds to complete conversion in Equation 40
ζ	constant defined by Equation 40 (s^{-1})
ξ	volume of a solid product produced per volume of a solid reactant consumed (-)
κ	apparent process rate constant (hr^{-1})
λ	ratio between critical product layer thickness and initial grain radius (-)
η_i	volume of the product formed per mole of transferred species (m^3/mol)
ρ_B	density of solid B (kg/m^3)
τ_i	time needed for complete conversion of a grain having a radius R_i (s)
θ	diffraction angle (°, i.e. deg)
θ_M	time defined by Equation 56 (s)
θ^i_{i-1}	time scale between two successive peeling occurrences (s)
Θ	time interval between two successive peeling occurrences (s)
Φ	electrostatic potential (V)
Ψ	function defined by Equation 57 (-)

NOTATION (continued)

Abbreviations

BSE	back-scatter electron
fwhm	full width at half maximum of a peak in a X-ray diffractogram
PDF	Powder Diffraction Files
RIR	Reference Intensity Ratio in X-ray diffraction
SCM	shrinking core model
SCMDC	shrinking core model wit ash diffusion control
SEM	scanning electron micrograph
SIM	sharp interface model
TEM	transmission electron microscopy
TGA	thermo-gravimetric analysis
XRD	X-ray diffraction

KINETIC STUDY ON THE PRODUCTION OF SILICON NITRIDE BY DIRECT NITRIDATION OF SILICON IN A FLUIDIZED BED: EXPERIMENT AND MODELING

1. INTRODUCTION

In the last decade, silicon nitride (Si_3N_4) became a very important material for making components which are to operate under severe mechanical and thermal stresses. Silicon nitride exists as an amorphous form as well as in two crystalline modifications designated α and β. The more desirable polymorph for high temperature engineering applications is β-silicon nitride because it has excellent thermal shock and oxidation resistance as well as high temperature strength (Lange, 1979). However, this polymorph cannot be directly used as the starting material for making a good quality components, thus the β-form is not the preferred product in production of raw silicon nitride material.

Fabricating β-silicon nitride parts for high temperature engineering applications is a complex, multistep process. The starting raw material is fine α-silicon nitride powder (ideally) which is mixed with special additives (Al_2O_3-Y_2O_3) and shaped into a desired component. Finally, the component is sintered at high temperatures (1700-1800°C) where the α-to-β phase transformation occurs, providing a dense microstructure of high mechanical and thermal strength.

The chemical and physical properties of the starting powder are critical to both success in fabricating a dense part and ensuring the required physical properties in the component. The major powder properties to be considered are phase composition and concentration, trace impurities (Fe, Ni, Ca, O, C) and size distribution of crystallites and/or agglomerates (Rhodes and Natansohn, 1989; Dijen et al., 1994; Yamada, 1993). The fact that α-to-β phase transformation plays an important role in the densification process and that the α-form dissolves faster in the sintering additives than does the β-form, makes it imperative to use a high α-phase content silicon nitride as the starting raw material. However, it has been proven useful to have some small amount of the β-form present to provide nucleating sites for α-to-β recrystallization during the final sintering step (Rhodes and Natansohn, 1989).

In summary, the desired product in the production of silicon nitride is a powder of a few tenths of micron in size, with at least 90% (preferably 95%) of α-form, little or no remaining unreacted silicon, and metallic trace impurities as low as possible. Such material is commercially produced by several typical processes which are briefly discussed in the next section. However, wide use of silicon nitride is constrained by its current high production cost. The main purpose of this work was to improve one of the methods for the production of this important material - the direct nitridation method based on the reaction between silicon powder and nitrogen gas, by using fluidized bed technology.

2. PROBLEM STATEMENT AND OBJECTIVES

2.1 Techniques for Producing Silicon Nitride Powder

There are four typical processes for producing silicon nitride powder (Yamada, 1993), each will be briefly described in this section. They yield final products which differ in quality and cost of production.

2.1.1 Carbothermic Reduction and Nitridation of SiO_2

In the presence of carbon and nitrogen, fine silica powder reacts according to the overall equation (Schwier, 1983):

$$3\ SiO_2 + 6\ C + 2\ N_2 \rightarrow Si_3N_4 + 6\ CO \qquad (\Delta H = 1270\ \text{kJ/mol at } 1227\ ^\circ\text{C}) \qquad (1)$$

A fine α-silicon nitride powder can be produced directly by using very fine silica. Since excess carbon black has to be used, a competitive reaction toward silicon carbide occurs and some free carbon can remain in the nitride powder. By annealing these powders in air, this carbon can be partially oxidized, but so is the silicon nitride. Consequently, the product produced by this method often suffers from purity problems associated with residual carbon and oxygen contents.

2.1.2 Vapor-Phase Reaction

This process is based on the gas phase reaction between silane, or chlorosilanes (diluted in nitrogen), and ammonia. Even though byproduct ammonium chloride decomposes at temperatures above 400°C, the overall process could be described as follows (Yamada, 1993):

$$3\ SiCl_4 + 16\ NH_3 \rightharpoonup Si_3N_4 + 12\ NH_4Cl \quad (\Delta H = -973\ \text{kJ/mol at } 1227\ ^\circ\text{C}) \tag{2}$$

$$3\ SiH_4 + 4\ NH_3 \rightharpoonup Si_3N_4 + 12\ H_2 \quad (\Delta H = -502\ \text{kJ/mol at } 1227\ ^\circ\text{C}) \tag{3}$$

The product in this case is amorphous silicon nitride of high purity with respect to metallic impurities, but it can have a high chlorine content when silicon tetrachloride is used. Production costs are high due to the use of costly silane or corrosive silicon tetrachloride. The reaction represented by Equation 3 has been used for producing micro-electronics components, while that by Equation 2 has never been commercialized.

2.1.3 Thermal Decomposition of Silicon Diimide

This process provides the best quality commercially available silicon nitride powder. The product is in the form of very fine particles and of a high α-content and purity. The process is very complex but could be described by

two steps. In the first step, chlorosilanes react in the liquid phase with ammonia at room temperature, or lower, to form silicon diimide:

$$3\ SiCl_{4\,(l)} + 6\ NH_{3\,(l)} \rightarrow Si(NH)_2 + 4\ NH_4Cl \qquad (4)$$

$$(\Delta H = -463\ \text{kJ/mol at } 25\ ^\circ\text{C})$$

After removing the ammonium chloride, the silicon diimide is given a polymerization heat treatment in nitrogen (Drew, 1989) or ammonia (Yamada 1993). The polymer is then pyrolized at 1100°C in nitrogen to produce amorphous silicon nitride. Subsequent heat treatment at temperatures higher than 1430°C converts amorphous product into the α-crystalline form, which may be represented by an overall stoichiometric equation as

$$3\,Si(NH)_2 \rightarrow Si_3N_4 + N_2 + 3\,H_2$$

The production costs of this process are high due to the use of silicon tetrachloride and the fact that extensive effort is required to purify the intermediate product before calcination.

2.1.4 Direct Nitridation Method

This is the most commonly used process in the production of α-silicon nitride (Cambier and Leriche, 1990). The process is based on contacting elemental silicon powder with nitrogen at high temperatures. Since this work concentrates on this method, the next section discusses the direct nitridation process in more detail. Although the self propagated nitridation or

combustion reaction uses the same reaction to nitride compressed silicon bodies, it is carried out at extremely high pressures, and this thesis does not deal with such nitridation.

2.2 Direct Nitridation of Silicon

Direct nitridation of silicon accounts for most of the silicon nitride produced commercially (Rhodes and Natansohn, 1989). During direct nitridation silicon is heated in a nitrogen atmosphere at temperatures between 1200-1500°C. This rather elaborate and long time cycle may be presented by the overall stoichiometric equation:

$$3\ Si_{(s)} + 2\ N_{2\,(g)} \rightarrow Si_3N_{4\,(s)} \qquad (\Delta H = -736\ \text{kJ/mol at } = 1227\ ^\circ\text{C}) \qquad (5)$$

This reaction is highly exothermic, and extreme care must be taken to control the reaction temperature to prevent melting of the silicon powder. Complete nitridation becomes virtually impossible if the temperature is not controlled properly resulting in melting of the silicon (Drew, 1989). Also, α-silicon nitride can dissolve in the liquid silicon and the β-crystal reprecipitates, thereby decreasing the yield of the desired α-form (Morgan, 1980).

The direct nitridation process is more complicated than Equation 5 implies. Although there are several models proposed to describe the reduction of grain size due to nitridation of silicon (Inomata, 1975; Inomata and Uemura,

1975; Atkinson et al., 1974 and 1975; Atkinson et al., 1976) there is no general agreement regarding the mechanism of nitridation.

According to Jennings (1983) and Jennings et al. (1988), the α-crystal is formed by the reaction between molecular nitrogen and silicon in the gas phase while the reaction between silicon and atomic nitrogen yields the formation of the β-phase. Once the silicon surface becomes covered by the nitride layer the consequent reaction becomes rather slow, with the supply of silicon to the reaction site being the rate-controlling step, at temperatures below the melting point of silicon (~1407°C).

The presence of oxygen as either a trace impurity in the nitriding atmosphere or in the native silica layer covering the silicon surface, may cause an entirely new set of the reactions to occur:

$$Si_{(s)} + O_{2\,(g)} \rightleftharpoons SiO_{2\,(s)} \qquad (6)$$

$$3\ SiO_{2\,(s)} + 2\ N_{2\,(g)} \rightleftharpoons Si_3N_{4\,(s)} + 3\ O_{2\,(g)} \qquad (7)$$

$$SiO_{2\,(s)} + Si_{(s)} \rightleftharpoons 2\ SiO_{(g)} \qquad (8)$$

$$2\ SiO_{(g)} + N_{2\,(g)} \rightleftharpoons 2\ Si_2N_2O_{(s)} + 0.5\ O_{2\,(g)} \qquad (9)$$

$$3\ SiO_{(g)} + 2\ N_{2\,(g)} \rightleftharpoons Si_3N_{4(s)} + 1.5\ O_{2\,(g)} \qquad (10)$$

Lindley et al. (1979) believed that the dominant reaction during nitridation is the reaction between silicon monoxide and nitrogen which yields the α-form (Equation 10). However ΔG° for this reaction is large and positive (545 kJ/mol at 1700 K) and an efficient sink of oxygen is required if this

reaction is to take place (Dervisbegovic and Riley, 1981). Barsoum et al. (1991) and Pigeon et al. (1993) also attributed an important role to gaseous silicon monoxide. Therefore, hydrogen is commonly added to the nitrogen to control the partial pressure of oxygen and to prevent the reoxidation of the silicon surface, which hinders nitridation (Dawson and Moulson, 1978; Morgan, 1980; Dervisbegovic and Riley, 1981; Itoh, 1991). Other workers have shown that the addition of hydrogen significantly enhances the extent of reaction and increases the α/β ratio (Barsoum et al., 1991; Itoh, 1990; Jennings, 1983). In some cases, ammonia, which is almost completely decomposed to hydrogen and nitrogen at the reaction temperature, was used as the nitriding gas (Yamada, 1993; Shimizu et al., 1991).

Another potential problem in this process is the presence of trace metallic impurities in the raw silicon powder (iron, aluminum, calcium) that may significantly affect the progress of nitridation. Campos-Loriz and Riley (1978) believed that the reaction yielding the β-phase takes place predominantly at impurity-rich sites. For example, iron tends to form a low melting point alloy with silicon, which provides a liquid phase that dissolves the α-phase and facilitates the growth of the undesired β-silicon nitride. On the other hand, the presence of liquid enhances the inter-phase contact which may explain the catalytic role of iron for increasing the reaction rate as well as the final extent of the reaction (Dervisbegovic and Riley, 1979; Pigeon et al., 1993). However, Pigeon et al. (1993) reported that the presence of liquid caused by the formation of low melting point eutectics does not necessarily increase the

yield of the β-form. They investigated calcium promoted nitridation which resulted in a very high α/β ratio ($W_\alpha/W_\beta \sim 10$). Another possible explanation for the iron effect is reported by Jennings et al. (1988) who believed that iron accelerates the reaction by participating in the removal of the native silica layer.

2.3 Objectives

The main goal of this work was to improve an existing, essentially packed bed, batch direct nitridation process. The main features requiring improvement are the following:

- long reaction times (of the order of days);
- poor temperature control which causes a non-uniform product quality both within a bed and from batch to batch;
- large chunks of produced silicon nitride which must be ground to a fine powder before further processing.

The proposed method would utilize fluidized bed technology which, in general, offers advantages for gas-solid reactions. A fluidized bed reactor requires relatively low power consumption and provides uniform distribution of system parameters such as temperature, enhanced heat transfer, and relatively easy solids handling and scale-up (Kunii and Levenspiel, 1991). The main problem in operating this type of reactor is the fact that very fine particles cannot be fluidized, since fines tend to agglomerate or form clusters and eventually the fluidized bed collapses into a packed bed (Geldart, 1984).

Good design of a fluidized bed reactor must compromise its advantages and disadvantages and should be based on reliable kinetic data. However, results of kinetic studies reported in literature are applicable only to the specific set of experimental conditions in which the data were obtained. Most of the kinetic data were obtained by TGA (thermo-gravimetric analysis) where heat and mass transfer effects on the overall process rate were neglected. Also, much of the variation in the published kinetic data can be attributed to the effects of a particle (grain) shape and grain size distribution. Reported fluidized bed nitridation results do not provide useful information because the results were obtained in continuously operating fluidized beds with a significant amount of inert silicon nitride added to the raw silicon material to make temperature control feasible (Shimizu et al., 1991).

Despite the complexity of the nitridation process, a number of observations point to the reaction temperature and the composition of reactant gas mixture (hydrogen and nitrogen concentrations) as being two of the key factors controlling both the overall conversion of silicon and the α/β ratio in the produced silicon nitride (Itoh, 1991; Morgan, 1980; Barsoum et al., 1991; Heinrich, 1980).

The objectives of this work were as follows:

- to determine an operating range of fluidization velocities, for chosen silicon particles, with respect to bed temperature and gas composition;
- to design an experimental set-up that enables investigation of nitridation

kinetics at isothermal conditions but using silicon as the raw material, with no inert solids added;

- to develop a reliable method for quantitative analysis of silicon/α-/β-silicon nitride mixtures;
- to investigate effects of reaction temperature, hydrogen and nitrogen concentration on both the overall conversion of silicon and on the α/β ratio in the product;
- to suggest a possible commercial process (batch, semi-batch or continuous), on the basis of experimental results;
- to elucidate a mechanism and to develop a mathematical model of the nitridation of silicon powder.

3. EXPERIMENTS

3.1 Experimental Setup, Materials and Methods

3.1.1 Characterization of Silicon Raw Material

As mentioned before, to be ready for further processing which provides a good quality sintered part, the produced silicon nitride should be, ideally, in the form of fine powder with a particle size on the order of one tenth of a micron. This would eliminate additional costs imposed by both excessive grinding and purification of the final product due to contamination during grinding. Since porous silicon compacts consisting of fine grains remain, practically, of the same size during nitridation, production of a fine silicon nitride powder would impose the use of very fine raw silicon particles.

Micron-size silicon particles, however, behave as a difficult to fluidize Geldart C powder (Kunii and Levenspiel, 1991), even at room temperature (Liu and Kimura, 1993). Since inter-particle forces and "stickiness" of particles generally increase with temperature, the idea of using fine silicon particles for this study was not employed. Therefore, to make fluidization feasible, first the choice of a suitable silicon raw material had to be made.

To overcome the above size problem, the raw material particles used in this work were porous silicon pellets provided by Shin-Etsu Chemical Company, Ltd., which had also been used in the fluidized bed nitridation work of Shimizu et al. (1991). These pellets were prepared by starting with

fine silicon grains of an average particle size of ~ 2 μm in diameter and granulating them to an average size of ~ 400 μm with the aid of a suitable binder such as polyvinyl alcohol. The extruded resulting granules were, then, briefly sintered at 1100 to 1300°C, so they became slightly cemented together, but not melted (Shimizu et al., 1991a). The specification of silicon raw material is given in Table 1, and typical size distributions and the corresponding specific surface areas of the original grains, measured by a HORIBA CAPA-700 Particle Size Analyzer, are enclosed in Appendix A. As shown by the scanning electron micrograph (SEM) in Figure 1, the final pellets were rather cylindrical, hence their mean diameter determined by sieving analysis does not present pertinent information about their real size.

Table 1. Specification of raw silicon material.

Trace impurities (wt%)*					BET area**	mean diameter
Fe	Al	Ca	C	O	S_w (m^2/g)	d_p (μm)
0.08	0.10	0.02	0.02	0.51	1.7-2	~ 400
source: *Shin-Etsu Chemical Company Ltd.; **Micromeritics ASAP 2000						

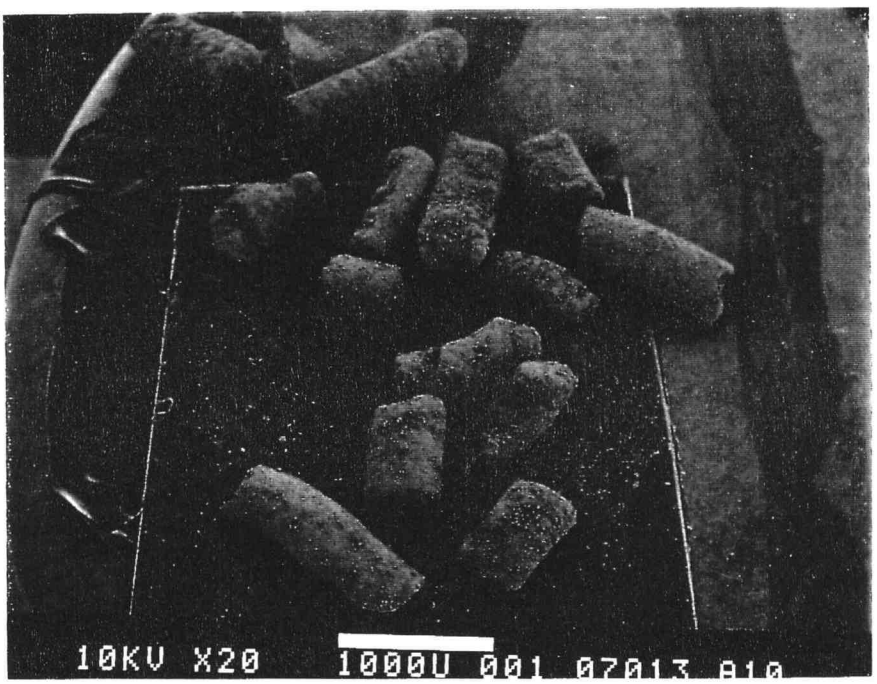

Figure 1. SEM photo of raw silicon pellet

3.1.2 Experimental Apparatus

Figure 2 illustrates the experimental apparatus, which consists of a high temperature fluidized bed reactor, a system for controlling the composition of gaseous reactant mixtures, and pneumatic solids charge and discharge systems.

Flow rates of individual gases (pre-purified grade nitrogen and hydrogen, standard grade argon) were measured by calibrated rotameters. The measured oxygen concentration in the gasses (Portable Trace Oxygen Analyzer, Teledyne Analytical Instruments Model # 311) was about ~ 5 ppm.

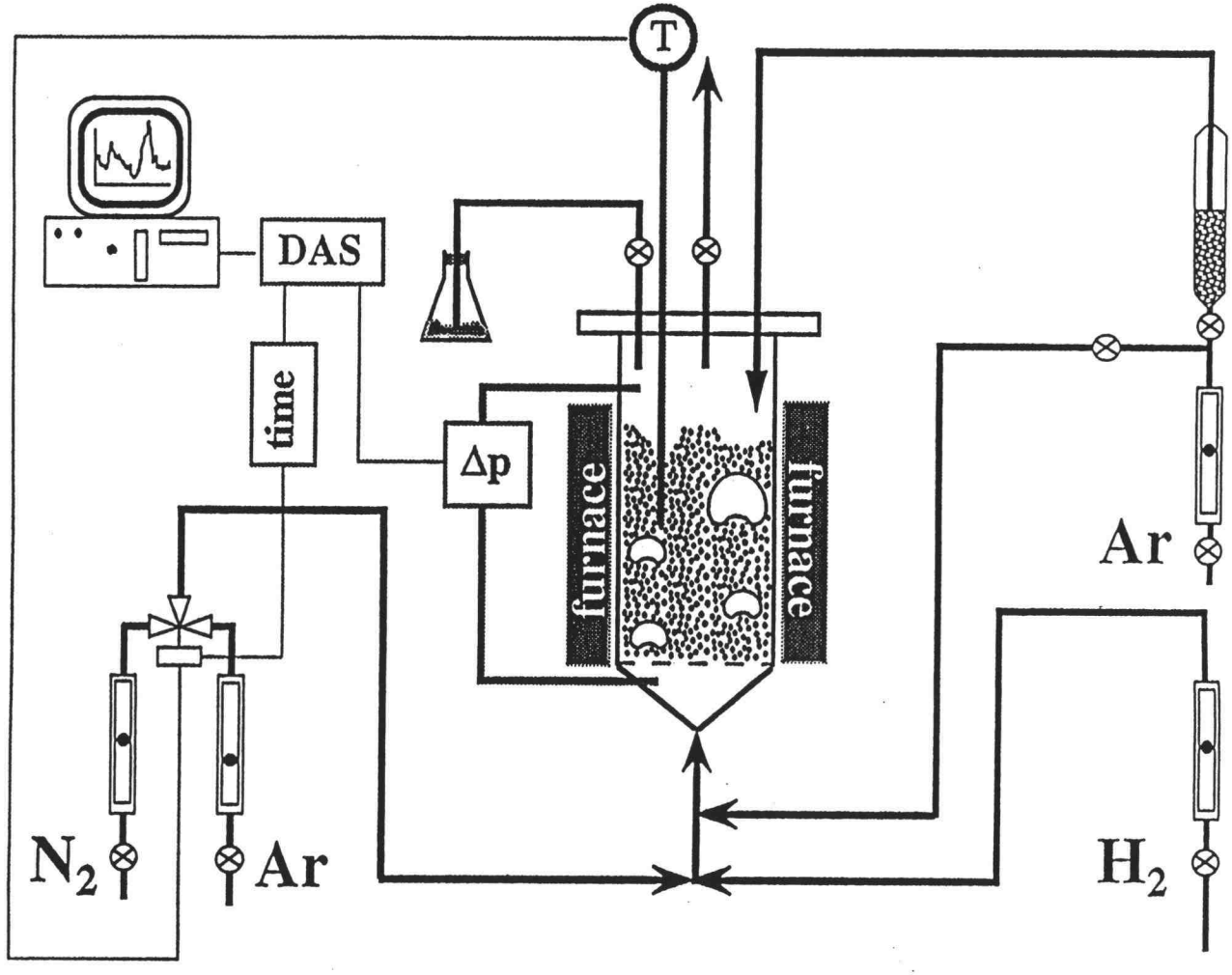

Figure 2. Schematic representation of experimental setup.

Bed temperature was measured with an R-type thermocouple inserted into the bed to about 3 cm above distributor. The thermocouple was shielded in an alumina tube to prevent its damage due to the reaction between platinum and hydrogen at high temperatures; this definitely affected the time response of the temperature readings. A pressure transducer and a data acquisition system (DAS) gave on-line pressure measurements and pressure drop fluctuations, and monitored the fluidization condition of the bed. The reactor pressure was slightly above atmospheric pressure. Detailed description of all the components of the experimental setup is presented in Table 2.

3.1.3 Choice of Operating Gas Velocity

Before the kinetic experiments were started, the choice of the operating gas velocity had to be made based on the following facts:

– the density of the particles increases by approximately a factor of 1.7 with the progress of nitridation;

– the experiments were intended to be carried out at various temperatures and at various hydrogen concentrations in the fluidizing gas resulting in different gas properties.

In order to determine an operating velocity which provides fluidization for the whole range of particle densities and the various properties gas mixtures, fluidization curves for previously nitrided pellets were determined at temperatures between 1200 and 1350°C and hydrogen gas concentrations

Table 2. Description of components of experimental setup.

REACTOR	
material	mullite
size	55 mm (ID) × 1200 mm (L)
distributor	perforated alumina plate with 69 holes (Ø = 1 mm)
FURNACE	
model	Lindberg 58475 (240 V/60 Hz) (A Unit of General Signal): three zones with silicon carbide rod heaters
max. temperature (°C)	1600
tube size	100 mm (ID) × 1500 mm (L)
temp. controllers	EUROTHERM: 818 (master), 2 × 847 (slaves)
INSTRUMENTATION	
temperature indicator	Microcomputer Thermometer DP-701 (OMEGA)
pressure transducer	Validine, P305-D: 0-14" H_2O (0-5 V DC)
DATA ACQUISITION SYSTEM (DAS)	
type and configuration	PCI 2000 series: 1C-2A (carrier), 2M (12-bit AI 0-10V) single-ended, 24T-2 (analog termination panel); Intelligent Instrumentation, A Burr Brown Company
software application	Labtech Notebook 6.2.0. (Lab. Tech. Corporation)

ranging from 0 to 50% by volume. The silicon nitride pellets were provided by Shin-Etsu Chemical Company, Ltd.

Figure 3 compares the fluidization curve obtained in pure nitrogen at 1200°C with the one obtained at 1350°C in 50% nitrogen - 50% hydrogen. One can see that the minimum fluidization velocity of the silicon nitride pellets ($u_{mf} \approx 9$ cm/s) does not vary significantly with extreme changes in temperature

and composition of the fluidizing gas. On the basis of these measurements, the operating gas velocity was chosen to be at least u_o = 25 cm/s, which is well above the minimum fluidization velocity of nitrided pellets. This velocity provided vigorously fluidized solids and good fluidization within a wide range of experimental conditions. However, as it will be discussed later, at temperatures of 1300°C and higher, the above velocity was insufficient to keep pellets apart, thus the fluidization velocity had to be increased to 35 cm/s to provide proper mixing of the bed.

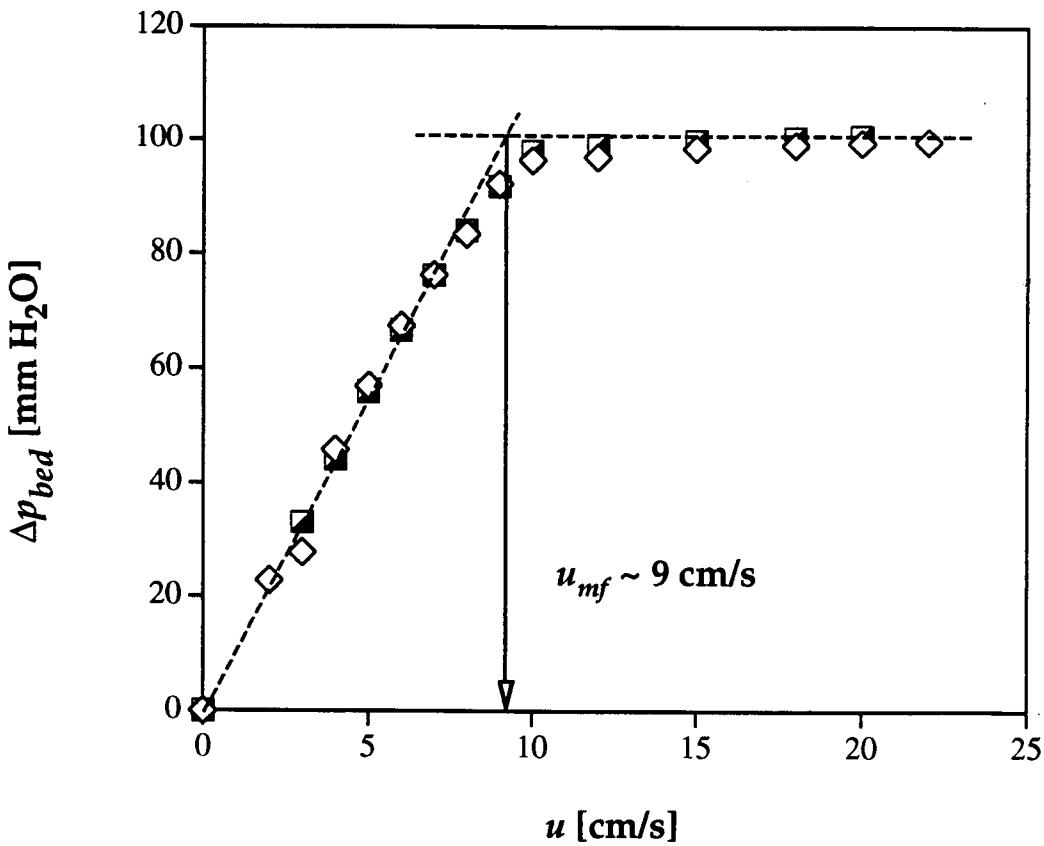

Figure 3. Determination of minimum fluidization velocity of silicon nitride pellets (d_p ~ 400 μm): diamonds -1200°C, 100% nitrogen; squares - 1350°C, 50% nitrogen - 50% hydrogen.

3.1.4 Experimental Procedure

All of the nitridation kinetics experiments were carried out in batch-solids operations. After the empty reactor was preheated to a prescribed reaction temperature, a gas mixture containing 60% argon - 40% hydrogen by volume was supplied to the bed at a superficial velocity u_o, based on the empty bed at the set-point temperature. Silicon particles (~ 100 g) were first fluidized for ~ 5 min by argon in the feeding container to decrease the oxygen content in the voids, after which they were charged into the bed by pneumatic transport using argon as the carrier gas. Since the cold silicon particles were suddenly supplied to the bed (within ~ 30 s), this caused the bed temperature to drop about 300-400°C below the set-point temperature. After the bed temperature had reached the set-point (in about 10 min), the particles were kept fluidized in the argon-hydrogen mixture for additional 60 min. This pretreatment was carried out to remove as much of the oxide coating on the silicon surface as possible, and to prepare the silicon for nitridation. To investigate the effect of the pretreatment, a few runs were also made by starting the reaction immediately after the bed temperature recovered to its set-point.

When the silicon particles were properly treated, the flow rates of hydrogen and argon were readjusted to set the hydrogen concentration at the desired level. The reaction was then initiated by actuating a solenoid valve (5V DC) which switched argon to nitrogen without changing the flow rate. As the bed temperature started to rise due to the heat released by nitridation, the

solenoid valve was deactivated, switching nitrogen back to argon, thus quenching the reaction mixture. The DC signal used to actuate the valve also triggered a timer in the data acquisition system, which provided the cumulative reaction and quenching times with a resolution of 1s. At the same time, the set point on the furnace controller was lowered to adjust the energy input to the furnace, which provided a stable bed operating temperature without quenching. This on/off procedure was used during the initial stage of nitridation, in particular, to keep the bed temperature within ± 3°C of the set-point during most of the reaction time. It should be mentioned that the hydrogen feed line was independent and unaffected by an action of the solenoid (Figure 2), hence, hydrogen was supplied to the reactor at a desired flow rate to maintain a constant concentration throughout the run.

The reaction could be terminated (by quenching), and resumed again (by enabling the nitrogen flow through the bed) in seconds. Slow response of the temperature indicator, however, hindered the information about the actual reaction temperature in this unsteady-state reaction regime. Hence, it was of particular interest to operate the bed in this reaction regime as short as possible, usually less than 5 min (reaction time).

The volumetric flow rates of argon (the quencher) and nitrogen (the reactant) were kept the same to maintain the fluidizing velocity at the set point u_o. This was done to compensate for the error caused by the gas flow lag time between the solenoid valve and the actual physical appearance of the either quencher or reactant in the bed, i.e. the errors in counting corresponding to

either reaction or quenching times. In experiments where separate effects of nitrogen and hydrogen concentrations were investigated, an additional argon line was used to supply inert gas into the bed and adjust both nitrogen and hydrogen concentrations to a desired level.

At various reaction times, samples of reacted solids were withdrawn from the reactor through a pneumatic discharge line without disturbing the reaction conditions in the bed. Each sampling mass was about 1 - 3 g and the total mass of sample solids withdrawn throughout the run was kept small so that the fluidization condition was not altered significantly. Sampled particles were sieved into three groups : > 425, 355 - 425 and < 355 μm. The samples were ground and the compositions of α-, β-silicon nitride and silicon were determined by the powder X-ray diffraction (XRD), as it will be explained in the following section.

The key feature of the experimental setup described above is that it enabled a stable nitridation process, even though the amount of silicon used was much higher than that used in the reported studies where melting of silicon was observed (Sheldon et al., 1992). Moreover, due to the high fluidized solids/immersed bodies heat transfer coefficient (Kunii and Levenspiel, 1991), it is believed that the measured bed temperature represented the pellet temperature well. A rough estimate of the temperature gradient in a gas film (Levenspiel, 1993), based on the particle-to-gas fluidized bed heat transfer coefficients reported by Turton and Levenspiel (1989), gives ΔT_{film} ~ 23°C, and of the one within a pellet ΔT_{max} ~ 2°C (Levenspiel, 1993).

3.2 Quantitative Analysis of the Product

The silicon/α-/β-silicon nitride phase compositions of sample solids were determined by powder X-ray diffraction. Sample particles were ground to fine powder having a mean size of about 2 μm, measured by a HORIBA CAPA-700 particle size analyzer. The XRD analysis was then performed by using a solid state detector (Si, Li) SIEMENS D5000 diffractometer with CuK_α radiation. In the range of 2θ = 27-37°, each sample was continuously scanned with a spinner with a step size of 2θ = 0.01°, and a counting time of 5 s/step. The data was collected by using a variable slit size and then corrected by multiplying measured intensities by $1/sin\theta$. Peak areas, background noise, and separation of overlapped peaks were determined by fitting the profiles using a modified Voigt function in the Diffrac-AT Software package.

Due to the discrepancy found in the reported methods for determining α-/β-silicon nitride ratios and possible effects of preferred orientation and extinction on the determination of Si/α-silicon nitride ratios, an original method to evaluate the calibration constants was developed (Jovanovic and Kimura, 1994) and described in details in Appendix B. Thus, the integrated intensities of the (102), (210), and (201) peaks of α-silicon nitride, (101) and (210) peaks of β-silicon nitride, and (111) peak of silicon were used for determining mass fractions of these three phases in the following equations:

$$\frac{I_\alpha(102) + I_\alpha(210)}{I_\beta(101) + I_\beta(210)} = 0.647 \frac{W_\alpha}{W_\beta} \tag{11}$$

$$\frac{I_{Si}(111)}{I_\alpha(201)} = 5.53 \frac{W_{Si}}{W_\alpha} \tag{12}$$

$$W_\alpha + W_\beta + W_{Si} = 1 \tag{13}$$

where $I_\delta(hkl)$ signifies the integrated intensity of the *hkl* reflection of phase δ, and W_δ is the mass fraction of corresponding phase δ in a mixture.

From measured mass compositions of a sample, the overall conversion of silicon, X, and the fractional yields into the α and β forms, X_α and X_β, respectively, were calculated as follows:

$$X = \frac{\text{moles of } Si \text{ converted}}{\text{initial moles of } Si} = \frac{1 - W_{Si}}{1 + \left(\frac{M_{SN}}{3M_{Si}} - 1\right) W_{Si}} \tag{14}$$

where M_{Si} and M_{SN} are the molar masses of silicon and silicon nitride, respectively. Recognizing that $M_{SN} / 3M_{Si} = 1.665$, the fractional yields become

$$X_\alpha = \frac{1 - W_{Si}}{1 + 0.665\ W_{Si}}\ W_\alpha'$$
$$X_\beta = \frac{1 - W_{Si}}{1 + 0.665\ W_{Si}}\ W_\beta' \tag{15}$$

where W'_α and W'_β represent the mass fractions of the corresponding phases but on the silicon-free basis. i.e.

$$W_\alpha' = \frac{W_\alpha}{W_\alpha + W_\beta}$$
$$W_\beta' = \frac{W_\beta}{W_\alpha + W_\beta} \quad (16)$$

The overall conversion of silicon and the two yields are correlated by

$$X = X_\alpha + X_\beta \quad (17)$$

Figure 4 is an example of X-ray diffraction scan, which indicates the result of solids processed in 30% nitrogen-10% hydrogen-60% argon for 8.5 hours at 1250°C. Based on Equations 11-17, the sample scan gives $X = 0.853$, $X_\alpha = 0.774$ and $X_\beta = 0.079$.

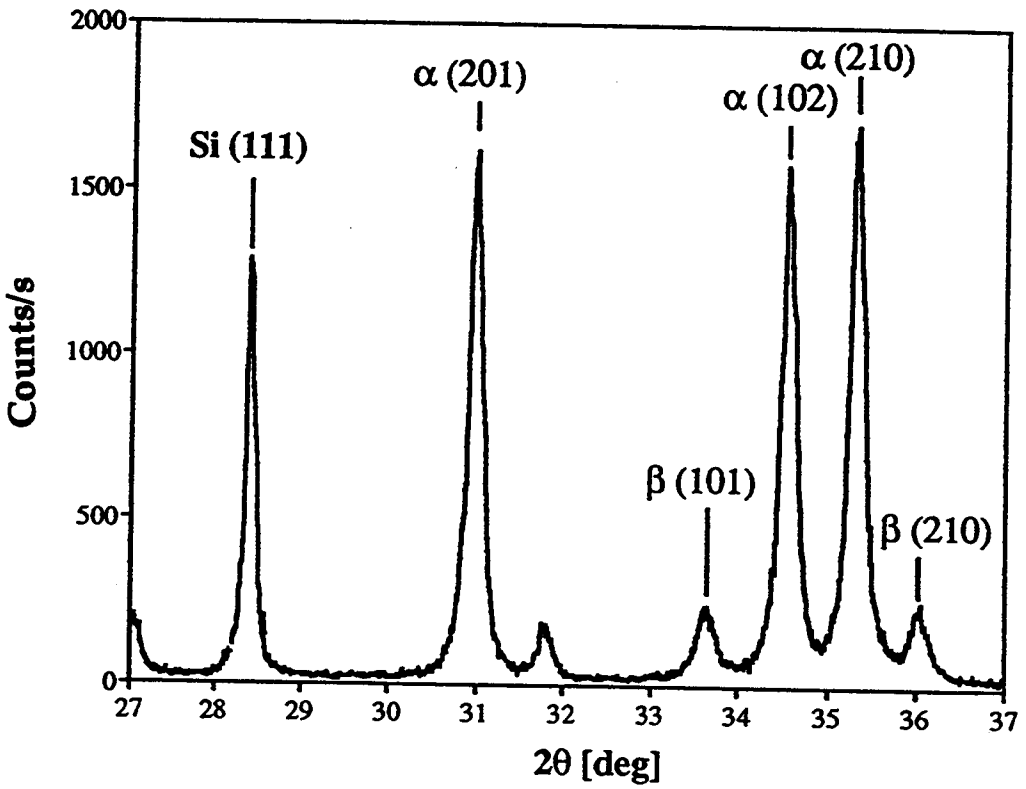

Figure 4. Example of an X-ray diffraction scan of the product.

3.3 Results and Discussion

The total of twenty four nitridation experiments were done and discussed in this study: twenty single-staged and four multi-staged. For the sake of brevity, these experiments are coded and listed in Tables 3 and 4, together with fully specified experimental conditions. Gas compositions in the tables as well as any further discussion in the text are given in volume percent. The summary of the results for each of the runs is tabulated in Appendix C. The table captions in Appendix C correspond to the run code number from Tables 3 and 4, and each of the tables contains the following information:

- time stamp of a sample;
- deconvoluted integrated intensities of the peaks used in Equations 11 and 12, together with
  - full widths at half maximum (**fwhm**) of all the peaks,
  - crystallite sizes of each of the phases, roughly estimated on the basis of the wavelength of Cu_{K_α} radiation (1.5406 Å), **fwhm**'s and the diffraction angle of the peak (θ) as (Cullity, 1978)

$$d \approx \frac{1.5406}{\mathbf{fwhm}\,\cos(\theta)} \quad [\text{Å}] \;; \tag{18}$$

- mass fractions of all the phases, overall conversion and fractional yields of each of the silicon nitride phases, calculated by Equations 11-17;
- the size range of the pellets the sample originates from.

Table 3. Single-staged experiments: coding of runs and corresponding experimental conditions.

	Reaction Conditions					Pretreatment Conditions**		
Code	temp. (°C)	N_2 (%)	H_2 (%)	Ar (%)	u_0 (cm/s)	temp. (°C)	u_0 (cm/s)	Results in Table
run-01	1200	90	10	0	25	1250	25	C- 1
run-02	1225	90	10	0	25	1225	25	C- 2
run-03	1250	90	10	0	25	1250	25	C- 3
run-04	1275	90	10	0	25	1275	25	C- 4
run-05	1300	90	10	0	35	1300	35	C- 5
run-06	1250	90	10	0	25	1250	25	C- 6
run-07	1275	90	10	0	25	1275	25	C- 7
run-08	1275	90	10	0	35	1275	25	C- 8
run-09	1250	30	10	60	25	1250	25	C- 9
run-10	1250	50	10	40	25	1250	25	C-10
run-11	1250	70	10	20	25	1250	25	C-11
run-12	1275	50	10	40	25	1275	25	C-12
run-13	1250	30	5	65	25	1250	25	C-13
run-14	1250	30	30	40	25	1250	25	C-14
run-15	1250	30	50	20	25	1250	25	C-15
run-16	1300	60	40	0	25	1300	25	C-16
run-17	1250	90	10	0	25	1300	25	C-17
run-18	1200	90	10	0	25	not pretreated		C-18
run-19	1200	60	40	0	25	not pretreated		C-19
run-20*	1300	90	10	0	25	1300	25	C-20

*Unreliable run: very frequent quenching; product chunked and the actual bed temperature uncertain (1280-1300°C); **Duration of pretreatment: 60 min.

Table 4. Multi-staged experiments: coding of runs and corresponding experimental conditions.

		Reaction Conditions						Pretreatment Conditions			
Code	Stage	temp. (°C)	N_2 (%)	H_2 (%)	Ar (%)	duration (min)	u_0 (cm/s)	temp. (°C)	duration (min)	u_0 (cm/s)	results in Table
run-21	1	1200	90	10	0	120	25	1250	60	25	C-21
	2	1300	90	10	0	20	25				
	3	1350	90	10	0	20	25				
	4	1390	90	10	0	30	25				
run-22	1	1300	90	10	0	30	25	1300	60	25	C-22
	2	1390	90	10	0	110	25				
run-23	1	1300	60	40	0	45	35	1300	60	35	C-23
	2	1390	90	10	0	150	35				
run-24	1	1250	30	10	60	150	25	1250	60	25	C-24
	2	1200	90	10	0	570	25				

On the basis of their primary objective, the experiments from Tables 3 and 4 may be classified as follows:

- temperature effect (runs 01-05);
- reproducibility of the results (runs 06 and 07);
- effect of fluidizing velocity (run-08);
- effect of nitrogen (runs 09-12);
- effect of hydrogen (runs 13-16);
- effect of pretreatment (runs 17-19);
- simulation of multi-staged batch-solids operation (runs 21-22);
-"seeding effect", i.e. effect of the initial reaction conditions on the nitridation continued at altered reaction conditions (runs 23-24).

3.3.1 Shape of Conversion Curves

A typical conversion curve obtained in fluidized bed nitridation is shown in Figure 5. It exhibits an induction period followed by a rapid rise in overall conversion after which it levels off. The highest reaction rates were generally observed not at the very beginning of the reaction, but at conversions between 20 and 40%, depending on reaction conditions. It can be seen in Figure 5 that the extent of the reaction does not reach 100% even after an extended reaction time. These observations are in agreement with previous findings reported in the literature (Rahaman and Moulson, 1984; Sheldon et al., 1992; Myhre and Motzveld, 1990).

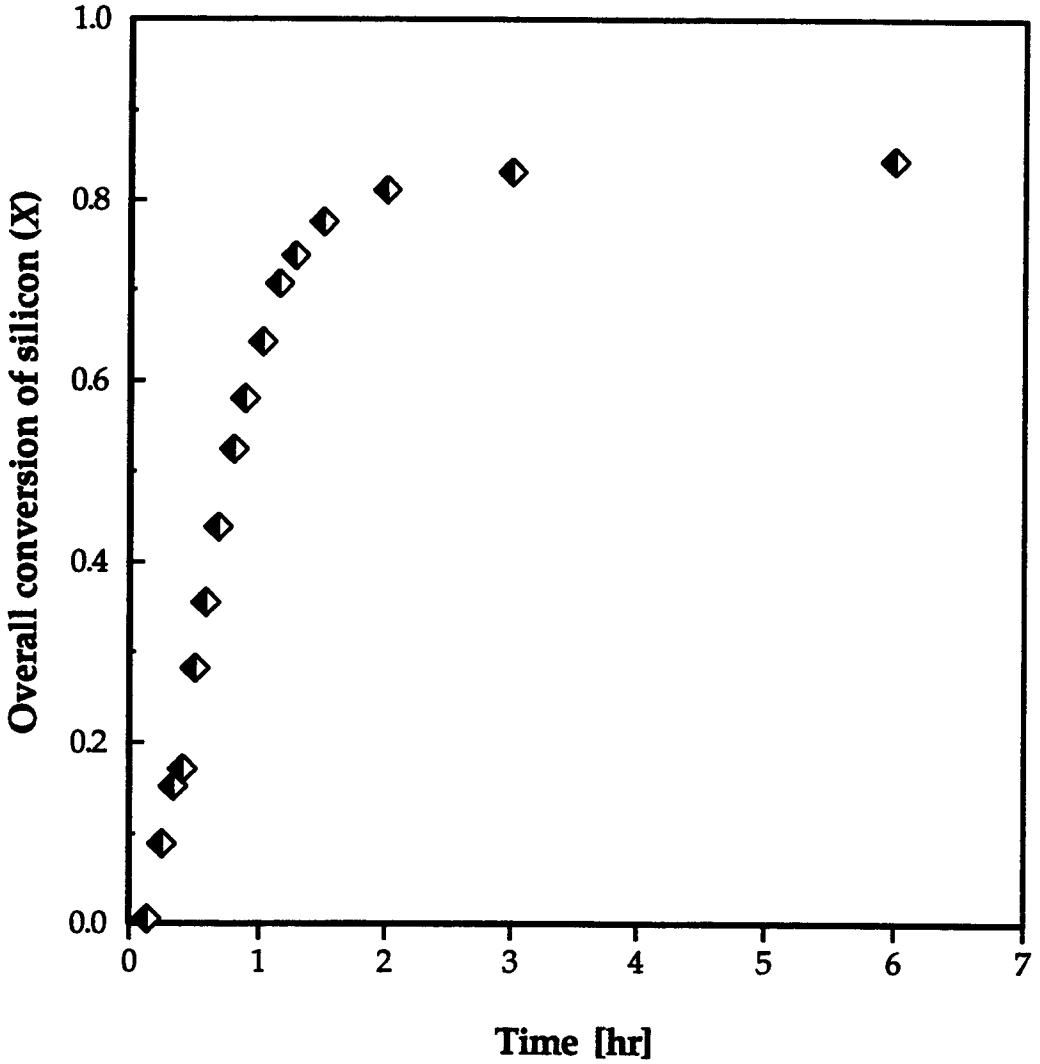

Figure 5. Typical conversion curve (run-04).

The existence of an induction period is usually attributed to the native silica layer covering the silicon surface which hinders nitridation (Dawson and Moulson, 1978; Morgan, 1980; Dervisbegovic and Riley, 1981; Itoh, 1991). Sheldon et al. (1992) reported that a relatively small amount of oxygen leads to longer induction times. However, these authors observed an induction period in the nitridation of unoxidized silicon samples as well. In

this case, the induction period became shorter as reaction temperature was increased, which is, on the other hand, consistent with crystallization and growth kinetics (Avrami, 1939; Shi et al., 1990 and 1991). A closer look at literature data shows that the induction period is seldom observed at reaction temperatures above 1300°C and is more pronounced at lower temperatures.

3.3.2 Inspection of Intra-Pellet Diffusion Resistance

Reactant pellets do not significantly change in their size and original shape during nitridation, as shown in Figure 6. However, preparing porous particles using fine powder occasionally introduces intra-particle diffusion resistance which slows the overall reaction of solids (Szekely et al., 1976). This effect might become particularly important in the case of direct nitridation of silicon where the ratio of product volume formed per reactant volume consumed is (Pigeon and Varma, 1993)

$$\xi = \frac{\text{volume of the product}}{\text{volume of the reactant}} = 1.216 \qquad (19)$$

A higher product volume decreases the porosity of the pellet which occasionally may be reflected by increased diffusion resistances for reacting species.

To preliminary test any possible effect of the intra-pellet diffusion resistance, sampled particles were sieved into three groups, and the overall conversion of silicon in particles larger than 425 μm was compared with the conversion in the particles smaller than 355 μm.

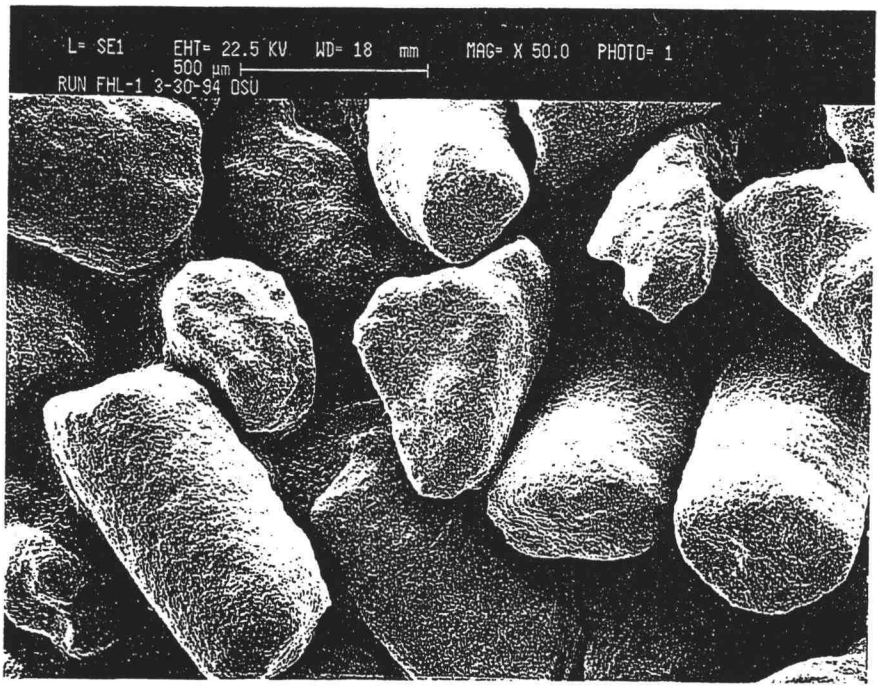

Figure 6. SEM picture of nitrided pellets.

Figure 7 shows that the particle size in the range investigated does not affect the overall conversion of silicon. The difference between the two spherical particle sizes compared here should cause a difference of at least 43% in the reaction time to reach the same overall conversion, if the intra-particle diffusion had limited the gas-solid reaction (Levenspiel, 1993). This conclusion, however, could be wrong if the above calculation is applied to non-spherical pellets. Moreover, attrition of the bed may alter particle size distribution, so the age of the pellet of a particular size is generally unknown. From all of these reasons, the distribution of the product within a pellet was observed by microprobe analysis.

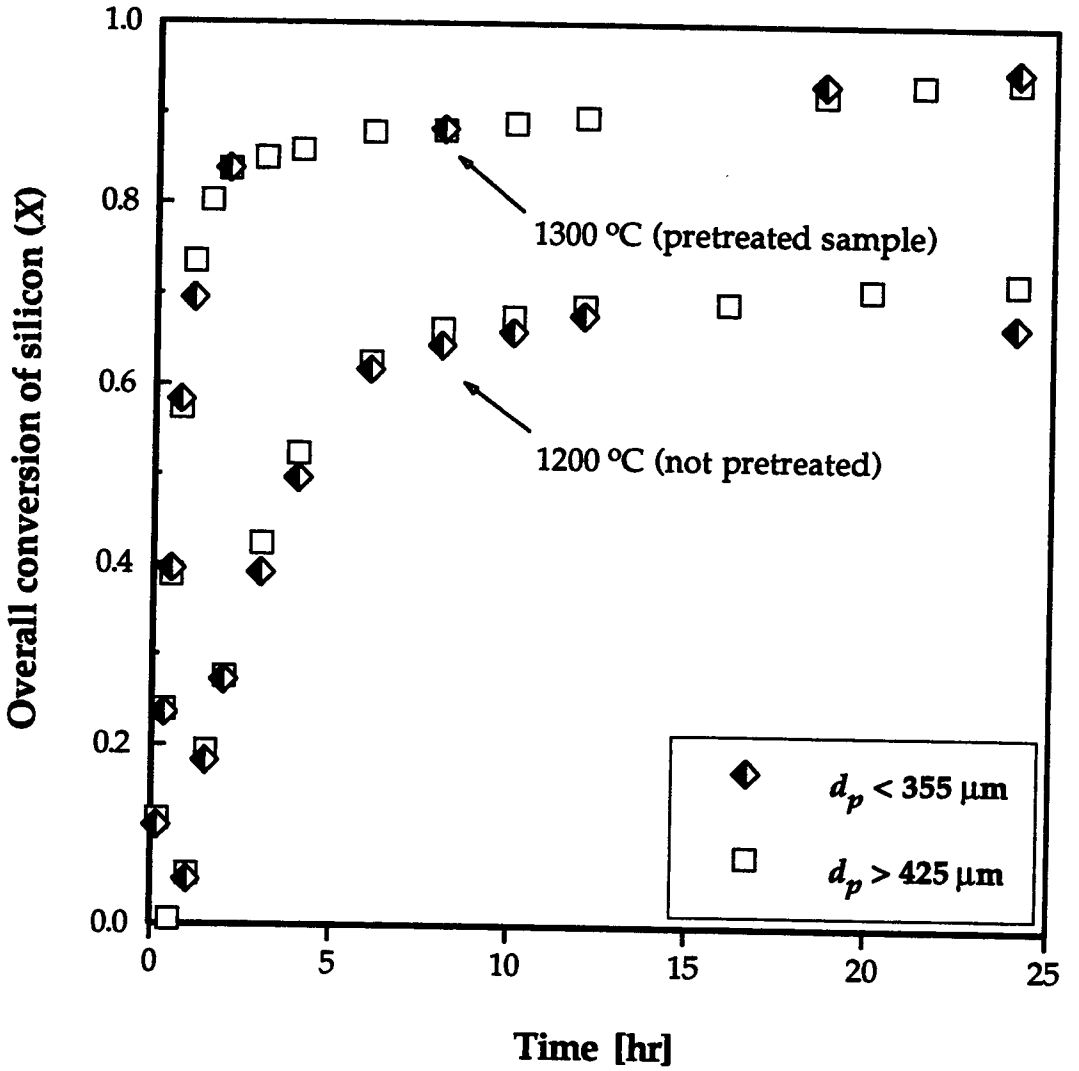

Figure 7. Effect of pellet size on overall conversion of silicon.

Unfortunately, electron microprobe analysis (CAMECA SX-50, E=15 kV, I=50 nA) could not provide a reliable quantitative elemental analysis of the samples obtained from the fluidized bed nitridation. The main reasons for this may be summarized as follows:

- surface of the sliced product pellets could not be properly polished and prepared for the analysis;

- the spatial probe resolution was about 1μm, which is several orders of magnitude larger than the scale of the actual reaction site;

- the aluminum nitride crystal, used for the nitrogen elemental analysis as the only available nitrogen containing standard (Nielsen, 1993), was extremely heterogeneous, which prevented adequate calibration of the analysis.

The roughness of the surface being analyzed extremely affects accuracy of the analysis by both electron scattering and diffraction of emitted X-rays. On the other hand, inadequate resolution of the probe gave integral elemental analysis within the sphere of ~ 1μm in diameter, which was often larger than even a grain diameter. Thus, residual polishing material remaining in inter-grain voids often contributed to the overall result of the analysis.

Still, obtained back-scatter electron (BSE) images provided important evidence about the morphology of the reacting pellet. Figure 8 shows the silicon grains in a particle sampled at the very beginning of the nitridation in one of the experiments, i.e. just at the end of the induction period. It can be seen that these grains are of an irregular shape and that they have a wide size distribution with a fraction of very large grains or, maybe, grain clusters. The size distribution of 1114 grains from this figure is presented in Appendix A. It was determined after measuring by a ruler two characteristic sizes of the grains shown in the plane and taking the smaller of these as the third characteristic length of an ellipsoid.

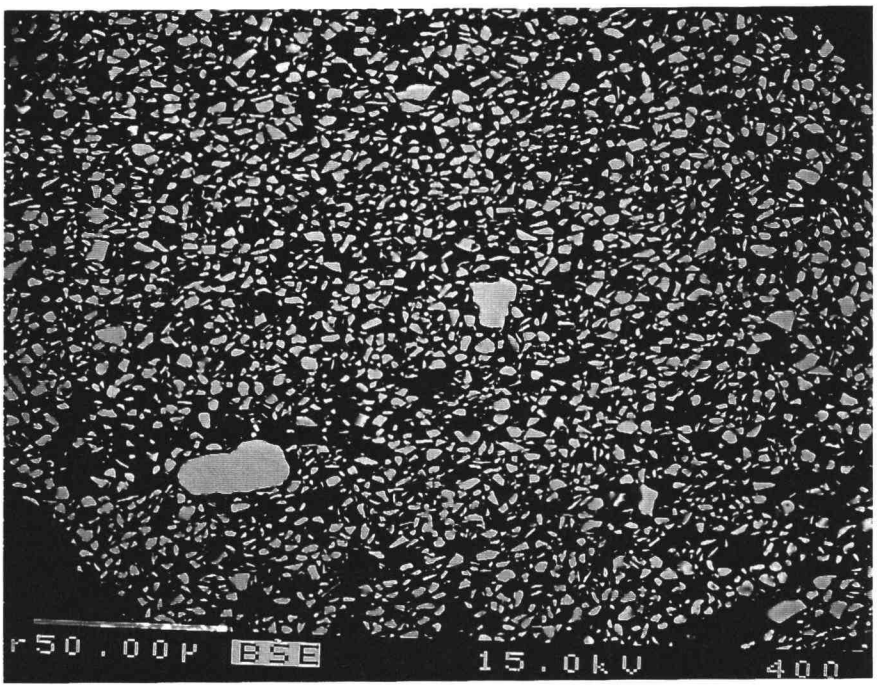

Figure 8. BSE photo of a pellet at the very beginning of the reaction (run-15, 49 min, $X \sim 0$): light areas-silicon, grey-silicon nitride.

Figure 9, where light areas represent unreacted silicon and grey areas silicon nitride, shows that individual grains of produced nitride are much smaller than original silicon grains. It should be noted that this sample was taken at the condition where nitridation became very slow. Even though it can be seen everywhere within the pellet, unreacted silicon is remarkably concentrated in the larger grains. This figure indicates that the reaction does not proceed from the outer surface of pellet to inward but proceeds rather uniformly throughout the pellet.

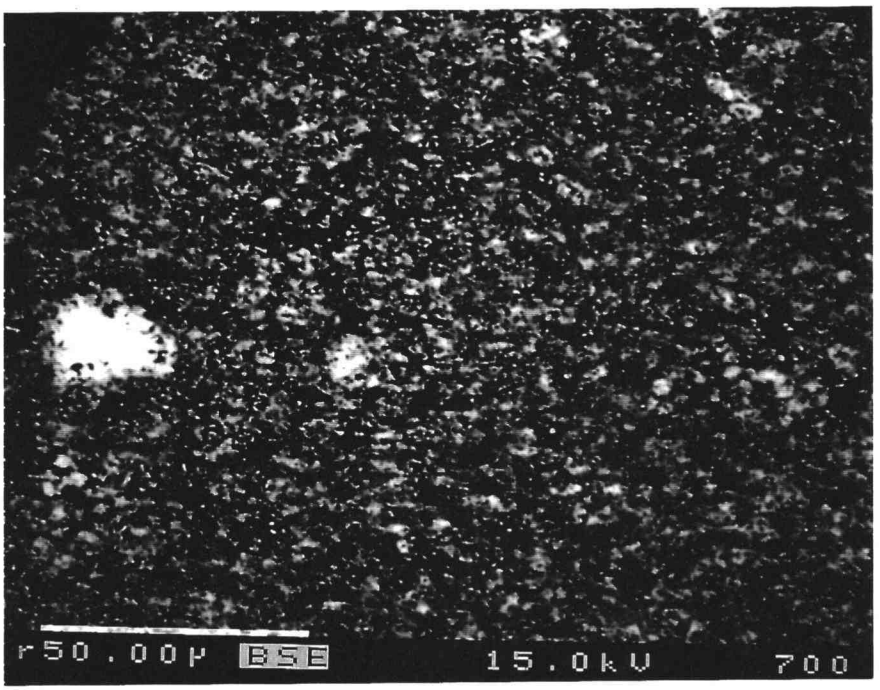

Figure 9. BSE photo of a pellet at high conversion (run-06, 6 hours, X = 83%): light areas-silicon, grey-silicon nitride.

The results described above indicate that, on a large scale, the extent of nitridation does not depend on the position of grains in the pellet. A much more detailed insight on structural changes that occur during nitridation will be presented and discussed in Chapter 4. This evidence, provided by transmission electron microscopy (TEM), will show that the structure of the reacting pellet is, however,extremely heterogeneous on a micro-scale.

3.3.3 Effect of Pretreatment

The effect of particle pretreatment on the conversion of silicon for the nitridation at 1200°C is presented in Figure 10. Figure 10a shows that pretreatment increases the total extent of nitridation. However, the composition of the produced silicon nitride was not significantly affected by pretreatment, as illustrated by Figure 10b (~ 2%). This effect is in agreement with the result of Rahaman and Moulson (1984). However, according to Pompe and Hermanson (1985), the removal of surface silica should decrease both the nitridation rate and α/β ratio in the nitrided product. It is interesting to note that an induction period prior to the start of nitridation can be seen in either case, with or without pretreatment.

Figure 11 presents the effect of the pretreatment temperature on nitridation at 1250°C. Even though the difference is not too significant, it may be seen that the particles pretreated at 1300°C exhibit a bit shorter induction period and slightly higher conversions. This is consistent with the thermodynamic study of Shaw and Zeleznik (1982) which predicts a more pronounced effect of hydrogen in the removal of surface silica as reaction temperature increases.

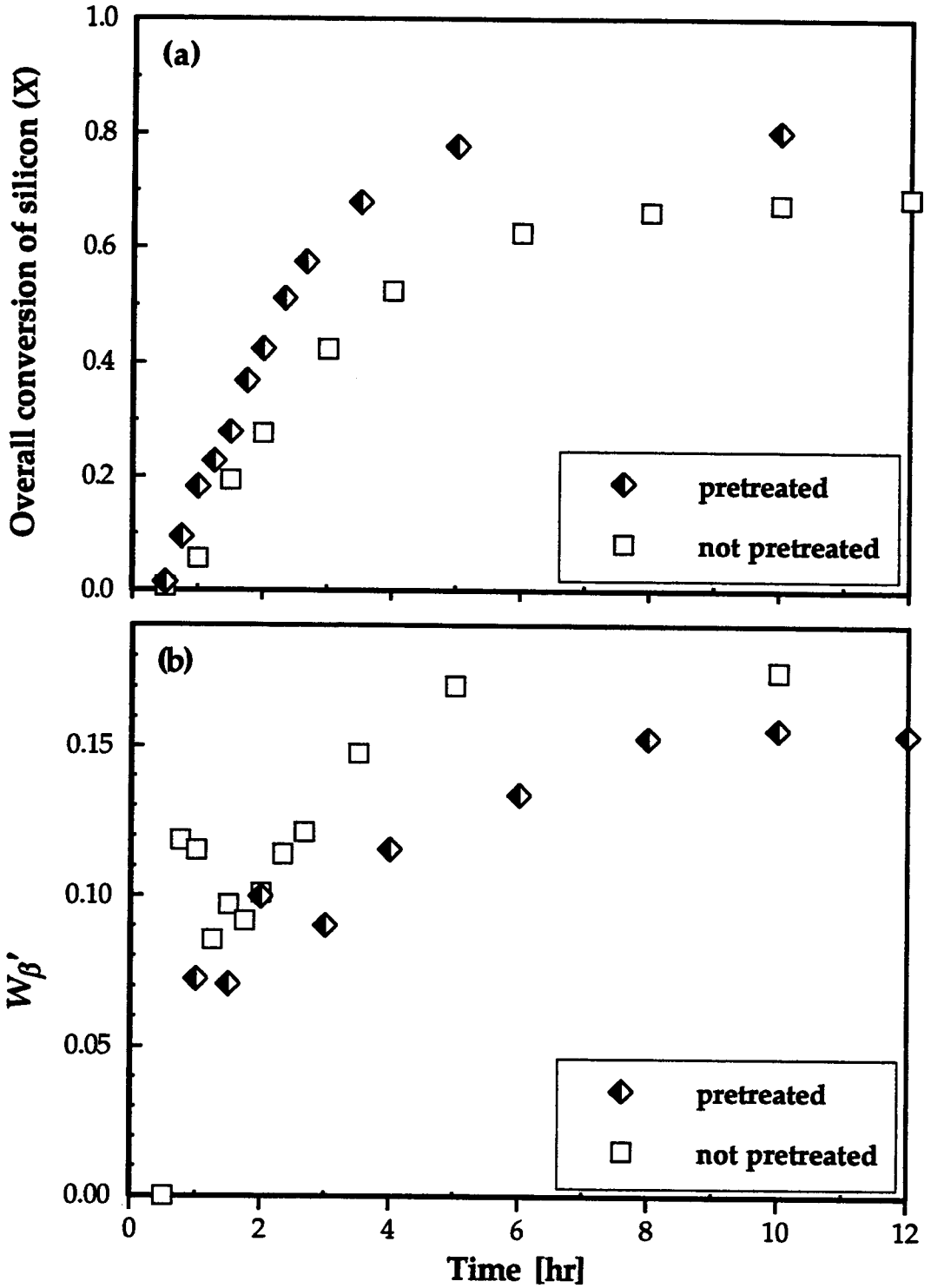

Figure 10. Effect of pretreatment on overall conversion of silicon (a) and mass fraction of β-form in produced silicon nitride (b) (runs 01 and 18).

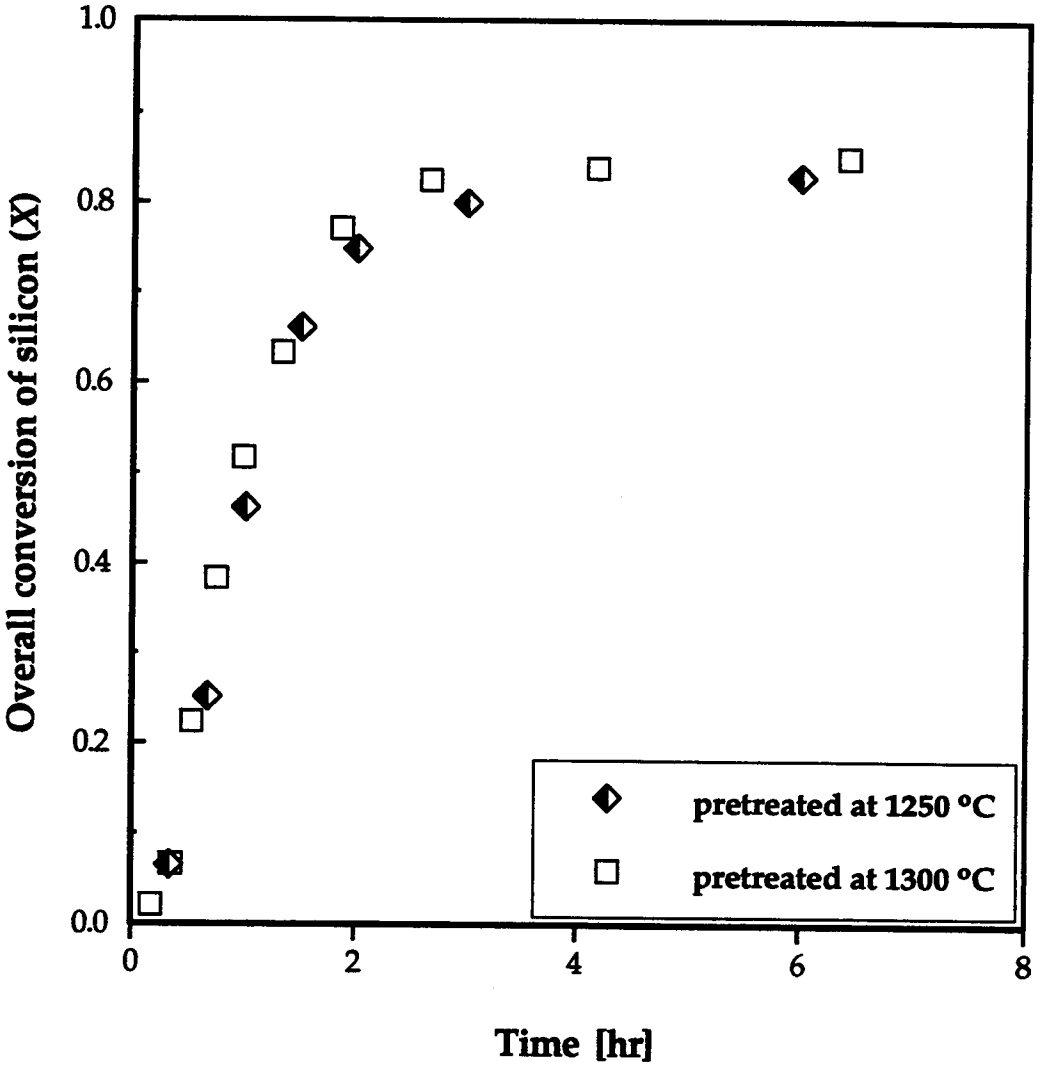

Figure 11. Effect of pretreatment temperature on nitridation at 1250°C in 90% nitrogen - 10% hydrogen gas mixtures.

The role of solid pretreatment in the mechanism of silicon nitridation could not be clarified in this work. The main reason for this is that trace oxygen analysis in an oxygen free atmosphere of the solid samples was not available for this study, so the effect of pretreatment on the oxygen content in the pellets could not be determined. However, due to the enhanced nitridation

of pretreated particles all the experimental data presented in the following sections of this work were obtained after the raw silicon pellets were pretreated as described in section 3.1.2.

3.3.4 Effect of Reaction Temperature and Operating Gas Velocity

The effect of reaction temperature on the overall conversion of silicon and on the yield of α-silicon nitride is presented in Figures 12 and 13. The data shown in these figures were obtained using a nitrogen-hydrogen gas mixture containing 10% hydrogen. As shown in Figure 12, the overall conversion did not reach 100% even after a fairly long reaction time (for example, after 24 hours in run-16 the conversion was 99%). The initial induction period decreased with an increase in reaction temperature, and at 1300°C the reaction started practically immediately.

Figures 12 and 13 show that both the overall conversion of silicon and yield of α-silicon nitride increased with an increase in reaction temperature. On the other hand, the yield of β-silicon nitride decreased with the increase in reaction temperature, as shown in Figure 14.

After the first few hours, the mass compositions of product silicon nitride were roughly constant with respect to reaction time, as shown in Figure 15. Also, higher reaction temperatures produce a smaller fraction of the undesired β-silicon nitride, thus giving a higher α/β ratio. Data scatter at shorter reaction times seen in Figure 15 may be explained by very weak

β-peaks due to a small amount of this phase, i.e. by associated errors of quantitative XRD analysis.

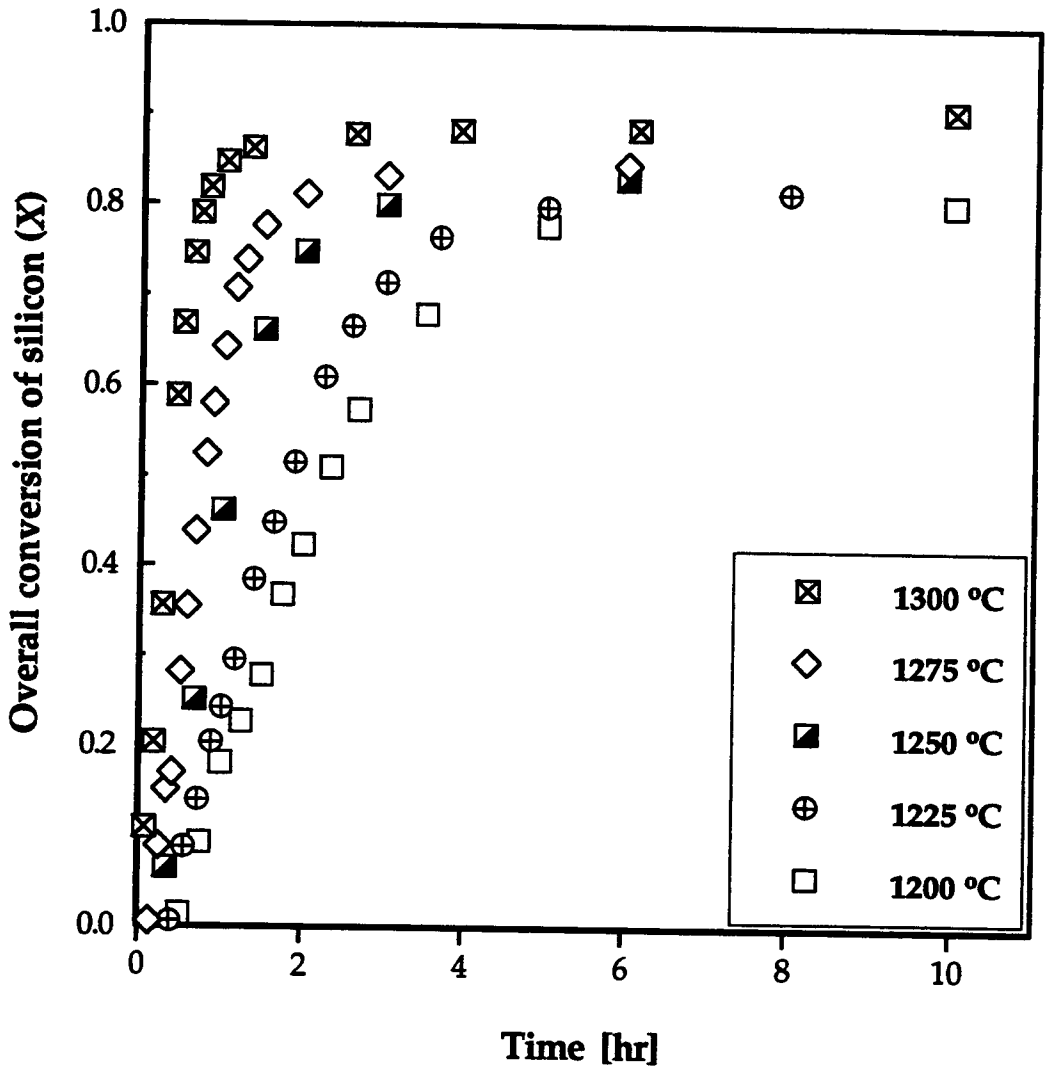

Figure 12. Effect of temperature on overall conversion of silicon in 90% nitrogen - 10% hydrogen (u_0 = 35 cm/s at 1300°C, u_0 = 25 cm/s at all other temperatures).

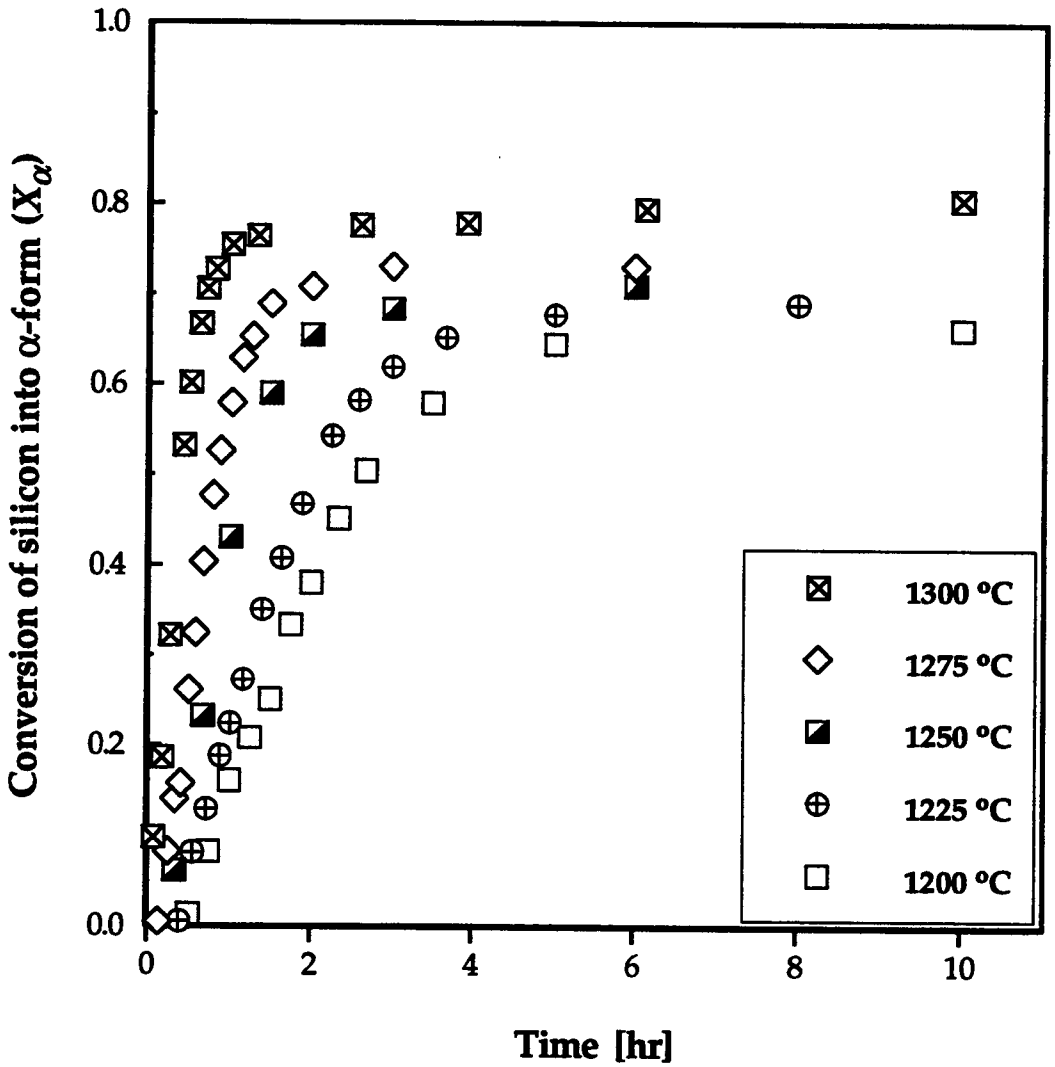

Figure 13. Effect of temperature on yield of α-form in 90% nitrogen - 10% hydrogen (u_0 = 35 cm/s at 1300°C, u_0 = 25 cm/s at all other temperatures).

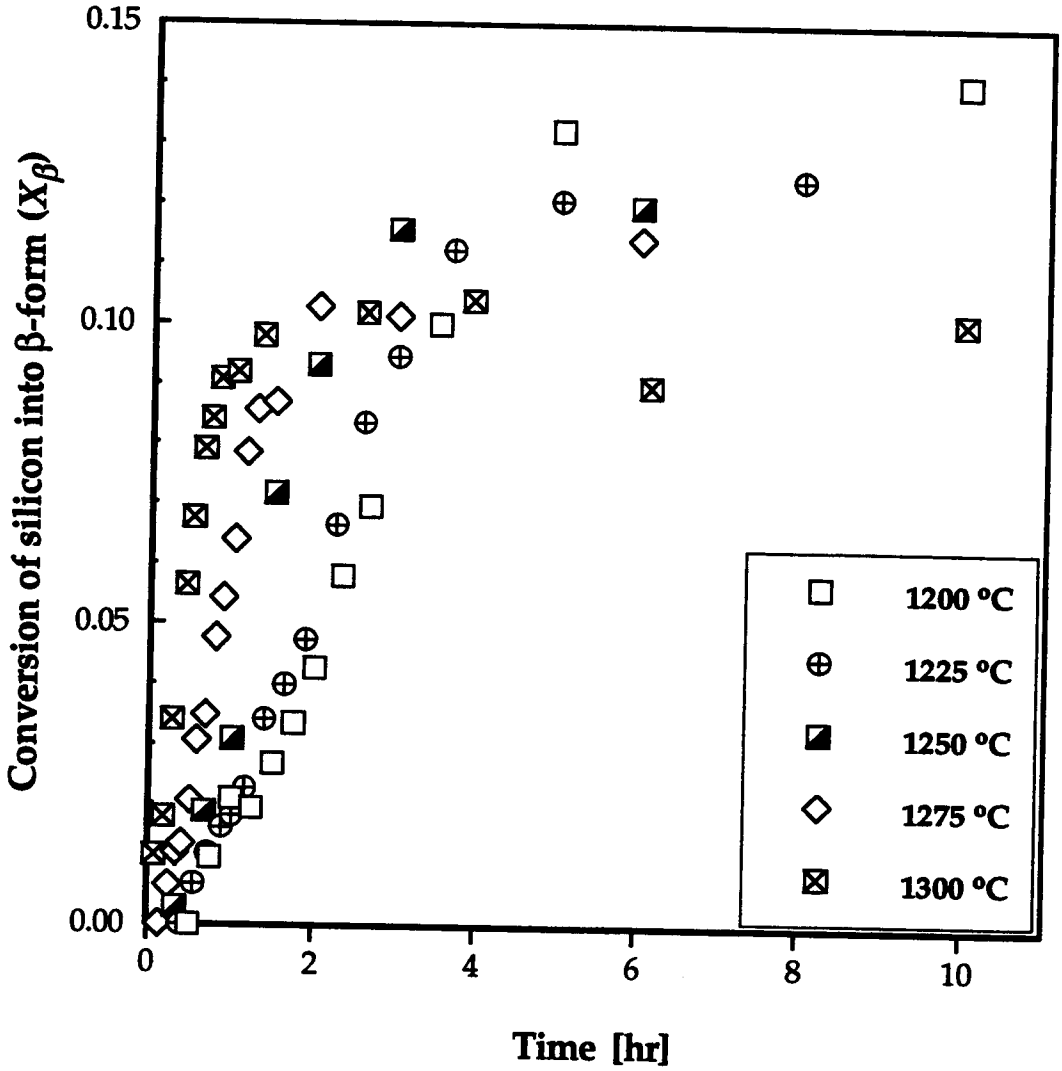

Figure 14. Effect of temperature on yield of β-form in 90% nitrogen - 10% hydrogen (u_0 = 35 cm/s at 1300°C, u_0 = 25 cm/s at all other temperatures).

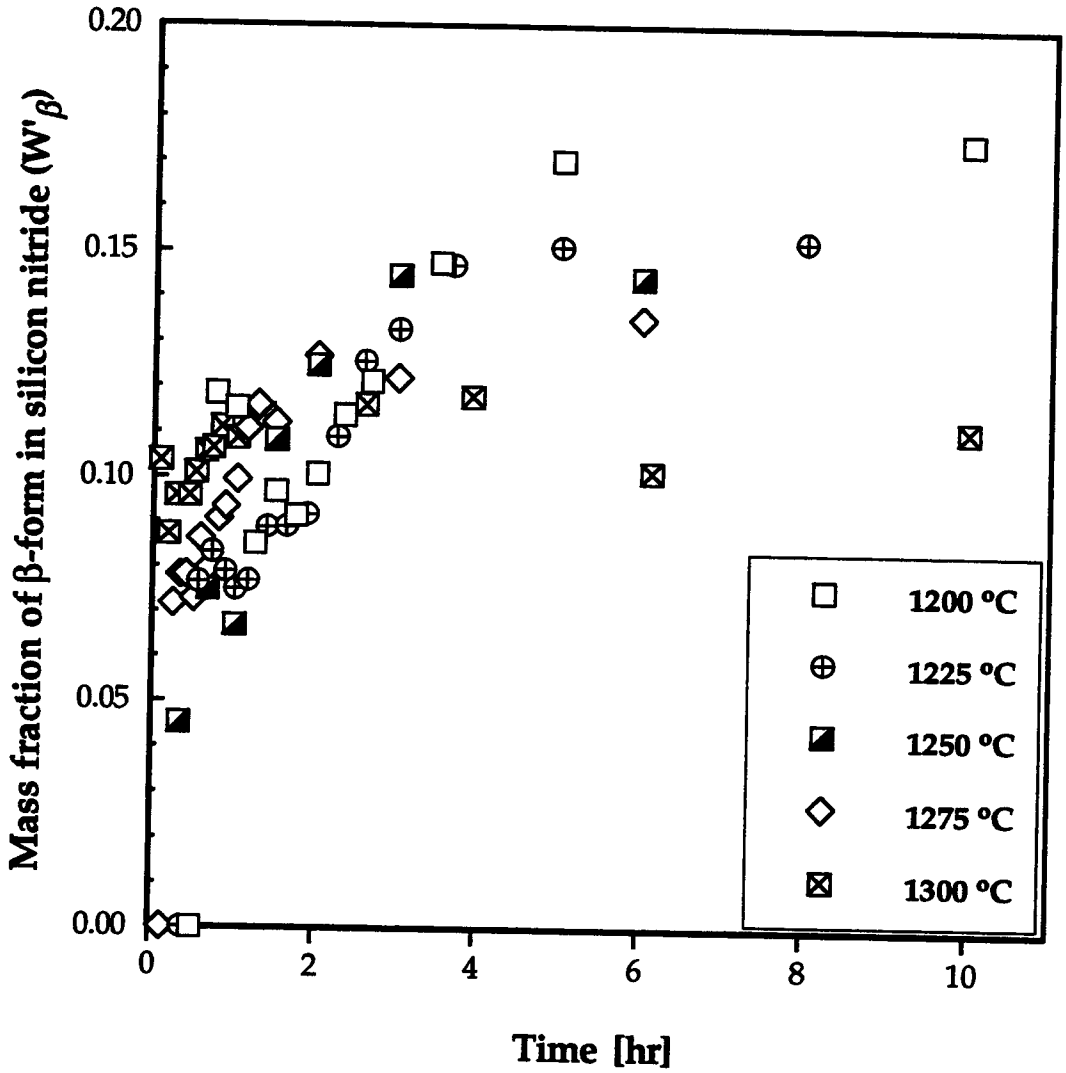

Figure 15. Effect of temperature on mass fraction of β-form in produced silicon nitride.

All experiments shown in Figures 12 through 15 were done at u_0=25 cm/s, except the one at 1300°C. When the bed was operated at this velocity at 1300°C, even during pretreatment, pellets often agglomerated and collapsed into a sponge-like packed bed. Only one of a number of experiments repeated at this conditions was possible to complete. However, even during this experiment, the observed standard deviation of pressure fluctuations was exceptionally low, which indicated poor fluidization, i.e. inadequate mixing of the bed. Also, very frequent quenching was necessary to avoid temperature runaway, which, on the other hand, occasionally overcooled the bed. When the bed inventory was inspected after the run, it was found that only a top portion of the bed (about 60% by mass) consisted of dispersed pellets. These pellets were analyzed and their overall conversion was compared with that of a run at the same temperature but at 35 cm/s which had no any technical difficulty. The figure shows a significant difference between the data in the first part of the reaction. The remaining portion of the product (about 40% by mass) was agglomerated into a compact chunk of apparently melted pellets sitting on distributor. Shape of the compact indicated that thermocouple was immersed into it, so, most probably, the measured temperature was not relevant to the temperature of the analyzed dispersed pellets from the top portion of the bed. This may explain the trend of the data seen in Figure 16 as follows. In the fast reaction regime in the run at 25 cm/s, because of the location of thermocouple, the set point temperature followed the temperature of the packed bed which was higher than the

temperature of the pellets fluidized in upper portion of the bed. Hence, during this stage of the process, it is believed that the temperature of analyzed pellets was below 1300°C. With the progress of reaction and a decrease in the overall process rate, temperatures of the compact and of the fluidized pellets approached each other, so the final stages yielded the same results.

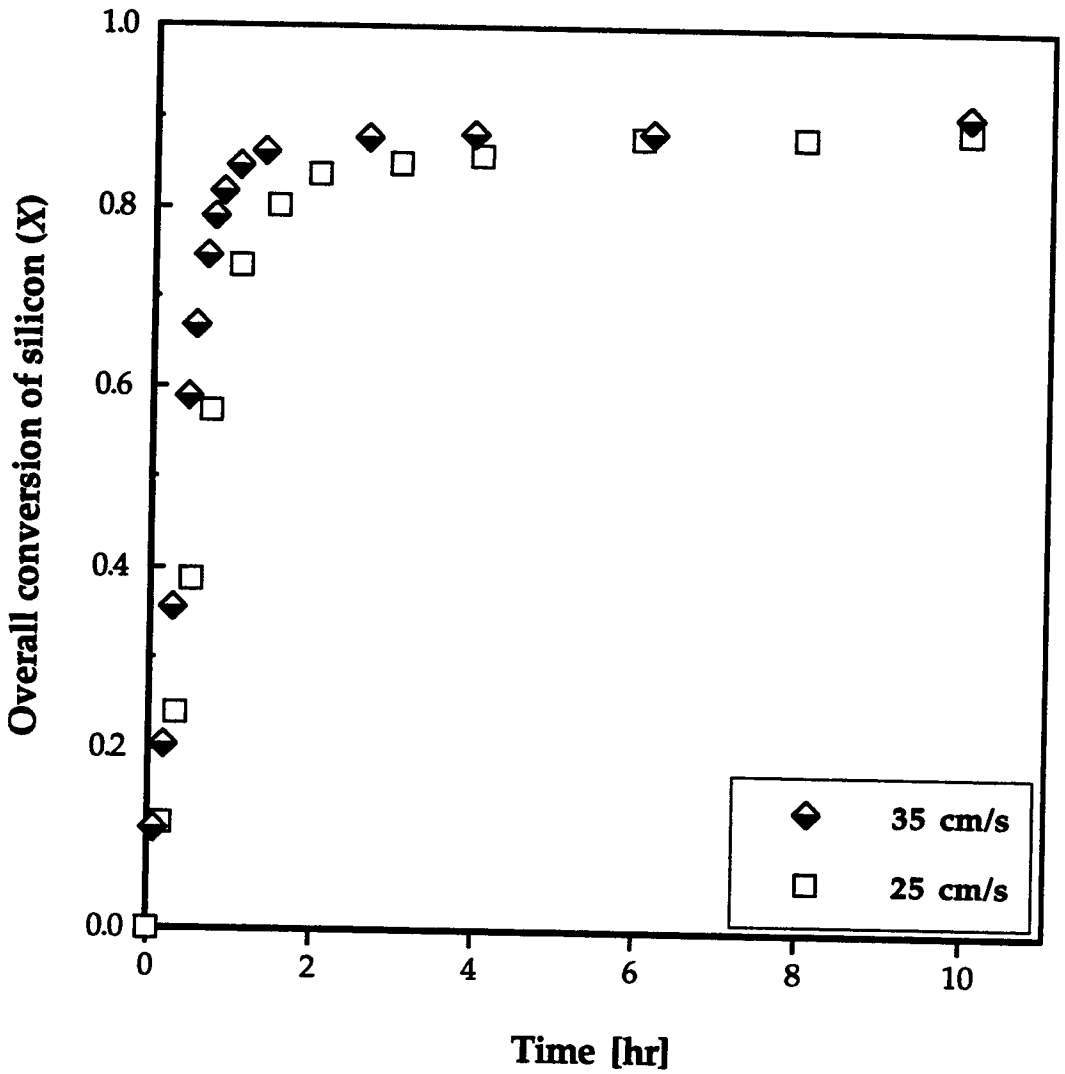

Figure 16. Comparison of runs at 1300°C in 90% nitrogen-10% hydrogen at two operating velocities.

The above discussion explained the discrepancy of the data in Figure 16 with inadequate temperature measurement rather than with the effect of the operating gas velocity, i.e. effect of external mass transfer resistance. Figure 17 supports this explanation by comparing the results of two runs at 1275°C performed at 25 and 35 cm/s. It can be seen that the data agree well, which also indicates that the kinetic experiments were not intruded by external heat and mass transfer effects. In general, the experiments were remarkably reproducible as illustrated by Figure 18.

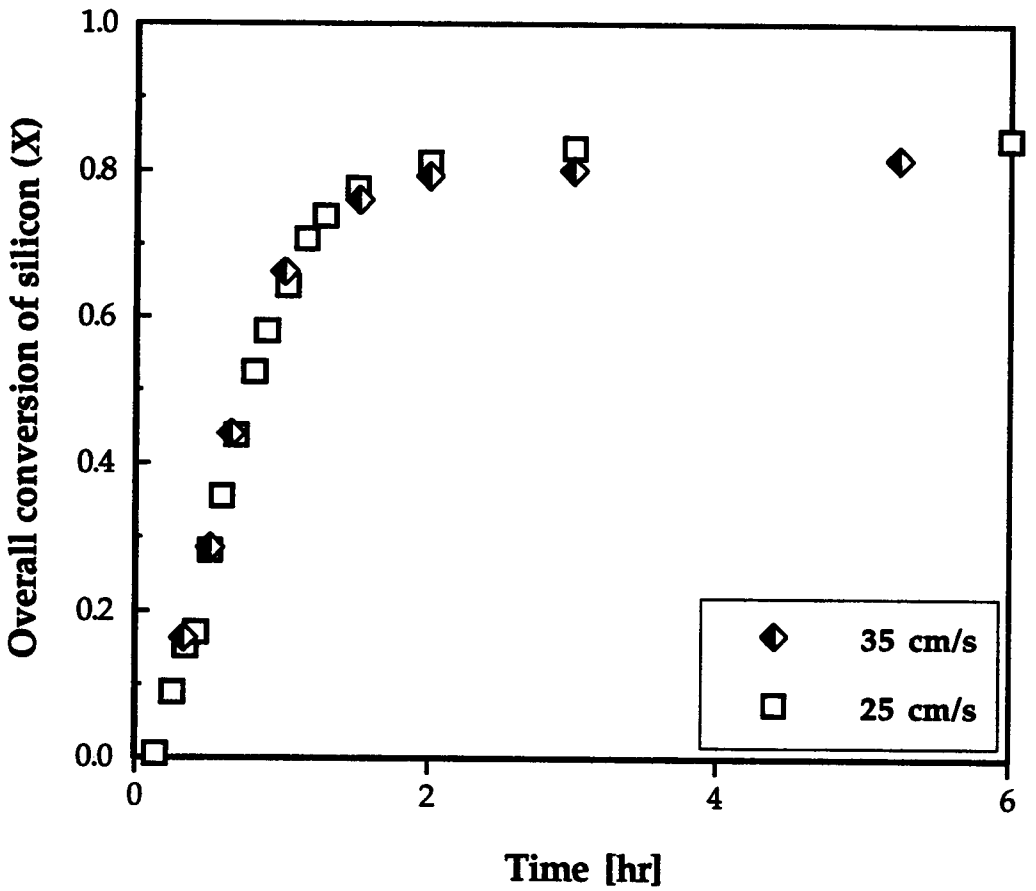

Figure 17. Effect of operating velocity on nitridation at 1275 °C.

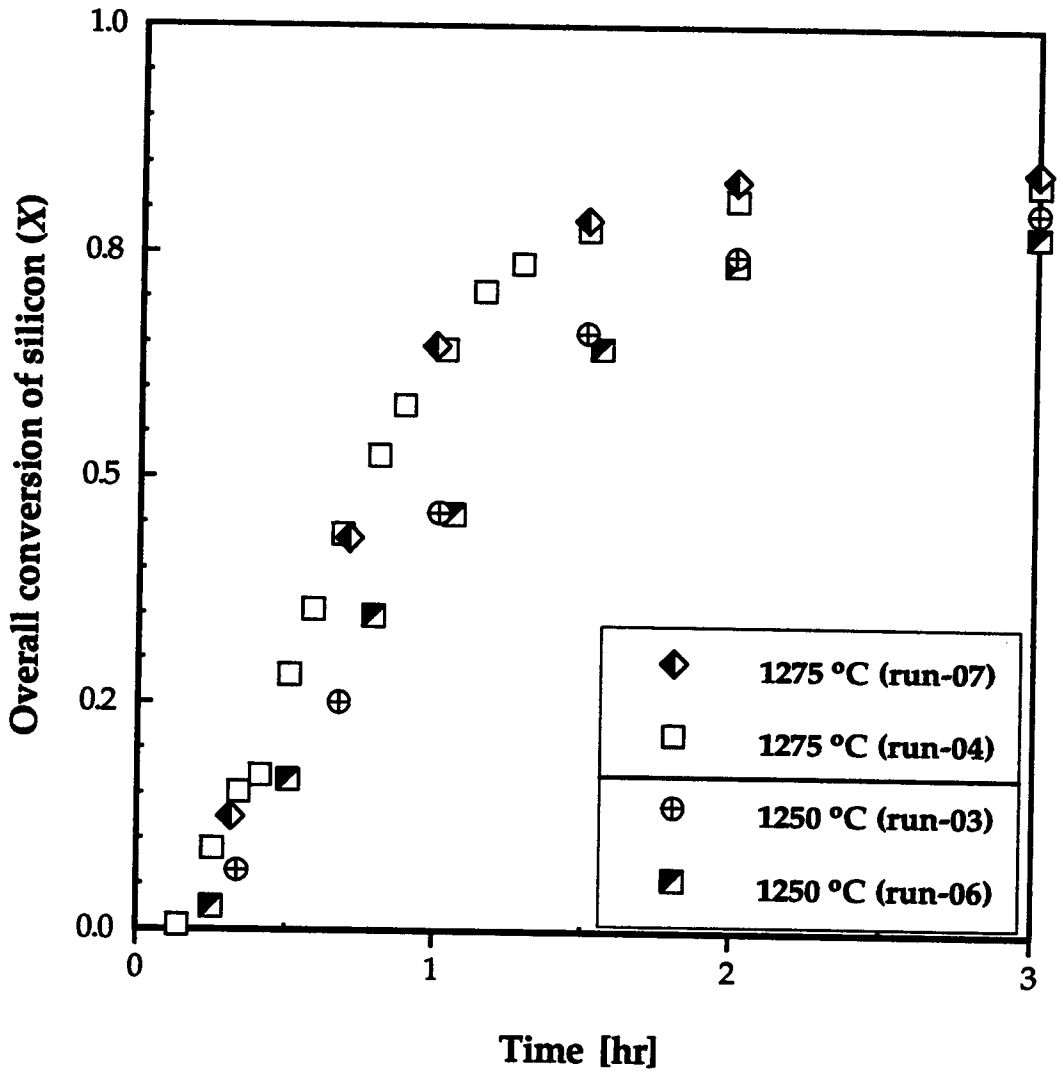

Figure 18. Reproducibility of results.

The consistent decrease in the content of the undesired β-form in the produced silicon nitride with the increase in reaction temperature shown in Figure 15 is in disagreement with the prediction of Rossetti and Denkewicz (1989) as well as with the experimental observations by Albano et al. (1991). The differences in trace impurities in both the silicon raw material and nitriding gases hinder rigorous comparison between this work and other

reported results. According to Pompe et al. (1985) impurities in silicon strongly affect phase compositions. Rossetti and Denkewicz (1989) emphasized that their prediction of the α/β ratio had been based on measurements carried out under isothermal conditions with high-purity deoxidized silicon powder. Albano et al. (1991) used high-purity nitrogen but used silicon with impurities in about the same range as in this study.

One of the possible explanations for the disagreement between this work's observation and some of the reported data regarding the effect of reaction temperature on the α/β ratio may be the limitation in heat transfer often observed in packed bed experiments, where most of the previous kinetic data were collected. Sheldon et al. (1992) reported a more than 160°C difference between the claimed reaction temperature and the estimated temperature in the center of a packed bed sample, even when a very small amount of silicon powder was used (~5 g). A temperature difference as high as this may cause the melting of silicon, in which case the growth of β-form is favored (Jennings, 1983; Hojo et al., 1975). The high efficiency of heat transfer achievable in a fluidized bed may eliminate this problem.

In closing this section, it should be mentioned that although the overall silicon conversion in fluidized bed nitridation does not reach 100% even after extended reaction times, the reaction in final nitridation stage, generally, does not cease, i.e. the conversion still slowly increases. As it will be discussed in subsequent sections, the reaction rate in this stage depends on reaction conditions: in some cases the conversion practically levels off but in some it

continuously increases until the reaction is almost completed. From practical reasons, however, the overall conversion after which the conversion rate becomes only a few percent per hour will be, further in this text, termed as the *final overall conversion* or the *final extent of reaction.*

3.3.5 Effect of Hydrogen and Nitrogen

The graph shown in Figure 19 illustrates the effect of the hydrogen concentration on nitridation of both pretreated and not pretreated silicon pellets in nitrogen-hydrogen mixtures. It can be seen that in both cases nitridation with higher hydrogen concentration slowed the nitridation down during the initial stage, but increased the final overall conversion of the silicon (Figure 19a). As seen in Figure 19b, an increase in the hydrogen concentration radically decreased the β-form content in the product silicon nitride obtained from silicon which was not pretreated, while, in the pretreated pellets, the yield of β-silicon nitride was not appreciably affected. This finding is in agreement with previously reported experimental observations and was explained by the fact that hydrogen in a nitriding atmosphere enhances the reaction toward the formation of α-silicon nitride (Itoh, 1991; Barsoum et al., 1991; Heinrich, 1980; Jovanovic et al., 1994). It is believed that hydrogen reacts with oxygen liberated from surface silica to form water vapor, which not only prevents the re-oxidation of silicon but also assists the generation of silicon monoxide and hence the formation of α-silicon nitride (Barsoum et al., 1991; Heinrich, 1980).

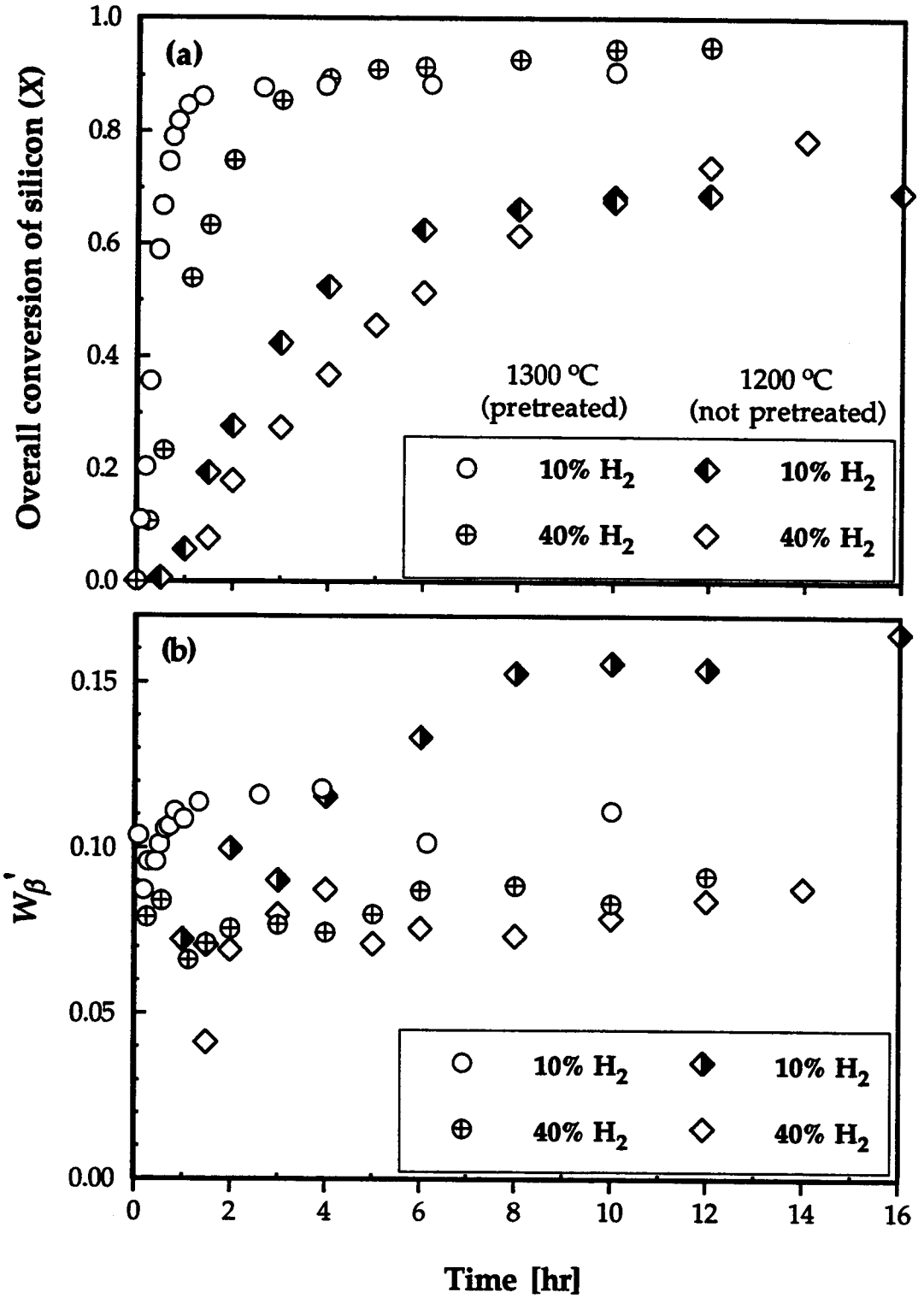

Figure 19. Effect of hydrogen on nitridation in nitrogen-hydrogen mixtures on overall conversion of silicon (a) and composition of produced silicon nitride (b).

A change in concentration of one component in a binary mixture, however, inevitably causes a change in concentration of the other. Therefore, the finding shown in Figure 19 could be attributed to the role of hydrogen only in the case when nitridation is not affected by the nitrogen concentration. To investigate separate effects of hydrogen and nitrogen concentrations on the overall conversion and α/β ratio in the product, two series of runs at 1250°C were made (in all of these experiments argon was used as an inert balance as needed):

- the nitrogen concentration was fixed at 30% but the hydrogen concentration varied (5, 10, 30 and 50%);

- the hydrogen concentration was fixed at 10% but the nitrogen concentration varied (30, 50, 70 and 90%).

Figure 20a presents an interesting finding about the effect of hydrogen. It can be seen that neither the induction period nor the initial reaction stage changes with the increase in the hydrogen concentration. At overall conversions greater than 20%, however, the nitridation rate decreases as the hydrogen concentration increases. The final conversions are approximately the same regardless of the hydrogen content in the gas. Also, as shown in Figure 20b, the content of β-form in produced silicon nitride only slightly decreases as the hydrogen concentration increases (~3%). However, it is difficult to make a strong conclusion here since as the β-form content decreases, its X-ray peaks become weaker and comparable to the background noise during the X-ray

diffraction analysis, which may affect an accuracy of the quantitative determination of this phase.

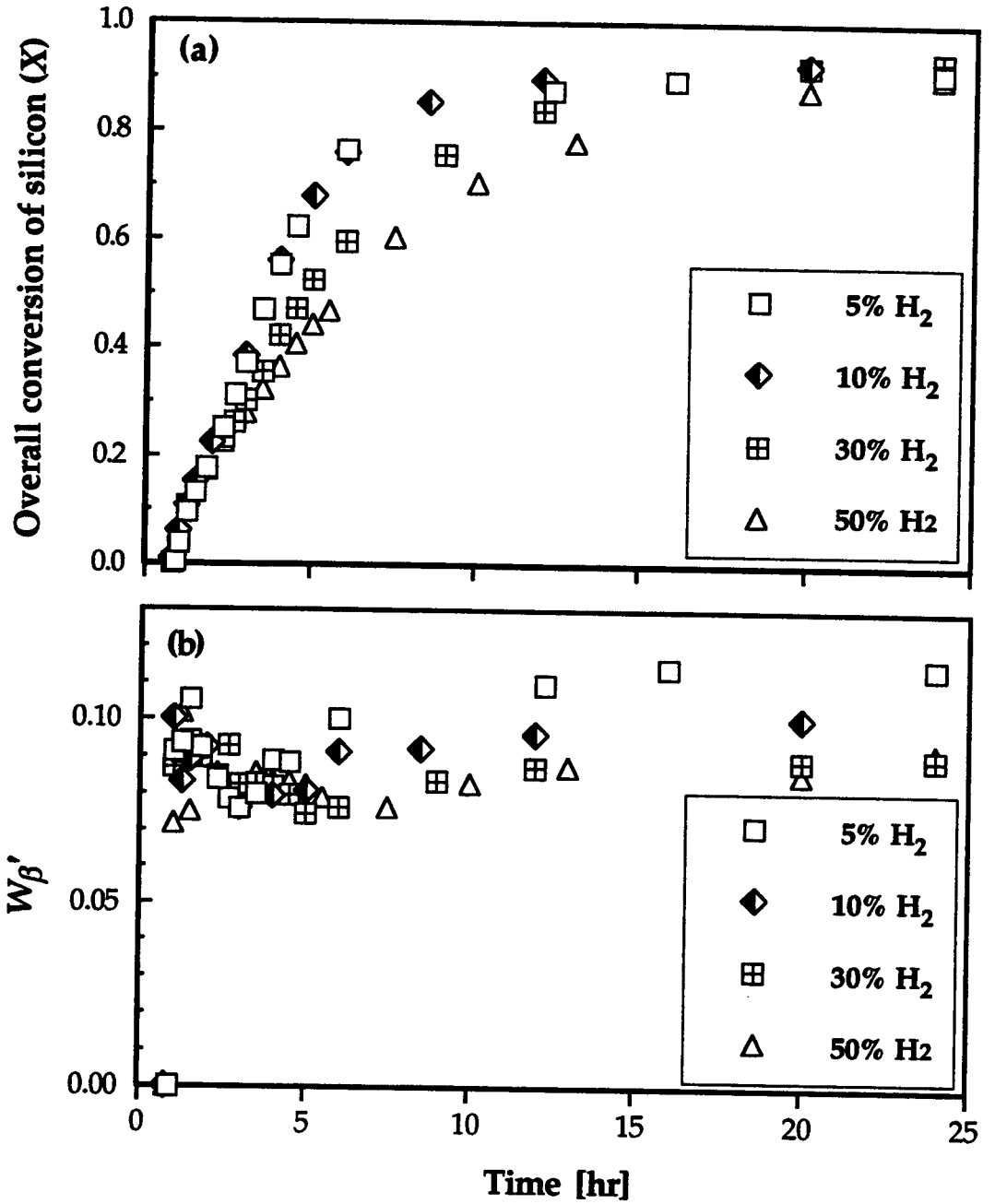

Figure 20. Effect of hydrogen on nitridation in nitrogen-hydrogen-argon mixtures with 30% nitrogen on overall conversion of silicon (a) and composition of produced silicon nitride (b).

It should be noted that an attempt at nitridation at 1250°C of pretreated silicon pellets but with no hydrogen in the gas phase during the run resulted in an extremely low nitridation rate. This was demonstrated by the fact that the heat released by the reaction was so low that the bed temperature did not change even after several hours. Even though the oxygen content in the gases used was low (~5 ppm) it might have been sufficient to reoxidize the silicon surface. On the other hand, Pigeon et al. (1993) observed that mullite (reactor tube material) could be a significant oxygen source at high temperatures.

Findings about the effect of hydrogen described above indicated that previous investigators might have neglected the effect of nitrogen on nitridation, which is confirmed by Figure 21a, showing the effect of nitrogen concentration on the overall conversion of silicon when the hydrogen concentration was kept constant. It can be seen in this figure that, as the nitrogen concentration increases, the nitridation rate increases but the final overall conversion decreases. As shown in Figure 21b the decrease in the nitrogen concentration caused a more pronounced effect on the decrease in the yield of β-form than was observed with an increase in the hydrogen concentration (Figure 20b). It is easy to fail to recognize this "hidden" nitrogen effect while explaining the increase in both the α/β ratio and the final extent of reaction by the increase of hydrogen content in nitrogen-hydrogen mixtures (Jovanovic et al., 1994).

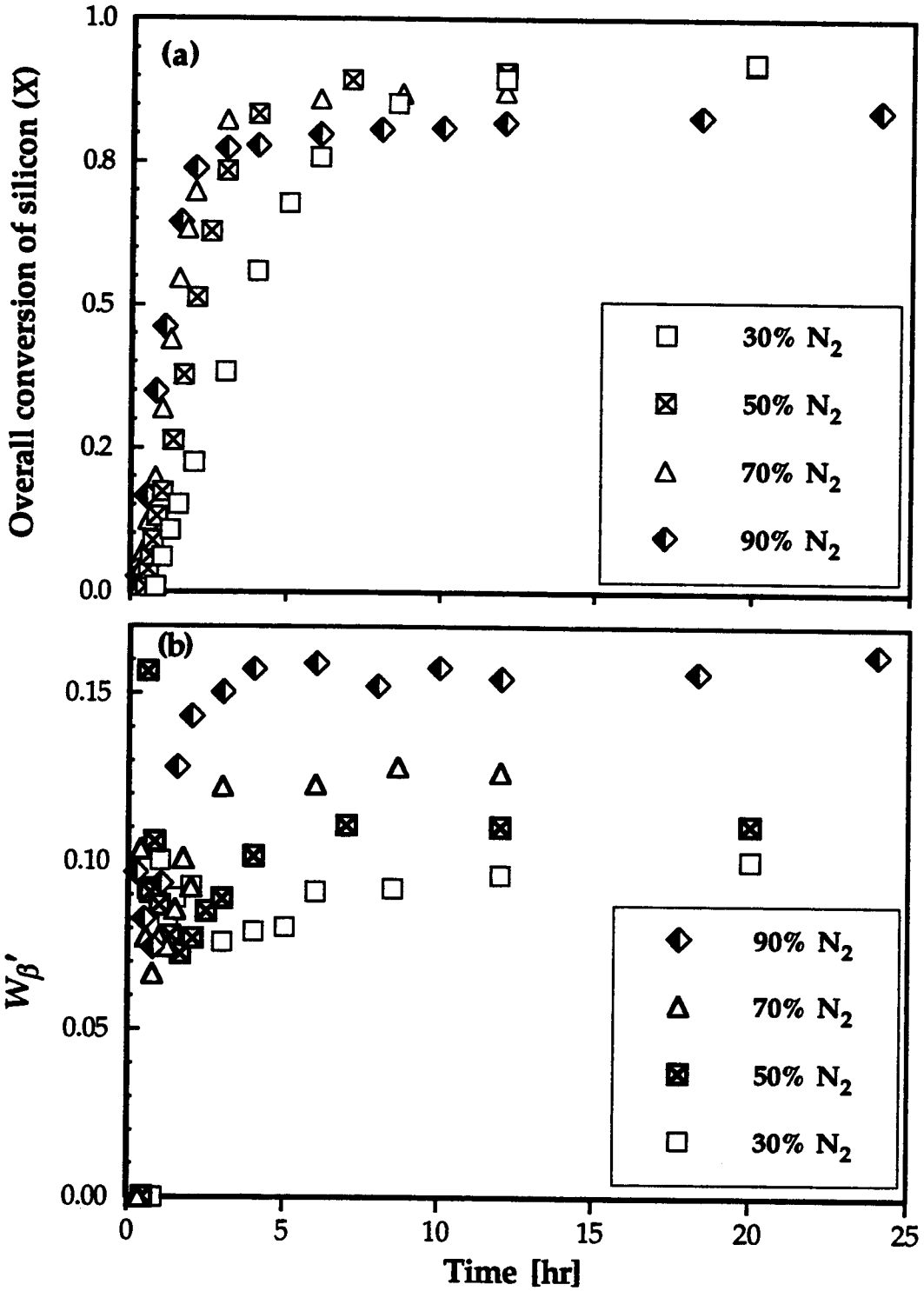

Figure 21. Effect of nitrogen on nitridation in nitrogen-hydrogen-argon mixtures with 10% hydrogen on overall conversion of silicon (a) and composition of produced silicon nitride (b).

Another interesting observation, provided by the experiments at various nitrogen concentrations, is a decrease in the induction period with an increase in the nitrogen concentration, shown in Figure 22. One of the explanations for this effect could be that nitrogen helps in disrupting the residual protective silica layer on silicon surface, not completely removed during the pretreatment, by the reaction toward silicon oxynitride. From another viewpoint, it is possible that an increase in the nitrogen concentration enhances the nucleation of silicon nitride. The real mechanism is not yet clear.

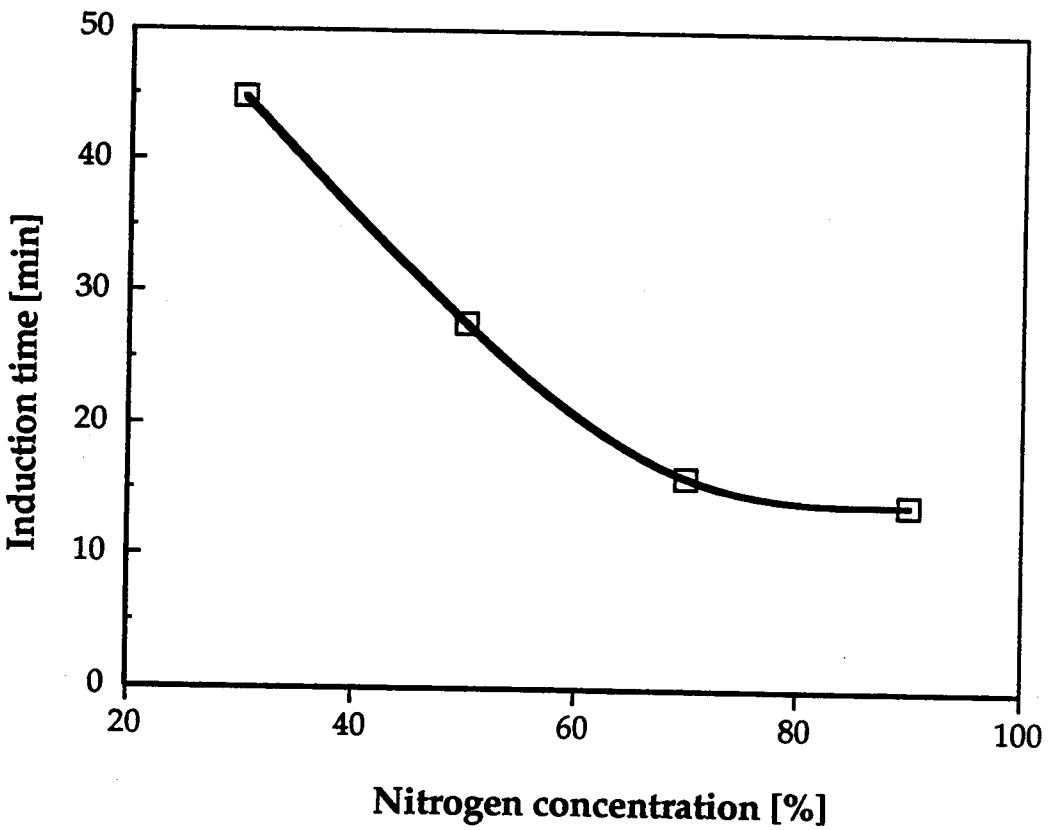

Figure 22. Effect of nitrogen on induction period in nitridation by nitrogen-hydrogen-argon mixtures with 10% hydrogen.

The decrease in the final extent of nitridation with an increase in the nitrogen concentration is an intriguing finding which, according to the study of Shaw and Zeleznik (1982), cannot be explained from the thermodynamics standpoint. It is possible that, at higher nitrogen concentrations, faster nitridation on the surface of polycrystalline silicon grains generates silicon nitride that clogs openings between single-crystal silicon micro-domains and prevents the diffusion of nitrogen along the grain boundaries connected to the openings. The unconverted silicon in large clusters may significantly reduce the overall silicon conversion. This will be discussed in much more detail in Chapter 4.

3.3.6 Operation with Programmed Temperature Increase

The long reaction time needed to achieve a high conversion is undesirable for commercial applications. On the other hand, the results presented in section 3.3.4 showed that an increase in reaction temperature leads to the desired effect, i.e. shorter reaction times, higher overall conversions and higher α/β ratios. Since the increase in operating velocity from 25 to 35 cm/s eliminated all technical problems related to chunking of the bed inventory and hence, enabled good fluidization, the reasonable question is what happens at temperatures above 1300°C?

Two experiments, at 1330 and 1350°C, both at 35 cm/s in 90% nitrogen-10% hydrogen gas mixture, were carried out without any technical difficulty, but they brought up an intriguing finding. Even though the reaction was very

fast in these experiments (the difference between reaction temperature and set point temperature on furnace controller was as high as 180°C), this was not correspondingly reflected by high pellet conversion. The samples were not uniform as was the case in runs at temperatures of up to 1300°C, i.e. they consisted of apparently converted white-gray particles mixed with black silicon pellets. For example, XRD analysis of the sample taken after 2 hours at 1350°C showed that the produced silicon nitride contained ~ 96% of the α-form but the overall conversion of silicon was only ~ 80%, which is considerably lower than it had been expected from the trend of data in Figure 13. Although very important, this finding was not investigated further, thus, it cannot be explained further in this work. However, if the silicon surface had been coated by a layer of silicon nitride during the initial stage of nitridation at a lower temperature, nitridation at temperatures above 1300°C yielded the results which are fully consistent with the trend of data with respect to reaction temperature presented in Figure 12.

Two batch runs, in Table 4 coded as runs 21 and 22 , were made with the programmed temperature being increased stepwise, with the stages specified in Table 4. In these experiments, the reaction was ceased during the temperature ramps by switching the reactant, nitrogen, to the inert, argon. The content of hydrogen was kept at 10% throughout the run.

Figure 23 presents the results obtained when the nitridation started at 1200°C and was carried out at milder temperatures shifting up to 1390°C in

four steps. This run yielded about 80% α-silicon nitride and an overall conversion of 96% of silicon in 3.2 hours.

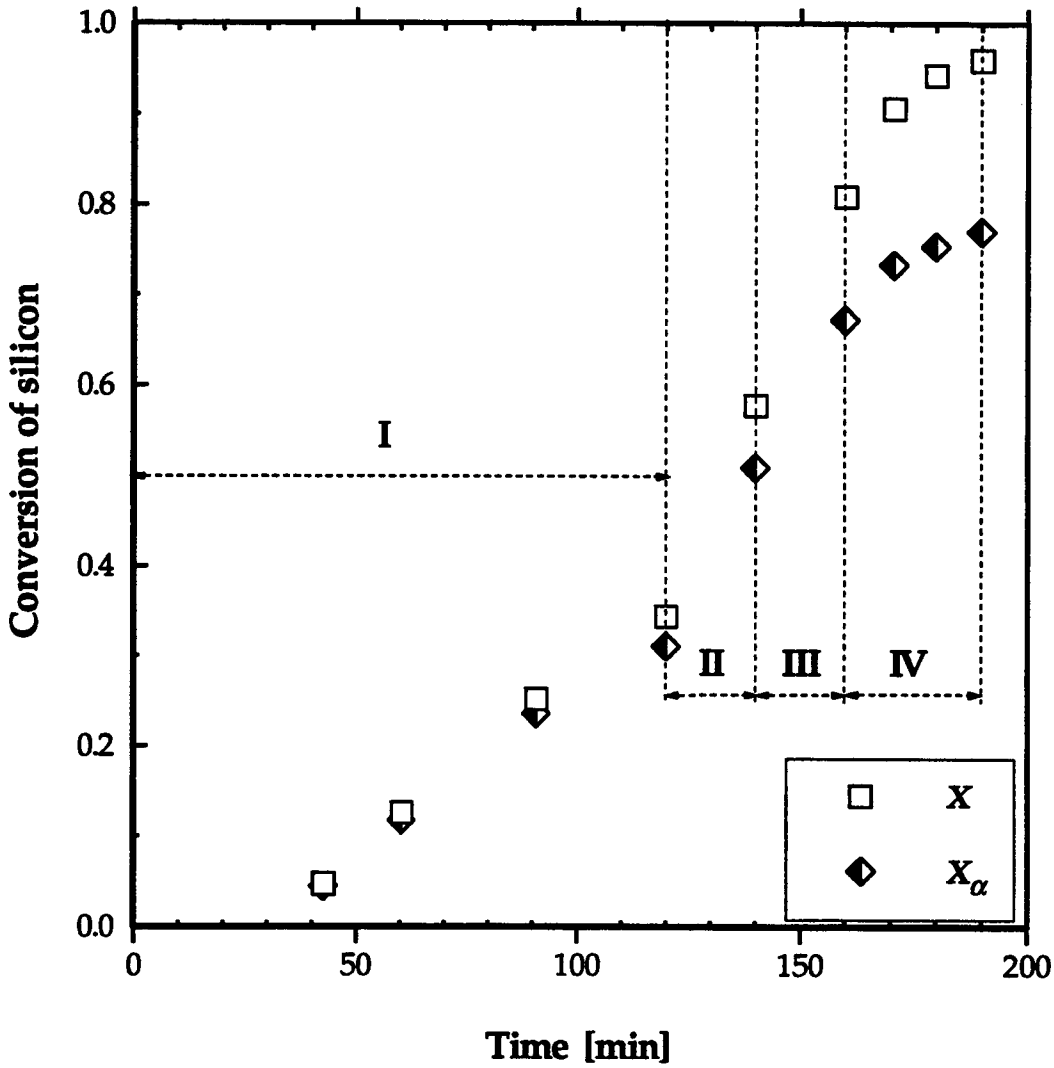

Figure 23. Results of multi-staged nitridation in 90% nitrogen-10% hydrogen (run 21): I = 1200°C , II = 1300°C, III = 1350°C, IV = 1390°C.

The other run, shown in Figure 24, started at 1300°C and then continued at 1390°C. The figure shows that an overall conversion of 99% of silicon was

achieved in less than 2.5 hours, leading to a yield of about 85% α-silicon nitride. The reaction time indicated in Figures 22 and 23 represents only the time during which nitrogen was supplied to the reactor. Hence, a multistage operation with a programmed temperature increase significantly reduced the time for almost complete conversion.

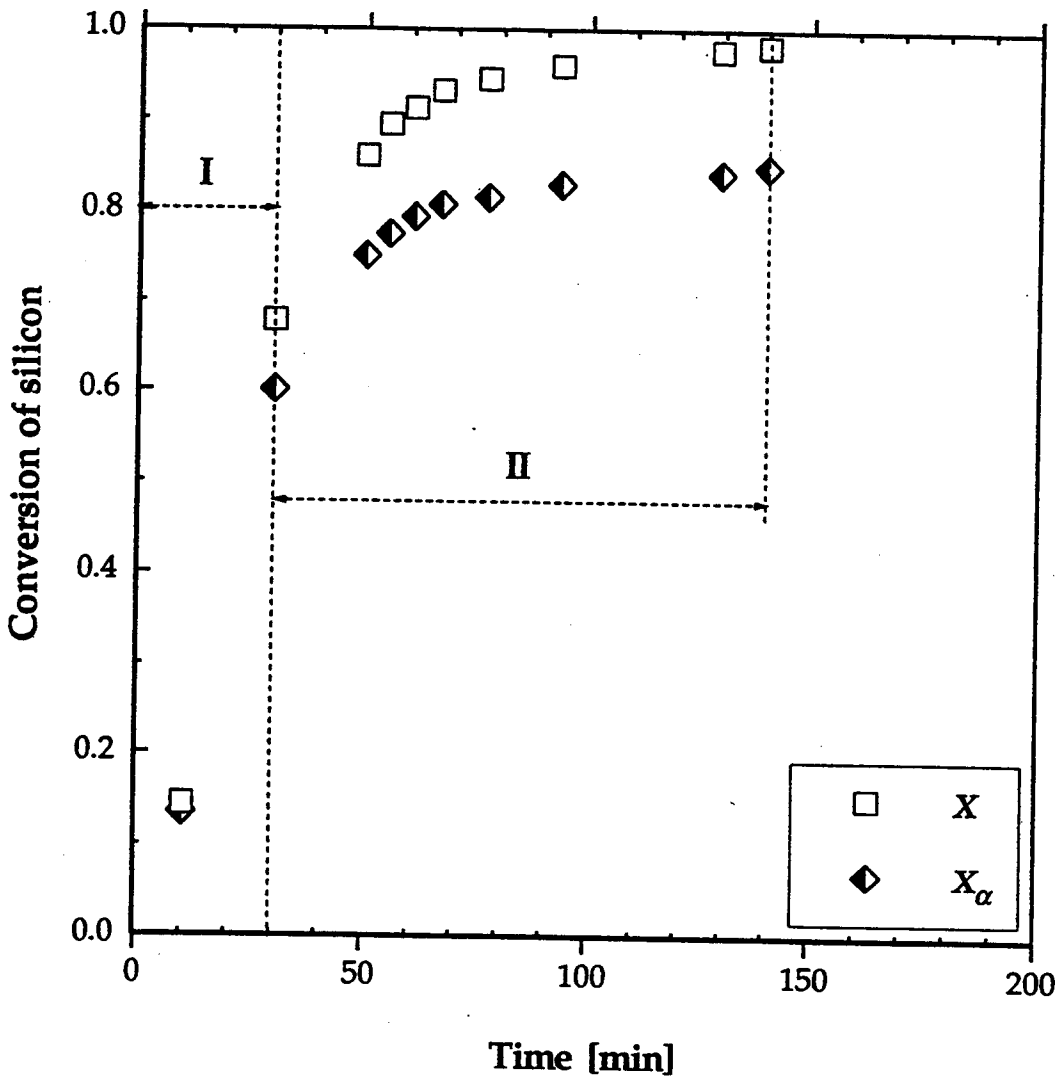

Figure 24. Results of two-staged nitridation in 90% nitrogen-10% hydrogen (run 22): I = 1300°C, II = 1390°C.

3.3.7 Inspection of the "Seeding" Effect

The results presented in Figures 23 and 24 not only showed an improvement of the direct fluidized bed nitridation process but, also, indicated that the temperature during the initial stage of nitridation might be mainly responsible for the final α/β ratio, regardless of the succeeding temperature history. Namely, the run shown in Figure 23 started at lower temperature than the run from Figure 24, and gave a lower final yield of α-form, which is consistent with the finding presented in Figure 13. This would agree with the "seeding" effect observed by Morgan (1980) and Campos-Loriz and Riley (1980), i.e. the observation supporting the view that the phase nature of the initial silicon nitride nuclei is one of the factors determining the final α/β ratio in the product. To investigate this effect, important for further understanding of mechanism of the nitridation, two additional multi-staged experiments were done, coded run-23 and run-24 in Table 4. In these experiments, the stages varied not only in temperature but in composition of the nitriding atmosphere as well.

Figure 25 presents the run carried out in only nitrogen-hydrogen mixtures. It started at 1300°C and 40% hydrogen, i.e. the conditions which, according to Figure 19b, should lead to a high α/β ratio. The mass composition of the silicon nitride produced by this run, represented by the mass fraction of the β-form, is compared in Figure 26 with its counter-part from run-22 which also started at 1300°C but was carried out with 10% hydrogen (illustrated by Figure 24). It can be seen in Figure 26 that the final

compositions of the silicon nitride products produced by these two runs do not differ significantly.

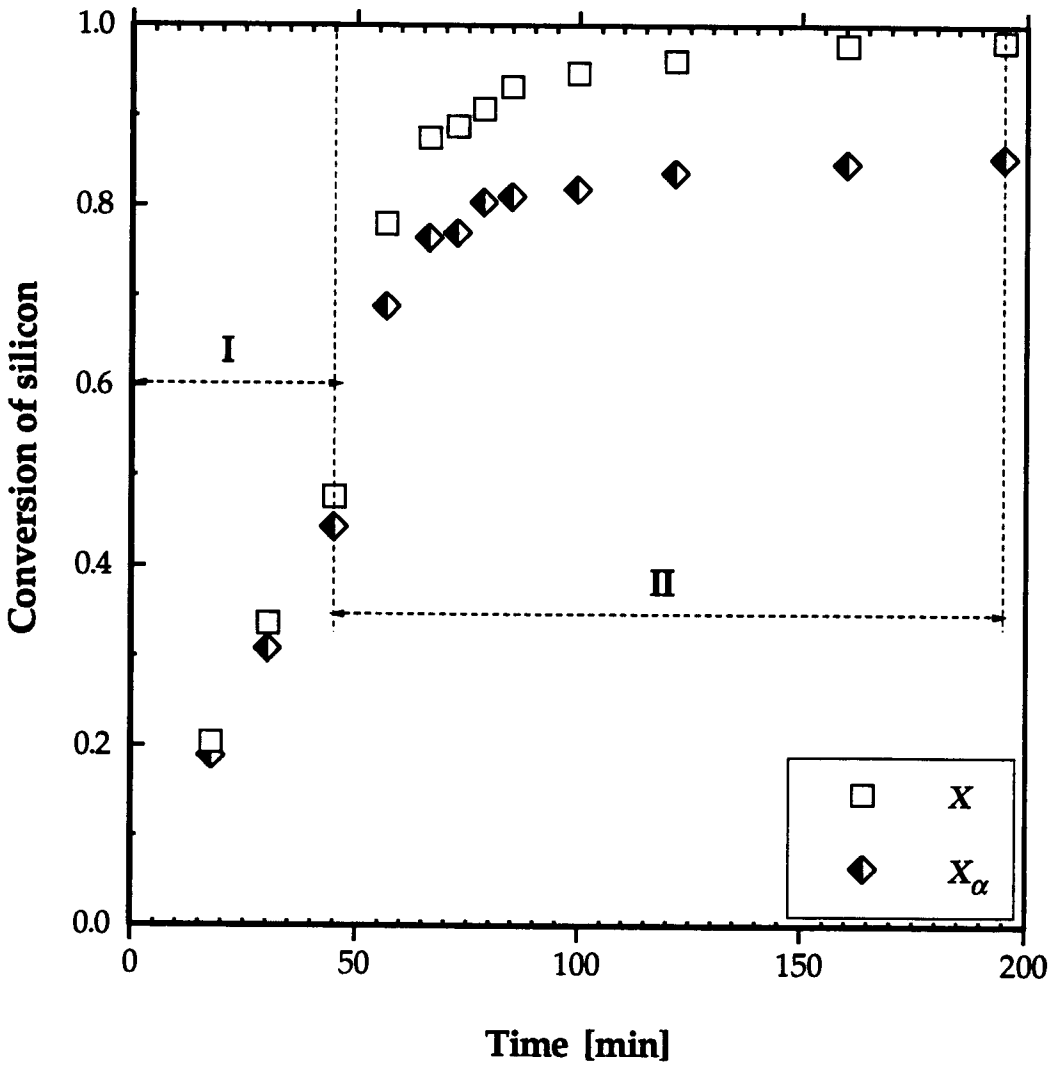

Figure 25. Results of two-staged nitridation in nitrogen-hydrogen mixtures (run 23): I = 1300°C, 40% hydrogen; II = 1390°C, 10% hydrogen.

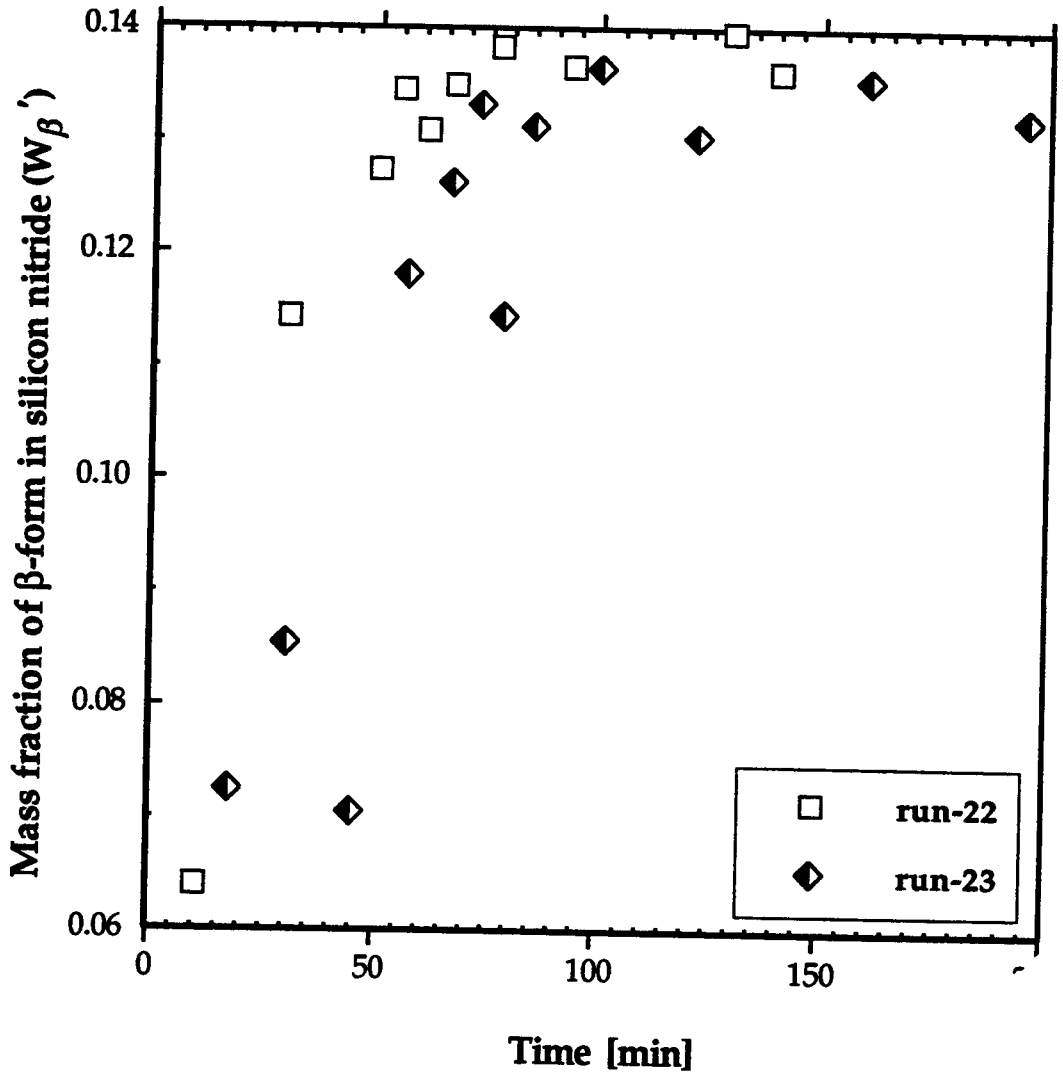

Figure 26. Comparison of composition of silicon nitride produced by run-22 and run-23 (conditions given in Table 4, the runs illustrated in Figures 24 and 25, respectively).

The above finding, however, could not strongly deny presence of the "seeding" effect because neither the results from Figure 19b for 10 and 40% hydrogen at 1300°C, i.e. for the initial stages of runs 22 and 23, respectively, differ significantly. For this reason, the other run (run-24) was programmed to

take place in two steps which were expected to differ significantly in the final yields of the α-form:

- the first stage at 1250°C and 30% nitrogen-10% hydrogen-60% argon, i.e. at the conditions that gave only about 9% by mass of β-form (Figure 21b), and

- the second stage at 1200°C and 90% nitrogen-10% hydrogen, i.e. the conditions that yielded twice as much β-form, i.e. about 17% by mass (Figure 15).

Overall conversion and yield of α-form in the second stage of the run-24 are compared in Figures 27 and 28, respectively, with those from an experiment in which the same conditions were kept constant throughout the run (run-01 shown in Figures 12 and 13). When the time scale for the second stage of run-24 was shifted 1.1 hours to the left, i.e. adjusted to account for a longer time to reach the same conversion due to slower initial stage, the overall conversions agreed well, as illustrated by Figure 29a. To compare the yields of α-form, however, an additional correction had to be made since the first stage yielded about 4% more this phase. As shown by Figure 29b, after subtracting 0.04 from the α-yields and plotting these adjusted values on the time scale shifted as mentioned above, again good agreement with the original run was achieved. This indicated that the conversion curves were additive, i.e. no effect of the initial process stage on subsequent progress of nitridation was found.

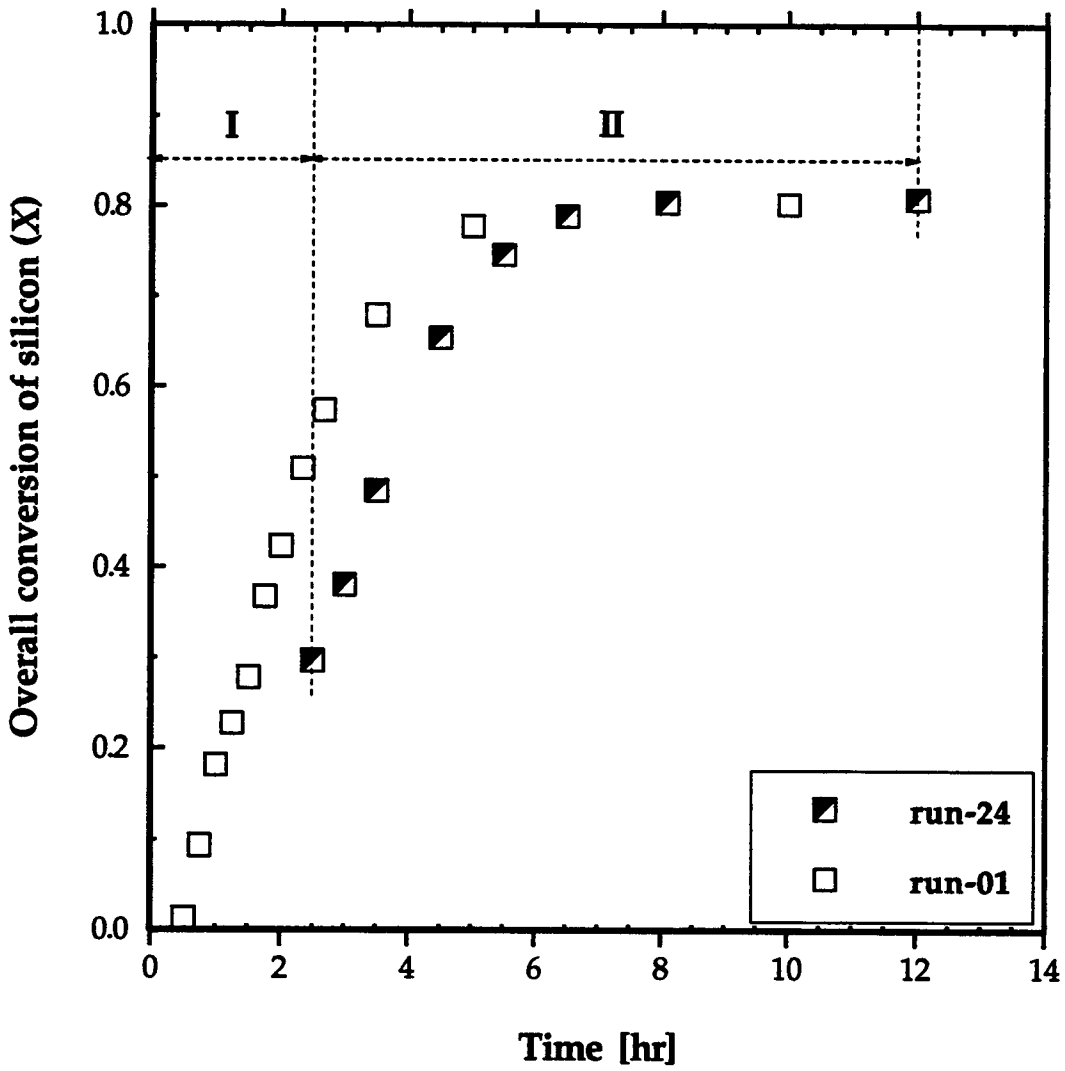

Figure 27. Progress of nitridation at 1200°C in 90%nitrogen-10% hydrogen: comparison of second stage of run-24 with results of run-01.

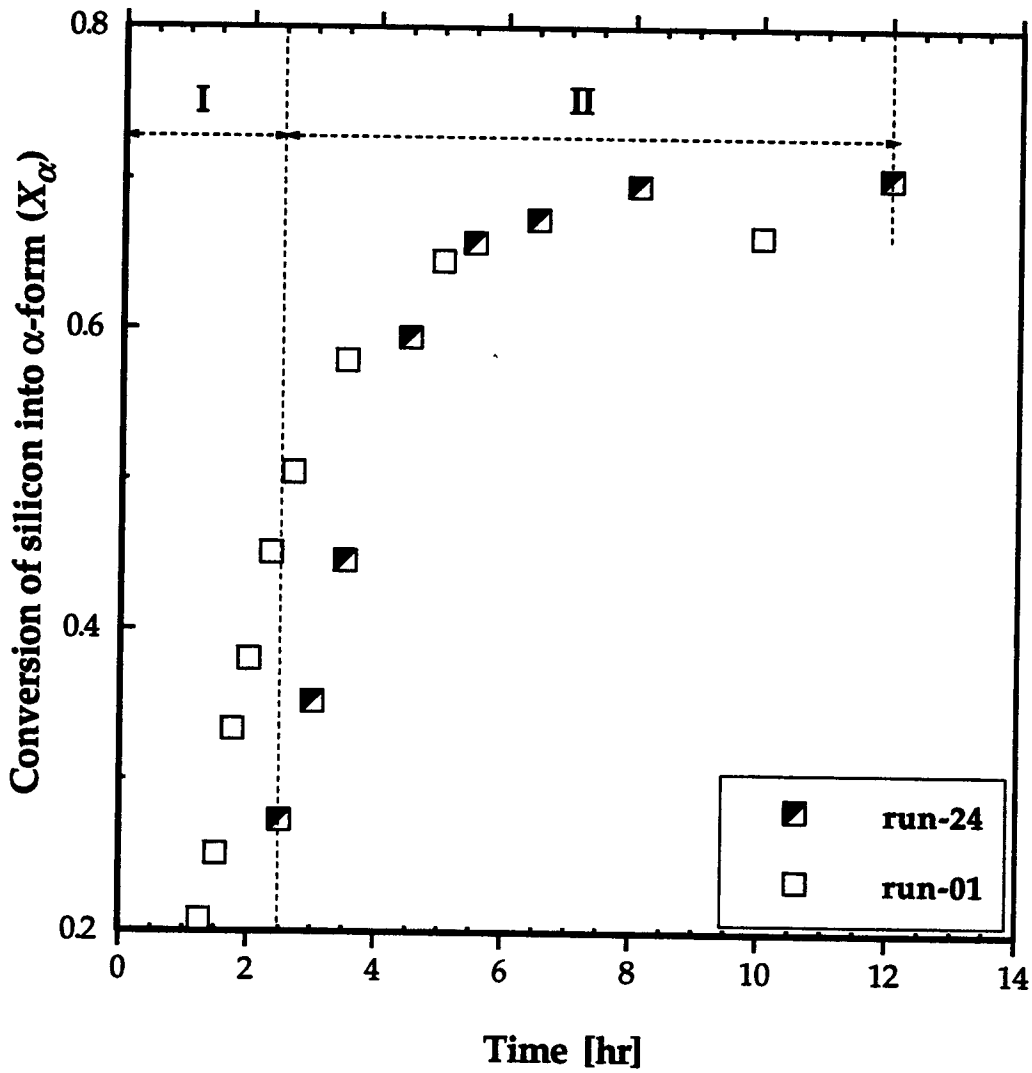

Figure 28. Conversion of silicon into α-form in nitridation at 1200°C in 90%nitrogen-10% hydrogen: comparison of second stage of run-24 with results of run-01.

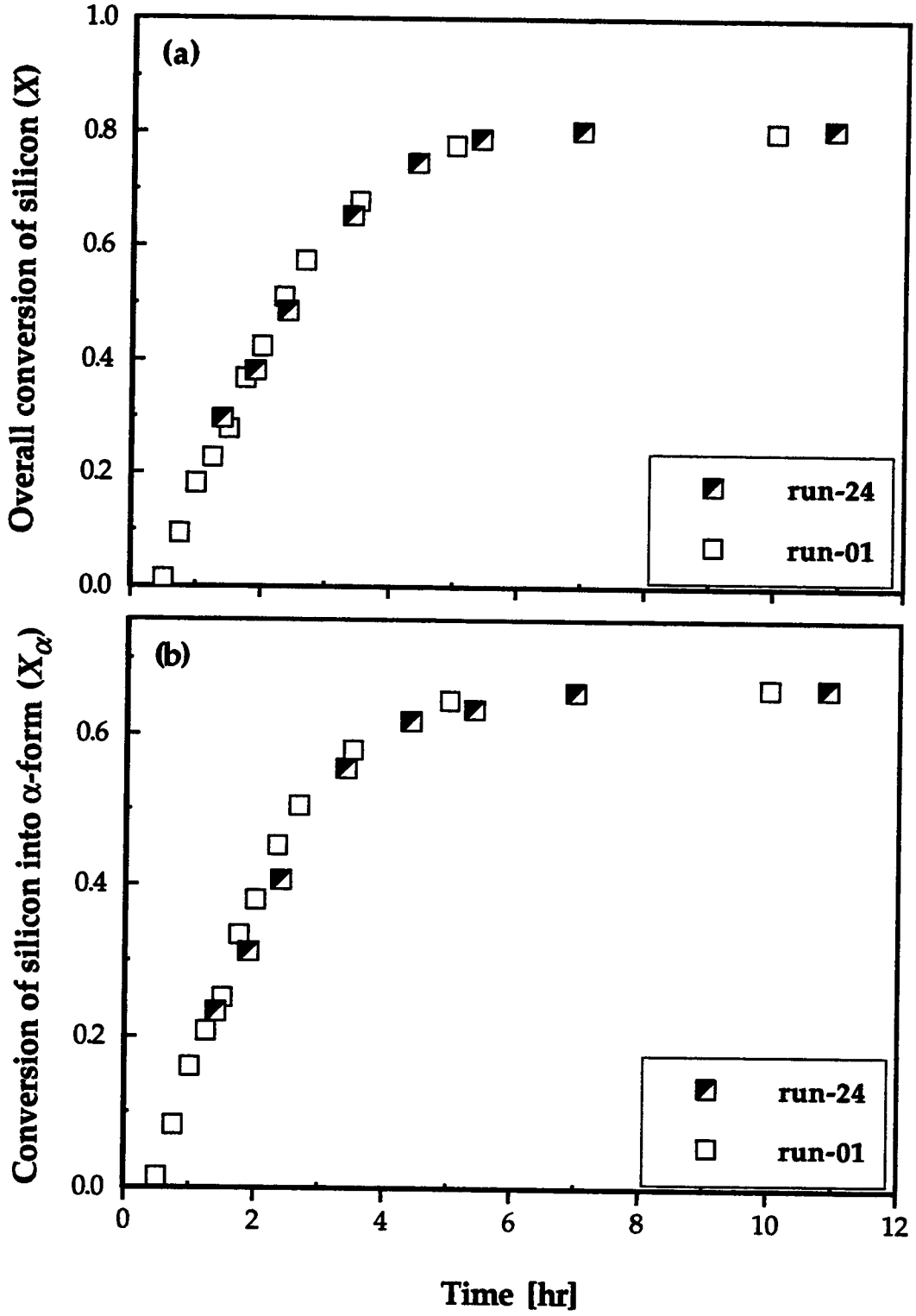

Figure 29. Comparison of results of run-01 and run-24:
(a) X from run-24 plotted versus (time - 1.1) [hr];
(b) (X_α-0.04) from run-24 plotted versus (time - 1.1) [hr].

The results of Figure 29 clearly show that the α-crystal does not play the role of a "seed" which favors a further formation of this phase. It is possible that the addition of the α-form to raw silicon material in previous experimental studies (Campos-Loriz and Riley, 1980) increased the α/β ratio because of better temperature control, by diluting solid reactant and providing an inert heat absorber. This hypothesis can be supported by the finding of Itoh (1990) who also observed an increase in the α/β ratio in the final product when, instead of the α-silicon nitride, the α-silicon carbide was added to the raw silicon material prior to nitridation.

All the findings discussed and presented in this section are still not sufficient to close the question about a possible effect of an initial process stage on subsequent nitridation at altered reaction conditions, which could be manifested as a "seeding" effect. The reason for this are possible structural changes that might occur during nitridation and which depend on reaction conditions (temperature, nitrogen concentration). Jennings and Richman (1976) observed that the α/β ratio in produced silicon nitride increases with an increase in specific surface area of raw silicon grains. On the other hand, Dervisbegovic and Riley (1979) obtained very low final overall conversions (less than 50% even after extended reaction times) in nitridations of larger silicon grains (10-20 μm). Since the results presented in Figures 12-14 and 21 show that both the final overall conversion and the yield of the α-form increase with an increase in the reaction temperature and/or a decrease in the nitrogen concentration, it is possible that higher reaction temperatures and/or

lower nitrogen concentrations might increase the effective reaction surface area by affecting the size distribution of the silicon grains. In the case of a multistage nitridation where the reaction conditions at an initial nitridation stage favor higher overall conversion than do those at a subsequent stage (run-24), the effect of this initial stage on subsequent nitridation was not observed, as shown by Figure 29. If, however, the initial nitridation stage is carried out at conditions which give a lower overall conversion (lower reaction temperature, higher nitrogen concentration) then the situation might be different because the effective reaction surface area could be reduced by this stage, which would affect the further progress of nitridation. Possible effects of reaction conditions on structural changes during nitridation will be discussed in Chapter 4.

3.4 Conclusions and recommendations

A fluidized bed reactor process was applied to the direct nitridation of porous silicon particles composed of fine silicon grains, at temperatures in the range of 1200-1390°C. Nitrogen (30-90%)-hydrogen (5-50 %)-argon mixtures were used as the nitriding gas. The effects of reaction temperature, hydrogen, nitrogen and pretreatment of raw materials on the nitridation of silicon and the yields of α- and β-silicon nitride were investigated.

The results presented in this section indicate that a fluidized bed reactor enables silicon nitride to be produced from silicon powder, with a high α/β ratio and a small amount of silicon remaining unconverted, by controlling the

reaction temperature and the content of hydrogen in nitrogen. The results are summarized as follows:

(1) Nitridation of silicon proceeds uniformly throughout the individual porous silicon particles having sizes in the range investigated.

(2) Nitridation is initiated after an induction period which becomes shorter with an increase in reaction temperature and/or an increase in nitrogen concentration, but remains unaffected by an increase in the hydrogen concentration.

(3) Although the pretreatment of silicon particles with argon containing 40 vol% hydrogen facilitates the nitridation, neither the induction period nor α/β ratio are significantly affected by the pretreatment.

(4) The final overall conversion of silicon into silicon nitride and the yield of α-silicon nitride increase with an increase in the reaction temperature and/or with a decrease in the nitrogen concentration.

(5) The ratio of α- to β-form in the product silicon nitride remains roughly unchanged throughout the nitridation reaction. Depending on reaction conditions it varies between ~5 and ~10. The higher the temperature and/or the lower the nitrogen concentration, the higher the ratio.

(6) Hydrogen in the range of 5-50% does not significantly affect either the final conversion or the yield of the α-form in the nitridation of pretreated silicon particles. The increase in the hydrogen concentration slows the middle nitridation stage down, but does not eliminate the induction period. However, the reaction is extremely slow in absence of hydrogen.

(7) The nitridation of silicon particles can be accelerated and completed (~99% conversion) in as short as 2.5 hours by raising the reactor temperature stepwise with the progress of nitridation.

(8) In the range of experimental conditions investigated, no evidence for "seeding" by the initial α-silicon nitride nuclei was found.

Porous silicon particles used in this study enabled good fluidized conditions. The operating gas velocities of 25 and 35 cm/s provided up to 1275 and 1350°C, respectively, stable operation without agglomerating and chunking of the bed inventory. However, since silicon nitride as a raw material is required to be fine enough to be ready for sintering (< 1 μm), porous silicon nitride particles produced in the fluidized bed need to be pulverized into fine powder, which increases production cost. Hence, the direct use of fine silicon powder in a fluidized bed will be of great advantage over the use of large particles even when the latter are free from additional diffusion resistance. One way to overcome this problem will be the use of fine silicon powder mixed with large silicon nitride particles which are easily fluidized (Liu and Kimura, 1993).

The loss of the silicon due to both attrition and entrainment of fines and evaporation at high temperatures was not monitored in this study. A rough estimate is that, during the 24 hours operation, the loss of silicon due to the entrainment of fines was typically about 10%, the majority of which resulted from the elutriation of fine powder originally mixed with large particles. Although the solids carried out of the bed were not recycled back to the bed in

this experimental study, a problem of this type could be solved by using cyclones in a continuous process even if fine silicon powder were used as a raw material in place of large silicon particles. Despite this, reliable information about the amount of silicon being entrained from the bed is pertinent to the cost evaluation of the fluidized bed nitridation.

A possible loss of the silicon by evaporation could be checked for by an additional accurate porosimetry, i.e. density, measurements. Since the densities of all the major phases being present in the reacting pellets are known (silicon, α-and β-silicon nitride), such an analysis could provide the test if the results of XRD quantitative analysis method close the material balance, i.e. if the amount of the silicon consumed corresponds to the amount of the silicon nitride produced.

Even though it has many advantages, the fluidized bed with a well mixed inventory has the worst residence time distribution (RTD) for solids of any continuous reactor, i.e. it behaves as a continuous stirred tank reactor (Levenspiel, 1993). Even the reaction times needed for almost complete conversion achieved in this study are significantly shorter than majority of those encountered in literature, yet they are still quite long to make a continuous direct nitridation process practical. A multi-staged continuous system could improve RTD of the solids, but, on the other hand, it introduces additional costs compared to a batch or semi-batch process. Therefore, it is of particular interest to explain unexpected nitridation results at temperatures above 1300°C, where the observed reaction was very fast yielding a high α/β

ratio (after 2 hours at 1350°C in 90% nitrogen-10% hydrogen, ~ 96% of the product was the α-form) but, on the other hand, unusually low overall conversion of the silicon.

Finally, one of the most significant impacts on the production costs due to both its high cost and safety measures required for its use, is the need for hydrogen in the nitriding atmosphere. Hence, additional research should be dedicated to explaining the role of hydrogen in nitridation as well as to understanding the nature of the induction period. To do this, however, special analytical techniques are needed which can measure the oxygen content of sample solids in an oxygen free atmosphere and/or monitor oxygen concentration in situ, i.e. in the bed during the reaction.

4. MECHANISM AND MATHEMATICAL MODELING

4.1 Discussion of Previous Work

At present, there is no general agreement regarding the kinetics of not only the formation of α- or β-silicon nitride, but the overall conversion of silicon into silicon nitride. A rigorous comparison of reported experimental data and proposed kinetic models is obscured by the fact that various investigators used different experimental conditions such as particle size distribution, raw silicon purity and trace gas impurities. Moreover, in considering a mechanism of the nitridation process, attention was seldom paid to heat and mass transfer effects which might have controlled the overall reaction rate in the TGA kinetic studies, the experimental procedure widely used in the investigation of nitridation.

Rosetti and Denkewicz (1989) applied kinetic analysis on experimental nitridation results of Rahaman and Moulson (1984) and concluded that the α-forming reaction obeyed a first order rate law with respect to silicon, whereas the β-phase formation was described by the shrinking core model with a reaction control. It is important to mention that they analyzed a normalized conversions obtained by dividing the yields of each of the phases by the total conversion into that phase.

Mendelson (1979) explained silicon nitridation as a multistep process: the initial stage described by an approximately constant rate law followed by the nucleation and growth process. Jennings and Richman (1976) considered

the nitridation as a process in which diffusion and sintering take place simultaneously.

None of the studies mentioned above resulted in a model which reliably fitted the experimental data in a whole range of conversion. The two models described below attempted to do this.

4.1.1 Chain Nucleation and Pore Blockage

Myhre and Motzfeld (1990) proposed a model according to which nitridation in pure nitrogen occurs in gas phase and proceeds in three distinct steps: the initial stage described by a zeroth order kinetics (constant reaction rate), the stage of an increasing reaction rate, considered as chain nucleation or "branching" (Harrison, 1969), and the final stage of a decreasing reaction rate which terminates at overall conversions lower than 100%. Their experimental results show a remarkable increase in the final overall conversion with the decrease in the nitrogen pressure.

The model equation they derived fitted the time (t) required to reach the conversion evaluated on the basis of the specific surface areas of samples (α) as follows:

$$t = \frac{1}{k_2} \ln\left[\alpha \left(\frac{k_2}{B\, k_1}\right)^3\right] - \frac{1}{k_a} \ln\left(1 - \frac{\alpha}{\alpha_f}\right), \quad 0 < \alpha < \alpha_f \qquad (20)$$

where:

- k_1 is the rate constant for linear growth of nuclei,

- k_2 is the rate constant for chain nucleation,

- B is the constant that accounts for a shape factor of crystallites and the number of initial nucleation sites,

- k_a is the rate constant of pore blockage, and

- α_f is the asymptotic final conversion.

Equation 20, essentially a four-parameter model, showed an excellent agreement with their experimental data in a whole range of conversion-time data sets, but this is not surprising due to the number of adjustable parameters used in the fitting relatively smooth conversion-time curves. Moreover, the authors made a meaningless conclusion that three nitrogen atoms are necessary for the linear nitride growth because of the proportionality between k_1 and $p_{N_2}^{1.5}$.

The work of Myhre and Motzfeld (1990) deserves attention because of their explanation of the final reaction stage by the effect of nitrogen pressure, i.e. nitrogen concentration. This asymptotic reaction stage the authors attributed to the gradual blocking of pores which prevents the silicon vapor from passing through and reacting with the nitrogen. An increase in the final conversion with a decrease in the total (nitrogen) pressure they explained as follows:

• the reaction takes place by means of silicon vapor diffusing through the pores of the nitride layer already formed;

- if the rate of diffusion of the silicon vapor is large, most of the reaction will take place outside the pore, on top of the nitride layer;
- low diffusion rate would increase growth of the product inside the pore, with gradual blocking as the result;
- gas diffusivity is inversely proportional to the total pressure, which means that the time the silicon vapor spends inside a pore, reacting and eventually clogging the pore by producing the product, would be proportional to the nitrogen pressure.

The overall scenario presented above is reasonable from the standpoint of the amount of reacting species that are present in a pore but it cannot be explained by gas diffusion. The diffusion through micro-pores is controlled by the either Knudsen or energy activated diffusion mechanisms, but neither of these mechanisms indicates dependence of diffusion coefficient on total pressure. The decrease in the nitrogen pressure, however, decreases its diffusion flux through a pore because of the decrease in its concentration gradient, thereby decreasing the reaction rate in the pores and their blockage. The results of the fluidized bed nitridation shown in Figure 21, obtained at various nitrogen concentrations but at the same total pressure, support this argument. Even though all the data in this figure was obtained at the same total pressure, the decrease in the nitrogen concentration increases the overall extent of nitridation.

4.1.2 Diffusion of Nitrogen through Expanding Product Layer

Thee work of Pigeon and Varma (1993) is the most recent published attempt at modeling the complex nitridation process. This work presents a quantitative model for the direct nitridation of silicon which can, according to the authors' claim, successfully describe the progress of the nitridation in the whole range of conversion curves that follows the initial and relatively short linear conversion-time nitridation stage.

The model proposed by Pigeon and Varma (1993) is based on the sharp interface model (SIM) (Valensi, 1936; Carter, 1961) where diffusion of gas through the product layer controls. This model accounts for the increased volume of the silicon nitride product developing on the surface of silicon grain compared to the volume of the silicon reacted, hence, as schematically shown in Figure 30, as the reaction proceeds the radius of unreacted core decreases but the outer radius of a grain increases.

Ku et al. (1990) also used this model in a computer simulation of the microstructure developed in reaction sintered silicon nitride. In their analysis they included the size distribution of silicon grains and the random packing model with special attention being paid to the change of the effective diffusion coefficient due to the swelling of the grains. Their model, however, predicts an increase in the final extent of reaction with an increase in nitrogen concentration which contradicts the experimental results of this work (Figure 2.21) as well as the previously reported observations (Myhre and Motzfeld,

1990; Atkinson et al., 1976). Also, the model predicts only an 85% conversion of silicon grains as small as 0.03 μm in 25 hours.

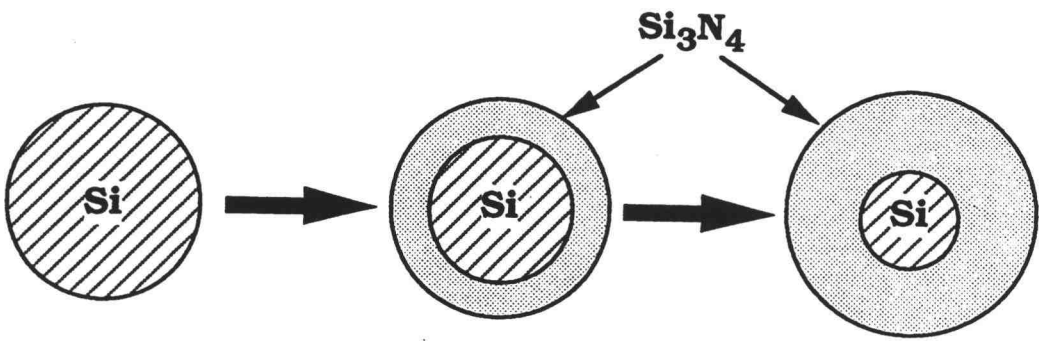

Figure 30. Schematic representation of the sharp interface model (SIM).

Since the sharp interface model is being of projected importance for future development of the field (Pigeon and Varma, 1993), this model is to be presented in this section in more detail.

For a heterogenous reaction of gas with a solid represented by

$$A\ (g)\ +\ b\ B\ (s)\ \Rightarrow\ products \qquad (21)$$

the integral equation that relates conversion of a spherical grain of solid with the reaction time according to SIM is (Pigeon and Varma, 1993)

$$\frac{\xi - \left[(1-\xi)(1-X) + \xi\right]^{\frac{2}{3}}}{\xi - 1} - (1-X)^{\frac{2}{3}} = \left[\frac{2\, b\, C_A\, M_B\, D_{eff}}{\rho_B\, R_0^2}\right] t \qquad (22)$$

where X, defined by a radius of unreacted core (r_c) and the initial grain radius (R_0) as

$$X = 1 - \left(\frac{r_c}{R_0}\right)^3 \qquad (23)$$

represents the conversion of the solid reactant (Levenspiel, 1993), b is the stoichiometric coefficient from Equation 21, C_A is the concentration of the gaseous reactant, D_{eff} is the effective diffusion coefficient of gaseous reactant through the product layer, M_B and ρ_B are the molecular weight and density of solid B, respectively, and ξ represents the volume of the silicon nitride formed per unit volume of silicon reacted. Since three moles of silicon produce one mole of silicon nitride, ξ may be obtained as

$$\xi = \frac{\left(\frac{M}{\rho}\right)_{Si_3N_4}}{3\left(\frac{M}{\rho}\right)_{Si}} = 1.216 \qquad (24)$$

Equation 22 may be rewritten in the linear form as

$$f(X, \xi) = K\, t \qquad (25)$$

with

$$f(X, \xi) = \frac{\xi - \left[(1 - \xi)(1 - X) + \xi\right]^{\frac{2}{3}}}{\xi - 1} - (1 - X)^{\frac{2}{3}} \qquad (26)$$

and

$$K = \left[\frac{2\, b\, C_{N_2}\, M_{Si}\, D_{eff}}{\rho_{Si}\, R_0^2}\right] \qquad (27)$$

It should be mentioned here that SIM described by Equation 22 is valid only for pseudo-steady state conditions, i.e. conditions at which the time dependence of concentration profile of a gas in the product layer can be neglected. Also, for $\xi = 1$ it reduces to the shrinking core model with ash diffusion control - SCMDC, i.e.

$$f(X, \xi) \rightarrow \frac{1}{3}\left[1 - 3(1 - X)^{\frac{2}{3}} + 2(1 - X)\right] \quad as \quad \xi \rightarrow 1 \qquad (28)$$

Figure 31 illustrates that for the case of silicon nitride, i.e. for ξ=1.216, SIM and SCMDC do not yield significantly different results (for the same K, the time for complete conversion predicted by SIM is only 6.7% longer than the one estimated by SCMDC).

Pigeon and Varma (1993) reported that their experimental TGA kinetic data of the nitridation of small amounts of silicon samples can be successfully fitted by Equation 22 in the range of conversion ~ 20-100% (the range subsequent to the initial linear region). They presented eight conversion-time data sets describing the "intrinsic kinetic behavior", five for nitridation of

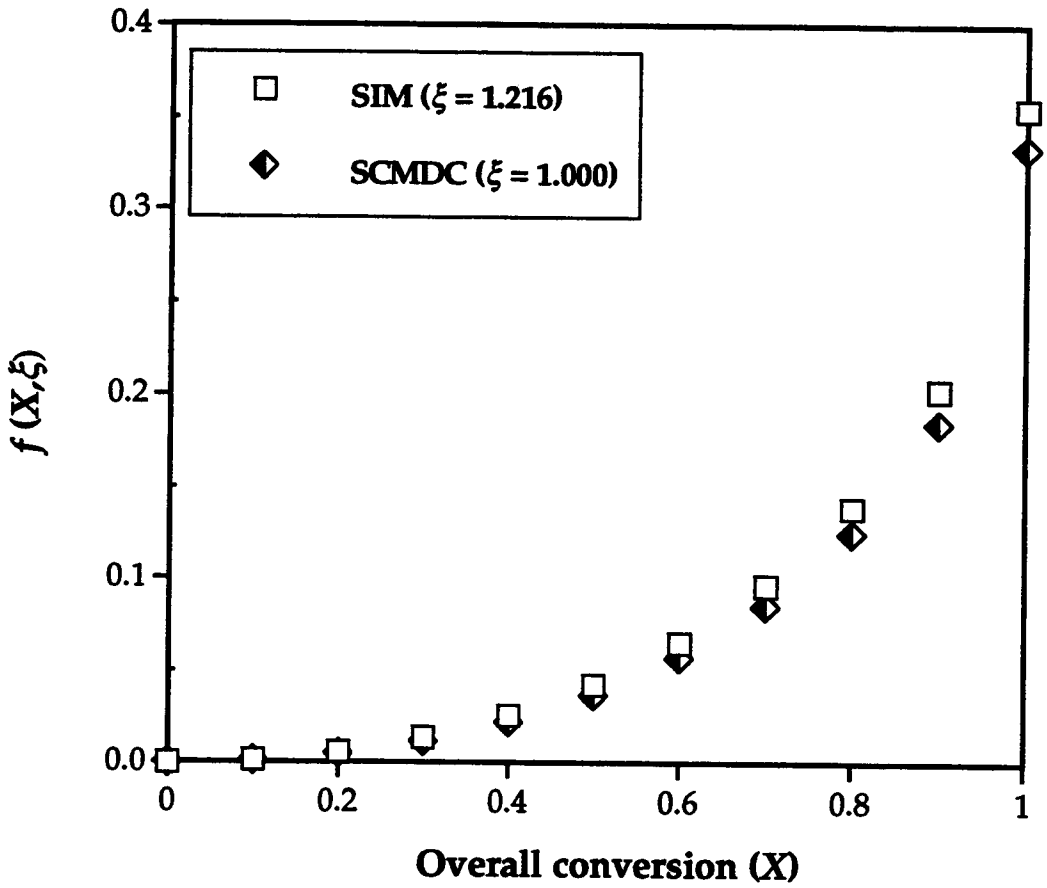

Figure 31. Comparison of SIM and SCMDC for case of silicon nitride growth on spherical silicon grain.

5-10 μm silicon grains at five temperatures in the range 1200-1350°C, and additional three for nitridation of three different grain sizes at 1350°C. All of these experiments were done in an extremely careful experimental setup with specially prepared, nearly spherical, silicon particles, the size of which was measured both by a particle size analyzer and by statistical analysis of digitized SEM images. Even though ultra pure nitrogen was used, the nitriding atmosphere contained a 5% of hydrogen to eliminate any possible effect of a trace oxygen impurity. The amount of silicon sample used (4.6 mg)

assured no heat and/or mass transfer effects intruding the progress of nitridation. In all of these experiments the reaction could be fully completed, even in the case of the nitridation of 20-37 μm silicon grains.

Pigeon and Varma (1993) checked/supported their model by the following three facts:

1: casting the raw conversion/time data into the form of Equation 25 ($\xi = 1.216$) and checking for linearity. The authors demonstrated this procedure on only one data set (5-10 μm silicon grains, 1350°C) which gave an excellent linearity;

2: comparing the activation energy of the diffusion coefficient evaluated by their model (~310 kJ/mol) with the previously reported experimental value for the diffusion of nitrogen through the α-silicon nitride (~233 kJ/mol; Kijima and Shirasaki, 1976);

3: good prediction of the time for complete conversion of the 5-10 μm silicon grains in the temperature range investigated.

As shown by Figure 31, even though being much more complicated, the model given by Equation 22 does not give significantly different results, for $\xi = 1.216$, from the shrinking core model with ash diffusion control. The fact that it has been shown that the latter could not successfully describe the progress of nitridation (Rosetti and Denkewicz, 1989) warranted a thorough analysis of the data reported by Pigeon and Varma (1993). Since the numerical raw data was not presented in their paper, it was recreated from the graphs in the paper and the model was then checked as suggested by the authors. The

three remarks that follow will show that the model of Pigeon and Varma (1993) is not consistent with the data presented in the paper, i.e. that the sharp interface model actually does not fit their nitridation data.

(1) When cast in the form of Equation 25 only their reported data for 5-10 μm at 1350°C gives a linear plot and thus does fit their proposed model (again, this was the only data set they used to demonstrate a validity of the proposed model). Analogous plots generated from the remaining seven conversion-time curves indicate a distinct and consistent deviation from linearity and a S-shaped behavior which cannot be attributed to experimental scatter. Two of such curves are shown in Figure 32.

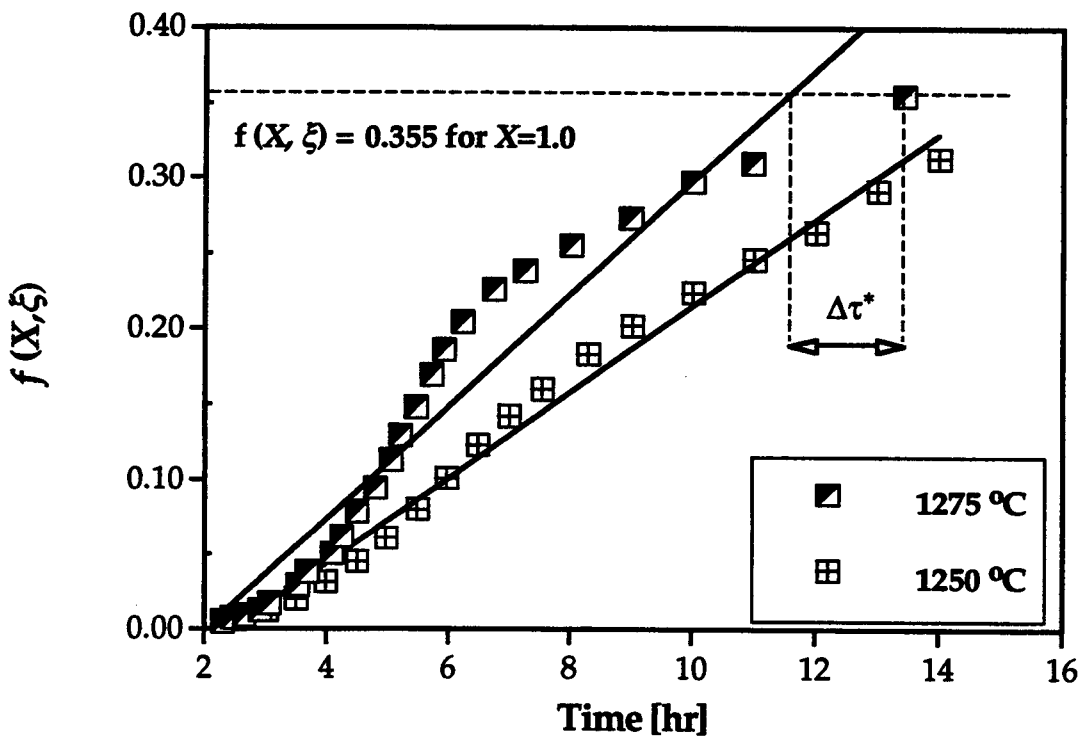

Figure 32. Inconsistency of the data of Pigeon and Varma (1993) with the sharp interface model (the data recreated from the original paper).

(2) The straight lines in Figure 32 do not fit experimental data, therefore the diffusion coefficients evaluated from their slopes (K) by Equation 27 are not representative of the experimental results. This means that the value of the activation energy evaluated from these diffusion coefficients has no meaningful basis, no matter how close it is to the activation energy for the diffusion of a nitrogen atom through α-silicon nitride. Moreover, the authors developed the model considering the nitrogen molecule as the reactive nitrogen species, hence it is unreasonable to assume that the activation energy of its lattice diffusion coefficient is the same as the one for the diffusion of the nitrogen atom. Finally, as it will be discussed in the subsequent sections, the apparent activation energy of the process might contain the contributions of the surface reactions leading toward the formation of reactive nitrogen species.

(3) Once the K is known, the time to reach any given conversion can be readily calculated according to Equation 25. The authors demonstrated in the paper that the times for the complete reaction of 5-10 μm grains, predicted by the model, agree well with those experimentally observed at various temperatures. This should not be surprising since even a completely inappropriate fit gives a reasonable deviation from the experimental time for full conversion, $\Delta\tau^*$, as shown in Figure 32. Therefore, a good prediction of the time needed for 5-10 μm grains to completely react at a particular temperature cannot be used to justify the proposed model.

On the other hand, for any diffusion controlled process the time to reach any given conversion of a spherical grain is proportional to the square of the

grain size. This is also clearly shown by Equations 25 and 27. Consequently, to reach any given conversion the time needed for 20-37 μm grains should be at least four times the time for complete conversion of 5-10 μm grains (this ratio should be independent of the extent of the reaction). Yet, the results of the nitridation at 1350°C indicate that this ratio changes from 4 at the beginning of the reaction to only ~ 1.5 at complete conversion.

4.2 Possible Mechanisms of the Silicon Nitridation and Model Considerations

The previous brief review of reported mechanisms and proposed kinetic models showed that many different approaches were taken to describe direct nitridation of silicon. It is obvious that this complex process cannot be considered without detailed insight in microstructural changes that occur during the reaction. BSE photos, already presented in section 3.3.2, are part of this evidence, but their resolution enabled only the discussion of possible intra-pellet diffusion resistance and provided the important finding that the unreacted silicon remains in large grains and/or grain clusters. However, the photos obtained by TEM analysis (transmission electron microscopy) that are to be presented in this section, offer the important information about structure of the reacting pellet at a sub-micron level. The detailed description of the analytical setup for this analysis is available elsewhere (Koike and Kimura, 1994).

Figures 33 and 34 present TEM pictures of samples taken at various reaction times in one of the runs. It can be seen in these figures that, in the beginning of the reaction, silicon nitride (most probably α-form) was generated partly in the form of fine whiskers bridging silicon grains (Figure 33) and partly as a shell partially covering silicon surface (Figure 34). The formation of whisker-like product is typical for chemical vapor deposition processes (CVD) which may indicate that, during this stage of nitridation, a gas phase reaction dominates (either between silicon vapor and nitrogen or between silicon monoxide and nitrogen in presence of hydrogen).

The pictures of the sample converted to ~54% presented in Figures 33b and 34b show that the silicon surface becomes completely and rather uniformly covered with a silicon nitride layer even at this intermediate conversion. Silicon grains decrease in size but only a part of the produced silicon nitride remains as a shell around unreacted silicon, while majority of silicon nitride can be seen in the form of flake-like crystals filling the inter-grain space. The important finding is that these crystallites are of elongated shape and of similar thicknesses. Hence, it is reasonable to assume that the flake-like product in the inter-grain voids was generated by subsequent spallation of the product layer. Figure 35 clearly supports this hypothesis showing the two adjacent silicon nitride crystallites, one of them being detached from silicon surface.

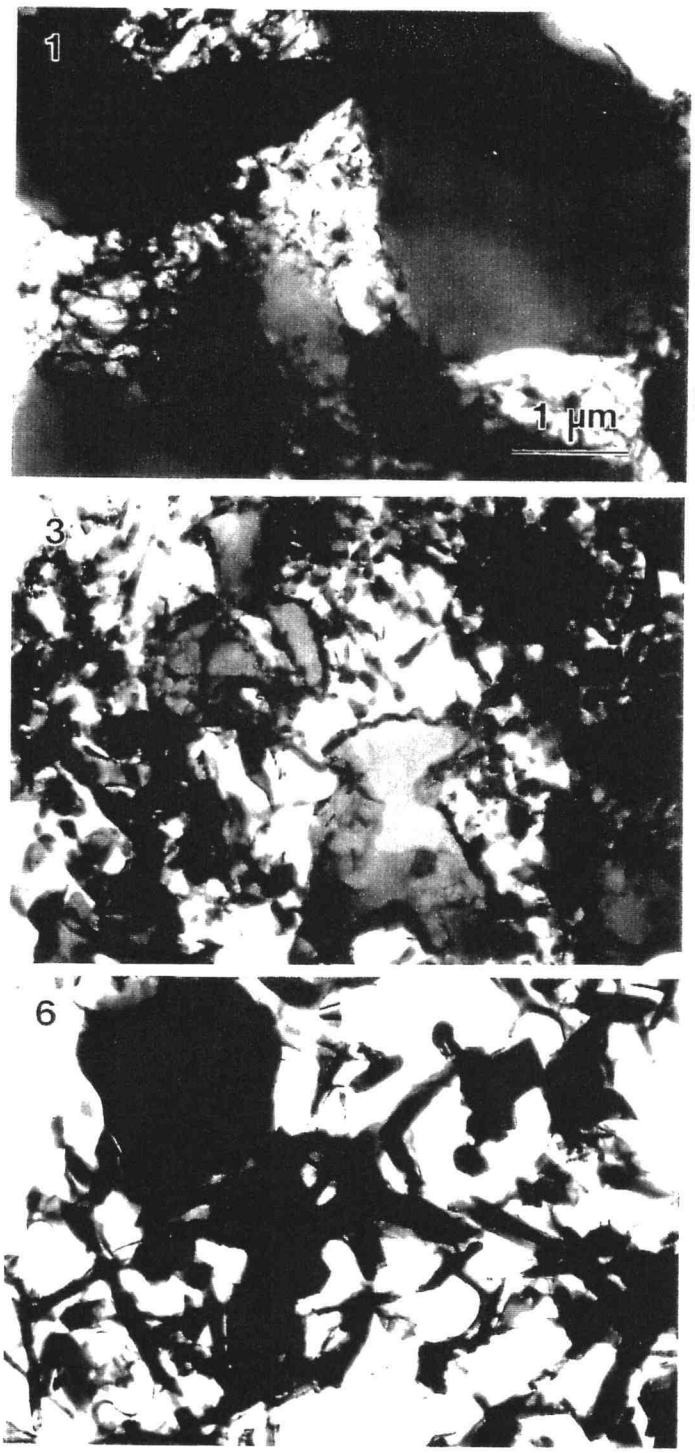

Figure 33. TEM pictures of product pellets at various conversions (run-16): samples-(1) *X*~11%; (3) *X*~54%; (6) *X*~86% (dark-Si_3N_4, bright-Si).

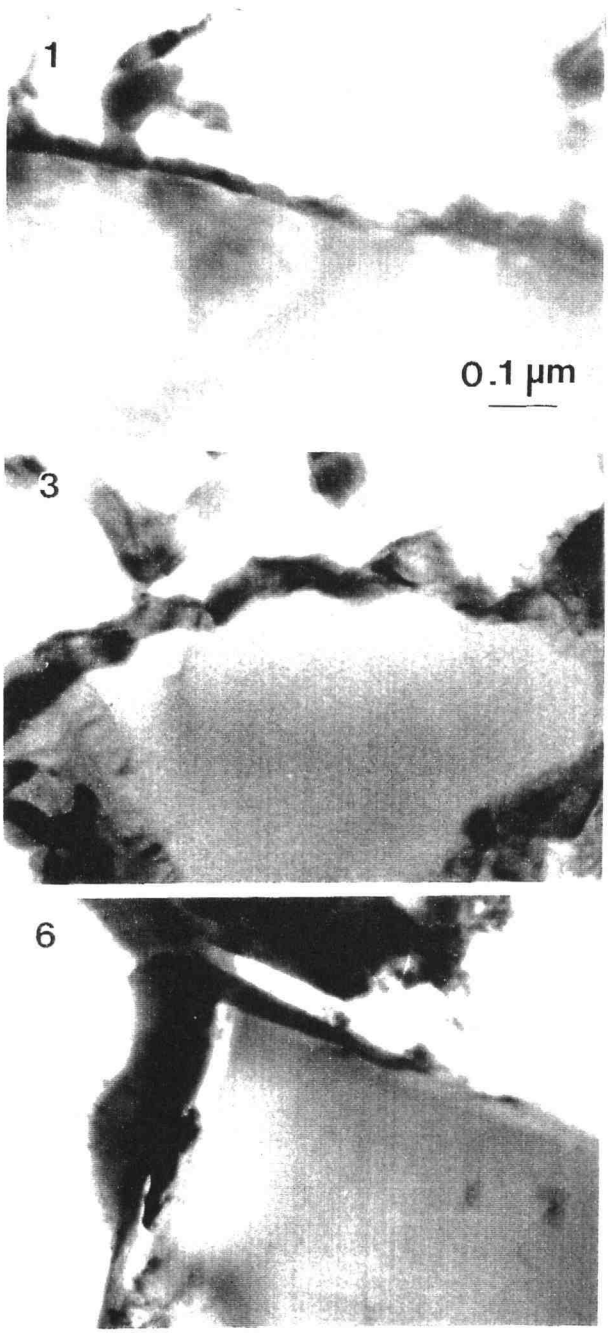

Figure 34. TEM pictures of product pellets at various conversions (magnified details of grains shown in Figure 33).

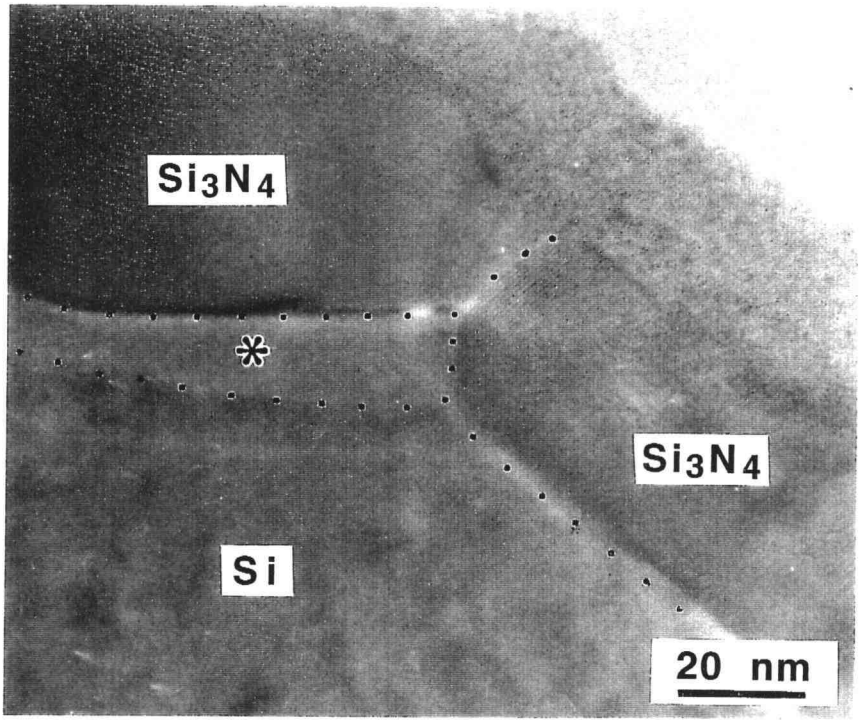

*** Empty gap due to detachment.**

Figure 35. Silicon nitride crystallites detached from the silicon surface.

It is important to mention that the presence of the product flakes could not be attributed to the breakage of the product layer due to a sudden temperature change during the sampling. At the end of run-13 (the reaction conditions specified in Table 3), after the last sample had been taken (24 hr) the nitrogen was switched off and the bed inventory was slowly cooled by argon (5°C/min) to a room temperature. The measured BET areas of the sample taken from the reaction temperature and of the sample taken from the cooled bed were 4.50 and 4.43 m^2/g, respectively (Micromeritics ASAP 2000 Accelerated Surface Area and Porosimetry System). This discrepancy is rather

attributed to the experimental error of measuring the specific surface area than to the crackling of the product due to sudden temperature change.

According to Koike and Kimura (1994) spallation of the produced silicon nitride from silicon grains can be explained by the stress due to the structural misfit at the silicon/silicon nitride interface. On the basis of the direction of the crystal growth shown in Figure 36, these authors determined this misfit and predicted that, in the presence of a crack, i.e. non-uniformity at the silicon/silicon nitride interface, it will make the silicon nitride layer unstable. Their calculations show that at the thicknesses of ~ 50 nm the cracks would propagate and, eventually, detach the nitride from the silicon surface. This estimated critical thickness is roughly in agreement with the observation of Inomata and Uemura (1975). On the basis of Figure 36, Koike and Kimura (1994) also suggested that presence of reactive nitrogen at the silicon/silicon nitride interface is the key factor for the reaction to take place, i.e. that the reaction zone is at silicon/silicon nitride interface.

Figures 33, 34 and 35, showing the physical evidence of the mechanism of nitridation, combined with Figures 21 and 20 from Chapter 3, which demonstrate the effect of nitrogen and hydrogen concentrations on the overall conversion, lead to one more important finding. It is often suggested in literature that the supply of silicon to the reaction site, either as vapor or ion, is the rate controlling step and that silicon, rather than nitrogen, diffuses through the product shell once a shell has been created (Jennings et al, 1988; Myhre and Motzfeld 1990). If this was true, then, as soon as the silicon surface

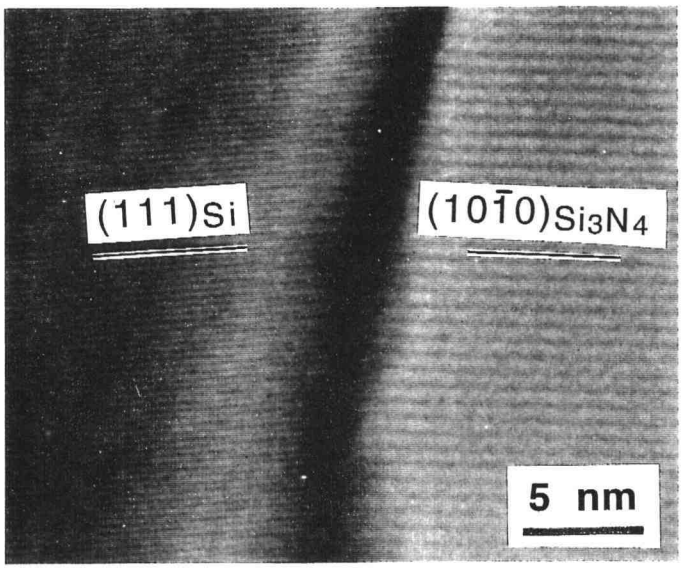

Figure 36. TEM picture of the silicon/silicon nitride interface.

becomes covered with the product layer, the reaction rate would become independent of nitrogen concentration. Figure 21 shows, however, that at intermediate conversions (~50%), when, according to Figures 33 and 34, silicon has been already covered with the product, the conversion curves become steeper as nitrogen concentration increases. This means that the process rate increases with an increase in the nitrogen concentration, assuming that in all the experiments shown in Figure 21 grain size distributions, i.e. effective surface areas, are about the same at the same conversions. Hence, the controlling step could be either the reaction at the gas/silicon nitride interface or the transport of nitrogen through the nitride layer but certainly not the transport of silicon to the outer surface.

The above conclusion is also consistent with Figure 20, i.e. the effect of hydrogen, showing a decreasing reaction rate trend after the initial stage of nitridation with an increase in hydrogen concentration. If the hydrogen does not participate in the reaction as the reactant, this effect could be explained by its higher mobility. Because of the small dimensions of its molecule, atom or ion, if present in the gas phase, hydrogen would probably diffuse easier through the product layer interacting with other diffusing species. This would increase the diffusion resistance to both silicon and nitrogen transport through the nitride layer if these species diffuse by energy activated diffusion, but in any case it would dilute the concentration of reacting species. However, if the process is controlled by the generation of the nitrogen reactive species at the silicon nitride/gas surface, then the inhibiting effect of hydrogen could be due to covering of available surface sites.

As the reaction proceeds, the product is observed mainly in the form of flake-like crystallites, as shown in Figure 33 for $X \sim 86\%$. The product crystallites, like those presented in Figure 37, indicate that they originate from the very same silicon grain. At the same time, as it was already shown in section 3.3.2, unreacted silicon remarkably remains in larger silicon grains (Figure 9).

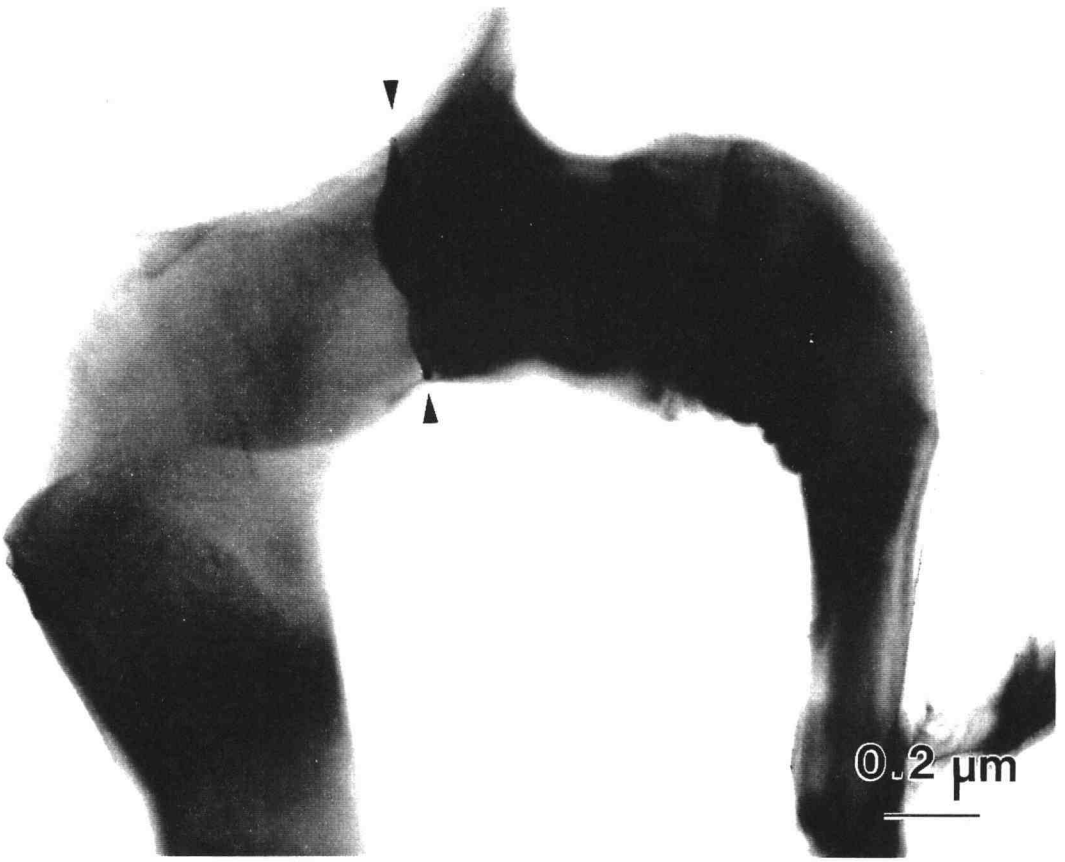

Figure 37. Flake-like silicon nitride product in inter-grain void.

Figure 38 presents one of the most important findings about the microstructure of the reacting pellet. This figure clearly shows that nitridation takes place along grain boundaries in polycrystalline silicon grain. Just a visual comparison of the nitride crystallites shown in this figure with those seen in Figure 35 may indicate that the nitride in the boundaries grows as the fiber-like, elongated, β-form while the α-form is generated at the outer surface of

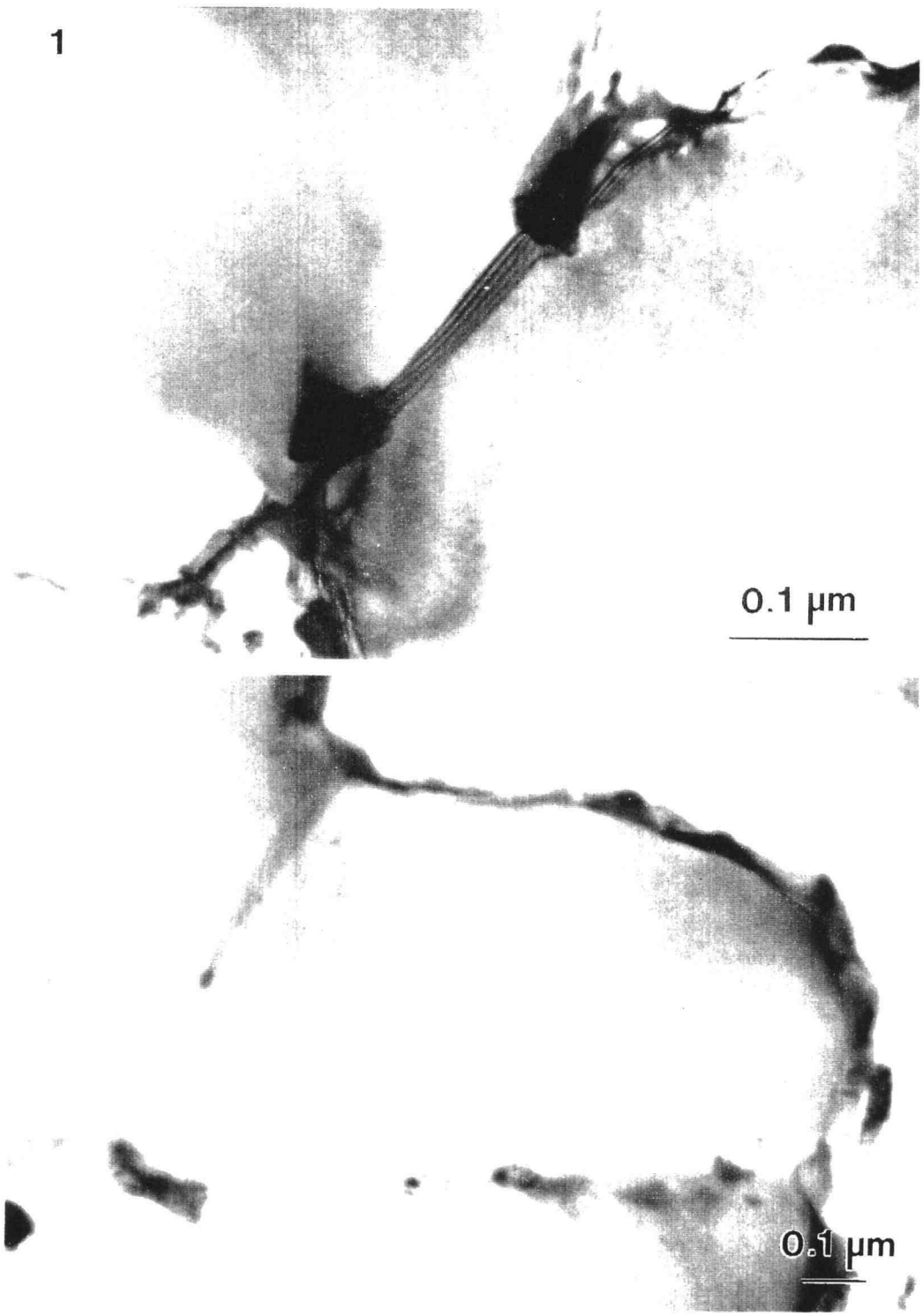

Figure 38. Silicon nitride growth along grain boundaries in polycrystalline silicon grain.

the grains. This would, also, be consistent with published observations which relate a high surface area of the raw silicon material with a high α/β ratio (Jennings and Richman, 1976). Moreover, Figure 38 may serve as the basis for the assumption that the crystal growth along the boundaries may cause a partial disintegration of the polycrystalline grain and hence increase the effective surface area of the pellet.

Apparently, it is very difficult to elucidate the mechanism of the nitridation, even after neglecting the fact that it might consist of two separate paths, each leading to the formation of either α- or β-silicon nitride. Even the high resolution evidence about microstructural changes presented in this section could not provide certain information about any of the following:

- possible form of reactive species (nitrogen atom or ion);

- rate determining step (diffusion, reaction, or both);

- reaction site (silicon nitride surface, silicon/silicon nitride interface, the nitride layer, grain boundaries between product crystallites, or the free silicon surface exposed after spallation of the product shell).

Another difficult task in explaining the nitridation is to distinguish the intrinsic kinetic effects from possible structural effects, such as:

- various extent of the disintegration of polycrystalline silicon grains at various reaction conditions;

- clogging of the grain boundaries by the product;

- termination of the product peeling process.

These all might be the reasons for different final conversions at different temperatures and/or nitrogen concentrations.

Hence, on the basis of information available at present, any attempt of modeling the direct nitridation of silicon is subject to a serious speculation, and, thus, the results must be carefully discussed. The most reasonable assumption for the mechanism of nitridation, however, seems to be to consider it as a process controlled by the transport of a reactive species through the crackling, polycrystalline product layer covering the silicon surface.

4.2.1 Nitridation Controlled by Diffusion of Electro-Neutral Species

The differential form of the mass conservation equation in rectangular coordinates for the one-dimensional nitrogen diffusion through silicon nitride, may be presented as follows

$$\frac{\partial C_N}{\partial t} = D \frac{\partial^2 C_N}{\partial y^2} \tag{29}$$

Introducing the nitrogen concentrations at distances $y = 0$, $y \to \infty$ and $y = \delta$, and scale parameters for time and distance as t_* and y_*, respectively, Equation 29 may be rewritten in terms of dimensionless variables

$$\overline{C} = \frac{C_N\big|_{y=\delta} - C_N\big|_{y\to\infty}}{C_N\big|_{y=0} - C_N\big|_{y\to\infty}}, \qquad \overline{t} = \frac{t}{t_*}, \qquad \overline{y} = \frac{y}{y_*} \tag{30}$$

as

$$\left[\frac{y_*^2}{Dt_*}\right]\frac{\partial \overline{C}}{\partial \overline{t}} = \frac{\partial^2 \overline{C}}{\partial \overline{y}^2} \qquad (31)$$

According to Equation 31, for the pseudo-state condition, i.e. ,

$$\frac{\partial^2 \overline{C}}{\partial \overline{y}^2} = 0$$

it must be

$$\left[\frac{y_*^2}{D\,t_*}\right] << 1 \qquad (32)$$

Based on measurements of the self-diffusion coefficients of nitrogen in polycrystalline α- and β-silicon nitride by a gas-solid isotope exchange using ^{15}N as a tracer, Kijima and Shirasaki (1976) reported that in a temperature range 1200-1410°C these can be predicted as

$$D_{N\text{-}\alpha} = 1.2 \times 10^{-16} \exp\left[-\frac{233{,}205}{R\,T}\right] \left[\frac{m^2}{s}\right]$$
$$D_{N\text{-}\beta} = 6.8 \times 10^{+2} \exp\left[-\frac{777{,}489}{R\,T}\right] \left[\frac{m^2}{s}\right], \qquad (33)$$

The nitrogen diffusion coefficient through α-silicon nitride at 1350°C calculated from Equation 33 is $D_{N\text{-}\alpha} = 3.74 \times 10^{-24}$ m^2/s. Hence, to assume time independent concentration of the nitrogen diffusing through the α-silicon nitride layer as thin as 50 nm (5×10^{-8} m), the time scale estimated by inequality from Equation 32 must be

$$t_* >> \frac{(5 \times 10^{-8})^2}{3.74 \times 10^{-24}} = 6.7 \times 10^8 \text{ sec} \sim 21 \textit{ years.}$$

This means that it would take a several years for the nitrogen atom to penetrate the distance of 50 nm diffusing through α-silicon nitride. The situation for the diffusion through β-silicon nitride is not much better, i.e. the time scale should be much longer than 1.2 years ($D_{N\text{-}\beta} = 6.44 \times 10^{-23}$ m^2/s at 1350°C).

The above result shows that the diffusion of nitrogen atom through a silicon nitride layer cannot be considered as the rate controlling step during nitridation. In general, the transport described by Equation 29 could be facilitated by a fast irreversible reaction occurring either at the silicon/silicon nitride interface or everywhere within the nitride layer; however, the result of the above scale analysis still applies to the former but the latter scenario does not seem to be realistic according to the ordered nitride growth seen in Figure 36. Moreover, a possible effect of the fast reaction within the diffusion distance presumes the presence of both reactants everywhere within the layer, i.e. the transport of the silicon reactive species must be considered as well.

The preceding analysis concentrated on the nitridation controlled by the diffusion of nitrogen through the single-crystal silicon nitride layer, on the basis of reported values for the nitrogen atom diffusion coefficients. It can be also applied for the case when the diffusion of silicon controls the overall process rate. Even though data for the silicon diffusion coefficients are scarce,

Kunz et al. (1988) reported for the ^{30}Si self-diffusion coefficient through the α-silicon nitride a value of 4.5×10^{-20} m^2/s at 1400°C. This value is much higher than the diffusion coefficient of nitrogen through the α-form (~ 4 orders of magnitude) but still gives an order of days for the diffusion time.

When considering which of the fluxes, nitrogen or silicon, might prevail during the nitridation it is not sufficient to compare only the diffusion coefficients of these species. This can provide a rough estimate, but for a detailed comparison of the fluxes it is necessary to include the analysis of the corresponding driving forces as well. The only information available in literature about the concentrations of the reactants during nitridation, however, are the partial pressures of nitrogen (~1 atm) and silicon (~10^{-7} atm at 1350°C; Moulson, 1979). Since these are the surface, not bulk concentrations of the diffusing species which are relevant for solid state diffusion, these must be related to above partial pressures. To do so, one must know the exact form of the diffusing species as well as the mechanism of its generation on a surface. For example, gas dissociation constants of nitrogen molecule toward its atom at usual nitriding temperatures is very small , i.e. of the order $10^{-23} \sim 10^{-28}$ (Roine, 1993), so the most probable source of the diffusing nitrogen atom would be a chemisorbtion of the nitrogen molecule on the silicon nitride surface followed by the decomposition of the precursor. One of the possible scenarios for this could be described by the following set of reactions:

$$N_2\,(g) + [S] \rightleftharpoons N_2\,(s)$$
$$N_2\,(s) + [S] \rightleftharpoons 2\ N\,(s) \qquad (34)$$

If the mechanism, rate constant of the controlling step and equilibrium constants of remaining equations are known, the surface concentration of a diffusing nitrogen species could be evaluated and related to a partial pressure of the molecular nitrogen. Hence, the surface concentrations of the diffusing species are, in general, functions of equilibrium and rate constants of several intermediate reactions involved in the mechanism of the formation of such species. Without knowing them, driving forces cannot be determined.

The discussion so far has concentrated on the feasibility of nitridation being controlled solely by the transport of neutral species, and it has been based on the reported transport coefficients for the both silicon and nitrogen atoms through the single, i.e. reasonably perfect silicon nitride crystal. In the case of the transport through polycrystalline media, the overall diffusion coefficient could be significantly higher. The main effect caused by grain boundaries is a decrease in the activation energy up to one half of that for lattice diffusion (Christian, 1975), which may increase the overall diffusion coefficient several orders of magnitude (Khormaei, 1989). For example, if the corresponding activation energies for the diffusion of a nitrogen atom through α- and β-silicon nitride are reduced by a factor of 0.5, then, at 1300°C, $D_{N\text{-}\alpha}$ increases from ~ 10^{-24} to only ~ 10^{-20}, but $D_{N\text{-}\beta}$ increases from ~ 10^{-23} to 10^{-11} m^2/s. The later value seems much more reasonable from the standpoint of

observed nitridation rates, but, as it was mentioned in Chapter 3, vast majority of the product is the α-, not the β-form.

In closure, one more possibility for transport of atomic or molecular (nitrogen) species should be mentioned. If the peeling of the product generates micro-cracks everywhere within the product shell as well as between silicon and silicon nitride interface (Figure 35), then the transport of species could be by pore diffusion. The exact diffusion mechanism would depend on the size of pores and the interaction of the species with the surface (Knudsen diffusion, surface diffusion, molecular sieving), but in any case the effective diffusion coefficient would be higher than one for lattice diffusion.

4.2.2 Nitridation and Charged Species

The discussion to this point has illustrated that, according to reported diffusion coefficients, the diffusion of atomic species through either crystalline or polycrystalline silicon nitride does not seem to be a probable nitridation mechanism. On the other hand, one may ask the reasonable question: what if the species for which transport coefficients were reported (Kunz et al., 1988; Kijima and Shirasaki, 1976), are not relevant to the process at all? The reported diffusion coefficients of silicon and nitrogen atoms are separately measured by the annealing of these atoms into the nitride, but this was done under conditions which do not exist during the actual nitridation. As shown in section 4.2, the actual process takes place in presence of both nitrogen molecules and silicon surface, which are separated by a layer of silicon nitride.

This environment, under high reaction temperatures, might provide charged species, the transport of which could be facilitated by various electrostatic effects (Fromhold, 1976).

Literature data that treat nitridation as an electrochemical process are scarce. Hayafuji and Kojima (1982) showed that the growth of a thin silicon nitride film (< 55 Å) is limited not by the transport of charged species but with the surface reactions that participate in the formation of N^{3-} which was believed to be the reactive nitrogen form. As one of the possible mechanisms of N^{3-} formation could be described by the below set of reactions, with the rate determining step being the third reaction in the set:

$$\begin{aligned} N\,(s) + e^- &\rightleftharpoons N^-(s) \\ N^-(s) + e^- &\rightleftharpoons N^{2-}(s) \\ N^{2-}(s) + e^- &\rightarrow N^{3-}(s) \end{aligned} \qquad (35)$$

These reactions might occur subsequently to the reactions given by Equation 34. The result of Hayafuji and Kojima (1982), however, gave the overall nitridation rate independent of a partial pressure of nitrogen, i.e of the nitrogen concentration.

The transport of the charged species through the nitride layer could be faster than the one of those that are electro-neutral, but the question arises: what the origin of such species might be? The answer to this question is also important for relating the surface concentrations of diffusing species with bulk partial pressures. Equations 34 and 35 are only one of the possible scenarios for the formation of active ionic nitrogen form(s), but it is sensible to assume

that hydrogen also participates in the mechanism of surface adsorption. Free electrons and/or holes are needed in any case.

At room temperature (27°C) silicon behaves as a semiconductor, having the intrinsic charge carrier (electron and hole) density ~ 10^{10} cm^{-3}, and the gap energy, i.e. the energy between valence and conduction bands, of 1.12 eV (Sze, 1981). With an increase in temperature, however, the number of intrinsic silicon charge carriers per unit volume dramatically increases, becoming ~$10^{19}cm^{-3}$ at usual nitridation temperatures (1200-1400°C) (Sze, 1981). This means that silicon, under these conditions, behaves almost like a metal and that possible participation of charged species in the direct nitridation should not be neglected.

The rigorous analysis of the possible mechanisms involving the charge effects during nitridation is beyond the scope of this work. However, a reasonable assumption is that such a process could be affected by the migration of the electrons from silicon surface to the gas/silicon nitride interface through the nitride layer. These electrons might participate in the formation of negatively charged ionic nitrogen forms at outer nitride surface (N^{-X}), which would be driven back toward the positive silicon holes at the silicon/product interface. Thus, the transport of nitrogen would be facilitated by the electric field generated by the electron transport, which is the effect extensively studied in cases of oxide growth on metals (Fromhold, 1976). The discussion that follows will show that, in particular cases, the transport of

charged species could be described by the same models used in describing the processes controlled by the diffusion of electro-neutral species.

In general, the total flux of a charged species in an electric field can be expressed by the contribution of three terms:

- the concentration gradient driving force (Fick's diffusion),
- the electric field facilitatation (usually termed as migration), and
- the bulk flow of the diffusion medium, i.e. the convection term.

Since the convection term does not participate in solid state diffusion, the total flux of a particular charged species, *i*, through a solid layer could be expressed as

$$J_i = - z\, u_i\, F\, C_i\, \nabla\Phi - D_i\, \nabla C_i \qquad (36)$$

where F represents Faraday's constant, z the number of proton charges carried by the species, C_i the concentration of the species, D_i the effective diffusion coefficient of the species, Φ the electrostatic potential and u_i the mobility approximated by the Nernst-Einstein equation (Newman, 1991), strictly valid only at infinite dilution, as

$$u_i = \frac{D_i}{R\,T} \qquad (37)$$

Equation 36 is usually considered for pseudo-steady state conditions (Newman, 1991). The problem discussed by Cabrera and Mott (1949) deals with the two reacting species case when a potential difference is generated by the rapid flow of one electronic species while the flux of the other is strongly rate limiting. The solution of this problem in rectangular coordinates, for a

constant potential difference $\Delta\Phi$, negligible Fick's diffusion, and the assumption that surface concentration does not change significantly with the distance, describes the growth of metal oxides by the parabolic law, i.e.

$$\delta^2 = 2\, D_{CM}\, t \tag{38}$$

where δ represents the oxide thickness at time t and D_{CM} is the apparent diffusion constant defined as

$$D_{CM} = \eta_i\, F\, z_i\, u_i\, C_{i,S}\, \Delta\Phi \tag{39}$$

In above equation, η_i is the constant that relates the volume of the product formed per mole of the transferred species and $C_{i,S}$ is the concentration of the species at surface at which the species is being generated. Since the film thickness is directly related to the conversion, it is convenient to recognize that Equation 38 actually has the form which is the result of the SCM model with ash diffusion for a flat plate (Levenspiel, 1993).

$$X^2 = \zeta\, t \quad \left(\zeta = \frac{2\, D_{CM}}{\delta^2_{max}} = const \quad \text{where } X = 1 \quad \text{for } \delta = \delta_{max} \right) \tag{40}$$

In the study of thick (> 1 μm) films growth by the simultaneous transport of electrons and electron holes with the electro-neutrality being preserved everywhere within the diffusion layer except near both interfaces, the same result can be obtained without neglecting Fick's diffusion, but with a different meaning of D_{CM} (Kimura, 1992). If the derivation, with the assumptions that lead to Equation 38, is repeated for the case of the layer

growing on a spherical surface, then relating the migration flux of the reactive charged species with the consumption of the substrate at the boundary at $r = r_c$, and using Equation 36, gives

$$-\frac{dN_i}{dt} = -\frac{1}{b}\frac{dN_B}{dt}$$

$$z_i\, u_i\, F\, C_{i,S}\, \frac{d\Phi}{dr_c}\, 4\pi r_c^2 = -\frac{1}{b}\, 4\pi r_c^2\, \frac{\rho_B}{M_B}\, \frac{dr_c}{dt} \qquad (41)$$

Integrating this equation from the outer surface inward and relating the change of the outer radius R^*, with the help of Equation 24, with conversion defined by Equation 23 as

$$R^* = \left[1 + (\xi - 1)\, X\right]^{\frac{1}{3}} \qquad (42)$$

the final equation, that relates the conversion with time, may be expressed as follows:

$$\frac{\xi_i - \left[(1 - \xi_i)(1 - X) + \xi_i\right]^{\frac{2}{3}}}{\xi_i - 1} - (1 - X)^{\frac{2}{3}} = \frac{2b\, C_{i,S}\, M_B \left[z_i\, u_i\, F\, \Delta\Phi\right]}{\rho_B\, R_0^2} \qquad (43)$$

The above equation for

$$D^* = z_i\, u_i\, F\, \Delta\Phi \qquad (44)$$

has the same form as the result for the sharp interface model given by Equations 26 and 27, i.e. SCMDC if $\xi = 1$.

Equations 40 and 43 imply that solutions for a completely different transport mechanism, i.e. migration, could coincide, under a specific conditions, with the solutions obtained for the very same geometries but for Fick's diffusion. This is much easier to understand by recognizing that migration is driven by the electric field which, at constant potential difference decreases with an increase in the layer thickness. However, the temperature dependance of the apparent diffusion coefficient of Equation 43 must be carefully approached. Its apparent energy activation, in general, consists of the contribution of D_i through Equations 44 and 37, but also includes the free energies of the reactions that participate in formation of the active charged species at the surface. The effect of these reactions appears through the relation between the bulk gas concentration and the surface concentration participating in Equations 34 and 35.

4.2.3 Summary

After combining the experimental observations presented in Chapter 3 and the most reasonable hypothesizes regarding the mechanism of the silicon nitridation, the clues and information pertinent for understanding of this complicated process may be summarized as follows.

→ The initial stage of the process follows a mechanism different from the one in the subsequent stage.

→ The silicon grains are of irregular shape and have a wide size distribution.

→ The vast majority of silicon grains are covered by the nitride layer during the nitridation.

→ The product shell has a limiting thickness after which it peels off.

→ The product crystallites grow at the silicon/silicon nitride interface which means that nitrogen must be supplied through the product layer.

→ The product also grows along grain boundaries intervening agglomerated silicon grains.

→ The process rate increases with an increase in the nitrogen concentration in the gas phase.

→ After the initial stage, the process rate decreases with an increase in the hydrogen concentration in the gas phase.

→ Final overall conversion is not related to thermodynamic constraints but to structural changes during nitridation and to grain size distribution (majority of the non-reacted silicon is concentrated in largest grains or grain clusters).

→ The contribution of the diffusion of electro-neutral species to the overall reaction rate, according to available literature data, does not seem probable. Even though the possible electrochemical effects were not properly justified in this work, the number of intrinsic charge carriers of silicon at reaction temperatures indicates that charged species might be involved in nitridation.

→ The nitrogen transport through the crackling silicon nitride shell or along the grain boundaries between silicon nitride crystallites, followed by

the subsequent nitrogen migration through the micro-cracks between the nitride and silicon surface (Figure 35), might be faster than any other transport mechanism.

→ The peeled silicon nitride might deposit in inter-grain voids, bridge the silicon grains and increase the overall intra-pellet diffusion resistance for the nitrogen transport.

4.3 Peeling Shell Model

According to the discussion in the preceding sections, it seems reasonable to consider nitridation as a process controlled by the nitrogen transport toward the silicon/silicon nitride interface through the polycrystalline, crackling silicon nitride layer growing on the silicon surface and occasionally detaching from the silicon grains. Despite the fact that neither the form of the reactive nitrogen species nor the exact transport mechanism of that species (diffusion through grain boundaries between silicon nitride crystallites, diffusion through micro-pores generated by crackling of the product, electric field facilitated transport) are known, the model devised and discussed below is based on the shrinking core model with ash diffusion control. The reasons for this are as follows:

- it was shown that the difference in volumes between reacted silicon and produced silicon nitride can be neglected (Figure 31), thus using more complicated sharp interface model is not justified;

- under certain conditions, SCMDC could describe different transport mechanisms of the reactive species through the product layer (section 4.2.2).

The growth of the product layer is, however, considered to be discontinuous, i.e. a silicon nitride shell around the unreacted silicon breaks and peels off from the silicon surface after reaching a critical thickness.

4.3.1 Model Assumptions

The summary of the assumptions used as the basis for the model approach devised below is as follows:

(1) Reactant pellets consist of spherical grains of an uniform size.

(2) Isothermal conditions prevail.

(3) "Grainy porous pellet" approach applies, i.e. there is no diffusion resistance between the grains of the pellet.

(4) A crackling, polycrystalline silicon nitride shell forms on all fresh silicon surfaces. This shell grows with time according to the shrinking core model with ash diffusion control, with the transport of nitrogen through the shell being the rate controlling step.

(5) The product shell grows up to a critical thickness designated δ^*, after which it peels off, and the process proceeds further according to the assumption (4).

4.3.2 Derivation of Model Equations

The pertinent equations for the model outlined above are Equations 25, 27 and 28, rewritten here as

$$f(x) = 1 - (1 - x)^{\frac{2}{3}} + 2(1 - x)$$
$$f(x) = \frac{t}{\tau_0} \tag{45}$$

In the previous equation

$$\tau_0 = \frac{\rho_{Si}}{6b\, M_{Si}\, C_{N^x}\, D} R_0^2 = a\, R_0^2 \tag{46}$$

represents the time for the complete conversion of the grain of silicon having an initial radius R_0, when a nitride layer grows continuously, i.e. when it does not peel from the silicon surface. In Equation 46, since neither the form of the nitrogen being supplied to the silicon surface nor the nitrogen transport mechanism are known, b is generally unknown ,C_{N^x} represents the concentration of the unspecified, but active nitrogen species at the gas/silicon nitride interface, having an apparent diffusion coefficient D, and a is the parameter defined as

$$a = \frac{\rho_{Si}}{6b\, M_{Si}\, C_{N^x}\, D} \tag{47}$$

In the process proceeding through the subsequent peelings of the product layer at particular times t_i, after it has reached the critical thickness δ^*, the conversion of silicon at the i^{th} peeling may be defined in the following two ways:

(a) The overall conversion, X_i, with respect to the initial grain diameter, R_0;

(b) The fractional conversion, x_i, with respect to the grain radius R_{i-1}, at the moment of the previous, $(i\text{-}1)^{th}$ peeling.

The above definitions may be expressed as follows:

$$x_i = 1 - \left(\frac{R_i}{R_{i-1}}\right)^3 \qquad (48)$$

$$X_i = 1 - \left(\frac{R_i}{R_0}\right)^3 \qquad (49)$$

In general, for any radius of the unreacted core between R_{i-1} and R_i, the corresponding conversions $x_{i-1}^{\,i}$ and $X_{i-1}^{\,i}$ are related by equations 48 and 49 as

$$\left(1 - x_{i-1}^{i}\right) = \left(1 - X_{i-1}^{i}\right)\left(\frac{R_0}{R_{i-1}}\right)^3 \qquad (50)$$

which means that these conversions are the same if the peeling does not take place.

It should be noted that, for being used in Equation 45, the conversion defined by Equation 48 requires the continuous relative time scale, θ_i^{i-1}, such

that between two successive peeling occurrences at moments t_i and t_{i-1}, the following applies:

$$\begin{aligned} \theta^i_{i-1} &= t - t_{i-1} \quad \text{for} \quad t_{i-1} \le t \le t_i \\ \theta^i_{i-1} &= \Theta_i \quad \text{for} \quad t = t_i \\ \theta^i_{i-1} &= \theta_M \quad \text{for} \quad i-1 = M \end{aligned} \tag{51}$$

In Equation 51, $t_0 = 0$ and M represents the total number of peelings that can happen during the time t.

The radius of the grain at the i^{th} peeling, R_i, may be related with δ^* and R_0 as follows

$$R_i = R_{i-1} - \delta^* = R_0 - i\delta^* = R_0\left[1 - i\left(\frac{\delta^*}{R_0}\right)\right] \tag{52}$$

$$i = 1, 2, \ldots, M$$

so the fractional conversion at each peeling occurrence can be determined by Equation 48 and related to the corresponding overall conversion by Equation 50.

Hence, according to the notation given by Equation 51, the overall reaction time t, at which the conversion is X, can be expressed as

$$t = \theta_M + \sum_{i=1}^{M} \Theta_i \tag{53}$$

If the time required for complete conversion of the grain formed after the i^{th} peeling is designated τ_i, then from Equation 46 it follows that

$$\tau_i = a\, R_i^2 \tag{54}$$

and from Equations 45 and 51

$$\Theta_i = \tau_{i-1} \; f(x_i) \tag{55}$$

Since the final conversion is related with the relative time scale after the M^{th} peeling through Equation 50, θ_M is obtained as

$$\theta_M = \tau_M \left[1 - 3(1-X)^{\frac{2}{3}} \left(\frac{R_0}{R_M} \right)^2 + 2(1-X) \left(\frac{R_0}{R_M} \right)^3 \right] \tag{56}$$

Finally, combining Equations 54-56, the overall conversion X obtained by XRD analysis can be related with the corresponding reaction time as

$$t = a \left[R_M^2 \, \Psi + \sum_{i=1}^{M} R_{i-1}^2 \, f(x_i) \right]$$

$$\Psi = 1 - 3(1-X)^{\frac{2}{3}} \left(\frac{R_0}{R_M} \right)^2 + 2(1-X) \left(\frac{R_0}{R_M} \right)^3 \tag{57}$$

Equation 57 may be, now, rewritten as its more convenient, linear, form

$$Y(X, R_0, \delta^*) = k^* \, t \tag{58}$$

where

$$k^* = \frac{1}{a} = \frac{6b \, M_{Si} \, C_{N^x} \, D}{\rho_{Si}} \tag{59}$$

and

$$Y(X, R_0, \delta^*) = R_M^2 \, \Psi + \sum_{i=1}^{M} R_{i-1}^2 \, f(x_i) \tag{60}$$

4.3.3 Model Inspection

In the case of single size grains, the pertinent equation for the model inspection is Equation 58. If the experimental data is available as the discrete set of conversions X^j at the corresponding experimental times t^j where j represents the number of the sample in the series of the length l, then the function Y^j can be calculated for each conversion X^j and for known R_0 and δ^*. If the model holds, then the time estimated by the model as the time required to reach the conversion X^j, is linearly related with the function Y^j defined by Equation 60. Therefore, the model may be checked by the linearity between the sets of calculated Y^j values and corresponding experimental times t^j. Keeping the meaning and the nomenclature in Equations 48-60 unchanged, the preceding algorithm can be summarized as follows:

#1 evaluate R_0;

#2 choose δ^*;

#3 $1 \leftarrow j$ (initialize the loop)

#4 do while $j \leq l$

- $X \leftarrow X^j$
- find M (integer) as

$$M = \left\{ \left[1 - (1 - X)^{\frac{1}{3}} \right] \frac{R_0}{\delta^*} \right\}$$

- 0 ← *sum* (initialize the sum term from Equation 43)
- 1 ← i (initialize the loop)
  - do while $i \leq M$
  - calculate radius at the next peeling, R_i, from Equation 52,
  - calculate x_i from Equation 48,
  - calculate $f(x_i)$ from Equation 45,
  - $sum \leftarrow sum + R_i^2 f(x_i)$
  - calculate Ψ by Equation 57
  - $Y^j \leftarrow sum + R_M^2 \Psi$ (Equation 60)
- $j \leftarrow j + 1$
- go to **#4**

#5 plot Y^j versus reaction time t^j and check for linearity;

#6 increment δ^* and repeat steps 3-5 until the highest correlation coefficient of the form given by Equation 41 is obtained.

It should be noted here that the above procedure is based on the assumption that only R_0 is known and does not require the time scale to be corrected for an induction period and an initial reaction stage which, according to Figure 20a, most probably follows another mechanism. The critical thickness (δ^*) is chosen to achieve linear form predicted by Equation 58. The remaining unknown parameters, D, C_{N^x} and b, remain embedded in the slope k^* of a straight line.

One important fact is, however, easily hidden by the abundant equations that led to the final equations, 58-60: even though δ^* and R_0 were considered as independent parameters, the procedure for checking the model is, in fact, sensitive to the ratio $\lambda = \delta^*/R_0$ and the value chosen for R_0. That is to say that if the model yields the straight line, predicted by Equation 58, for $R_0 = 1$ μm and $\delta^* = 0.1$ μm, so does it for $R_0 = 2$ μm and $\delta^* = 0.2$ μm. In other words, Y defined by Equations 58 and 60 is

$$\begin{aligned} Y &= Y(X, \lambda) \\ \lambda &= \frac{\delta^*}{R_0} \end{aligned} \tag{61}$$

This is more easily revealed by a closer look at Equation 52 which, in fact, generates all the data that are used further in reaching the pertinent Equations 58 and 60. Hence, if Equations 58 and 60 are combined in their normalized forms as

$$\left[\frac{k^*}{R_0^2}\right] t = \left(\frac{R_M}{R_0}\right)^2 \Psi + \sum_{i=1}^{M} \left(\frac{R_{i-1}}{R_0}\right)^2 f(x_i) \tag{62}$$

then the same δ^*/R_0 ratios give the same right-hand side while the bracketed term, k^{**}, becomes an universal parameter which scales the slope of fitted line dependent on R_0, k^*, as

$$k^{**} = \left[\frac{k^*}{R_0^2}\right] \tag{63}$$

Equation 63 actually means that the time to reach the particular conversion X is inversely proportional to the initial grain radius squared, which is the general approach in detecting the rate limiting step controlled by

a radial gradient in spherical coordinates (Levenspiel, 1993). However, if the thickness δ^* is fixed, i.e. if δ^*/R_0 decreases as R_0 increases, this would increase the apparent conversion rate of larger grains with respect to the smaller ones, decreasing the difference between times needed for these grains to reach the same conversions. Hence, this effect could explain the dependence of the overall conversion on a grain diameter observed in literature and discussed at the end of section 4.1.2. Finally, it should be mentioned that the insensitivity of the model on δ^*/R_0 ratio is not an intrinsic drawback of the approach taken, but it is rather imposed by constraints in the starting information.

The main objective of the analysis that follows was to check if the values of δ^*, that possibly fit the experimental data, fall in the range observed in TEM pictures (Figures 34-37) or reported in the literature (Inomata and Uemura, 1975; Koike and Kimura, 1994). To do this, a FORTRAN program is used to perform the calculations summarized by the algorithm on pages 115-116. The experimental data obtained at 90% nitrogen - 10% hydrogen at various temperatures and those collected at 1250 and 1275°C with 10% hydrogen and various nitrogen concentrations, were subject to this procedure.

The first problem that had to be solved prior to the analysis outlined above, was to choose a reasonable guess for an initial grain radius R_0. As it can be seen from the data presented in Appendix A, the silicon grains have a wide, multi-modal size distributions, in which case the overall conversion cannot be appropriately represented by the conversion of the grain having a size equal to the statistical mean of a distribution. For example, in the case of

the bimodal grain size distribution where 90% by mass of grains are 2 μm, and remaining 10% 20 μm in diameter, the calculated mean diameter (the calculation procedure presented in Appendix A) is only 2.2 μm. It is obvious that the time change in the conversion of a grain having this mean size would not adequately represent the time change in the overall conversion of the distribution, especially if diffusion controls an overall process rate. For this reason, all the calculations related to inspection of the peeling shell model were based on the assumption that R_0 = 1 μm, which is about the radius of the grains being a major part in all the distributions shown in Appendix A. In the first approximation, δ^* was varied from 15 to 155 nm with a step size of 20 nm, and after detecting the range of δ^* that fits the data best, that range was then further investigated with the reduced step size of 10 nm.

Typical relationships $Y(t)$ versus t are presented in Figure 39 for different values of δ^*, and for one of the experimental conversion-time data set. It can be seen that the linearity predicted by Equation 58 could be achieved only for a particular value of δ^*, but never over the whole range of conversion/time data. The trend of the graphs in Figure 39 pretty much follows the shape of the corresponding conversion curves presented in Chapter 3.

By further investigation of the effect of δ^* on the shape of Y-t curves, it was found that the best linearity over the largest range of conversions could be obtained for δ^* =75-85 nm, i.e. λ = 0.075-0.085, for all tested data sets. The fitting of the data was performed only on the points that were believed to belong to the regime subsequent to the initial process stage. This was

illustrated in Figure 40 which, at the same time, presents the typical quality of the linear fits (the fitted line in this figure does not originate from zero because the time was not corrected for an induction period and the initial reaction stage). Table 5 presents the summary of the results as well as the conversion ranges which were included in the analysis.

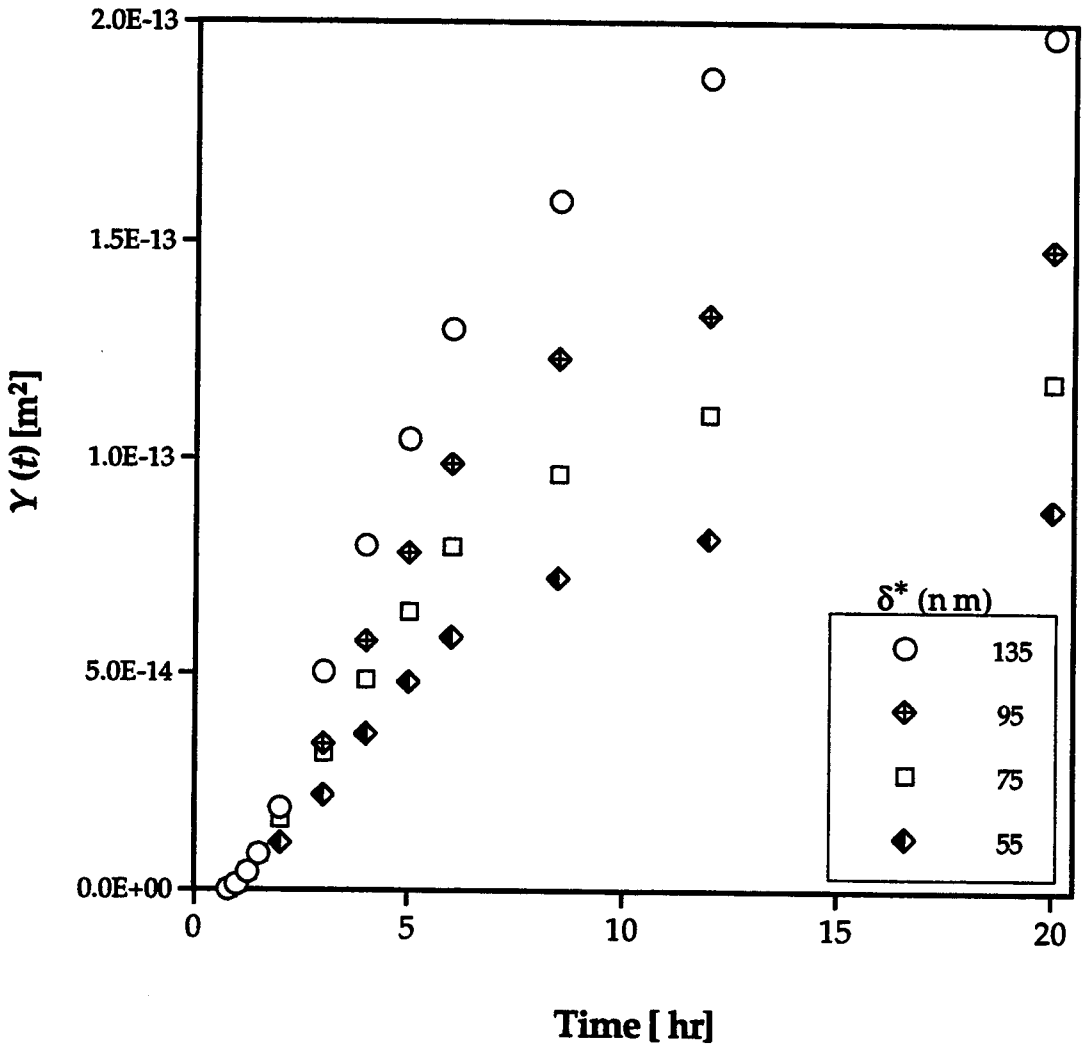

Figure 39. Typical results of testing the "peeling shell" model (run-09).

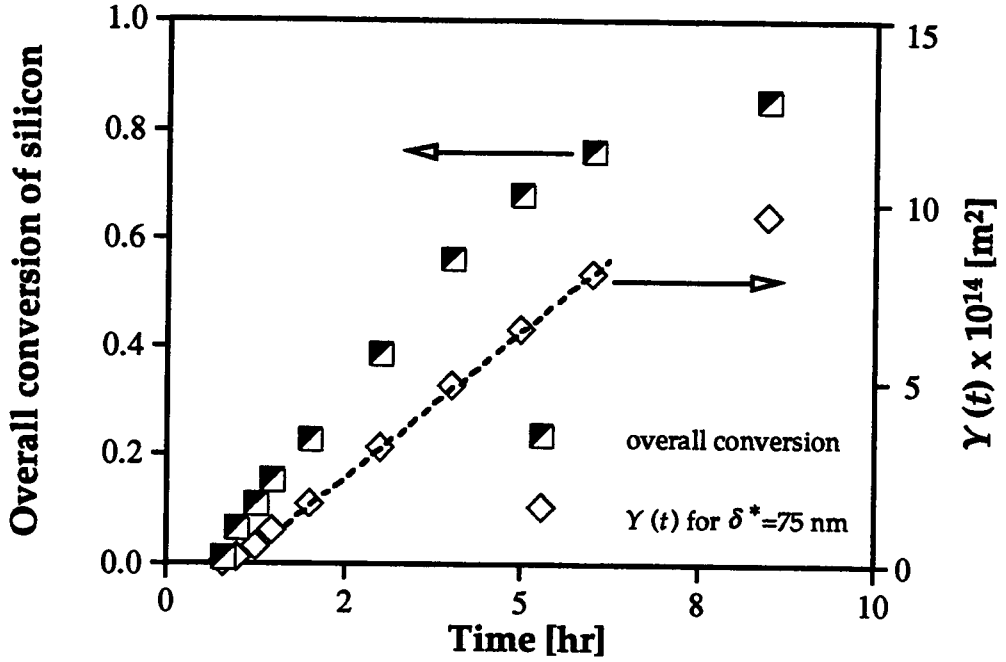

Figure 40. Determination of the parameter k^* (run-09).

Table 5. Summary of the results obtained from fitting experimental data by the "peeling shell" model (k^* is based on R_0 = 1 μm).

	REACTION CONDITIONS			RESULTS		
CODE	temp (°C)	N_2 (%)	H_2 (%)	δ^* (nm)	$k^* \times 10^{17}$ (m^2/s)	X_{min}-X_{max} (%)
run-01	1200	90	10	85	0.84	28-57
run-02	1225	90	10	85	0.91	30-67
run-03	1250	90	10	75	1.58	25-66
run-04	1275	90	10	75	2.15	17-71
run-05	1300	90	10	75	3.59	20-80
run-09	1250	30	10	75	0.44	23-69
run-10	1250	50	10	75	0.91	26-73
run-11	1250	70	10	75	1.23	20-70
run-12	1275	50	10	75	1.45	30-75

Hence, the estimate for the critical nitride layer thickness yielded the range $\delta^* \sim$ 75-85 nm. This range agrees with the observations shown in Figures 35 and 37, and is of the order of magnitude of the value estimated by Koike and Kimura (1994).

Figure 41a compares the conversion versus time curve predicted by the model, calculated for the case of the grain size distribution coded as dist-#1 in Table A1 (Appendix A) on the basis of estimated k^* and δ^*, with corresponding conversion-time experimental data set. It may be seen that the model does not fit the data well, which may be explained by the fact discussed earlier, i.e. that the mean grain size does not adequately represent the corresponding size distribution (the wiggly shape of the lines is due to the assumption that each nitride layer peels completely after reaching the thickness δ^*; the wider the size distribution, the smoother the calculated curves would be, because a smaller number of silicon grains become completely exposed to nitrogen at the very same moment). However, if a bimodal grain size distribution is assumed where only 10% by mass are large grains of $R_0 \sim$ 7.5 μm seen in Figure 8, then Figure 41b shows that the calculated conversion curve, in some cases, agrees well with the experimental result.

On the basis of the values for k^* tabulated in Table 5, nothing further could be deduced about the remaining unknown parameters that are lumped into it. Figure 42, however, showing the dependence of k^* on the nitrogen concentration, reasonably indicates that k^* varies linearly with the concentration of nitrogen. Since it is most reasonable to relate this finding to the C_{N^x},

Figure 42 might indicate that the concentration of the active nitrogen species at the surface is proportional to the bulk gas concentration of nitrogen.

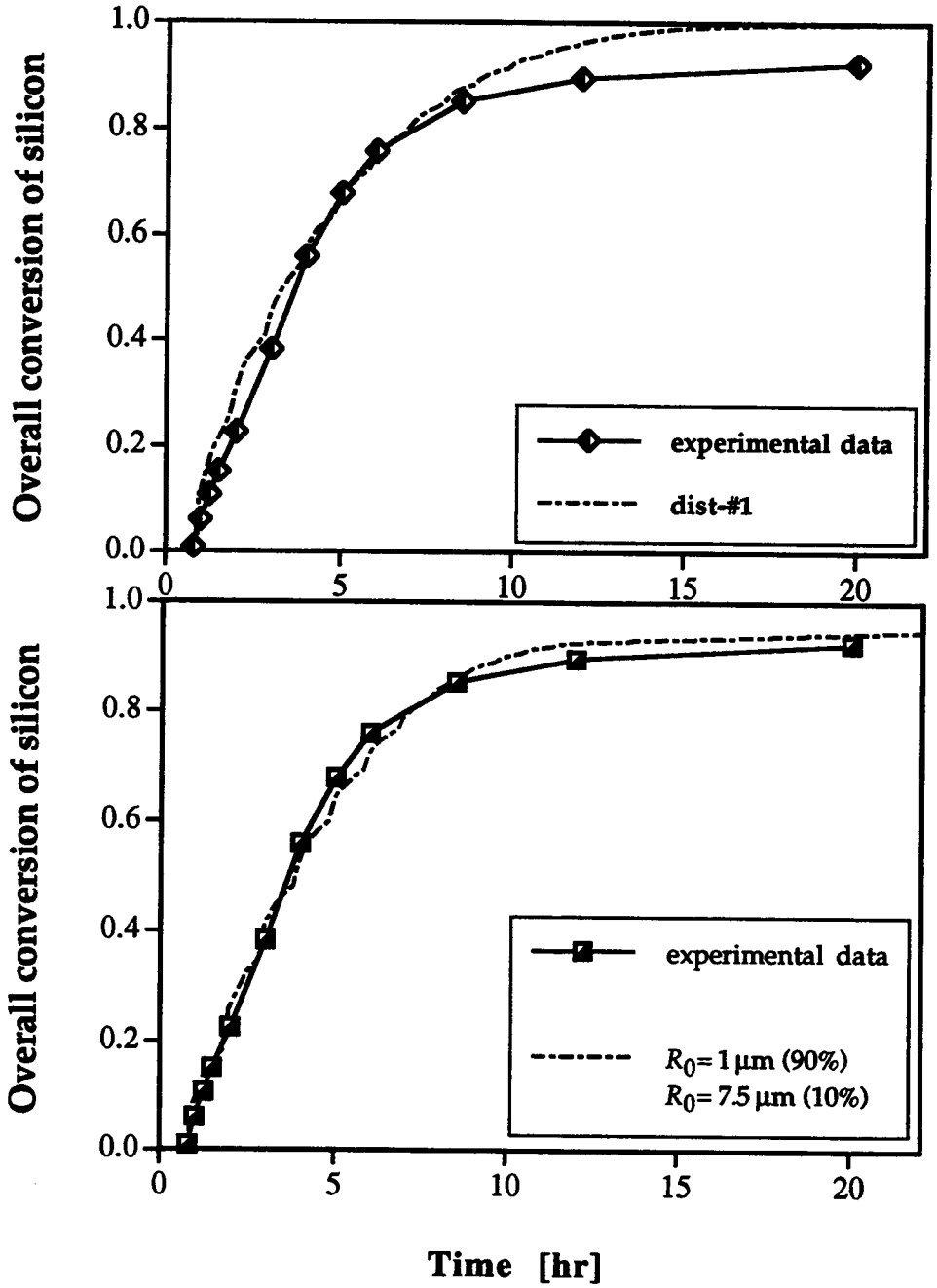

Figure 41. Comparison of "peeling shell" model with experimental results (run-09): (a) for the size distribution dist#-1 from Table A1; (b) for the bimodal size distribution.

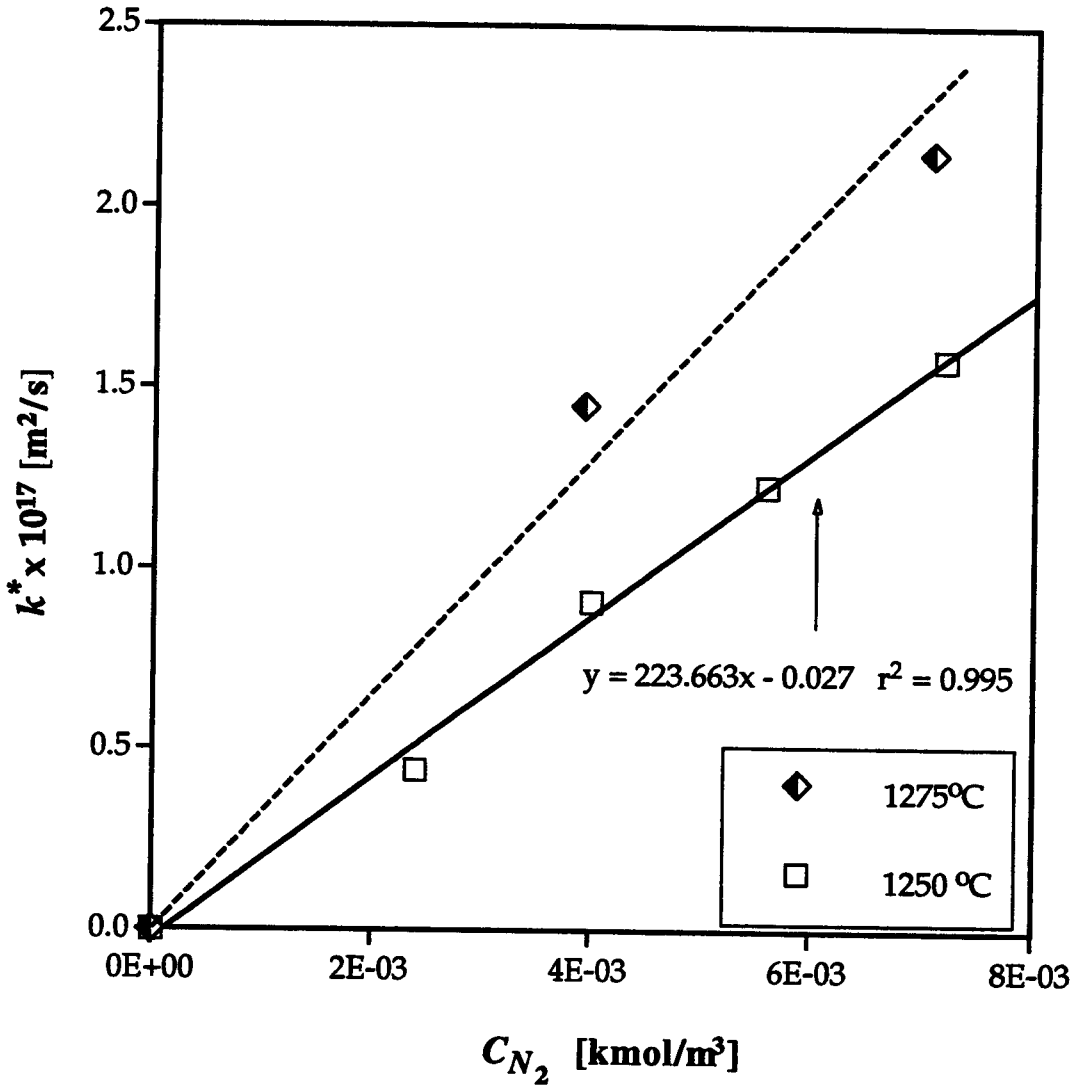

Figure 42. Dependence of k^* on nitrogen bulk concentration.

If the concentration of the active nitrogen species at the gas/silicon nitride surface can be related to the bulk nitrogen concentration as

$$C_{N^x} = H\, C_{N_2} \qquad (64)$$

where H is a partition coefficient (Cussler, 1989) then, from the slope of the straight line in Figure 42b and the molar volume of silicon of 83.6 kmol/m^3, the effective diffusion coefficient, D_{eff}, may be estimated as

$$D_{eff} = H\, D \sim 10^{-14} \ \frac{m^2}{s}$$

On the other hand, a reasonable linearity in Figure 43 illustrates that in the investigated temperature range the process has an apparent activation energy which could be estimated from the slope of the fitted line to E_{app} = 302 kJ/mol. Even though this information is insufficient to either further clarify the reaction mechanism at the gas/silicon nitride surface, or to distinguish the surface effects on the E_{app} from those that might be intrinsically carried by D, the estimated value for E_{app} is in the range characteristic for energy activated diffusion controlled gas-solid reactions.

Therefore, the preceding approach based on extremely limited but reasonable starting assumptions, yielded an acceptable prediction for δ^* and explained both kneeing of the conversion curves and their smoothness by a wide grain size distribution. At this point, however, no any strong conclusion could be drawn since the conversion of grains having a wide size distribution was represented by a conversion of a single grain, which significantly affects the results depending on how the size of the representative grain was chosen

(mean or median of the size distribution per mass or per number). The model fits the data only in the case of the bimodal size distribution when the mass fraction of significantly larger grains is so adjusted to match the fraction of the unreacted silicon, which, according to the findings presented in Chapter 3, varies with experimental conditions.

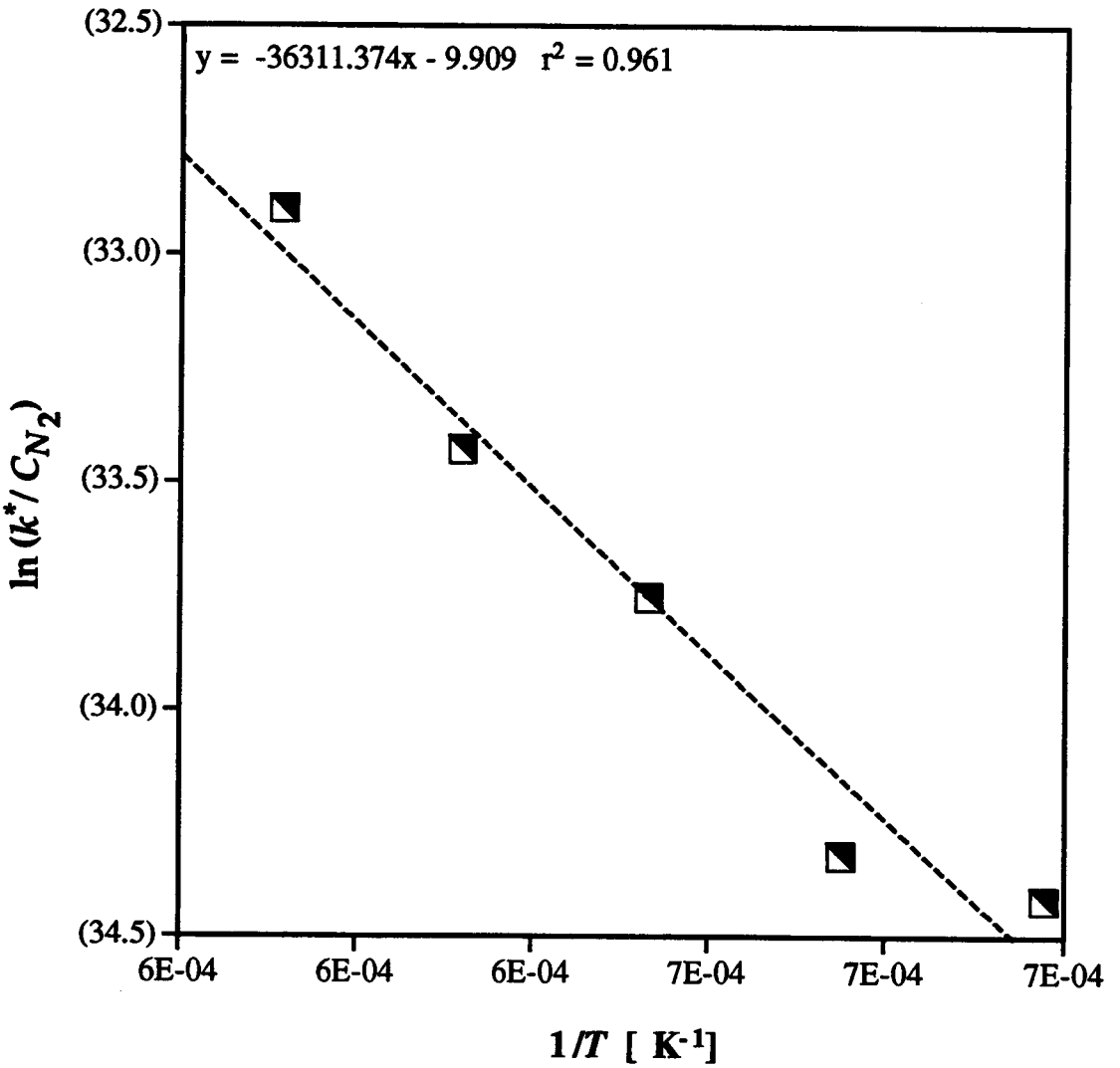

Figure 43. Determination of apparent activation energy on the basis of "peeling shell" model.

4.3.4 Grain Size Distribution Case

Even though derived for grains of uniform size, the model presented in the previous sections can be extrapolated on a known grain size distribution. In this case, the conversion of a particular size is the function of three parameters: its initial diameter R_0, lumped parameter k^*, and critical thickness of the silicon nitride layer δ^* at which it peels off from the silicon nitride/silicon interface.

Fitting the experimental data by this model and including the effect of the grain size distribution would also require the actual reaction time scale t to be corrected by the additional parameter t_0 to $t_c = t - t_0$. This would account for the induction period and the initial reaction stage that, as shown in Chapter 3 and particularly by Figure 20, probably follows another mechanism. However, t_0 could be reasonably estimated from the graphs presented in Chapter 3 by extrapolating the data from the conversion range $\geq \sim 30$ % to zero.

If the discrete size distribution of the silicon grains is known as the range of grains with a mean initial size R_0^m and its volume, i.e. mass fraction, w_m, the remaining two parameters, δ^* and k^*, could be evaluated by non-linear regression. For any overall conversion X^j, experimentally determined at corresponding corrected reaction time t^j, and given the initial guesses for δ^* and k^*, the conversion $X^{m,j}$ of each grain size R_0^m could be calculated by first evaluating the corresponding θ_M from Equations 52, 54, 48, 45, 55 and 53 and,

then, numerically solving Equation 56 for $X^{m,j}$. The overall conversion can then be calculated as

$$X^{j}_{calc} = \sum_{all\ m} w_m X^{m,j}$$

and new guesses for δ^* and k^* could be chosen by one of the multi-dimensional optimization methods (Edgar and Himmelblau, 1989; Press et al., 1990), until the objective function

$$\sum_{all\ j} \left[X^j - X^j_{calc} \right]^2$$

is minimized.

The main problem in taking the approach presented above is that the grain size distribution in the reacting silicon pellet cannot be reliably estimated. Measured size distributions of the original silicon grains showed different fractions of large grains, even when the measurements were carried out under the same conditions. The observed variability in the mass fraction of largest grains in a distribution would dramatically affect the calculated overall conversion while the specific surface area remained practically unchanged, as shown in Appendix A, Table A1, for the cases of size distributions #1 and #2. On the other hand, even if reliable information about grain size distribution of the original silicon grains was available, it is reasonable to expect that the grains agglomerated to some extent during the preparation of porous pellets. Still, as shown in Appendix A, the measured specific surface area of the raw silicon pellets used in the fluidized bed nitridation (~ 1.7-2 m^2/g) does not seem to be significantly different from the

specific surface area of the original silicon grains (~ 1.8-1.9 m^2/g), despite the fact that the former result was obtained by BET measurements and the latter by a particle size analyzer which might give a smaller area (reported area is based on the apparent particle sizes). Other facts that may also affect the actual grain size distribution in the reacting porous silicon pellet are grain shape and possible structural changes during nitridation, such as possible disintegration of polycrystalline grains by crystal growth in the grain boundaries, as shown in Figure 38. These structural effects can be neither controlled nor predicted but they are definitely dependent on reaction conditions, which is reflected by different final silicon conversions at different experimental conditions.

All the above considerations indicate that the specific surface area of the raw silicon pellet is a more certain parameter than a size distribution of the silicon grains in it, thus that it is more convenient to relate the overall silicon conversion to the overall effective silicon area than to the sizes of the grains of the pellet. One of the findings reported by Ku et al. (1990) provided the basis for the simplified treatment of the change in this effective surface area during the silicon nitridation. As mentioned in Section 4.1.2, these authors reported results of the computer simulation of the nitridation applied on the compacted silicon grains having a size distribution and reacting according to the sharp interface model. Their analysis accounted for the grain arrangement and the product growth in the compact and yielded the interesting result: the effective surface area of the compact, i.e. the surface area of the unreacted silicon

obtained from a series of calculations in which the overlapping area was deducted from the total surface area, changed roughly linearly with the overall silicon conversion in the range of X = 0-80%.

Even though the evidence provided by the TEM pictures from section 4.2 clearly showed that using the sharp interface model to describe the results from this work is not reasonable, the finding of Ku et al. (1990) warranted a further investigation of the relationship between the area of the unreacted silicon and the overall silicon conversion. To do this, the nitridation was simulated both as the diffusion controlled process with the product layer peeling off from the spherical silicon grains after reaching the thickness $\delta^* = 75$ nm and as the process proceeding according to the shrinking core model with reaction control. The relative change in the surface area of the unreacted silicon was calculated for the grain size distributions presented in Appendix A, according to the equations derived and explained in Appendix D. The typical results obtained by using the "peeling shell" model are plotted versus the overall silicon conversion in Figures 44 and 45, for the cases of dist-#2 (of original silicon grains used for making raw material pellets, measured by a particle size analyzer) and dist-#4 (of the grains shown in cross-section of the pellet in Figure 8, measured by a ruler), respectively. Figure 46 presents the result of a reaction controlled conversion simulation of the distribution dist-#4.

It can be seen in Figure 44 that the presence of very small grains rapidly decreases the unreacted silicon surface area at lower conversions. On the other

hand, the small fraction of very large grains practically decreases the total surface area of the unreacted silicon to zero before the reaction is even completed. However, both Figures, 44 and 45, illustrate that in a wide range of the overall silicon conversions, the decrease in the surface area of the unreacted grains could be reasonably approximated by a straight line in the case of the "peeling shell" model, as well as in the case of a reaction controlled process, shown in Figure 46. This finding will be utilized in the kinetic analysis approach taken in the following section, which enabled a simplified treatment of the effect of the effective grain size distribution in a reacting silicon pellet on overall silicon conversion.

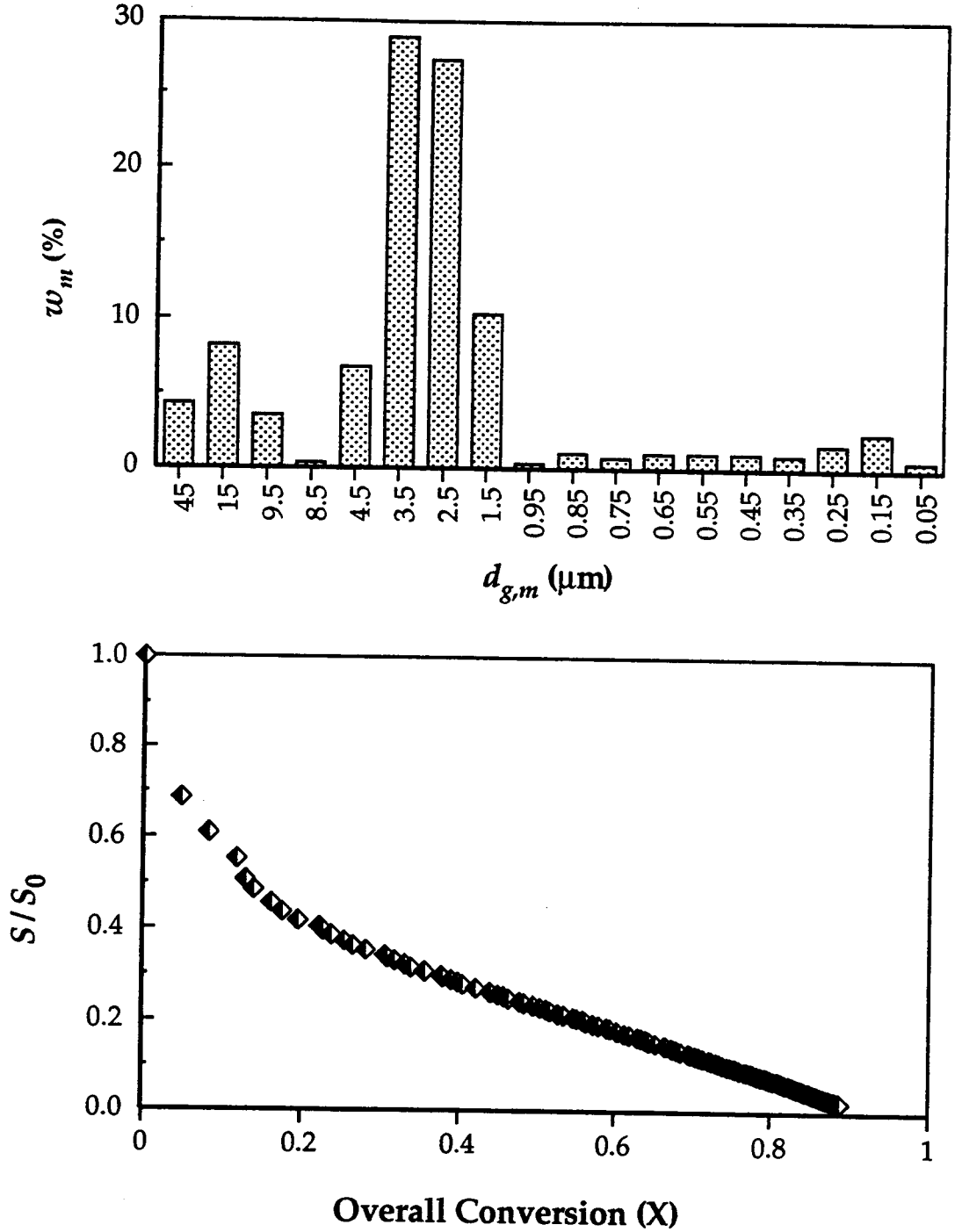

Figure 44. Change in relative surface area of the unreacted silicon with overall conversion for the grain size distribution dist-#2 from Appendix A (simulated on the basis of the "peeling shell" model, δ^*=75 nm).

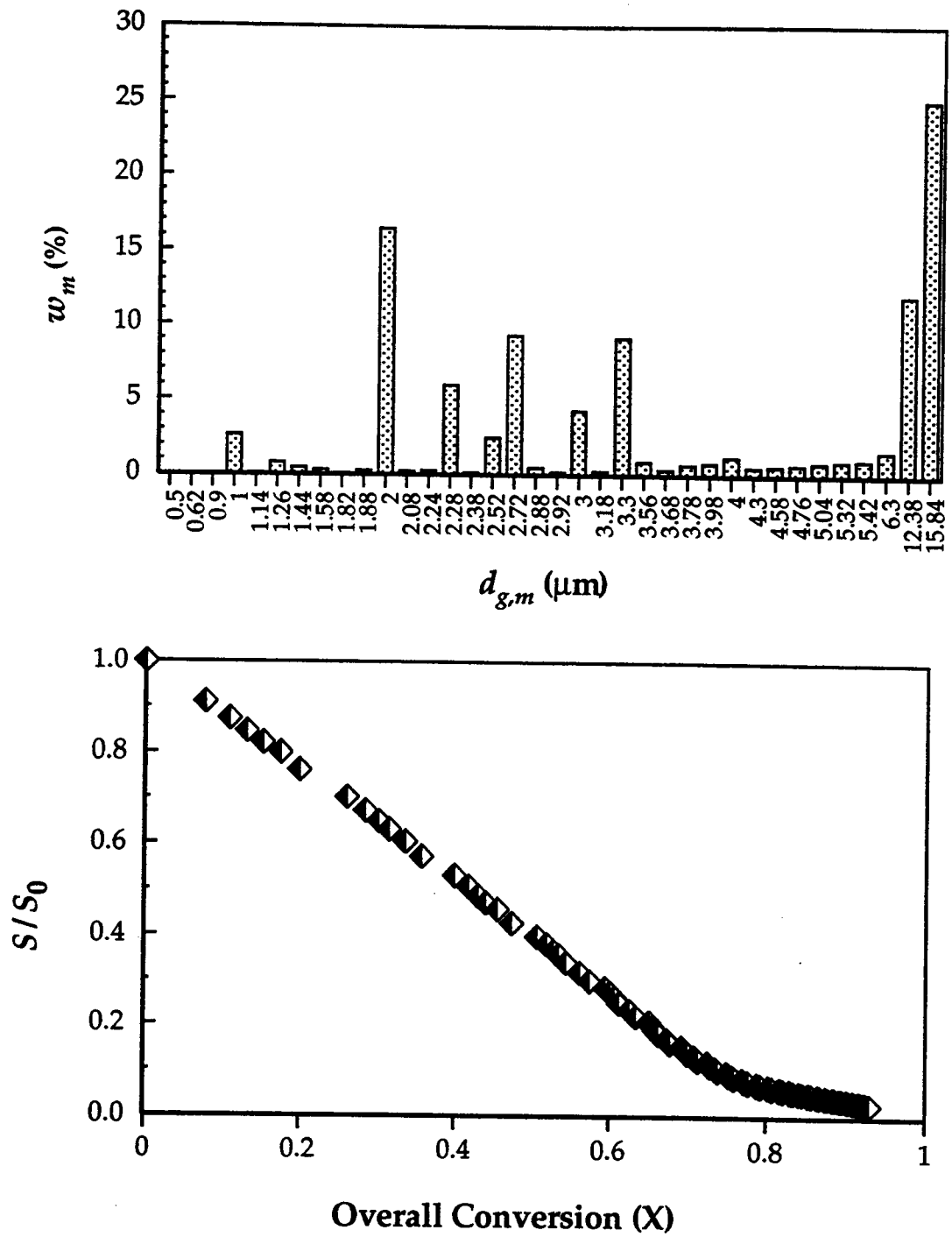

Figure 45. Change in relative surface area of the unreacted silicon with overall conversion for the grain size distribution dist-#4 from Appendix A (simulated on the basis of the "peeling shell" model, δ^*=75 nm).

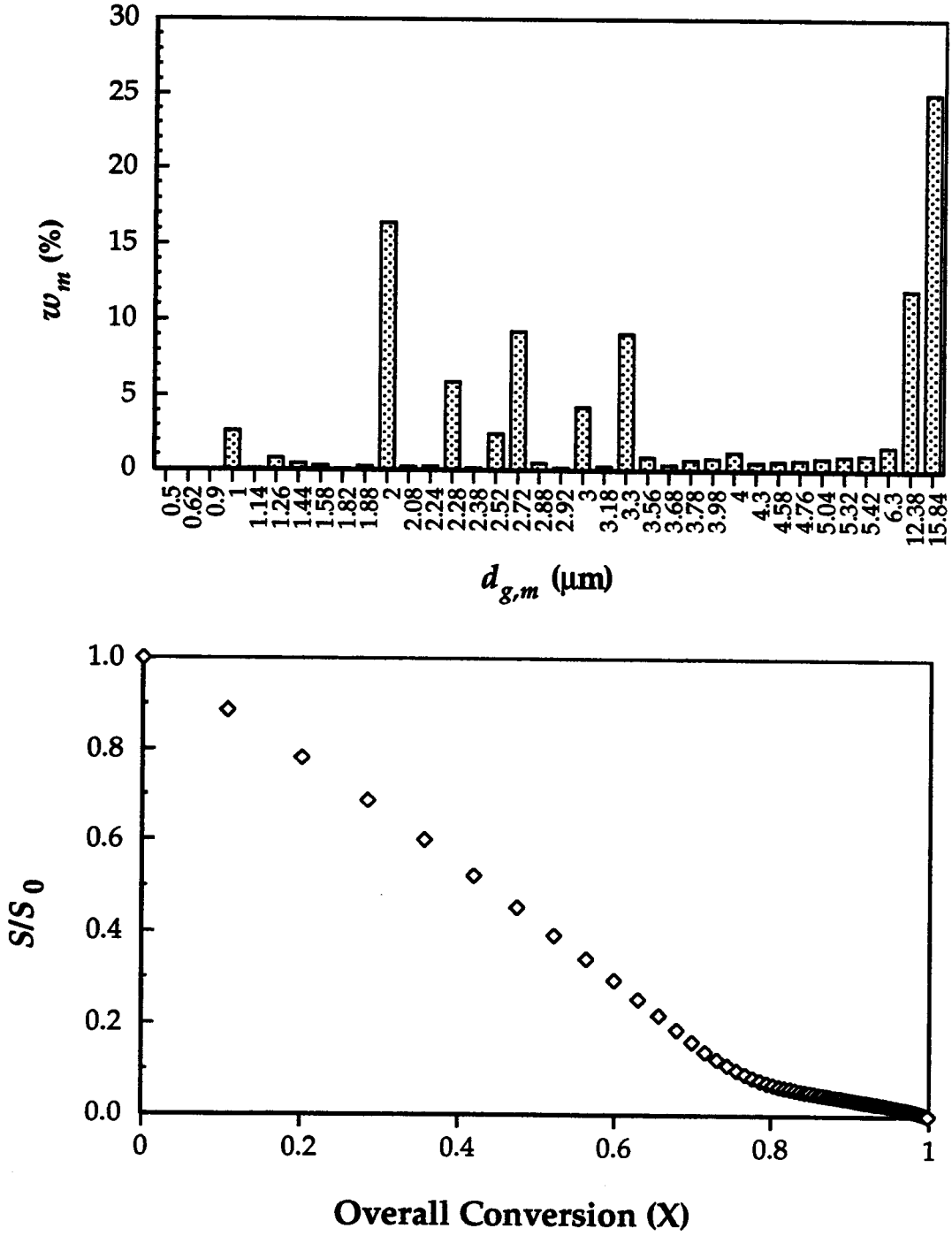

Figure 46. Change in relative surface area of the unreacted silicon with overall conversion for the grain size distribution dist-#4 from Appendix A (simulated SCM with reaction control).

4.4 Structural Factors and "Intrinsic" Process Rate

Discussion from the previous sections of this chapter showed that the available information about the mechanism of direct nitridation of silicon is not sufficient for reliable, quantitative modelling of this process. A particular problem arises in the attempts to distinguish intrinsic kinetic factors from structural factors. These factors are combined and it is impossible to decide which of them dominates the overall effect on the process rate.

The above difficulty was especially encountered in this work because the silicon pellets used for the experimental kinetic study presented in Chapter 3 were obtained by the sintering of silicon grains having a wide size distribution. Therefore, the variability in the final overall conversion with reaction conditions could not be explained with certainty. It is obvious, however, that the final conversion strongly depends on the grain size distribution, so the bending of conversion curves at different levels indicated that this distribution varied with experimental conditions. This section will demonstrate that the "intrinsic" process rate in fluidized bed nitridation, i.e. the process rate isolated from the effects of the above structural factors (Pigeon and Varma, 1993), still can be quantified, with a reasonable engineering assumption. Even though they are usually very complicated and complex, treatment of heterogeneous gas-solid reactions may be, sometimes, significantly simplified by the starting definition of the process rate.

Despite the fact that the TEM photos from section 4.2 could not reveal any certain conclusion for the mechanism of porous pellet nitridation, they

indicate that the transport of nitrogen through the micro-cracks and/or grain boundaries between silicon nitride crystallites growing on the silicon surface is the most reasonable assumption for the rate controlling step during nitridation. Figure 38 shows that grain boundaries between silicon single-crystal grains also behave as a reaction site and that is, as already mentioned, reasonable to expect that the nitride growth within large polycrystalline grains may partially disintegrate these grains. If the amount of such grains in the pellet is not negligible, then the above effect may alter an original grain size distribution and, hence increase the effective grain surface area. On the other hand, according to the reported nitridation mechanism of Atkinson et al. (1976), the morphology of the product grown on larger silicon grains seems to be different from that seen in Figures 33-35. In the case of nitridation of large grains, the uncovered silicon surface is depressed by the removal of silicon and the nitride grows around the edge of the depression. The product layer does not detach from the silicon surface but, instead, the nuclei eventually approach each other sealing the unreacted silicon and preventing further contacting of reactants, so the conversion rate of such grains does not appreciably contribute to the overall reaction rate (Figure 9). Since the amount of silicon captured in larger grains may significantly lower the overall conversion, the extent of disintegration of larger grains might be the clue to explain the bending of conversion curves at different levels at different reaction conditions.

Before proceeding any further, let the effective surface area during nitridation be defined as the total surface area of all silicon grains that

reasonably contribute to the reaction. Hence, if the local reaction rate per unit silicon surface area and the silicon surface area that contributes to the reaction are designated r''_{Si} and S_{eff}, respectively, then r''_{Si} will be negligible on the portion of the silicon surface equal to $S^* = S - S_{eff}$, where S represents the total surface area of unconverted silicon. This portion of the silicon surface may be affected by a number of various factors, some of which could be summarized as follows:

- change due to disintegration of grain clusters, possibly formed by sintering (decrease);
- disintegration of polycrystalline silicon grains caused by nitride growth in grain boundaries (decrease);
- crackling of grains during the reaction (decrease);
- covering of silicon surface with the nitride layer which does not detach (increase);
- clogging of micro-cracks in the nitride layer (increase);
- closure of grain boundaries by the crystal growth (increase);
- deposition of product flakes in inter-grain voids (increase).

Apparently it is impossible to either predict or control the overall effect of these factors. Some of them are general, but some of them are specific for a particular set of experimental conditions. According to experimental observations from Chapter 3 and considerations from section 4.2, in the analysis that follows is assumed that the major structural factor, dependent on

reaction conditions, is the change in the effective grain size distribution at various reaction conditions. In other words, the portion of the silicon surface that does not contribute to the reaction is attributed mainly to the fraction of largest grains in an actual grain size distribution, which react much slower than the rest of the grains.

According to the definitions stated previously, the overall silicon consumption rate at a particular time t^* may be expressed as follows:

$$-\left.\frac{dN_{Si}}{dt}\right|_{t^*} = \int_0^{S(t^*)} r''_{Si}\, dS = \int_0^{S_{eff}(t^*)} r''_{Si}\, dS \tag{66}$$

Dividing both sides of the above equation by S_{eff} gives the average process rate per effective surface area, i.e.

$$r''_0 = -\frac{1}{S_{eff}(t^*)}\left.\frac{dN_{Si}}{dt}\right|_{t^*} = \frac{1}{S_{eff}(t^*)}\int_0^{S_{eff}(t^*)} r''_{Si}\, dS \tag{67}$$

Since nitridation is controlled by the diffusion of nitrogen toward the silicon/silicon nitride (*Si/SN*) interface, then

$$r''_{si} = D\left.\frac{\partial C_{N^x}}{\partial r}\right|_{Si/SN} \tag{68}$$

so using the mean integral theorem gives

$$\int_0^{S_{eff}(t^*)} r''_{si}\, dS = \int_0^{S_{eff}(t^*)} \left[D\left.\frac{\partial C_{N^x}}{\partial r}\right|_{Si/SN}\right] dS = \left[D\left.\frac{\partial C_{N^x}}{\partial r}\right|_{Si/SN}\right]_{mean} S_{eff}(t^*) \tag{69}$$

Therefore, combining Equations 67 and 69 gives the average process rate per the effective surface area as

$$r_0'' = \left[D \left. \frac{\partial C_{N^x}}{\partial r} \right|_{Si/SN} \right]_{mean} \tag{70}$$

If the right-hand-side of Equation 70 can be represented as

$$\left[D \left. \frac{\partial C_{N^x}}{\partial r} \right|_{Si/SN} \right]_{mean} = \left[\frac{D}{\delta} \right]_{mean} \left[\left. C_{N^x} \right|_{gas/SN} - \left. C_{N^x} \right|_{SN/Si} \right] \tag{71}$$

one may assume, based on the assumption that the process is controlled by diffusion, that the concentration of the nitrogen species at the silicon surface is

$$\left. C_{N^x} \right|_{SN/Si} = 0 \tag{72}$$

Finally, after relating the concentration of the reactive nitrogen species at the gas/silicon nitride interface to the bulk nitrogen concentration with the help of Equation 64, the average process rate per the effective surface area may be expressed as

$$r_0'' = \left[\frac{DH}{\delta} \right]_{mean} C_{N_2} = \left[\frac{D_{eff}}{\delta} \right]_{mean} C_{N_2} = k_0 C_{N_2} \tag{73}$$

with

$$k_0 = \left[\frac{D_{eff}}{\delta} \right]_{mean} \tag{74}$$

serving as an apparent coefficient of the nitrogen transport through the crackling, polycrystalline silicon nitride layer toward the silicon surface.

Further, with the assumption that the average consumption rate of silicon per the effective surface area does not depend on time, the main factor for the process to proceed becomes the availability of this area. In other words, the time change in the overall consumption rate of silicon may be attributed solely to the disappearance of S_{eff} with time. Recognizing that $S_{eff} = S_{eff}(t)$, provides the condition to define the average "intrinsic" process rate as follows:

$$-\frac{1}{S_{eff}}\frac{dN_{Si}}{dt} = \frac{N_{Si,0}}{S_{eff}}\frac{dX}{dt} = r_0''\left(c_{N_2}, c_{H_2}, T\right) = const \qquad (75)$$

However, in order to relate the conversion with the time, this approach requires the additional equation which relates S_{eff} with X.

The results presented in Figures 44 and 45, based on the most reasonable assumptions for the mechanism of nitridation that could be stated at this point, show that, in the case of a wide grain size distribution, the unreacted silicon surface area reasonably linearly decreases with an increase in an overall conversion, in a wide range of conversions. A various reaction conditions may alter the size distribution, but is sound to assume that the new distribution also obeys the trend similar to those seen in both figures 44 and 45. If one neglects the contribution to the effective surface area coming from the surface area of the largest grains, seen in Figure 45 in the conversion range X>~78%, then the change in the effective surface area can be linearized as

$$\frac{dS_{eff}}{dX} = -a_{rs} = const \tag{76}$$

In the above equation, a_{rs} represents an approximated decrease rate of the effective surface area with the conversion of silicon. One should note that, in Figure 45, the total unreacted silicon surface area and the effective surface area coincide up to conversion X~78% , after which the former decreases rather slowly while the latter decreases according to Equation 76 faster, and causes the maximum achievable conversion being X~83%. Since the constant a_{rs} in Equation 76 depends on a given grain size distribution affected by the structural changes during nitridation, it describes the change in the effective surface area due to both reaction, i.e. physical consumption of silicon, and these structural effects.

The solution of Equation 76 for the boundary condition

$$X = 0 \Leftrightarrow S_{eff} = S_0 \tag{77}$$

gives

$$S_{eff} = S_0 - a_{rs} X = S_0 \left(1 - f_{rs} X\right) \tag{78}$$

where dimensionless factor f_{rs} represents

$$f_{rs} = \frac{a_{rs}}{S_0} \tag{79}$$

Substituting Equation 78 into Equation 75 yields

$$\frac{N_{Si,0}}{S_0} \frac{1}{1 - f_{rs} X} \frac{dX}{dt} = r_0'' \left(c_{N_2'}, c_{H_2'}, T\right) \tag{80}$$

Since S_0 can be related to the initial specific surface area of the pellet S_w as

$$\frac{S_0}{N_{Si,0}} = M_{Si}\, S_w, \tag{81}$$

Equation 80 can be integrated for $X = 0$ at $t = 0$ to give

$$X = \frac{1}{f_{rs}} \left\{ 1 - \exp\left[- \left(M_{Si}\, S_w\, f_{rs}\, r_0'' \right) t \right] \right\} \tag{82}$$

The last equation may be rewritten as

$$X = X_f \left[1 - \exp\left(- \kappa\, t \right) \right] \tag{83}$$

where X_f has the meaning of the asymptotic final overall conversion, and κ represents the apparent rate constant which includes combined structural and reaction effects, thus, it depends on specific reaction conditions. According to Equations 82 and 83

$$\begin{aligned} X_f &= \frac{1}{f_{rs}} \\ \kappa &= M_{Si}\, S_w\, f_{rs}\, r_0'' \end{aligned} \tag{84}$$

Finally, Equation 84 enables the elimination of the unknown parameter f_{rs} and the evaluation of the "intrinsic" process rate as

$$r_0'' = \frac{1}{M_{Si}\, S_w}\, \kappa\, X_f \tag{85}$$

Even though Equation 83 has the form of the first order reaction rate law for the case of a homogeneous reaction constrained by an equilibrium, it is the

equation which in this case describes a diffusion controlled, heterogeneous gas-solid process proceeding according to the assumptions given by Equations 75 and 76. It should be also noted that Equation 83 has the same form as the asymptotic rate law derived by Evans (1967) who considered the processes controlled by simultaneous transport through pores and pore closure with the progress of reaction.

Unfortunately, to approach the experimental results from this work by Equation 83 , the time scale needs to be corrected for the induction period and initial process stage for which the assumptions leading to these equations might not hold. This introduces the additional fitting parameter, t^*. Because of this, the overall conversions from the experiments in this work were fitted as

$$X = X_f \left\{ 1 - \exp \left[- \kappa \left(t - t^* \right) \right] \right\} \qquad (86)$$

The parameters X_f, κ and t^* were optimized by the Marquardt algorithm in PSI Plot (Poly Software International, 1993) and are presented in Table 6 together with the lowest conversion included in the fit (the points that were believed to belong to the initial reaction stage were excluded).

Table 6. Results of fitting experimental data by Equation 86.

	REACTION CONDITIONS			RESULTS			
CODE	temp (°C)	N_2 (%)	H_2 (%)	X_f (%)	κ (hr^{-1})	t^* (hr)	X_{min} (%)
run-01	1200	90	10	81.2	0.698	0.906	28
run-02	1225	90	10	82.0	0.872	0.705	38
run-03	1250	90	10	82.6	1.468	0.432	25
run-04	1275	90	10	84.2	2.079	0.318	28
run-05	1300	90	10	88.8	3.440	0.110	20
run-09	1250	30	10	91.8	0.395	1.629	38
run-10	1250	50	10	91.5	0.734	0.903	26
run-11	1250	70	10	87.1	1.137	0.614	32
run-12	1275	50	10	97.5	0.972	0.536	30
run-13	1250	30	5	90.4	0.391	1.57	25
run-14	1250	30	30	94.1	0.207	1.162	30
run-15	1250	30	50	92.8	0.154	0.748	28

The typical fits are compared with the corresponding conversion curves in Figure 47, which demonstrates a good agreement between the model and the experiment. The discrepancy from the experimental data could be seen only for extended reaction times, especially for the data obtained at lower nitrogen concentrations and/or higher temperatures. This may be explained by the fact that Equation 83 neglects the contribution of larger grains to the overall process rate, which is appropriate for the case shown in Figure 44. However, in the case of the grain size distribution in which the surface area

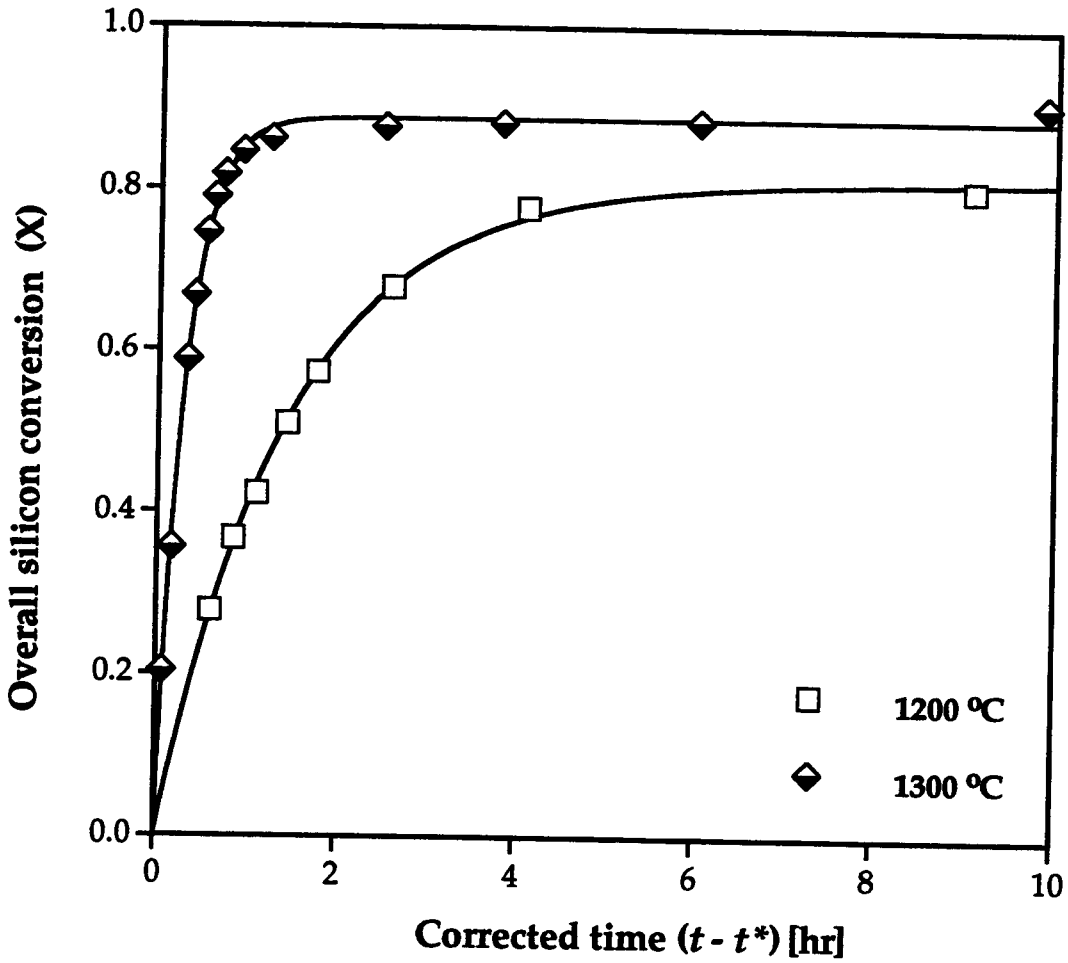

Figure 47. Comparison of experimental data with the results predicted by Equation 86.

contributed by larger grains is not negligible (because of either a higher fraction of large grains or a smaller difference in sizes between the largest and the smallest grains in the distribution), the change in the effective surface area could be better explained by the trend shown in Figure 45. If the relationship presented in this figure is used instead of Equation 76, the overall conversion would never level off, i.e. it would slowly increase at longer reaction times until reaction is completed.

In the light of the previous discussion, combined with the effects of temperature and nitrogen concentration on the overall silicon conversion presented in Chapter 3, it seems that lower nitrogen concentrations and/or higher temperatures affect larger polycrystalline grains and cause an increase in the effective surface area. At lower reaction temperatures and/or higher nitrogen concentrations the reaction at entrances of grain boundaries may be faster than the diffusion along the boundaries. Openings of the boundaries get clogged so the nitrogen cannot get through and continue to react within the grain. Anticipating that the diffusion through the clogged openings of the boundaries has a higher activation energy than the reaction, the effect of the former would be more pronounced at higher temperatures. Hence, as the reaction temperature increases, despite the faster reaction at the entrance of a grain boundary, the diffusion rate through the clogs increases, which enables the nitrogen to continue to react along the boundaries. On the other hand, lowering the nitrogen concentration, at any reaction temperature, decreases the closure of the boundaries because of the slower reaction at their entrances, which provides an easier nitrogen diffusion along the boundaries. Once the product is able to grow along the boundaries within a polycrystalline grain, it may detach the single-crystal silicon micro-domains and, hence, facilitate an increase in the effective surface area during nitridation.

Even though various grain size distributions do not give significantly different specific surface areas, the available information for the initial surface area of the pellets is not reliable (Appendix A). Hence, instead of r_0'', the

parameter K^o is considered as a measure of the intrinsic process rate, defined by

$$K^o = r_0'' M_{Si} S_w = \kappa X_f \quad (87)$$

The modeling of nitridation data is often approached in the literature (Atkinson et al., 1976; Rosetti and Denkewicz, 1988; Myhre and Motzfeld, 1990) by fitting normalized conversions by Equation 83, rewritten in the linear form as

$$-\ln\left[1 - \frac{X}{X_f}\right] = \kappa t \quad (88)$$

This utilizes κ as the apparent rate constant. However, according to the meaning given to this parameter in the discussion of this section, it is obvious that κ includes, not only the constant "intrinsic" process rate, but it also reflects structural changes occurring during nitridation. Therefore, the dependence of κ on the nitrogen concentration includes the coupled effects of the nitrogen on both the intrinsic process rate and on various structural changes. For example, when plotted against the nitrogen concentration, κ, obtained at constant hydrogen concentration, gives a parabolic dependence, as seen in Figure 48. This may lead to the strange reaction orders with respect to nitrogen, indicating complex process controlling step(s). However, when corresponding K^o is plotted versus nitrogen concentration, perfect linearity was achieved, as shown in Figure 49. Hence, "intrinsic" fluidized bed silicon nitridation obeys

first order rate law with respect to nitrogen, which is in agreement with the assumption given by Equation 73.

Once the relationship between K° and nitrogen concentration is known, the temperature effect brought by the nitrogen concentration into $r_0^{"}$ may be eliminated, and an apparent activation energy of the process could be determined. Hence, E_{app} was obtained by plotting K°/C_{N_2} (at constant hydrogen concentration) versus $1/T$, as shown in Figure 50. It may be seen that, in the temperature range 1200-1300°C, the process has the apparent activation energy of $E_{app} \approx$ 340 kJ/kmol.

The effect of hydrogen, at constant nitrogen concentration, does not show a particular trend. As seen in Figure 51, it seems that hydrogen has a dual effect in nitridation: catalytic, at lower, and inhibiting, at higher concentrations. This is consistent with the consideration of the possible roles of the hydrogen in the surface phenomena (removal of the surface silica or participation in surface reactions yielding the reactive nitrogen species) and in the diffusion of reactive species, as discussed earlier.

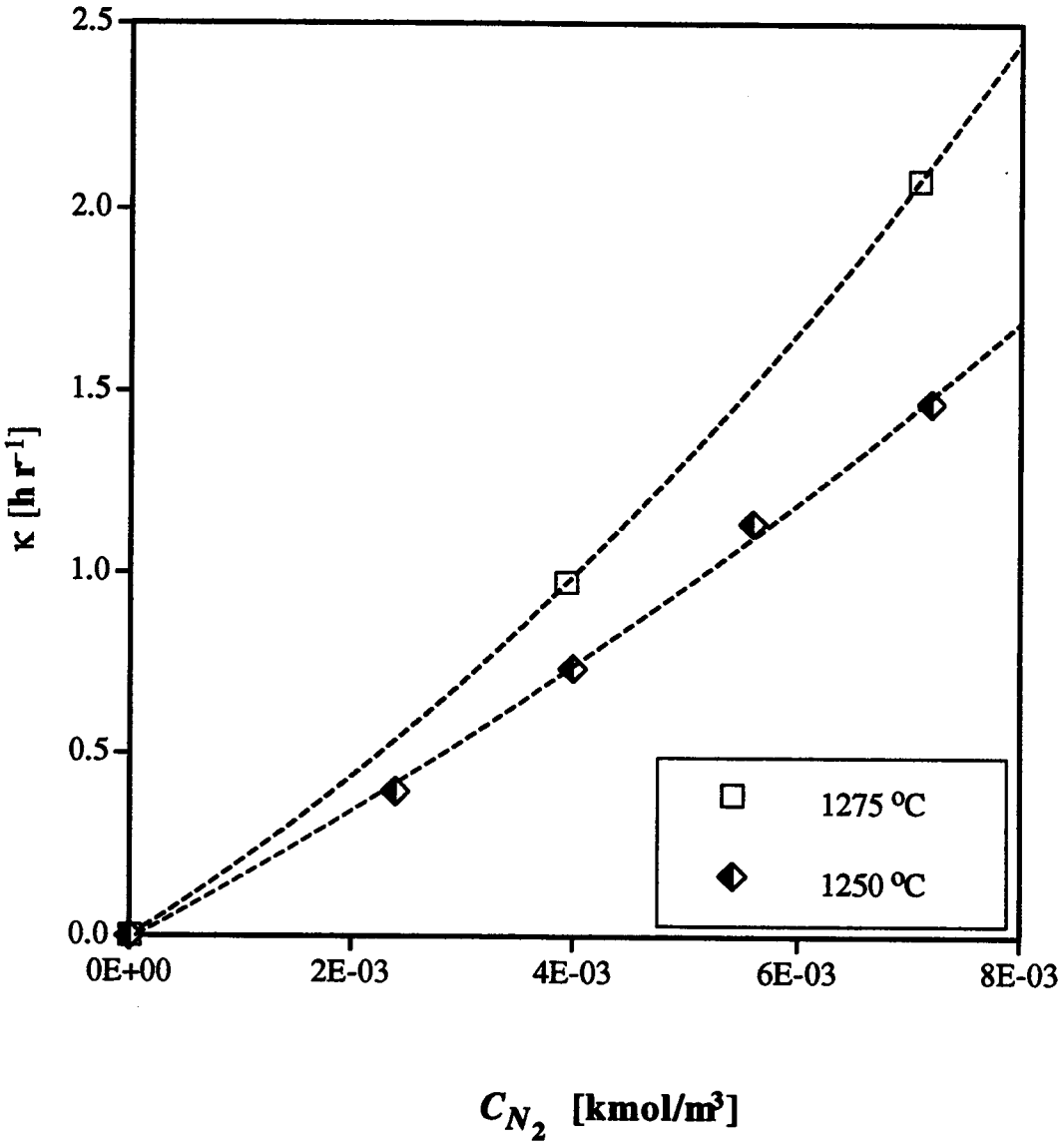

Figure 48. Dependence of fitting parameter κ on nitrogen concentration.

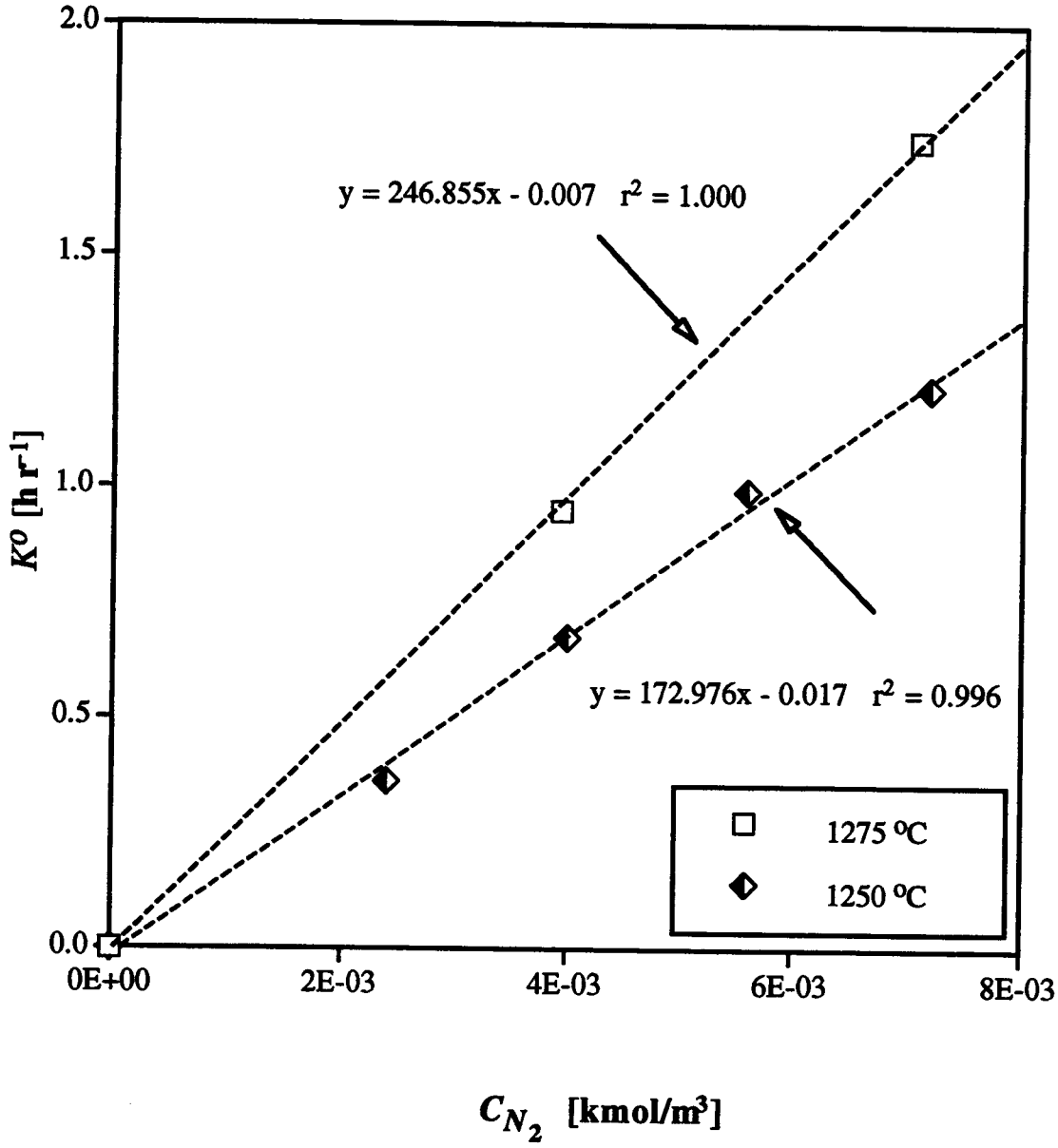

Figure 49. Dependence of K^o on nitrogen concentration.

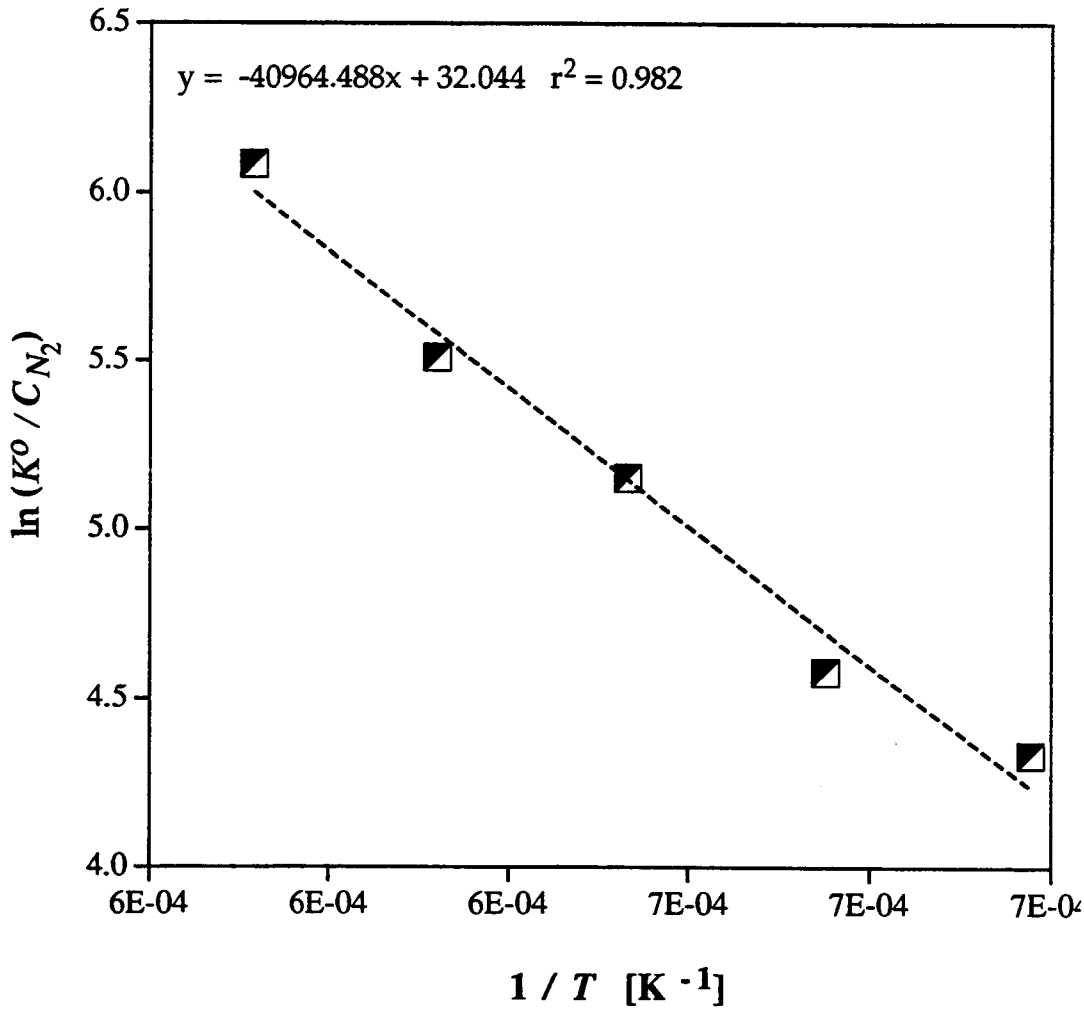

Figure 50. Determination of apparent activation energy.

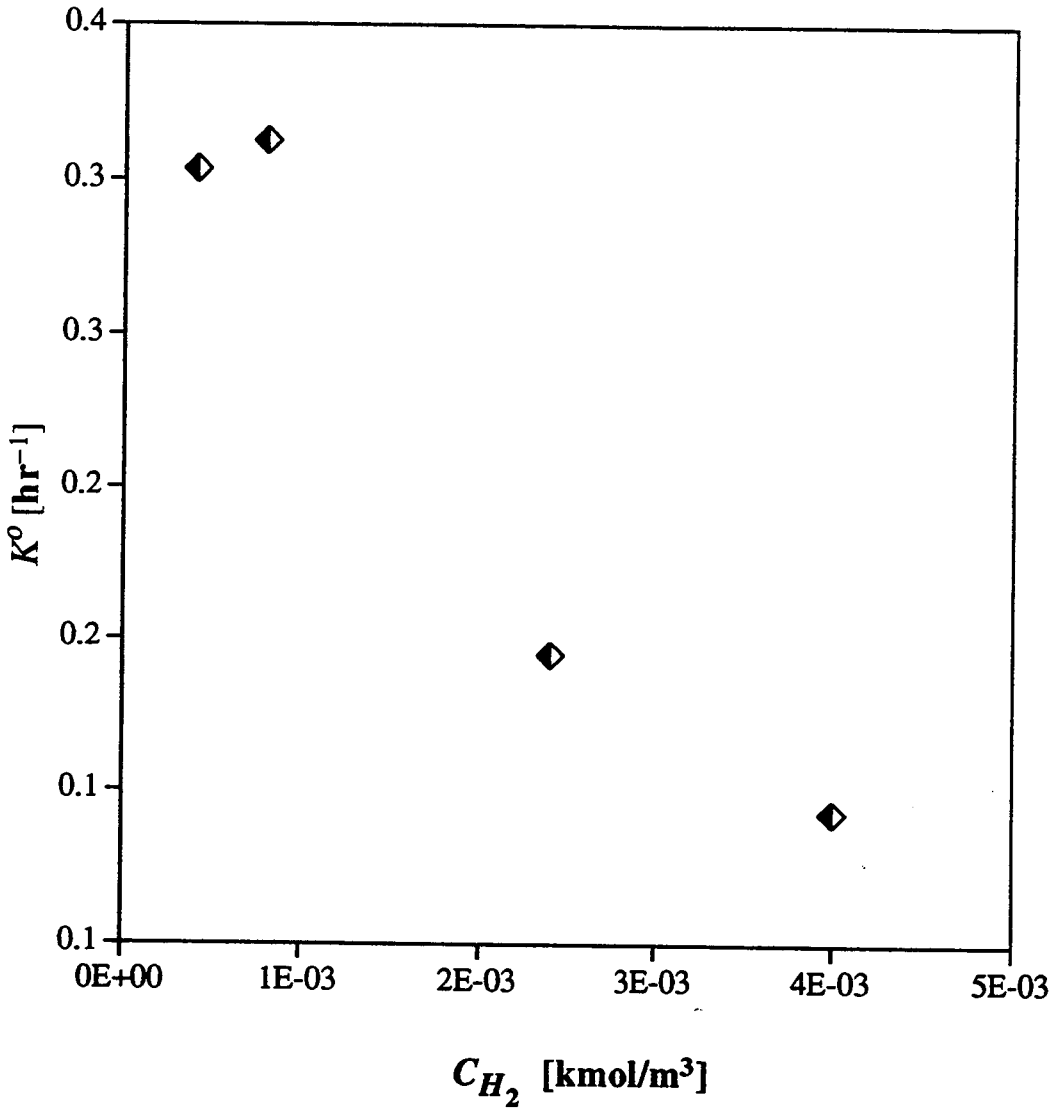

Figure 51. Effect of hydrogen on K^o.

Therefore, the preceding approach based on the assumptions of a linear change in the effective surface area during the silicon nitridation due to a wide and irregular grain size distribution of the grains in reacting pellets and a constant average process rate per this area, provided a good prediction of the experimental data from fluidized bed nitridation in a wide range of experimental conditions. Combined with the findings regarding both additivity of the conversion curves in the investigated range of experimental conditions and a good reproducibility of the experimental results discussed in Chapter 3, the results presented in Table 6 may serve as a basis for a reliable prediction of a progress of nitridation in a continuous multi-staged fluidized bed operation. Despite undesired residence time distribution for solids, a continuous fluidized bed nitridation process might be a final goal since it yields a product of a more uniform quality than a batch operation; this is a very important factor in producing sintered parts having reliable mechanical properties.

The modeling approach devised and explained in this section also provided a mechanicistic support of the asymptotic rate law given by Equation 86, first reported by Evans (1967) and often used in the literature to fit nitridation data (Atkinson et al., 1976; Rosetti and Denkewicz, 1988; Myhre and Motzfeld, 1990). This work showed that Equation 86 could be explained by the effect of size distribution of the grains on the effective reacting surface area. Moreover, the effect of a decrease in the nitrogen concentration on an increase in the asymptotic final conversion might be consistently explained by

the nitrogen effect on a dynamic change in the effective grain size distribution, i.e. the role of the nitrogen in disintegration of polycrystalline silicon grains due to silicon nitride growth along grain boundaries. Finally, despite the fact that Equation 86 has the form used to explain a first order homogeneous reaction, it does not mean that the kinetics of the direct silicon nitridation is reaction controlled (Rosetti and Denkewicz, 1988).

4.5 Conclusions

Considerations presented in this chapter provided a critical review of some of the most recent reported work dedicated to modeling a complex direct silicon nitridation process and resulted in two approaches to describe the progress of nitridation. Since there was no basis to elucidate the mechanisms of formation of either the α- or β-silicon nitride forms, these approaches dealt only with effects of experimental conditions on the overall silicon conversion in fluidized bed nitridation.

The main factors affecting the final overall conversion of silicon are believed to be structural factors related to a change in effective surface area during the process, i.e. change in the effective grain size distribution. The effect of these structural factors could be a reason for a number of different opinions regarding the mechanism of the nitridation reported in literature.

A high resolution evidence about the morphology of the reacting pellet provided by TEM photos in this study, indicates that the most reasonable assumption for the nitridation mechanism is that this process is, in overall,

controlled by the nitrogen transport through the polycrystalline, crackling nitride layer which, occasionally, peels off and exposes the fresh silicon surface. However, neither the form of reactive nitrogen species nor real diffusion mechanism of that species is yet clear (grain boundary diffusion, diffusion through micro-cracks).

This work also opened the question about the role of charged species in the nitridation, the analysis of which may yield a completely new picture about this process. Unfortunately, this work author's background in this field is, at present, far from being sufficient to provide a deeper and more reasonable consideration of this problem than the one presented in section 4.2.2 which only related charged-species phenomena to classical chemical engineering problems. However, even the considerations presented in this work show that the effect of charged species should deserve an attention in further research dedicated to understanding of this process. For example, the effect of metallic trace impurities on the nitridation is discussed in literature only from the standpoint of forming a low melting point eutectics with silicon, but it is reasonable to assume that the presence of various metals in the silicon raw material could affect number of charged carriers in it. Additional experiments with the silicon doped with appropriate materials which facilitate either electron (phosphorus) or hole generation (boron), would be helpful to either eliminate or to confirm this hypothesis.

On the basis of the observation that the silicon nitride product crystallites, seen either in intra-grain voids or on the silicon surface, are

roughly of the same thickness regardless of the extent of the reaction, a mathematical model was developed based on the shrinking core model with ash diffusion control for grains of an uniform size. The model, termed in this work as "peeling shell" model, assumes that the diffusion of a nitrogen reactive species through the product layer controls the overall process rate and that the product shell breaks and peels after reaching a critical thickness. The value of the critical silicon nitride thickness predicted by the model is roughly in agreement with experimental observations as well as theoretical calculations based on a crack propagation theory. The effective nitrogen diffusion coefficient estimated by this model is of the order of 10^{-14} m^2/s.

The main problem in validating the model mentioned above was a wide and uncertain size distribution of the grains in raw silicon pellets, as well as a dependence of the effective grain size distribution on experimental conditions. To overcome this problem, another approach was taken which assumes a constant process rate per the effective reacting surface area, but requires a known relationship between this area and the overall conversion. The computer simulations of the "peeling shell" model and the shrinking core model with reaction control applied to measured grain size distributions of the original silicon grains (used for making the raw silicon pellets) indicated that it is reasonable to assume that the effective surface area during nitridation linearly decreases with an increase in overall conversion. This assumption yielded a three parameter model which accurately predicts experimental fluidized bed nitridation data in wide range of experimental conditions. The

model is consistent with an observed effect of the nitrogen concentration on final silicon conversion which is explained by the availability of the nitrogen in grain boundaries, i.e. clogging the openings of the boundaries by the reaction followed by the product deposition. Once the nitrogen is present within the boundary, the product may grow and, since the volume of produced product is greater than the volume of the reactant consumed, this can cause a partial disintegration of polycrystalline grains, hence enhance renewal of the effective surface area. It was also shown that the "intrinsic" process rate, i.e. the nitridation rate obtained after eliminating the effects of a grain size distribution on the overall conversion rate, is of the first order with respect to the nitrogen, and that the process has an apparent activation energy in the temperature range 1200-1300°C, estimated to E_{app} = 340 kJ/mol.

BIBLIOGRAPHY

Albano, P., A. Scian and E. Pereira, "Secondary Phases in Nitrided Si Powders", *Mater. Lett.*, **11**[8-9], 261-266 (1991).

Atkinson, A., P .J. Leatt, A. J. Moulson, and E.W. Roberts, "A Mechanism for the Nitridation of Silicon Powder Compacts", *J. Mater. Sci.*, **9**[6], 981-984 (1974).

Atkinson, A., A. J. Moulson, and E. W. Roberts, "Nitridation of High-Purity Silicon," *J. Mater. Sci.*, **10**[7], 1242-1243 (1975).

Atkinson, A., A. J. Moulson, and E. W. Roberts, "Nitridation of High-Purity Silicon", *J. Am. Ceram. Soc.*, **59**[7-8], 285-289 (1976).

Avrami, M., "Kinetics of Phase Change - I: General Theory", *J. Chem. Phys.*, **7**[12], 1103-1112 (1939).

Barsoum, M., P. Kangutkar, and M. J. Koczak, "Nitridation Kinetics and Thermodynamics of Silicon Powder Compacts", *J. Am. Ceram. Soc.*, **74**[6], 1248-1253 (1991).

Berg, H., personal communication, Department of Statistics, Oregon State University, Corvallis, OR 97331 (1994).

Cabrera, N. and N. F. Mott, *Rept. Progr. Phys.*, **12**, 163 (1949)., as cited in Fromhold, A. T. Jr.,"Deffects in Crystallyne Solids: Theory of Metal Oxidation, Volume 1-Fundamentals", editors S. Amelinckx, R.Gevers, J. Nihoul, North-Holland publishing Company, 131 (1976).

Cambier, F. and A. Leriche, "Silicon Nitride: Relations Between Powder Characteristics and Sinterability", The Physics and Chemistry of Carbides, Nitrides and Borides, edited by R. Freer, Kluwer Academic Publishers, Netherlands, 13-28 (1990).

Campos-Loriz, D. and F. L. Riley, "Factors Affecting the Formation of the α- and β-Phases of Silicon Nitride," *J. Mater. Sci. Lett.*, **13**[5], 1125-1127 (1978).

Campos-Loriz, D. and F. L. Riley, "The α/β Si_3N_4 question," *J. Mater. Sci. Lett.*, **15**, 2385-2386 (1980).

Carter, R .E.,"Kinetic Model for Solid-State Reactions, "*J. Chem. Phys.*, **34**[6] 2010-15 (1961).

Cristian, J.W.,"The Theory of Transformations in Metals and Alloys: Part I-Equilibrium and General Kinetic Theory" 2nd ed., Pergamon Press Ltd., Headington Hill Hall, Oxford, 410-417 (1975).

Cullity, B. D.,"Elements of X-ray Diffraction", 2nd. ed., Addison-Wesley Series in Metallurgy and Materials, Addison-Wesley Publishing Company, Inc., 102 (1978).

Cussler, E. L., "DIFFUSION: Mass Transfer in Fluid Systems", Cambridge University Press, 23 (1989).

Dawson, W. M. and A. J. Moulson, "The Combined Effect of Fe and H2 on the Kinetics of Silicon Nitridation", *J. Mater. Sci. Lett.*, **13**, 2289-2290 (1978).

Dervisbegovic, H. and F. L. Riley, "The role of Hydrogen in the nitridation of Silicon Powder Compacts", *J. Mater. Sci.*, **16**, 1945-1955 (1981).

Dervisbegovic, H. and F. L. Riley," The influence of Iron and Hydrogen in the Nitridation of Silicon", *J. Mater. Sci. Lett.*, **14**, 1265-1268(1979).

Devlin, D. J. and K. E. Amin, "A Method for Quantitative Phase Analysis of Silicon Nitride by X-Ray Diffraction," *Pow. Diff.*, **5**[3], 121-124 (1990).

Dijen, F. K., A. Kerber, U. Vogt, W. Pfeiffer and M. Schulze, "A Comparative Study of Three Silicon Nitride Powders, Obtained by Three Different Syntheses, *Key Engineering Materials*, **89-91**, Trans. Tech. Publications, Switzerland, 19-28 (1994).

Drew, R. A. L., "Commercial Silicon Nitride Powder Characteristics, Synthesys and Sintering", *CERÂMICA*, **35**(237), 129-134 (1989).

Edgar, T. F. and D. M. Himmelblay, "Optimization of Chemical Processes", McGraw-Hill, Inc., (1988).

Evans, U. R., "The Corrosion and Oxidation of Metals: Scientific Principles and Practical Applications ",Edward Arnold (Publishers) ltd., London, 834 (1967).

Fromhold, A. T. Jr.,"Deffects in Crystallyne Solids: Theory of Metal Oxidation, Volume 1-Fundamentals", editors S. Amelinckx, R.Gevers, J. Nihoul, North-Holland publishing Company, 131 (1976).

Gazzara, C. P. and D. R. Messier, "Determination of Phase Content of Si_3N_4 by X-Ray Diffraction Analysis," *Am. Ceram. Soc. Bull.*, **56**[9], 777-780 (1977).

Geldart, D., "Fluidization of Powders Showing Degrees of Cohesiveness – I. Bed Expansion", *Chem. Eng. Sci.*, **39** [10], 1481-1488 (1984).

Harrison, L. G., "The Theory of Solid Phase Kinetics" in "Comprehensive Chemical Kinetics", Vol.2, ed. by C. H. Banford and C. H. Tipper, Elsevier Publ. Comp., 377-462 (1969).

Hayafuji, Y. and K. Kojima, *J. Electrochem. Soc.*: Solid State Science and Technology, **129**, 2102 (1982).

Heinrich, J., "Influence of Processing Conditions on Microstructure and Mechanical Properties of Reaction Sintered Silicon Nitride," *European Space Agency Rept.*, No. N-81-22113, December (1990).

Hojo, J., T. Shoji, and A. Kato, "The Formation of α- and β-Silicon Nitride in the Nitriding of Si Powder," *Denki-Kagaku (Electrochemistry)*, **43**[2], 100-105 (1975).

Hubbard, R. C. and R. Snyder, "RIR-Measurement and Use in Quantitative XRD", *Powder. Diffr.*, 3[2], 186-193 (1992).

Inomata, Y., "Nitridation of Silicon Powder," *J. Ceram. Soc. Japan*, **83**[10], 497-500 (1975).

Inomata, Y. and Y. Uemura, "Nitridation Kinetics of Silicon Powder," *J. Ceram. Soc. Japan*, **83**[5], 244-248 (1975).

Itoh, T., "Preparation of Pure α-Silicon Nitride from Silicon Powder," *J. Mater. Sci. Lett.*, **10**[1], 19-20 (1991).

Jennings, H. M. and M. H. Richman, "Structure, Formation Mechanism and Kinetics of Reaction-Bonded Silicon Nitride", *J. Mater. Sci.*, **11**, 2087-2098 (1976).

Jennings, H. M., "Review on Reactions Between Silicon and Nitrogen: Part 1-Mechanisms," *J. Mater. Sci.*, **18**[4], 951-967 (1983).

Jennings, H. M, B.J. Dagleish and P.L. Pratt, "Reactions between Silicon and Nitrogen",.*J. Mater. Sci.*, **23**, 2573-2583 (1988).

Jenkins, R., T. G. Fawcet, D. K. Smith, J. W. Visser, M. C. Morris and L. K. Frevel, "JCPDS-International Center for Diffraction Data Sample Preparation Methods in X-Ray Powder Diffraction", *Powder Diffr.*, **1**[2], 51-63 (1986).

Jovanovic, Z. R., S. Kimura and O. Levenspiel, "Effects of Hydrogen and Temperature on the Kinetics of the Fluidized-Bed Nitridation of Silicon", *J. Am. Ceram. Soc.* 77[1], 186-192 (1994).

Jovanovic, Z. R. and S. Kimura, "Use of Two-Phase Standards of Unknown Compositions to Determine Calibration Constants for Powder XRD by Linear Regression", *J. Am. Ceram. Soc.*, 77[8] (1994).

Khormaei, I., "Improved Stability in ACTFEL Devices", *Ms. Thesis*, Department of ECE, Oregon State University, Corvallis, OR 97331 (1989).

Kijima, K. and S. Shirasaki, "Nitrogen self-diffusion in silicon nitride", *J. Chem. Phys.*, 65[7], 2668-2671 (1976).

Kimura, S., "CHE 540: Chemical Reactors I", handouts, Department of Chemical Engineering, Oregon State University, Corvallis, OR 97331, spring (1992).

Kimura, S., personal communication, Department of Chemical Engineering, Oregon State University, Corvallis, OR 97331 (1993).

Klug, H. P. and L. F. Alexander,"Quantitative Analysis of Powder Mixtures", in X-Ray Diffraction Procedures, 2nd. ed., John Wiley, New York, 531-565 (1974).

Koike, J. and S. Kimura, "Mechanism of Nitridation of Silicon Powder in a Fluidized Bed Reactor", submitted to *J. Am. Ceram. Soc.*, (1994).

Ku, W., O. Gregory and H. M. Jennings, "Computer Simulation of the Microstructure Developed in Reaction-Sintered Silicon Nitride Ceramics", *J. Am. Ceram. Soc.*, 73[2], 286-296 (1990).

Kunii, D. and O. Levenspiel, "Fluidization Engineering", 2nd ed., Butterworth-Heinemann, Boston, (1991).

Kunz, K., V. Sarin, R. F. Davis and S. R. Bryan, "Self-diffusion of Silicon-30 and Nitrogen-15 in alpha-phase Silicon Nitride", Materials Science and Engineering, A105/A106, 47-54 (1988).

Lange, F. F., "Fracture Toughness of Si_3N_4 as a Function of the Initial α-Phase Content," *J. Am. Ceram. Soc.*, 62[7-8], 428-430 (1979).

Levenspiel, O., The Chemical Reactor Omnibook, OSU Book Stores, Inc., Corvallis, OR 97331, (1993).

Lindley, M. W., D. P. Elias, B. F. Jones and K. C. Pitman, "The influence of hydrogen in the nitriding gas on the strength, structure and composition of reaction-sintered silicon nitride", *J. Mater. Sci.*, **14**, 70-85 (1979).

Liu, Y. D. and S. Kimura, "Fluidization and Entrainment of Difficult-to-Fluidize Fine Powder Mixed with Easy-to-Fluidize Large Particles", *Powder Technol.*, **75**, 189-196 (1993).

Mencik, Z., M. A. Short, and C. R. Peters, "Quantitative Phase Analysis of Synthetic Silicon Nitride by X-Ray Diffraction"; in Adv. X-Ray Anal., Vol.23., Edited by J. R. Rhodes, C. S. Barrett, D. E. Leyden, J. B. Newkirk, P. K. Predecki, and C. O. Ruud. Plenum Press, New York, 375-379 (1980).

Mendelson, M.I., "On Si nitriding kinetics and mechanisms", *J. Mater. Sci. Lett.*, **14**, 1752-1754 (1979).

Morgan, P. E. D., "The α/β-Si_3N_4 Question," *J. Mater. Sci.*, **15**[3], 791-793 (1980).

Myhre, B. and K. Motzfeldt, "Kinetics of the Nitridation of Silicon", in The Physics and Chemistry of Carbides; Nitrides and Borides, Edited by R. Freer, Kluwer Academic Publishers, The Netherlands, 29-44 (1990).

Nakamura T., K. Sameshima, K. Okunaga, Y. Suigira, and J. Sato, "Determination of Amorphus Phase in Quartz Powder by X-Ray Powder Diffractometry", *Powder Diffr.*, **4**[1], 9-13 (1989).

Newman, J. S., "Electrochemical Systems", 2nd. ed., Prentice Hall Inc., (1991).

Nielsen, R., GEO 528-course in Electron Microprobe Analysis, Department of Geosciences, Oregon State University, Corvallis, OR 97331 (1993).

Pigeon, R. G., A. Varma and A. E. Miller, "Some Factors Influencing the formation of Reaction Bonded Silicon Nitride", *J. Mater. Sci.*, **28**, 1919-1936 (1993).

Pigeon, R. G. and A. Varma, " Quantitative Kinetic Analysis of Silicon Nitridation", *J. Mater. Sci.*, **28**, 2999-3013 (1993).

Pompe, R., L. Hermansson, T. Johansson, E. Djurle, and M. E. Hatcher, "Characterization of Silicon Powders for the Production of Si_3N_4", *Mater. Sci. Eng.*, **71**, 355-362 (1985).

Press, W. H., B. P. Flannery, S. A. Teukolsky and W. T. Vetterling, "Numerical Recepies-The Art of Scientific Computing", Cambridge University Press, (1989).

PSI-Plot, "Technical Polotting and Data Processing", Poly Software International, Ltd. (1993)

Rahaman, M. N. and A. J. Moulson, "The Removal of Surface Silica and Its Effect upon Silicon Nitridation Kinetics", *J. Mater. Sci. Lett.*, **16**, 2319-2321 (1981).

Rahaman, M. N. and A. J. Moulson, "The Removal of Surface Silica and Its Effect on the Nitridation of High Purity Silicon", *J. Mater. Sci.*, **19**[1], 189-194 (1984).

Rhodes, W. H. and S. Natansohn, "Powders for Advanced Structural Ceramics", *Ceram. Bull.*, **68**[10], 1804-1812 (1989).

Rossetti, G. A. Jr. and R. P. Denkewicz, Jr., "Kinetic Interpretation of α- and β-Si_3N_4 Formation from Oxide-Free High Purity Silicon Powder", *J. Mater. Sci.*, **24**[9], 3081-3086 (1989).

Schafer, D., personal communication, Department of Statistics, Oregon State University, Corvallis, OR 97331 (1994).

Schwier, G., "On the Preparation of Fine Silicon Nitride Powders", Progres in Nitrogen Ceramics, edited by F.L. Riley, Martinus Nijhoff Publishers, Boston/The Hague/Dordrecht/Lancaster, Netherlands, 157-166 (1983).

Shaw, N. J., and F. J. Zeleznik, "Thermodynamics of Silicon Nitridation: Effect of Hydrogen", *Communication of the Amer. Ceram. Soc.*, C-180-181 (1982).

Sheldon, B. W., J. Szekely and J. S. Haggerty, "Formation of Reaction-Bonded Silicon Nitride from Silane-Derived Silicon Powders: Macroscopic Kinetics and Related Transport Phenomena," *J. Am. Ceram. Soc.*, **75**[3], 677-685 (1992).

Shi, G., J. H. Seinfeld, and K. Okuyama, "Transient Kinetics of Nucleation", *Phys. Rev.*, **41**[4], 2101-2108 (1990).

Shi, G. and J. H. Seinfeld, "Transient Kinetics of Nucleation and Crystallization: Part I-Nucleation; Part II-Crystallization," *J. Mater. Res.*, **6**[10], 2091-2102 (1991).

Shimizu, M., H. Fukuoka, and M. Fukuhira, "Preparation of Silicon Nitride Powder," U.S. Pat. No.5073358, December, (1991).

Shimizu, M., European Patent Application No. 0410459 A2, (1991a).

Snyder, R.L., "The Use of Reference Intensity Ratios in X-Ray Quantitative Analysis," *Pow. Diff.*, 7[4], 186-193 (1992).

Suzuki, K. and Y. Kanno, "A Convenient Determination of α Phase Fraction in Si_3N_4", *Yogyo-Kyokai-Shi*, 92[2], 101-102 (1984).

Sze, S. M.,"Physics of Semiconductor Devices", John Wiley & Sons Inc. (1981).

Szekely, J., J. W. Evans, and H. Y Sohn, Chapter 4, "Reactions of Porous Solids," in Gas-Solid Reactions, Academic Press, New York, (1976).

Turton, R. and O. Levenspiel, *Int. J. Heat. Mass Transfer*, 32, 289 (1989).

Valensi, G., "Kinetics of the Oxidation of Metallic Spherules and Powders', *Compt. Rend.*, 202 [4], 309-12 (1936).

Yamada, T., "Preparation and Evaluation of Sinterable Silicon Nitride Powder by Imide Decomposition Method", *Am. Ceram. Soc. Bull.*, 72[5], 99-106 (1993).

APPENDICES

APPENDIX A.
MEASURED SIZE DISTRIBUTIONS OF SILICON GRAINS

Grain size distributions of the original silicon grains used for making porous raw material silicon pellets are measured by a HORIBA CAPA-700 Particle Size Analyzer. The typical distributions, coded as dist-#1, -#2 and -#3, are presented in Table A1. The instrument also provided a median of a distribution and estimated specific surface area of the grains, which are also shown in the table. The distributions #1 and #2 were measured after stirring the grains in water and then dispersing them by an ultra-sound for eight minutes. The distribution #3 was obtained after the grains were only stirred.

The remaining grain size distribution presented in the table, distr-#4, was obtained by measuring by a ruler 1114 grains shown in Figure 8: the smaller of two characteristic sizes of the grains shown in the plane was taken as the third characteristic length of an ellipsoid to estimate an equivalent diameter of a grain as the diameter of the sphere having the same volume.

In all cases, the mean grain diameter was estimated as (Kunii and Levenspiel, 1991)

$$d_{g,mean} = \frac{100}{\sum_{all\ m} \left(\frac{w}{d_g} \right)_m}$$

and reported in the table.

Table A1. Size distributions of original silicon grains.

range d_g (μm)	w_m (%)			
	dist-#1	dist-#2	dist-#3	dist-#4
40-50	-	4.3	4.1	-
10-20	-	8.2	-	37.1
9-10	-	3.5	2.1	-
8-9	-	0.3	0.8	-
7-8	-	-	-	-
6-7	-	-	0.7	1.6
5-6	-	-	-	2.8
4-5	-	6.8	16.7	3.0
3-4	13.0	28.9	34.0	16.2
2-3	54.3	27.3	28.3	35.1
1-2	21.4	10.3	11.5	4.3
0.9-1	2.1	0.3	-	-
0.8-0.9	0.3	1.0	-	-
0.7-0.8	1.0	0.7	0.3	-
0.6-0.7	1.3	1.0	0.7	-
0.5-0.6	1.5	1.0	0.4	-
0.4-0.5	1.1	1.0	0.3	-
0.3-0.4	1.5	0.9	-	-
0.2-0.3	1.2	1.6	-	-
0.1-0.2	0.8	2.4	-	-
0-0.1	0.5	0.5	0.1	-
median (μm)	2.32	3.07	3.25	3.2
S_w (m^2/g)	1.899	1.844	0.898	1.7-2
mean* (μm)	1.33	1.40	2.65	3.52

APPENDIX B.
DETERMINATION OF THE CALIBRATION CONSTANTS FOR QUANTITATIVE POWDER X-RAY DIFFRACTION ANALYSIS OF SILICON/ α- / β-SILICON NITRIDE MIXTURES

Introduction

Increasing demand for a better quality and lower cost of silicon nitride powder is reflected by an intensive research dedicated to an improvement of existing commercial routes for the production of this, nowadays, very important material. On the other hand, a phase composition of the product is the pertinent information for evaluating the quality of the produced silicon nitride powders. Hence, an accurate monitoring of the fractions of the undesired β-silicon nitride form and remaining unreacted silicon (in case of direct nitridation of silicon), makes it imperative to use a reliable quantitative analysis method. Because of the crystalline structure of all three components of interest, powder X-ray diffraction (XRD) technique has been known as a convenient tool for quantitative determination of silicon/α-/β-silicon nitride mixtures (Gazzara and Messier, 1977; Devlin and Amin, 1990; Suzuki and Kanno, 1984).

Theoretical background

The basic relationship for quantitative X-ray diffraction analysis (Klug and Alexander, 1974; Hubbard and Snyder, 1988; Snyder, 1992) is

$$I_{i,\delta} = K^{o}_{i,\delta} \frac{W_\delta}{\rho_\delta \left(\frac{\mu}{\rho}\right)_m} \qquad \textbf{(B1)}$$

which relates the intensity of a X-rays beam diffracted from reflection *i* of phase δ to the mass fraction of phase δ (W_δ), mass absorption coefficient for the mixture $(\mu/\rho)_m$ and density of phase δ (ρ_δ). In the above equation $K^{*}_{i,\delta}$ represents a constant for a given crystal structure δ, a diffraction line *i*, and a set of experimental conditions.

The mass ratio of phases β and γ in the same mixture may be correlated with intensity ratios of these phases according to Equation B1 as follows (Devlin and Amin, 1990; Snyder, 1992):

$$\frac{\Sigma I_{i,\delta}}{\Sigma I_{i,\gamma}} = K_{\delta/\gamma} \frac{W_\delta}{W_\gamma} \qquad \textbf{(B2)}$$

where

$$K_{\delta/\gamma} = \frac{\rho_\gamma}{\rho_\delta} \frac{\Sigma K^{o}_{i,\delta}}{\Sigma K^{o}_{i,\gamma}} \qquad \textbf{(B3)}$$

represents the calibration constant for δ-/γ-phase mass ratios, dependent on the chosen reflections. The summation terms in Equation B3 include several reflections of corresponding phases, which minimizes the effects of preferred

orientation in nearly randomly oriented crystals (Devlin and Amin, 1990). The use of relative intensity ratios for the determination of calibration constants does not depend on a particular diffractometer used (Hubbard and Snyder, 1988).

Since the main goal of the analysis is determination of mass fractions, Equation B2 may be rewritten in the form

$$\frac{\Sigma\, I_{i,\delta}}{\Sigma\, I_{i,\delta} + \Sigma\, I_{i,\gamma}} = K_{\delta/\gamma}\, \frac{W_\delta'}{1 + W_\delta' \left(K_{\delta/\gamma} - 1\right)} \qquad \textbf{(B4)}$$

where W_δ' represents the mass fraction of phase δ in the δ-γ mixture, i.e. the mass fraction on the basis free of all other phases that are present in the actual mixture:

$$W_\delta' = \frac{W_\delta}{W_\delta + W_\gamma} \qquad \textbf{(B5)}$$

Hence, in binary mixture $W_\delta' = W_\delta$. The form given by Equation B4 is commonly used in literature for graphical presentation of calibration data (Gazzara and Messier, 1977; Suzuki and Kanno, 1984).

Equation B2 implies that the determination of calibration constants for mass ratios of two phases reduces to a straightforward linear regression of measured intensity ratios versus mass ratios of pure phases, or mass fraction ratios of phases in impure but specified standards. The major problem in the development of a quantitative XRD method for the analysis of silicon/α-/β-silicon nitride mixtures is the fact that neither the pure α-silicon nitride nor the

silicon nitride with specified α-β composition are available commercially. Moreover, reported calibration data are difficult to interpret as some authors used peak-heights to approximate peak intensities (Gazzara and Messier, 1977), while the others used peak-areas (Devlin and Amin, 1990; Suzuki and Kanno, 1984). These two methods give the same results only when the corresponding peaks have the same widths, approximated by full-widths-at-half-maximums (**fwhm**'s), but peak width is directly related to a crystallite size which may change with operational conditions during production of silicon nitride.

One way to overcome the problem related to non-availability of the pure α-silicon nitride standard is the use of an internal standard together with Reference Intensity Ratios (RIR's) from the Powder Diffraction Files (PDF). However, this method is based on the use of constants from the literature, each of which may contain significant error (Hubbard and Snyder, 1988; Snyder, 1992).

Devlin and Amin (1990) obtained the calibration constant $K_{\alpha/\beta}$ for determination of α-/β-silicon nitride mass ratios, using mixtures of unspecified silicon nitride samples in known mass ratios. They used (102) and (210) peak intensities for α-silicon nitride, (101) and (210) for β-silicon nitride, and obtained $K_{\alpha/\beta} = 0.647 \pm 0.005$ by iterative trial and error procedure. This result agrees well with the calibration data of Gazzara and Messier (1977) but gives consistently smaller α-silicon nitride contents than those obtained by the method of Mencik et al. (1980) (referenced by Devlin and Amin, 1990). Suzuki and Kanno (1984) used pure β-silicon nitride as an internal standard and

reported $K_{\alpha/\beta}$ = 0.527 based on intensities of the same peaks. This constant also predicts higher α-form contents than the result of Devlin and Amin (1990).

The reported values for the calibration constants for the silicon determination in silicon-silicon nitride mixtures are scarce. The method most frequently applied to quantitative XRD analysis of free silicon mixed with silicon nitride is the work of Gazzara and Messier (1977). These authors reported a theoretical calibration curve for determining silicon/α-silicon nitride mass ratios. The use of this curve is based on use of only two peaks (111 for the silicon and 201 for the α-form), hence it requires an accurate approximation of peak intensities and appropriate analytical setup free of any effects such as preferred orientation and powder size distribution.

Due to discrepancies of reported calibration constants for quantitative analysis of silicon/α-/β-silicon nitride mixtures, an original method for evaluating these constants was developed and described below. This method is based on the approach which eliminates the need for having a pure calibration standards of either α- and/or β- silicon nitride phases. Two silicon nitride standards of unknown compositions can be used with a pure silicon standard to provide calibration data. Instead of trial-and-error approach used in the work of Devlin and Amin (1990), the four unknown parameters - the two calibration constants and the two compositions of the unspecified silicon nitride standards, are obtained by using linear regression (Jovanovic and Kimura, 1994).

Description of the method

To reliably determine calibration data by the approach discussed in this section, the following three "standards" are needed:

- standard #1 – predominantly α-silicon nitride;
- standard #2 – predominantly β-silicon nitride, and
- standard #3 – pure Si.

The mass fractions of the α- and the β-forms in standards #1 and #2 are denoted as a_1 and a_2, and b_1 and b_2, respectively, and are initially unknown. A number of mixtures can be prepared by mixing together arbitrary masses m_i from each of the standards, where subscript i represents the standard number. The mixtures then can be analyzed by XRD to measure the intensities of the following peaks: (102), (210), and (201) for α-silicon nitride; (101) and (210) for β-silicon nitride, and (111) for Si. These peaks are chosen to be the same as the peaks used in the previous work (Devlin and Amin, 1990; Suzuki and Kanno, 1984; Gazzara and Messier, 1977) to provide the basis for the comparison of the obtained results with those already reported in the literature.

For the chosen reflections, intensity terms in equation B2 reduce to

$$\Sigma I_{i,\alpha} = I_\alpha(102) + I_\alpha(210) = I_\alpha \qquad \textbf{(B6)}$$

$$I_\alpha(201) = I_\alpha^* \qquad \textbf{(B7)}$$

$$\Sigma I_{i,\beta} = I_\beta(101) + I_\beta(210) = I_\beta \qquad \textbf{(B8)}$$

$$\Sigma I_{i,Si} = I_{Si}(111) = I_{Si} \qquad \textbf{(B9)}$$

Combining Equations B2 and B6-B9 one may obtain

$$\frac{I_\alpha}{I_\beta} = K_{\alpha/\beta}\,\frac{W_\alpha}{W_\beta} \qquad \textbf{(B10)}$$

$$\frac{I_{Si}}{I_\alpha^*} = K_{Si/\alpha}\,\frac{W_{Si}}{W_\alpha} \qquad \textbf{(B11)}$$

Once $K_{\alpha/\beta}$ and $K_{Si/\alpha}$ are known, from measured peak intensities and Equations B10 and B11, as well as from the following additional constraint

$$W_\alpha + W_\beta + W_{Si} = 1 \qquad \textbf{(B12)}$$

it is possible to determine compositions of all the components in a mixture. Hence, the main objective is to determine $K_{\alpha/\beta}$ and $K_{Si/\alpha}$.

The mass ratios W_α / W_β and W_{Si} / W_α in a mixture of standards **#1**, **#2**, and **#3** are given in terms of the α-form mass fractions a_i and the sample mass m_i of the standard **#*i*** by

$$\frac{W_\alpha}{W_\beta} = \frac{a_1 m_1 + a_2 m_2}{(1 - a_1)\, m_1 + (1 - a_2)\, m_2} \qquad \textbf{(B13)}$$

and

$$\frac{W_{Si}}{W_{\alpha}} = \frac{m_3}{a_1 m_1 + a_2 m_2} \tag{B14}$$

Combining Equations B10-B13, B11-B14, gives

$$\frac{a_1 m_1 + a_2 m_2}{(1 - a_1) m_1 + (1 - a_2) m_2} = \frac{1}{K_{\alpha/\beta}} \frac{I_{\alpha}}{I_{\beta}} \tag{B15}$$

$$\frac{m_3}{a_1 m_1 + a_2 m_2} = \frac{1}{K_{Si/\alpha}} \frac{I_{Si}}{I_{\alpha}^*} \tag{B16}$$

Equations B15 and B16 are two of a number of forms of Equations B13 and B14 that can be used as the working equations for determining the four unknowns: a_1, a_2, $K_{\alpha/\beta}$, and $K_{Si/\alpha}$. From the mathematical standpoint, the equation set B15-B16 is underdetermined (two equations, four unknowns). However, if each of these equations is rewritten into its linear form, the above set yields four parameters, two slopes and two intercepts, which are sufficient to determine the four unknown parameters. This is the key idea for the approach presented further (Kimura, 1993).

Equations B15 and B16 can be rewritten in the analogous linear forms on a number of ways. For example, the equivalent linear forms of Equation B15 are given by Equations B17 and B18 as

$$\left[\frac{I_{\beta}}{I_{\alpha}}\right] = \frac{1}{K_{\alpha/\beta}\, a_1} \left[\frac{m_1 + m_2}{m_1 + \frac{a_2}{a_1} m_2}\right] - \frac{1}{K_{\alpha/\beta}} \tag{B17}$$

$$\left[\frac{I_\alpha}{I_\beta}\right] = \frac{K_{\alpha/\beta}}{1 - a_1}\left[\frac{m_1 + m_2}{m_1 + \frac{1 - a_2}{1 - a_1} m_2}\right] - K_{\alpha/\beta} \qquad \textbf{(B18)}$$

and those of Equation B16 as

$$\left[\frac{I_{Si}}{I_\alpha^*}\frac{m_1}{m_3}\right] = -\frac{a_2}{a_1}\left[\frac{m_2}{m_3}\frac{I_{Si}}{I_\alpha^*}\right] + \frac{K_{Si/\alpha}}{a_1} \qquad \textbf{(B19)}$$

$$\left[\frac{I_{Si}}{I_\alpha^*}\frac{m_2}{m_3}\right] = -\frac{a_1}{a_2}\left[\frac{m_1}{m_3}\frac{I_{Si}}{I_\alpha^*}\right] + \frac{K_{Si/\alpha}}{a_2} \qquad \textbf{(B20)}$$

$$\left[\frac{m_1}{m_2}\right] = \frac{K_{Si/\alpha}}{a_1}\left[\frac{m_3}{m_2}\frac{I_\alpha^*}{I_{Si}}\right] - \frac{a_2}{a_1} \qquad \textbf{(B21)}$$

$$\left[\frac{m_2}{m_1}\right] = \frac{K_{Si/\alpha}}{a_2}\left[\frac{m_3}{m_1}\frac{I_\alpha^*}{I_{Si}}\right] - \frac{a_1}{a_2} \qquad \textbf{(B22)}$$

If the silicon/β ratios are used instead of the silicon/α ratios, one may write a new set of equations, analogous to Equations B14 and B16, as follows:

$$\frac{W_{Si}}{W_\beta} = \frac{m_3}{b_1 m_1 + b_2 m_2} \qquad \textbf{(B23)}$$

$$\frac{m_3}{b_1 m_1 + b_2 m_2} = \frac{1}{K_{Si/\beta}}\frac{I_{Si}}{I_\beta} \qquad \textbf{(B24)}$$

The last two equations yield another four linear forms which are fully analogous to the equation set B19-B22. The only difference is that a_1, a_2, I_α^* and $K_{Si/\alpha}$ are resembled by b_1, b_2, I_β and $K_{Si/\beta}$, respectively, (one should recognize that $b_i = 1 - a_i$, $i = 1, 2$):

$$\left[\frac{I_{Si}}{I_\beta}\,\frac{m_1}{m_3}\right] = -\frac{b_2}{b_1}\left[\frac{m_2}{m_3}\,\frac{I_{Si}}{I_\beta}\right] + \frac{K_{Si/\beta}}{b_1} \qquad \textbf{(B25)}$$

$$\left[\frac{I_{Si}}{I_\beta}\,\frac{m_2}{m_3}\right] = -\frac{b_1}{b_2}\left[\frac{m_1}{m_3}\,\frac{I_{Si}}{I_\beta}\right] + \frac{K_{Si/\beta}}{b_2} \qquad \textbf{(B26)}$$

$$\left[\frac{m_1}{m_2}\right] = \frac{K_{Si/\beta}}{b_1}\left[\frac{m_3}{m_2}\,\frac{I_\beta}{I_{Si}}\right] - \frac{b_2}{b_1} \qquad \textbf{(B27)}$$

$$\left[\frac{m_2}{m_1}\right] = \frac{K_{Si/\beta}}{b_2}\left[\frac{m_3}{m_1}\,\frac{I_\beta}{I_{Si}}\right] - \frac{b_1}{b_2} \qquad \textbf{(B28)}$$

The bracketed quantities in Equations B19-B22 and B25-B28 can be independently determined from the measured quantities, m_1, m_2, m_3, I_α, I_α^*, I_β, and I_{Si}, thus, these equations may be represented in general regression form as

$$Y_1 = A\,X_1 + B \qquad \textbf{(B29)}$$

Therefore, linear regression of any of the forms B19-B22 yields the solution for the ratio of unknown silicon nitride compositions a_1 and a_2 ,which may be utilized further to generate independent variables in Equation B17 (bracketed terms on right-hand-sides). One should notice that the form given by Equation B18 cannot be used with any of the equations from the set B19-

B22 because it requires the solution for a_1 and a_2 (not their ratio). After recognizing that $1-a_i$ in Equation B18 represents, in fact, the mass fraction of β-form in silicon standards #1 and #2, b_i, this equation can be used with any of the equations B25-B28 to evaluate all unknown parameters except $K_{Si/\alpha}$, resembled here by $K_{Si/\beta}$. In any case, the equation sets B19-B22 and B25-B28 may be represented analogously to Equation B23 as

$$Y_2 = C\,X_2 + D \qquad \text{(B30)}$$

Thus, for this particular set of linear forms, there are eight possible combinations for the governing forms given by Equations B29-B30 that yield the results for the calibration data, i.e. the results that enable later determination of mass fractions of all the phases of interest:

- Equation B17 as the form B29 and any of the Equations B19-B22 as the form B30 (four combinations), and
- Equation B18 as the form B29 and any of the Equations B25-B28 as the form B30 (remaining four combinations).

Only in the ideal case, i.e. when all the forms represented by Equations B17-B22 and B25-28 are the perfect straight lines (correlation coefficient equal to 1), all possible combinations would give the same results. In reality obtained results would vary depending on the chosen combination, with overlapping confidence intervals of fitted parameters. However, the number of combinations can be reduced according the following practical consideration.

The primary objective of calibration of ternary mixtures is, generally, in covering as wide as possible ranges of mass fractions of all three phases with as less as possible measurements. Further, it is not desirable to mix masses of standards that are very different, since this may introduce an error of XRD measurements associated with non-uniformity of the mixtures, i.e. the effect on segregated phases on the overall mass absorption coefficient of a mixture being analyzed. This means that it is preferable to utilize mixtures made with as many as possible combinations of the standards. For example, the maximum and minimum possible α/β ratio that can be achieved in the prepared mixtures is constrained by the compositions of the predominantly α-silicon nitride standards #1 and #2, respectively. Hence, if one wants to cover as wide as possible range of mass fractions made from reasonably different masses of the starting standards, then it is convenient to be able to utilize the mixtures where either $m_1 = 0$ or $m_2 = 0$. From this standpoint, the forms B21-B22 and B27-28 are not convenient as not applicable for the cases $m_2 = m_3 = 0$ and $m_1 = m_3 = 0$, respectively, while the forms B19-B20 and B25-B26 cannot be used only if $m_3 = 0$, which does not make sense in this method.

Therefore, the convenient combinations of the working linear forms are reduced to the following four cases: B17 as the form given by Equation B29 with either of the forms B19 or B20 as Equation B30, and B18 as the form given by Equation B29 with either of the forms B25 or B26 as Equation B30. The procedure for determination of the calibration data will be presented for the

case B17-B19 and the results obtained by the another three combinations will be only discussed.

The above choice of Equations B17 and B19 for the working pair of linear forms specifies Equations B29 and B30 as follows:

$$Y_1 = \frac{I_\beta}{I_\alpha} \quad , \quad Y_2 = \frac{I_{Si}}{I_\alpha^*} \frac{m_1}{m_3} \tag{B31}$$

$$X_1 = \frac{m_1 + m_2}{m_1 + \frac{a_2}{a_1} m_2} \quad , \quad X_2 = \frac{m_2}{m_3} \frac{I_{Si}}{I_\alpha^*} \tag{B32}$$

$$A = \frac{1}{K_{\alpha/\beta}\, a_1} \quad , \quad B = - \frac{1}{K_{\alpha/\beta}} \tag{B33}$$

$$C = - \frac{a_2}{a_1} \quad , \quad D = \frac{K_{Si/\alpha}}{a_1} \tag{B34}$$

Hence, the linear regression of the form given by Equation B30 first yields the ratio a_2/a_1 from the slope C of the straight line (Equation B34). Using this ratio, X_1 can be calculated from Equation B32. Finally, fitting the linear form given by Equation B29 relates $K_{\alpha/\beta}$ and a_1 to the slope and intercept of the fitted straight line (Equation B33). The remaining unknowns, $K_{Si/\alpha}$ and a_2, may be obtained via Equation B33 with the known slope and intercept C and D from the linear regression performed first.

In general, this approach may be applied to the cases where the calibration constant is needed for two phases of interest, which are, however,

always available only as mixtures. Samples must be prepared by mixing two different standards, being composed of the two phases of unknown compositions, with third standard which is a pure third phase. When the third phase is also of interest, the calibration constant for this phase is also obtained.

Experimental

The powders used as standards were purchased from Aldrich, being designated silicon nitride of predominantly α-form, silicon nitride of predominantly β-form, and Si powder of 99.999% purity. They are denoted in this work as standards #1, #2, and #3, respectively. Particle size distributions in the standards were measured by a HORIBA CAPA-700 analyzer. The average particle sizes obtained from the distributions are shown in Table B1. A number of samples were prepared by mixing these powders, in different mass ratios, for 15-20 min by a pestle in a diamonite mortar.

XRD analysis of the samples was performed by using a solid state detector (Si,Li) SIEMENS D5000 diffractometer with CuK_α radiation. In the range of $2\theta = 27\text{-}37°$, each sample was continuously scanned with a spinner with a step size of $2\theta = 0.01°$, and a counting time of 5 sec/step. Data were collected by using a variable slit size and then corrected by multiplying measured intensities by $1/\sin\theta$. Peak areas, peak heights, full widths at half maximums, background noise and separation of overlapped peaks were determined by fitting peak profiles using a modified Voigt function in the Diffrac-AT Software package.

Table B1. Properties of the standard powders used.

standard	material	average particle size (μm)
#1	predominantly α-silicon nitride	0.4
#2	predominantly β-silicon nitride	1.0
#3	silicon (99.999%)	0.2
#3a	silicon grains(99.9%)	2.0
#3b	ground silicon pellets (99.9%)	2.1

Table B2 summarizes the experimental results. Samples No.1-8 were used for the linear regression based on Equation B30. Samples No.9-14, in which $m_3 = 0$, are used together with samples No.1-8 in the regression of the form B29 to test any effects of presence of the silicon on the determination of the constants based on Equation B29.

After performing the XRD analysis of the prepared mixtures, the procedure outlined earlier provides the values of a_1 and a_2, which specify the compositions of both the α- and β-forms in the silicon nitride standards #1 and #2. In order to further determine the effects of particle size and procedures for sample preparation on the silicon/α-silicon nitride calibration constant, the experimentally characterized silicon nitride, standard #1, was mixed with two other types of silicon powder standards: (i) Shin-Etsu 99.9 % Si, designated standard #3a and, (ii) the powder, designated standard #3b, which was

Table B2. The summary of the results obtained by using standards #1, #2 and #3.

No	m_1	m_2	m_3	I_{Si} (111)	I_α(201)	I_α(102)	I_α(210)	I_β(201)	I_β(210)
1	0.48607	0.28260	0.22201	83.62	68.59	66.13	72.45	39.46	53.34
2	0.27330	0.51355	0.24965	85.38	46.19	44.58	47.64	61.50	77.25
3	0.23596	0.50585	0.52082	121.87	28.46	30.68	31.57	43.28	53.76
4	0.51674	0.25928	0.50555	106.92	41.07	40.86	44.72	21.67	27.66
5	1.02888	0.00000	0.24824	78.28	108.60	99.14	109.41	9.01	10.89
6	0.25383	0.50627	1.01488	169.18	21.54	21.71	23.38	29.93	35.87
7	0.51023	0.40097	0.12168	45.77	77.54	77.08	80.38	59.21	72.60
8	0.00000	1.24485	0.42319	114.29	32.59	30.33	31.98	120.81	137.90
9	0.89879	0.12543	-	-	87.80	85.41	93.67	19.72	26.07
10	0.67474	0.31893	-	-	105.71	99.47	106.13	51.52	66.83
11	2.22997	0.00000	-	-	165.01	153.06	162.70	15.50	16.48
12	0.50162	1.61334	-	-	60.21	58.01	63.62	111.52	136.70
13	0.00000	1.00000	-	-	55.81	53.81	58.55	207.90	238.10
14	0.87506	0.00000	-	-	94.49	87.42	96.11	9.38	9.71

obtained by grinding porous pellets (300-400 μm) used as the raw material in fluidized bed nitridation discussed in Chapter 3. Average particle sizes of these standards are also shown in Table B1. In both the cases, all mixtures were sonicated in iso-propyl alcohol and dried on a hot stirred plate before performing the XRD analysis. The summary of the results is presented in Table B3.

Table B3. The summary of results for silicon standards **#3a** and **#3b**.

No	m_1	m_2	m_3	I_{Si} (111)	I_α(201)
A1	0.87506	0	0.73322	573.2	94.49
A2	0.73977	0	0.31217	371	116.07
A3	0.30242	0	0.6796	510.2	34.19
A4	1.00685	0	0.09012	100.09	160.22
B1	0.53766	0	0.37164	329.40	81.84
B2	0.67019	0	0.45733	372.50	93.94
B3	0.71997	0	0.27669	255.00	110.67
B4	1.04551	0	0.03616	37.58	184.8
B5	0.09720	0	0.60187	522.00	16.25
B6	1.40624	0	0.16179	106.10	148.14

Results and Discussion

From measured peak intensities, I_α^* and I_{Si}, and masses of standards #1, #2, and #3 in mixtures, (m_1, m_2, and m_3) the values of Y_2 and X_2 were first calculated and plotted as presented in Figure B1a. The ratio a_2/a_1 given by the

slope of the fitted line was then used to calculate values of X_1 (Equation B32), and generate the plot shown in Figure B1b according to Equations B29.

High correlation coefficients of the fitted lines shown in Figure B1, over a wide range of X_1 and X_2, i.e. mass fractions, confirm the consistency of the method. Also, the fact that all the data obtained by using samples with or without silicon fall on the same line indicates that the determination of the constants in Equation B29 was not affected by presence of the silicon in the samples.

Equations B33-B34 relate the fitted parameters from Figures B1 with two calibration constants and the compositions of α-silicon nitride in standards #1 and #2 as follows:

$$K_{\alpha/\beta} = 0.647 \ , \quad K_{Si/\alpha} = 2.913 \ , \quad a_1 = 0.947 \ , \quad a_2 = 0.276$$

It should be noted that, because the experimental determination of calibration constant $K_{\alpha/\beta}$ is not affected by the choice of an internal standard in obtaining such lines as shown in Figure B1, any pure crystal can be used in place of silicon. The value for the calibration $K_{\alpha/\beta}$ obtained by the procedure outlined above is identical to the result reported by Devlin and Amin (1990).

The summary of the results obtained by all four combinations discussed earlier is presented in Table B4. It should be mentioned that using Equation B18 introduces problems related to errors in fitting the XRD profiles. Namely, when the α/β ratios are high (~ 10), a small error in fitting the measured integrated intensities, i.e. in evaluating areas of the peaks, dramatically affects

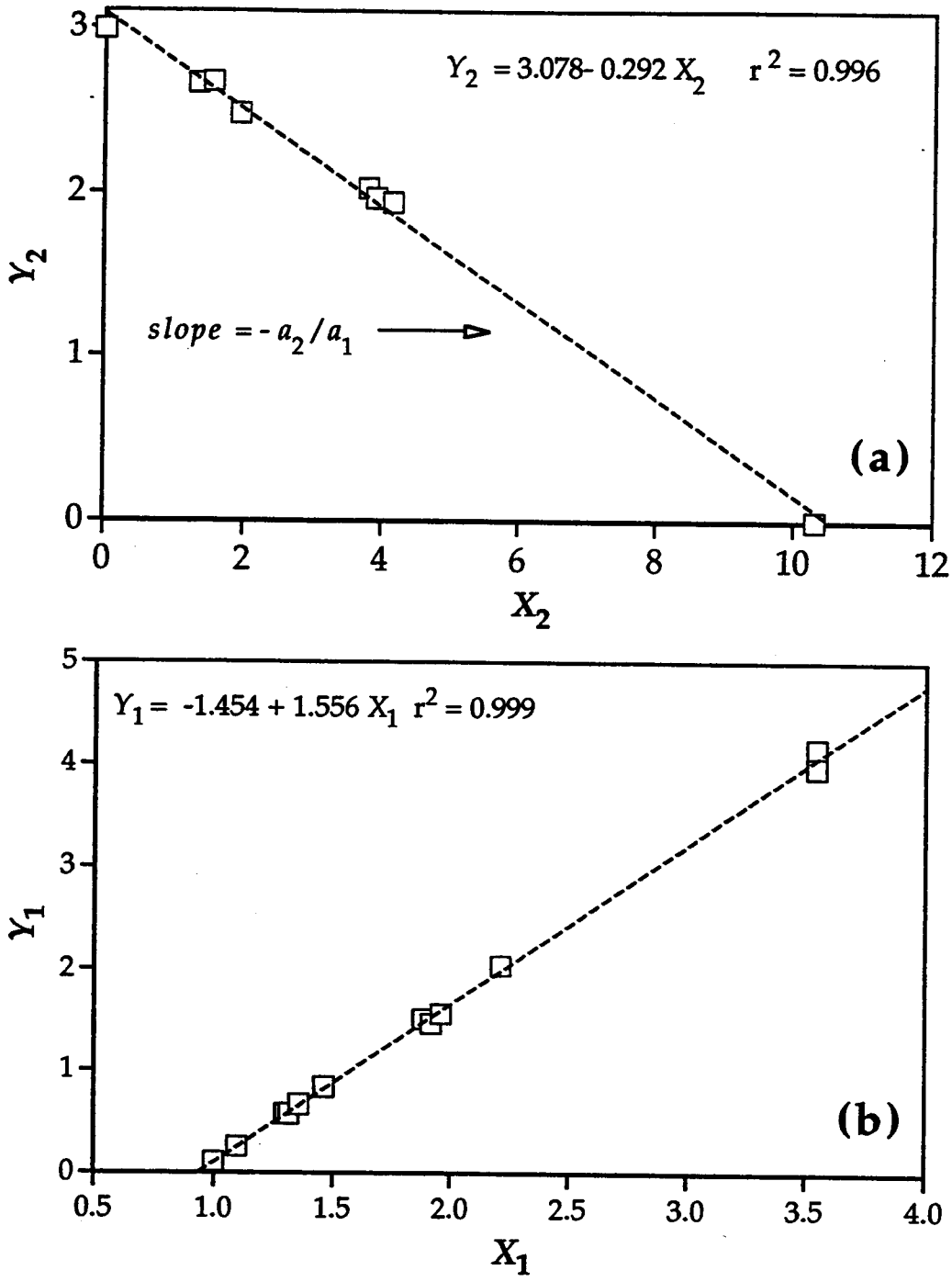

Figure B1. Determination of parameters defined by Equations B30-B34 (a) and B29-B23 (b).

their ratio. This affects the solutions for the calibration constants and the composition a_2 but leaves the parameter a_1 practically unchanged (this will be illustrated in more detail later). This effect could be reduced by a smaller step size in a 2θ during a XRD scan, i.e. by an increased resolution of the intensity measurements. For this reason, in fitting the form from Equation B18, the experiments No. 5, 13 and 14 from Table B2 were excluded . It can be seen in Table B4 that the results agree well except in only one case (~5.3% difference in $K_{\alpha/\beta}$).

Table B4. Comparison of the calibration results obtained by various linear forms

$Y_1 - X_1$	$Y_2 - X_2$	a_1	a_2	$K_{\alpha/\beta}$	$K_{Si/\alpha}$	$K_{Si/\beta}$
form B17	form B19	0.947	0.276	0.647	2.913	-
	form B20	0.948	0.279	0.640	2.923	-
form B18	form B25	0.945	0.307	0.607	-	0.897
	form B26	0.938	0.283	0.653	-	0.903

An appropriate error propagation analysis in this case is beyond the scope of this work. According to Schafer (1994) and Berg (1994) this is rather challenging "econometric" problem because a fitting parameter from one regression is used to generate independent variable used in another regression. However, three cases gave an excellent agreement with the most recent reported result for $K_{\alpha/\beta}$ so it was accepted that $K_{\alpha/\beta} = 0.647$ and $a_1 = 0.947$.

With the known compositions of silicon nitride standards, the calibration constants for the other silicon standards, **#3a** and **#3b**, is straightforward. When only standard **#1** is mixed with these silicon standards, the corresponding calibration constants can be determined by simple regression from Equation B16, rewritten for $m_2 = 0$, as

$$\left[\frac{I_{Si}}{I_{\alpha}^{*}}\right] = K_{Si/\alpha}\left[\frac{m_{Si}}{a_1 m_1}\right]; \quad m_{Si} \leftarrow m_{\#3a} \text{ or } m_{\#3b} \tag{B35}$$

Thus, mixing these standard silicon powders in known mass ratios with silicon nitride standard **#1** and measuring the corresponding peak intensities enables evaluation of $K_{Si/\alpha}$ as a slope of the fitted line defined by Equation B35.

The above procedure yielded two different values for $K_{Si/\alpha}$ for standards **#3a** (6.89) and **#3b** (5.53), both significantly different from the corresponding constant for silicon standard **#3**. It should be noted that, in both the cases, the outliers obtained at high silicon/α ratios were excluded from the regression, as shown in Figure B2. Also, even though the intercepts obtained from the fitted lines were close to zero, the fits were forced through the zero.

Excluding from linear regressions the outliers observed at high intensity, i.e. mass fraction, ratios, does not affect significantly an accuracy of the determination of mass fractions. Even though the outliers seen in Figure B2, which correspond to the mixtures coded A3 and B5 in Table B2, did not participate in the fits yielding the corresponding calibration constants, a relative error of predicting the mass fractions by obtained calibration constants

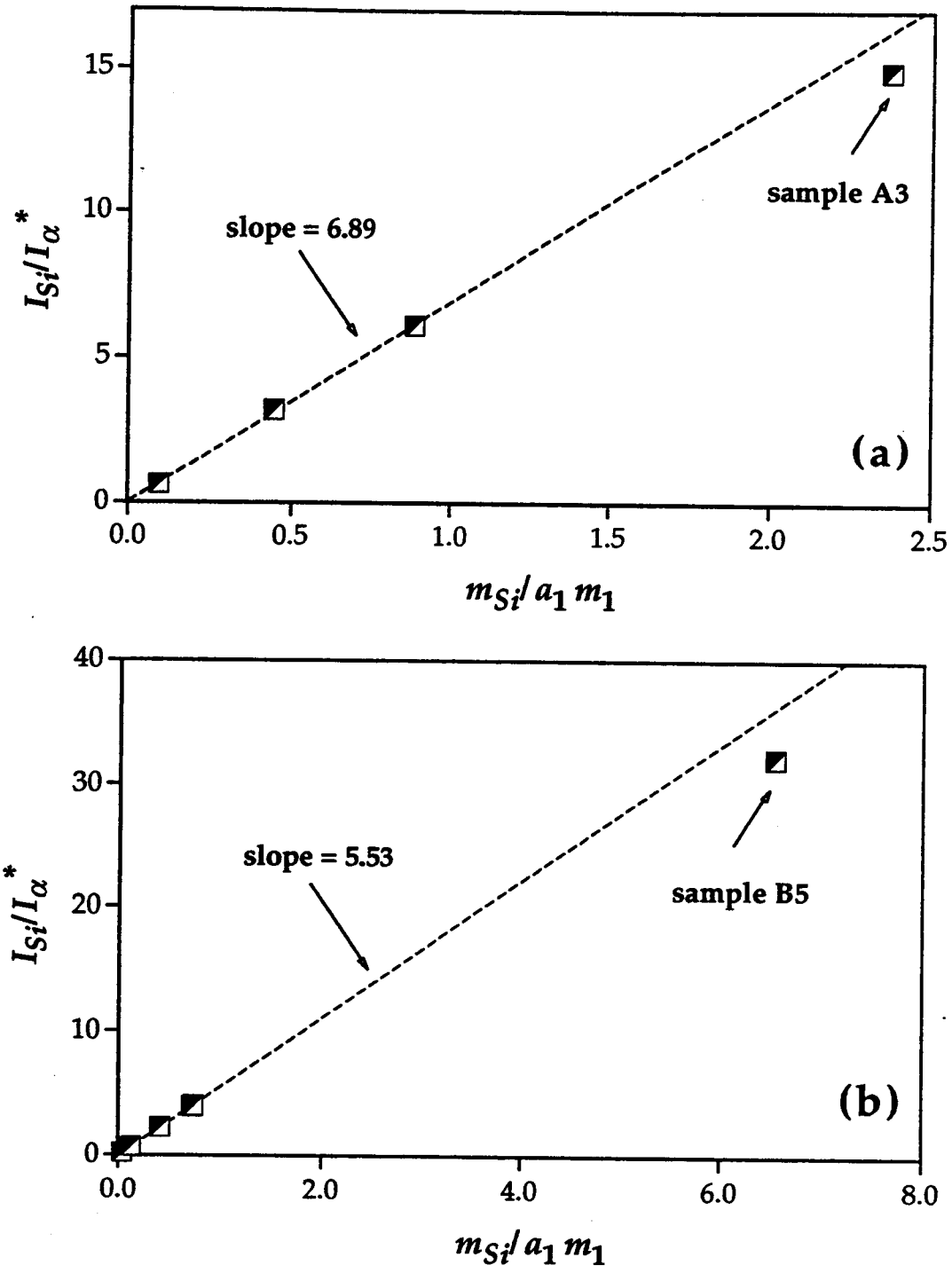

Figure B2. Determination of $K_{Si/\alpha}$ for silicon standard **#3a** (a) and **#3b** (b).

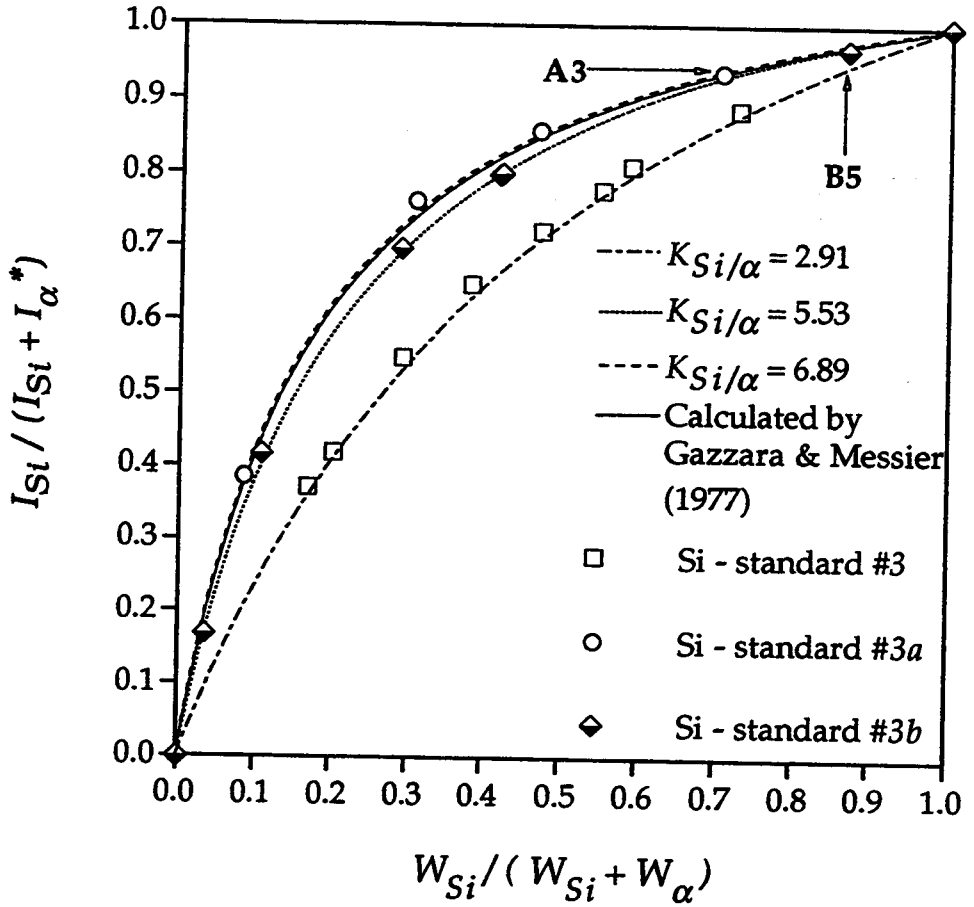

Figure B3. Effect of $K_{Si/\alpha}$ on determination of silicon mass fraction.

was only -2.8 and -1.7%, respectively, for these experimental points. This error was of the order of the error for the rest of the points. In Figure B3, plotted according to Equation B4, it can be seen that these outliers practically fall on the corresponding calibration lines. The figure also clearly shows that the calibration constants depended on individual silicon standards used, thus, no general calibration constant for silicon/α mass ratios can be proposed. Remarkable agreement with the calculated curve of Gazzara and Messier

(1977), recreated from the original paper, was achieved with silicon standard **#3a.**

The observed discrepancy in calibration constants for silicon/α determination is intriguing finding for which, at present, there is no clear explanation. The standard **#3** presents very fine powder which exhibits unusually broad X-ray peaks (the average **fwhm** for this standard was 0.215°2θ while for standards **#3a** and **#3b** it was 0.069 and 0.057, respectively). This may introduce an error in subtracting background noise while fitting the silicon peaks, or errors associated with preferred orientation of a very small crystallites. However, the discrepancy between the calibration curve for this standard and calculated theoretical data of Gazzara and Messier (1977) is still too big to be attributed to either of these facts. Another possible explanation for the observed difference in $K_{Si/\alpha}$ in cases of standards **#3a** and **#3b** was that standards preparation, i.e. grinding, generated either new additional crystalline phases or amorphous silica which would, in both cases, reduce the level of free silicon in analyzed mixture (Jenkins et al., 1986; Nakamura et al., 1989). This was disproved by additional scans of several samples in the range of 2θ =2-60°: these scans showed neither presence of additional crystalline phases nor amorphous silica peaks in the analyzed standard mixtures.

Conclusion

The original method is proposed for determining calibration constants for the quantitative analysis of silicon/silicon nitride mixtures. The method yielded the constant for determination of the α-/ β-silicon nitride ratios $K_{\alpha/\beta}$ = **0.647**, which is the value identical to the most recent published result (Devlin and Amin , 1990). On the other hand, calibration constants for silicon/α ratios evaluated by the 2-line (2-peak) method depended on the silicon standards used and no generally consistent value was found. Since the main goal is determining reliable mass compositions rather than obtaining the general calibration constant, the quick 2-line method described in this section, with a standardized procedure of a sample preparation, will give accurate enough results. Since the reacting pellets from fluidized bed reactor must be ground before the XRD analysis, i.e. prepared for the analysis in the same way as silicon standard **#3b**, the crystalline silicon content presented in Appendix B was determined by using $K_{si/\alpha}$ = **5.53**, which resulted from this particular silicon standard. Even though the mass fractions, overall silicon conversions and yields of the α- and β-forms, calculated by the calibration constants obtained by the procedure from this section, are given with four digits in Appendix C, according to the results from Table B2, only first two can be considered significant.

APPENDIX C.
TABLES OF RESULTS

This Appendix contains information obtained by powder X-ray diffraction analysis of the samples from twenty four runs discussed in this study. The corresponding experimental conditions for each of the runs are presented in Tables 3 and 4 (pages 26-27). The tables present the following:

- time stamp of a sample;
- deconvoluted integrated intensities of the peaks used in Equations 11 and 12, together with
  - peak diffraction angle (2θ [deg]),
  - full widths at half maximum (**fwhm**) of all the peaks,
  - crystallite sizes of each of the phases, roughly estimated on the basis of the wavelength of Cu_{K_α} radiation (1.5406 Å), **fwhm**'s and the diffraction angle of the peak (θ) as (Cullity, 1978)

$$d \approx \frac{1.5406}{\mathbf{fwhm}\,\cos(\theta)} \quad [\text{Å}] \;;$$

- mass fractions of all the phases, overall conversion and fractional yields of each of the silicon nitride phases, calculated by Equations 11-17;
- the size range of the pellets the sample originates from.

Table C1. Run-01: results of XRD analysis (d_p > 425 μm).

#	t [sec]	area	fwhm	2 θ	d [Å]	area	fwhm	2 θ	d [Å]
		SILICON (111)				ALPHA (201)			
1	1800	511.20	0.0625	28.277	1456	2.101	0.2000	30.835	458
2	2700	503.00	0.0502	28.315	1813	13.805	0.1766	30.869	519
3	3600	270.70	0.0638	28.185	1426	15.999	0.1925	30.742	476
4	4500	359.50	0.0574	28.266	1586	29.120	0.1574	30.823	582
5	5400	434.10	0.0725	28.321	1256	45.470	0.1737	30.885	527
6	6300	349.30	0.0623	28.316	1461	55.570	0.1768	30.879	518
7	7200	325.40	0.0636	28.323	1431	64.720	0.1655	30.887	553
8	8399	260.60	0.0769	28.297	1184	72.410	0.1659	30.865	552
9	9601	231.20	0.0700	28.311	1300	82.520	0.1603	30.877	571
10	12600	204.00	0.0906	28.374	1005	110.86	0.1711	30.947	535
11	18000	116.88	0.0887	28.288	1026	102.12	0.1642	30.861	558
12	36000	109.20	0.0944	28.294	964	110.31	0.1824	30.869	502
		ALPHA (102)				ALPHA (210)			
1	1800	1.946	0.0961	34.417	962	2.348	0.1328	35.181	697
2	2700	13.884	0.1608	34.438	575	16.664	0.2126	35.219	436
3	3600	16.875	0.1908	34.317	484	19.204	0.1796	35.094	515
4	4500	29.410	0.1873	34.398	493	33.300	0.1892	35.168	489
5	5400	42.260	0.1572	34.455	588	49.430	0.2037	35.228	455
6	6300	52.370	0.1756	34.450	526	56.820	0.1668	35.220	555
7	7200	62.070	0.1605	34.456	576	67.310	0.1657	35.228	559
8	8399	67.450	0.1823	34.435	507	78.500	0.1886	35.207	491
9	9601	78.730	0.1872	34.446	494	89.470	0.1951	35.218	475
10	12600	100.38	0.1838	34.511	503	113.72	0.1902	35.284	487
11	18000	98.810	0.1797	34.428	514	101.53	0.1729	35.200	536
12	36000	104.63	0.1746	34.438	529	113.26	0.1803	35.210	514

Table C1 (continued). Run-01: results of XRD analysis (d_p > 425 μm).

#	t [sec]	area	fwhm	2 θ	d [Å]	area	fwhm	2 θ	d [Å]
		BETA (101)				BETA (210)			
1	1800	0.000	****	****	****	0.000	****	****	****
2	2700	3.067	0.1970	33.539	468	3.273	0.4745	35.860	196
3	3600	3.994	0.3939	33.402	234	3.269	0.2565	35.809	362
4	4500	4.630	0.1982	33.491	465	4.407	0.3137	35.852	296
5	5400	7.844	0.2380	33.545	387	7.377	0.2160	35.910	430
6	6300	9.401	0.2226	33.544	414	7.609	0.2712	35.937	342
7	7200	12.784	0.2600	33.551	355	9.665	0.1736	35.939	535
8	8399	15.362	0.2819	33.531	327	13.609	0.2588	35.915	359
9	9601	18.532	0.2170	33.545	425	17.275	0.2342	35.927	396
10	12600	30.672	0.2600	33.610	355	26.588	0.2309	35.992	402
11	18000	33.205	0.2447	33.525	377	30.368	0.2483	35.909	374
12	36000	36.750	0.2482	33.532	371	34.672	0.2656	35.921	349
		W_α	W_β	W_{Si}	W_α'	W_β'	X	X_α	X_β
1	1800	0.0222	0.0000	0.9778	****	****	0.0135	0.0135	0.0000
2	2700	0.1293	0.0174	0.8533	0.8816	0.1184	0.0936	0.0825	0.0111
3	3600	0.2384	0.0311	0.7305	0.8848	0.1152	0.1814	0.1605	0.0209
4	4500	0.3004	0.0280	0.6716	0.9147	0.0853	0.2270	0.2077	0.0194
5	5400	0.3526	0.0379	0.6095	0.9030	0.0970	0.2779	0.2509	0.0269
6	6300	0.4466	0.0450	0.5083	0.9084	0.0916	0.3675	0.3338	0.0336
7	7200	0.4944	0.0555	0.4501	0.8991	0.1009	0.4232	0.3805	0.0427
8	8399	0.5618	0.0721	0.3661	0.8862	0.1138	0.5098	0.4518	0.0580
9	9601	0.6079	0.0837	0.3084	0.8789	0.1211	0.5739	0.5044	0.0695
10	12600	0.6639	0.1149	0.2212	0.8525	0.1475	0.6789	0.5788	0.1001
11	18000	0.7079	0.1453	0.1467	0.8297	0.1703	0.7774	0.6450	0.1324
12	36000	0.7187	0.1524	0.1288	0.8250	0.1750	0.8024	0.6620	0.1404

Table C2. Run-02: results of XRD analysis (d_p > 425 μm).

#	t [sec]	area	fwhm	2 θ	d [Å]	area	fwhm	2 θ	d [Å]
		SILICON (111)				ALPHA (201)			
1	1413	781.0	0.0468	28.420	1946	1.26	0.0985	30.971	930
2	2004	720.0	0.0507	28.418	1796	19.38	0.1412	30.974	649
3	2600	713.0	0.0503	28.478	1810	32.26	0.1499	31.033	611
4	3200	618.4	0.0639	28.428	1425	43.93	0.1650	30.990	555
5	3645	574.9	0.0536	28.416	1699	51.21	0.1452	30.974	631
6	4210	549.1	0.0564	28.426	1614	63.99	0.1693	30.985	541
7	5040	425.2	0.0537	28.366	1695	72.95	0.1559	30.927	587
8	5901	443.8	0.0571	28.445	1595	98.72	0.1593	31.006	575
9	6800	338.7	0.0591	28.371	1541	98.42	0.1573	30.934	582
10	8100	297.9	0.0657	28.403	1386	124.66	0.1527	30.970	600
11	9300	265.0	0.0759	28.425	1200	138.79	0.1514	30.995	605
12	10800	220.6	0.0706	28.415	1290	143.49	0.1518	30.984	603
13	13200	176.5	0.0765	28.391	1190	146.89	0.1601	30.960	572
14	18000	153.3	0.0785	28.402	1160	155.00	0.1550	30.974	591
15	28800	143.3	0.0752	28.419	1211	160.53	0.1484	30.991	617
		ALPHA (102)				ALPHA (210)			
1	1413	1.0729	0.1864	34.549	496	1.228	0.0914	35.312	1013
2	2004	18.076	0.1409	34.546	656	18.551	0.1570	35.313	590
3	2600	29.61	0.1584	34.604	584	35.840	0.1875	35.372	494
4	3200	40.6	0.1527	34.556	605	44.220	0.1567	35.328	591
5	3645	47.72	0.1480	34.543	625	51.580	0.1458	35.311	635
6	4210	59.76	0.1701	34.551	543	64.280	0.1868	35.323	496
7	5040	65.39	0.1506	34.496	614	73.240	0.1526	35.267	607
8	5901	90.59	0.1497	34.573	618	99.770	0.1687	35.346	549
9	6800	91.83	0.1527	34.502	605	96.560	0.1729	35.270	536
10	8100	114.16	0.1600	34.538	578	116.74	0.1654	35.306	560
11	9300	124.41	0.1638	34.562	564	131.98	0.1562	35.332	593
12	10800	131.9	0.1605	34.553	576	139.98	0.1597	35.324	580
13	13200	130.99	0.1603	34.531	577	141.90	0.1590	35.298	583
14	18000	141.37	0.1639	34.545	564	151.50	0.1585	35.313	584
15	28800	147.1	0.1612	34.561	573	160.88	0.1699	35.332	545

Table C2 (continued). Run-02: results of XRD analysis (d_p > 425 μm).

#	t [sec]	area	fwhm	2 θ	d [Å]	area	fwhm	2 θ	d [Å]
		BETA (101)				BETA (210)			
1	1413	0.000	****	****	****	0.000	****	****	****
2	2004	3.046	0.2011	33.657	459	1.645	0.2232	36.024	416
3	2600	4.580	0.2308	33.711	400	4.606	0.2522	36.063	368
4	3200	6.169	0.1633	33.648	565	5.066	0.1831	36.019	507
5	3645	6.901	0.2103	33.641	438	5.534	0.1492	36.002	622
6	4210	8.608	0.2379	33.650	388	7.362	0.2282	36.022	407
7	5040	10.465	0.1948	33.601	473	10.458	0.2689	35.971	345
8	5901	15.155	0.2443	33.672	377	13.629	0.2482	36.030	374
9	6800	16.246	0.2086	33.607	442	13.188	0.2347	35.978	395
10	8100	23.426	0.2404	33.633	384	20.261	0.2226	36.012	417
11	9300	29.073	0.2226	33.658	414	27.821	0.2617	36.041	355
12	10800	34.521	0.2432	33.649	379	29.757	0.2130	36.035	436
13	13200	38.120	0.2385	33.624	387	34.582	0.2355	36.007	394
14	18000	43.250	0.2451	33.635	376	37.420	0.2222	36.020	418
15	28800	45.060	0.2466	33.652	374	40.770	0.2165	36.042	429
		W_α	W_β	W_{SI}	W_α'	W_β'	X	X_α	X_β
1	1413	0.0088	0.0000	0.9912	1.0000	0.0000	0.0053	0.0053	0.0000
2	2004	0.1280	0.0106	0.8614	0.9235	0.0765	0.0882	0.0814	0.0067
3	2600	0.1964	0.0178	0.7858	0.9168	0.0832	0.1407	0.1290	0.0117
4	3200	0.2751	0.0236	0.7013	0.9211	0.0789	0.2037	0.1876	0.0161
5	3645	0.3212	0.0260	0.6528	0.9251	0.0749	0.2421	0.2239	0.0181
6	4210	0.3792	0.0316	0.5892	0.9231	0.0769	0.2952	0.2725	0.0227
7	5040	0.4645	0.0454	0.4902	0.9110	0.0890	0.3845	0.3503	0.0342
8	5901	0.5231	0.0512	0.4258	0.9109	0.0891	0.4475	0.4076	0.0399
9	6800	0.5800	0.0586	0.3614	0.9082	0.0918	0.5149	0.4676	0.0473
10	8100	0.6430	0.0787	0.2782	0.8909	0.1091	0.6091	0.5426	0.0664
11	9300	0.6715	0.0964	0.2321	0.8745	0.1255	0.6652	0.5817	0.0835
12	10800	0.6987	0.1069	0.1945	0.8673	0.1327	0.7133	0.6186	0.0946
13	13200	0.7195	0.1240	0.1565	0.8530	0.1470	0.7640	0.6516	0.1123
14	18000	0.7368	0.1313	0.1319	0.8487	0.1513	0.7980	0.6773	0.1207
15	28800	0.7452	0.1344	0.1204	0.8472	0.1528	0.8143	0.6899	0.1244

Table C3. Run-03: results of XRD analysis (d_p > 425 μm).

#	t [sec]	area	fwhm	2 θ	d [Å]	area	fwhm	2 θ	d [Å]
		SILICON (111)				ALPHA (201)			
1	1207	626	0.0609	28.331	1495	12.496	0.1467	30.893	624
2	2431	489.4	0.0686	28.294	1327	45.69	0.1413	30.858	648
3	3629	253.8	0.0745	28.212	1222	61.2	0.1436	30.780	638
4	5400	233.3	0.0748	28.325	1217	122.46	0.1477	30.896	620
5	7200	174.3	0.0859	28.334	1060	136.34	0.1472	30.907	622
6	10800	134.5	0.0896	28.312	1016	138.01	0.1477	30.887	620
7	21600	97.81	0.0795	28.257	1145	122.51	0.1616	30.918	567
		ALPHA (102)				ALPHA (210)			
1	1207	12.707	0.1573	34.462	588	13.432	0.1496	35.221	619
2	2431	43.85	0.1573	34.422	587	46.86	0.1486	35.196	623
3	3629	61.43	0.1544	34.351	598	64.17	0.1499	35.122	618
4	5400	111	0.1435	34.466	644	120.09	0.1464	35.235	633
5	7200	123.54	0.1576	34.466	586	131.42	0.1515	35.233	611
6	10800	125.03	0.1467	34.458	630	135.03	0.1503	35.228	616
7	21600	113.13	0.1461	34.402	632	124.95	0.1590	35.171	582

Table C3 (continued). Run-03: results of XRD analysis (d_p > 425 μm).

#	t [sec]	area	fwhm	2 θ	d [Å]	area	fwhm	2 θ	d [Å]
		BETA		(101)		BETA		(210)	
1	1207	0.8743	0.0856	33.571	1077	1.0349	0.2693	35.943	345
2	2431	5.74	0.1925	33.519	479	5.616	0.2280	35.887	407
3	3629	7.71	0.1883	33.431	489	6.215	0.1408	35.831	659
4	5400	23.953	0.2376	33.554	388	19.405	0.1962	35.953	473
5	7200	29.008	0.2553	33.557	361	27.081	0.2197	35.943	422
6	10800	34.984	0.2448	33.546	377	33.041	0.2561	35.933	362
7	21600	32.757	0.2464	33.491	374	29.322	0.2506	35.886	370
		W_α	W_β	W_{SI}	W_α'	W_β'	X	X_α	X_β
1	1207	0.0988	0.0047	0.8965	0.9549	0.0451	0.0648	0.0619	0.0029
2	2431	0.3311	0.0268	0.6421	0.9251	0.0749	0.2508	0.2320	0.0188
3	3629	0.5487	0.0394	0.4120	0.9331	0.0669	0.4616	0.4307	0.0309
4	5400	0.6820	0.0828	0.2352	0.8917	0.1083	0.6613	0.5897	0.0716
5	7200	0.7279	0.1036	0.1685	0.8754	0.1246	0.7477	0.6546	0.0932
6	10800	0.7431	0.1258	0.1311	0.8553	0.1447	0.7992	0.6835	0.1157
7	21600	0.7615	0.1285	0.1101	0.8556	0.1444	0.8292	0.7095	0.1197

Table C4. Run-04: results of XRD analysis (d_p > 425 μm).

#	t [sec]	area	fwhm	2 θ	d [Å]	area	fwhm	2 θ	d [Å]
		SILICON (111)				ALPHA (201)			
1	491	766	0.0460	28.416	1979	1.1198	0.1096	30.981	836
2	905	713.2	0.0592	28.417	1538	19.42	0.1355	30.973	676
3	1220	616.8	0.0499	28.383	1825	30.65	0.1117	30.939	820
4	1474	633.4	0.0514	28.403	1771	36.1	0.1319	30.959	694
5	1820	557.6	0.0558	28.408	1632	61.03	0.1185	30.965	773
6	2100	509.5	0.0566	28.413	1609	77.19	0.1200	30.974	763
7	2450	437.5	0.0578	28.420	1575	94.63	0.1199	30.980	764
8	2885	358.8	0.0695	28.474	1310	108.4	0.1283	31.037	714
9	3190	289.2	0.0631	28.381	1443	109.2	0.1288	30.947	711
10	3685	271.3	0.0723	28.467	1260	132.4	0.1379	31.036	664
11	4149	215.8	0.0685	28.411	1329	139.54	0.1269	30.978	722
12	4600	194.3	0.0710	28.424	1282	146.1	0.1302	30.994	704
13	5400	157.4	0.0764	28.451	1192	145.87	0.1375	31.018	666
14	7200	126.4	0.0738	28.456	1234	142.87	0.1316	31.025	696
15	10800	107.9	0.0909	28.405	1002	140.65	0.1468	30.979	624
16	21600	111.4	0.0738	28.415	1234	157.61	0.1333	30.987	687

Table C4 (continued). Run-04: results of XRD analysis (d_p > 425 μm).

#	t [sec]	area	fwhm	2 θ	d [Å]	area	fwhm	2 θ	d [Å]
		ALPHA (102)				ALPHA (210)			
1	491	1.451	0.1365	34.538	677	1.159	0.0604	35.318	1534
2	905	20.101	0.1505	34.541	614	20.7	0.1562	35.310	593
3	1220	27.9	0.1138	34.506	812	30.45	0.1237	35.276	749
4	1474	33.6	0.1350	34.527	685	36.58	0.1299	35.295	713
5	1820	56.48	0.1250	34.531	739	58.5	0.1201	35.302	771
6	2100	68.11	0.1150	34.541	804	74.11	0.1197	35.311	774
7	2450	83.64	0.1150	34.550	804	92.59	0.1283	35.318	722
8	2885	97.86	0.1522	34.606	607	108.18	0.1368	35.371	677
9	3190	100.42	0.1262	34.514	732	107.3	0.1287	35.285	720
10	3685	122.19	0.1348	34.602	686	133.73	0.1362	35.370	680
11	4149	123.99	0.1311	34.546	705	136.79	0.1342	35.316	690
12	4600	131.93	0.1264	34.561	731	143.88	0.1325	35.330	699
13	5400	130.46	0.1179	34.592	784	143.77	0.1423	35.351	651
14	7200	126.2	0.1391	34.594	665	136.31	0.1339	35.362	692
15	10800	135.92	0.1466	34.548	631	151.49	0.1483	35.316	625
16	21600	133.75	0.1306	34.557	708	149.41	0.1353	35.324	685

Table C4 (continued). Run-04: results of XRD analysis (d_p > 425 μm).

#	t [sec]	area	fwhm	2 θ	d [Å]	area	fwhm	2 θ	d [Å]
		BETA (101)				BETA (210)			
1	491	0	****	****	****	0	****	****	****
2	905	3.156	0.2899	33.641	318	1.7105	0.2756	36.022	337
3	1220	4.265	0.1640	33.602	562	3.367	0.1363	35.966	681
4	1474	4.572	0.2414	33.627	382	4.617	0.1839	35.984	505
5	1820	7.215	0.2155	33.629	428	6.735	0.2071	35.988	448
6	2100	9.802	0.2057	33.636	448	10.944	0.2745	36.007	338
7	2450	12.218	0.2407	33.649	383	11.322	0.2192	36.026	423
8	2885	16.497	0.2360	33.698	391	15.279	0.2523	36.080	368
9	3190	18.542	0.2324	33.606	397	14.567	0.1751	35.996	530
10	3685	21.875	0.1844	33.699	500	21.837	0.2040	36.077	455
11	4149	25.723	0.2022	33.643	456	24.468	0.2092	36.020	444
12	4600	30.29	0.2060	33.656	448	25.586	0.1888	36.037	492
13	5400	29.755	0.2002	33.685	461	23.69	0.1821	36.064	510
14	7200	32.454	0.2371	33.691	389	26.409	0.1780	36.067	522
15	10800	32.514	0.2307	33.640	400	29.133	0.2064	36.021	450
16	21600	36.04	0.2417	33.650	382	32.4	0.2144	36.035	433

Table C4 (continued). Run-04: results of XRD analysis (d_p > 425 μm).

#	t [sec]	W_α	W_β	W_{St}	W_α'	W_β'	X	X_α	X_β
1	491	0.0080	0.0000	0.9920	1.0000	0.0000	0.0048	0.0048	0.000
2	905	0.1294	0.0100	0.8606	0.9284	0.0716	0.0887	0.0823	0.006
3	1220	0.2115	0.0179	0.7706	0.9220	0.0780	0.1517	0.1398	0.011
4	1474	0.2345	0.0199	0.7455	0.9219	0.0781	0.1702	0.1569	0.013
5	1820	0.3659	0.0287	0.6053	0.9272	0.0728	0.2814	0.2609	0.020
6	2100	0.4368	0.0412	0.5220	0.9138	0.0862	0.3548	0.3242	0.030
7	2450	0.5200	0.0449	0.4352	0.9205	0.0795	0.4380	0.4032	0.034
8	2885	0.5886	0.0587	0.3527	0.9093	0.0907	0.5243	0.4767	0.047
9	3190	0.6319	0.0652	0.3030	0.9065	0.0935	0.5801	0.5259	0.054
10	3685	0.6750	0.0746	0.2504	0.9005	0.0995	0.6426	0.5786	0.063
11	4149	0.7120	0.0887	0.1994	0.8893	0.1107	0.7069	0.6286	0.078
12	4600	0.7289	0.0955	0.1755	0.8841	0.1159	0.7383	0.6527	0.085
13	5400	0.7567	0.0954	0.1478	0.8880	0.1120	0.7759	0.6890	0.086
14	7200	0.7661	0.1111	0.1227	0.8733	0.1267	0.8111	0.7083	0.102
15	10800	0.7827	0.1086	0.1087	0.8781	0.1219	0.8312	0.7299	0.101
16	21600	0.7786	0.1218	0.0996	0.8648	0.1352	0.8444	0.7302	0.114

Table C5. Run-05: results of XRD analysis (d_p > 425 μm)

#	t [sec]	area	fwhm	2 θ	d [Å]	area	fwhm	2 θ	d [Å]
		SILICON (111)				ALPHA (201)			
1	273	730	0.0519	28.447	1755	24.33	0.1014	30.996	903
2	651	624.2	0.0608	28.416	1498	43.89	0.1176	30.969	779
3	986	477.9	0.0588	28.397	1548	71.97	0.1128	30.955	812
4	1555	309.3	0.0631	28.410	1443	120.55	0.1084	30.975	845
5	1836	262.7	0.0761	28.456	1197	143.43	0.1236	31.020	741
6	2285	191.3	0.0660	28.405	1380	151.48	0.1112	30.970	824
7	2588	172.3	0.0681	28.457	1337	174.4	0.1202	31.022	762
8	2965	142.3	0.0693	28.412	1314	171.36	0.1223	30.981	749
9	3665	125.3	0.0757	28.457	1203	185.06	0.1283	31.025	714
10	4800	104.4	0.0704	28.412	1293	174.14	0.1235	30.982	742
11	9360	94.97	0.0911	28.476	1000	181.58	0.1258	31.046	728
12	14100	87.77	0.0729	28.393	1249	174.8	0.1085	30.964	844
13	22080	75.41	0.0710	28.378	1282	156.76	0.1148	30.950	798
14	36000	65.4	0.0717	28.385	1270	169.71	0.1136	30.955	806
		ALPHA (102)				ALPHA (210)			
1	273	23.04	0.1095	34.564	844	26.11	0.1182	35.333	784
2	651	41.04	0.1196	34.540	773	42.67	0.1196	35.307	775
3	986	61.95	0.1035	34.524	893	67.02	0.1085	35.291	854
4	1555	107.19	0.1122	34.544	824	115.03	0.1169	35.312	792
5	1836	128.9	0.1230	34.592	752	139.66	0.1297	35.359	714
6	2285	134.9	0.1102	34.542	839	150.69	0.1223	35.308	757
7	2588	154.6	0.1195	34.595	774	165.37	0.1187	35.360	781
8	2965	149.32	0.1153	34.552	802	162.16	0.1202	35.319	771
9	3665	164.99	0.1325	34.596	698	180.37	0.1329	35.364	697
10	4800	156.18	0.1245	34.550	742	167.14	0.1216	35.318	762
11	9360	161.98	0.1378	34.617	671	180.95	0.1342	35.386	690
12	14100	157.18	0.1172	34.535	789	167.08	0.1191	35.302	778
13	22080	148.32	0.1246	34.519	742	167.31	0.1209	35.286	766
14	36000	158.97	0.1200	34.529	770	172.7	0.1249	35.294	742

Table C5 (continued). Run-05: results of XRD analysis (d_p > 425 μm).

#	t [sec]	area	fwhm	2 θ	d [Å]	area	fwhm	2 θ	d [Å]
		BETA	(101)			BETA	(210)		
1	273	3.51	0.1551	33.643	595	5.281	0.2400	36.015	387
2	651	6.099	0.1586	33.631	581	6.267	0.2432	36.006	382
3	986	11.349	0.1931	33.609	478	9.791	0.1897	35.999	489
4	1555	19.711	0.2112	33.638	437	16.694	0.1773	36.012	523
5	1836	25.841	0.2010	33.681	459	20.807	0.1625	36.067	571
6	2285	27.874	0.2128	33.632	433	24.296	0.1807	36.019	514
7	2588	31.37	0.2002	33.683	461	27.59	0.1734	36.068	535
8	2965	32.92	0.1943	33.641	475	27.23	0.1667	36.028	557
9	3665	34.93	0.1777	33.689	519	30.11	0.1745	36.073	532
10	4800	33.38	0.1681	33.644	549	30.73	0.1956	36.024	475
11	9360	36.56	0.1913	33.706	482	33.03	0.1710	36.093	543
12	14100	36.73	0.2025	33.624	455	30.25	0.1638	36.014	567
13	22080	27.23	0.1565	33.614	589	27.96	0.1662	36.001	558
14	36000	35.21	0.1908	33.617	483	28.91	0.1713	36.002	542

		W_α	W_β	W_{SI}	W_α'	W_β'	X	X_α	X_β
1	273	0.1527	0.0177	0.8296	0.8963	0.1037	0.1098	0.0984	0.0114
2	651	0.2724	0.0260	0.7015	0.9128	0.0872	0.2035	0.1858	0.0178
3	986	0.4332	0.0459	0.5208	0.9041	0.0959	0.3559	0.3218	0.0341
4	1555	0.6367	0.0675	0.2958	0.9042	0.0958	0.5885	0.5321	0.0564
5	1836	0.6925	0.0778	0.2297	0.8990	0.1010	0.6683	0.6008	0.0675
6	2285	0.7425	0.0878	0.1698	0.8943	0.1057	0.7460	0.6672	0.0789
7	2588	0.7704	0.0918	0.1378	0.8935	0.1065	0.7898	0.7057	0.0841
8	2965	0.7841	0.0980	0.1179	0.8889	0.1111	0.8180	0.7271	0.0908
9	3665	0.8036	0.0979	0.0985	0.8914	0.1086	0.8461	0.7542	0.0919
10	4800	0.8085	0.1037	0.0878	0.8863	0.1137	0.8619	0.7639	0.0980
11	9360	0.8157	0.1071	0.0772	0.8839	0.1161	0.8777	0.7758	0.1019
12	14100	0.8166	0.1091	0.0742	0.8821	0.1179	0.8822	0.7782	0.1040
13	22080	0.8332	0.0943	0.0726	0.8984	0.1016	0.8847	0.7948	0.0899
14	36000	0.8369	0.1047	0.0584	0.8888	0.1112	0.9064	0.8056	0.1008

Table C6. Run-06: results of XRD analysis (d_p > 425 μm).

#	t [sec]	area	fwhm	2 θ	d [Å]	area	fwhm	2 θ	d [Å]
		SILICON (111)				ALPHA (201)			
1	900	634.2	0.0488	28.394	1866	4.356	0.1593	30.959	575
2	1814	536.7	0.0523	28.351	1741	29.37	0.1450	30.908	632
3	2839	366.3	0.0731	28.298	1245	54.47	0.1461	30.862	627
4	3800	273.2	0.0815	28.262	1117	63.63	0.1442	30.831	635
5	5580	180.4	0.1068	28.253	852	85.8	0.1611	30.825	568
6	7200	142.7	0.0919	28.277	991	104.03	0.1605	30.853	571
7	10800	138.1	0.0895	28.320	1017	120.49	0.1539	30.894	595
8	14400	148.4	0.0879	28.357	1036	132.06	0.1450	30.930	632
9	21600	124.4	0.0790	28.323	1152	124.63	0.1469	30.897	623
10	28800	116.37	0.1058	28.320	860	123.94	0.1650	30.893	555
11	36000	123.02	0.1039	28.343	876	133.12	0.1631	30.918	562
12	43200	98.19	0.0878	28.274	1037	113.32	0.1517	30.849	604
13	65988	105.44	0.0832	28.331	1094	130.8	0.1420	30.903	645
14	86400	102.82	0.0823	28.352	1106	137.52	0.1535	30.927	597
		ALPHA (102)				ALPHA (210)			
1	900	4.682	0.1324	34.498	698	4.382	0.1354	35.296	684
2	1814	28.19	0.1556	34.473	594	31.95	0.1591	35.247	582
3	2839	50.6	0.1607	34.429	575	55.26	0.1429	35.204	648
4	3800	61.39	0.1632	34.397	566	66.61	0.1518	35.167	610
5	5580	81.39	0.1543	34.394	599	89.91	0.1599	35.166	579
6	7200	98.98	0.1504	34.419	614	108.62	0.1619	35.191	572
7	10800	112.39	0.1577	34.461	586	122.71	0.1621	35.320	571
8	14400	124.21	0.1512	34.498	611	133.29	0.1551	35.268	597
9	21600	114.94	0.1562	34.464	592	124.05	0.1537	35.233	603
10	28800	114.58	0.1651	34.460	560	126.2	0.1632	35.230	567
11	36000	122.98	0.1555	34.487	594	136.05	0.1650	35.255	561
12	43200	107.62	0.1564	34.427	591	118.48	0.1601	35.192	578
13	65988	118.28	0.1536	34.473	602	136.34	0.1677	35.241	552
14	86400	128.79	0.1530	34.496	604	138.16	0.1534	35.263	604

Table C6 (continued). Run-06: results of XRD analysis (d_p > 425 μm).

#	t [sec]	area	fwhm	2 θ	d [Å]	araea	fwhm	2 θ	d [Å]
		BETA	(101)			BETA	(210)		
1	900	0	****	****	****	1.4972	0.2998	36.136	310
2	1814	4.624	0.2429	33.554	380	3.775	0.2423	35.977	383
3	2839	7.515	0.2232	33.526	413	5.641	0.1544	35.909	601
4	3800	10.394	0.2339	33.495	394	9.985	0.2676	35.866	347
5	5580	19.653	0.2272	33.492	406	19.256	0.2439	35.861	380
6	7200	27.332	0.2239	33.515	412	26.328	0.2467	35.904	376
7	10800	32.898	0.2624	33.557	351	31.451	0.2396	35.946	387
8	14400	37.85	0.2110	33.596	437	36.42	0.2302	35.977	403
9	21600	35.72	0.2267	33.552	407	34.1	0.2165	35.945	429
10	28800	35.02	0.2070	33.555	445	31.849	0.2451	35.941	379
11	36000	39.01	0.2288	33.578	403	35.98	0.2229	35.969	416
12	43200	33.13	0.2071	33.508	445	30.798	0.2236	35.899	415
13	65988	38.89	0.2408	33.561	383	34.04	0.2150	35.951	432
14	86400	41.21	0.2174	33.589	424	38.46	0.2201	35.979	422
		W_α	W_β	W_{Si}	W_α'	W_β'	X	X_α	X_β
1	900	0.0364	0.0039	0.9597	0.9034	0.0966	0.0246	0.0222	0.0024
2	1814	0.2273	0.0205	0.7521	0.9171	0.0829	0.1652	0.1515	0.0137
3	2839	0.4352	0.0350	0.5299	0.9256	0.0744	0.3477	0.3218	0.0259
4	3800	0.5318	0.0548	0.4134	0.9066	0.0934	0.4601	0.4171	0.0430
5	5580	0.6546	0.0962	0.2492	0.8719	0.1281	0.6441	0.5615	0.0825
6	7200	0.7064	0.1181	0.1754	0.8567	0.1433	0.7384	0.6326	0.1058
7	10800	0.7222	0.1279	0.1499	0.8496	0.1504	0.7731	0.6568	0.1163
8	14400	0.7194	0.1342	0.1464	0.8427	0.1573	0.7779	0.6556	0.1223
9	21600	0.7301	0.1380	0.1319	0.8410	0.1590	0.7980	0.6712	0.1269
10	28800	0.7409	0.1331	0.1260	0.8477	0.1523	0.8065	0.6836	0.1228
11	36000	0.7382	0.1383	0.1235	0.8422	0.1578	0.8100	0.6822	0.1278
12	43200	0.7464	0.1365	0.1171	0.8454	0.1546	0.8191	0.6924	0.1267
13	65988	0.7512	0.1392	0.1096	0.8437	0.1563	0.8299	0.7001	0.1297
14	86400	0.7527	0.1454	0.1019	0.8382	0.1618	0.8411	0.7050	0.1361

Table C7. Run-07: results of XRD analysis (d_p > 425 μm).

#	t [sec]	area	fwhm	2 θ	d [Å]	area	fwhm	2 θ	d [Å]
		SILICON (111)				ALPHA (201)			
1	1130	808.1	0.0700	28.437	1301	32.4	0.1364	30.994	672
2	2541	398.2	0.0623	28.351	1461	85.89	0.1280	30.915	715
3	3570	195.6	0.0845	28.263	1077	98.5	0.1349	30.834	679
4	5400	171.58	0.1461	28.459	623	169.48	0.1936	31.027	473
5	7200	109.26	0.0873	28.301	1043	143.89	0.1397	30.874	656
6	10800	121.67	0.0957	28.395	951	174.6	0.1449	30.968	632
7	21600	89.18	0.0899	28.312	1013	148.27	0.1405	30.885	652
		ALPHA (102)				ALPHA (210)			
1	1130	29.47	0.1490	34.561	620	32.87	0.1597	35.335	580
2	2541	78.1	0.1254	34.481	737	86.26	0.1341	35.252	691
3	3570	95.04	0.1511	34.402	612	107.17	0.1600	35.174	579
4	5400	153.77	0.2057	34.593	449	168.95	0.1917	35.362	483
5	7200	131.43	0.1482	34.440	624	142.47	0.1461	35.211	634
6	10800	160.41	0.1505	34.534	614	173.86	0.1538	35.305	602
7	21600	139.7	0.1475	34.455	627	146.56	0.1422	35.225	651

Table C7 (continued). Run-07: results of XRD analysis (d_p > 425 μm).

#	t [sec]	area	fwhm	2 θ	d [Å]	area	fwhm	2 θ	d [Å]
		BETA (101)				BETA (210)			
1	1130	3.556	0.2094	33.663	440	2.3139	0.2898	36.042	320
2	2541	9.251	0.2188	33.578	421	8.03	0.1751	35.961	530
3	3570	15.826	0.2375	33.498	388	13.271	0.1940	35.889	478
4	5400	33.896	0.2825	33.687	326	29.507	0.2279	36.074	407
5	7200	27.381	0.1963	33.536	470	26.462	0.2311	35.926	402
6	10800	35.96	0.2243	33.628	411	31.23	0.1943	36.014	478
7	21600	31.11	0.1968	33.545	468	27.796	0.2353	35.938	394
		W_α	W_β	W_{Si}	W_α'	W_β'	X	X_α	X_β
1	1130	0.1793	0.0109	0.8098	0.9426	0.0574	0.1237	0.1166	0.0071
2	2541	0.5243	0.0357	0.4401	0.9363	0.0637	0.4332	0.4056	0.0276
3	3570	0.6884	0.0641	0.2475	0.9148	0.0852	0.6461	0.5911	0.0550
4	5400	0.7631	0.0970	0.1399	0.8872	0.1128	0.7869	0.6982	0.0887
5	7200	0.7907	0.1006	0.1087	0.8872	0.1128	0.8312	0.7374	0.0938
6	10800	0.7960	0.1035	0.1004	0.8849	0.1151	0.8432	0.7462	0.0970
7	21600	0.8051	0.1072	0.0877	0.8825	0.1175	0.8621	0.7608	0.1013

Table C8. Run-08: results of XRD analysis (d_p > 425 μm).

#	t [sec]	area	fwhm	2 θ	d [Å]	area	fwhm	2 θ	d [Å]
		SILICON (111)				ALPHA (201)			
1	1178	607.1	0.0509	28.389	1789	32.49	0.1064	30.946	861
2	1819	537.2	0.0592	28.429	1538	59.69	0.1223	30.987	749
3	2336	431.4	0.0637	28.423	1429	92.89	0.1290	30.984	710
4	3622	243.5	0.0712	28.416	1279	127.59	0.1332	30.986	688
5	5463	174.8	0.0696	28.395	1308	147.48	0.1267	30.965	723
6	7200	161.9	0.0734	28.433	1241	162.5	0.1326	31.002	691
7	10800	152.3	0.0745	28.415	1222	160.39	0.1254	30.984	730
8	18900	140.1	0.0745	28.417	1222	163.31	0.1345	30.988	681
		ALPHA (102)				ALPHA (210)			
1	1178	30.34	0.1250	34.514	739	32.37	0.1168	35.282	793
2	1819	63.2	0.1213	34.557	762	70.19	0.1324	35.324	700
3	2336	77.85	0.1263	34.547	732	74.72	0.1306	35.322	709
4	3622	101.1	0.1275	34.557	725	115.28	0.1377	35.328	673
5	5463	137.93	0.1354	34.534	683	148.12	0.1401	35.305	661
6	7200	129.03	0.1201	34.574	770	155.23	0.1335	35.341	694
7	10800	145.98	0.1314	34.556	704	155.74	0.1350	35.323	686
8	18900	144.17	0.1306	34.560	708	158.14	0.1365	35.327	679

Table C8 (continued). Run-08: results of XRD analysis (d_p > 425 μm).

#	t [sec]	area	fwhm	2 θ	d [Å]	area	fwhm	2 θ	d [Å]
		BETA (101)				BETA (210)			
1	1178	4.535	0.2077	33.607	444	5.062	0.2290	35.976	405
2	1819	8.397	0.1654	33.656	558	8.665	0.2065	36.025	449
3	2336	14.091	0.2363	33.655	390	9.809	0.2015	36.035	461
4	3622	21.891	0.2356	33.651	391	19.968	0.2153	36.032	431
5	5463	32.59	0.2195	33.624	420	27.4	0.1800	36.013	516
6	7200	35.75	0.2195	33.664	420	30.67	0.1850	36.049	502
7	10800	36.68	0.2015	33.645	458	34.89	0.2064	36.032	450
8	18900	37.76	0.2392	33.652	386	33.52	0.1993	36.040	466
		W_α	W_β	W_{SI}	W_α'	W_β'	X	X_α	X_β
1	1178	0.2231	0.0221	0.7548	0.9099	0.0901	0.1632	0.1485	0.0147
2	1819	0.3687	0.0305	0.6008	0.9236	0.0764	0.2852	0.2634	0.0218
3	2336	0.5149	0.0522	0.4329	0.9080	0.0920	0.4403	0.3998	0.0405
4	3622	0.6799	0.0851	0.2350	0.8888	0.1112	0.6617	0.5881	0.0736
5	5463	0.7406	0.1005	0.1589	0.8805	0.1195	0.7607	0.6698	0.0909
6	7200	0.7510	0.1135	0.1355	0.8687	0.1313	0.7931	0.6889	0.1042
7	10800	0.7545	0.1158	0.1297	0.8669	0.1331	0.8012	0.6946	0.1066
8	18900	0.7646	0.1166	0.1188	0.8676	0.1324	0.8167	0.7086	0.1081

Table C9. Run-09: results of XRD analysis (d_p > 425 μm).

#	t [sec]	area	fwhm	2 θ	d [Å]	area	fwhm	2 θ	d [Å]
		SILICON (111)				ALPHA (201)			
1	2870	801	0.0474	28.363	1921	2.012	0.1055	30.922	868
2	3600	892	0.0573	28.445	1589	15.43	0.1677	31.001	546
3	4500	825	0.0512	28.430	1778	27.32	0.1689	30.985	542
4	5400	656	0.0472	28.345	1929	32.2	0.1399	30.902	655
5	7200	659.9	0.0502	28.391	1814	52.47	0.1267	30.945	723
6	10800	574.6	0.0722	28.443	1261	99.31	0.1310	31.003	699
7	14400	403.2	0.0970	28.444	939	142.13	0.1455	31.007	630
8	18028	291	0.1059	28.488	860	169.81	0.1608	31.055	570
9	21600	224.2	0.0703	28.448	1295	192.7	0.1194	31.016	767
10	30617	122.83	0.0930	28.382	979	195.18	0.1414	30.952	648
11	43200	91.92	0.0935	28.422	974	217.7	0.1368	30.996	670
12	72000	66.28	0.1193	28.501	763	221.8	0.1523	31.076	602
		ALPHA (102)				ALPHA (210)			
1	2870	1.8136	0.1242	34.488	744	1.6156	0.1242	35.223	746
2	3600	13.366	0.1192	34.576	776	16.022	0.1441	35.342	643
3	4500	25.77	0.1362	34.554	679	29.17	0.1738	35.324	533
4	5400	29.83	0.1287	34.468	718	30.71	0.1201	35.238	771
5	7200	46.57	0.1169	34.514	791	52.2	0.1429	35.282	648
6	10800	90.78	0.1468	34.571	630	101.18	0.1345	35.340	689
7	14400	128.86	0.1570	34.577	589	141.97	0.1526	35.345	607
8	18028	153.44	0.1618	34.623	571	170.05	0.1589	35.391	583
9	21600	174.49	0.1301	34.583	711	183.12	0.1240	35.351	747
10	30617	178.73	0.1411	34.522	655	191.22	0.1417	35.289	654
11	43200	197.69	0.1439	34.562	642	213.71	0.1411	35.331	657
12	72000	201.03	0.1562	34.644	592	221.78	0.1526	35.411	607

Table C9 (continued). Run-09: results of XRD analysis (d_p > 425 μm).

#	t [sec]	area	fwhm	2 θ	d [Å]	area	fwhm	2 θ	d [Å]
		BETA		(101)		BETA		(210)	
1	2870	0	0.0122	33.573	7557	0	0.3297	36.187	282
2	3600	2.6938	0.2496	33.671	369	2.3616	0.2251	36.009	412
3	4500	4.447	0.1834	33.641	503	3.263	0.2477	36.032	375
4	5400	4.448	0.2128	33.571	433	4.709	0.1999	35.953	464
5	7200	8.31	0.2192	33.615	421	7.25	0.1742	35.990	533
6	10800	13.484	0.1785	33.675	517	10.951	0.1297	36.048	716
7	14400	19.303	0.2073	33.673	445	16.749	0.1913	36.055	485
8	18028	23.373	0.2228	33.717	414	20.441	0.1805	36.094	514
9	21600	28.697	0.2125	33.678	434	26.803	0.2104	36.061	441
10	30617	31.12	0.2080	33.608	443	26.891	0.1801	36.001	515
11	43200	36.22	0.2084	33.655	443	31.38	0.1791	36.039	518
12	72000	39.17	0.2213	33.734	417	33.85	0.1830	36.121	507

		W_α	W_β	W_{SI}	W_α'	W_β'	X	X_α	X_β
1	2870	0.0137	0.0000	0.9863	1.0000	0.0000	0.0083	0.0083	0.0000
2	3600	0.0864	0.0096	0.9040	0.8998	0.1002	0.0599	0.0539	0.0060
3	4500	0.1525	0.0138	0.8337	0.9168	0.0832	0.1070	0.0981	0.0089
4	5400	0.2089	0.0204	0.7706	0.9109	0.0891	0.1516	0.1381	0.0135
5	7200	0.2959	0.0302	0.6739	0.9075	0.0925	0.2252	0.2044	0.0208
6	10800	0.4695	0.0387	0.4918	0.9239	0.0761	0.3829	0.3538	0.0291
7	14400	0.6251	0.0538	0.3211	0.9207	0.0793	0.5595	0.5151	0.0444
8	18028	0.7154	0.0627	0.2220	0.9194	0.0806	0.6780	0.6233	0.0546
9	21600	0.7627	0.0766	0.1607	0.9088	0.0912	0.7583	0.6891	0.0692
10	30617	0.8228	0.0835	0.0938	0.9079	0.0921	0.8531	0.7745	0.0786
11	43200	0.8455	0.0899	0.0646	0.9039	0.0961	0.8968	0.8106	0.0862
12	72000	0.8577	0.0958	0.0464	0.8995	0.1005	0.9250	0.8321	0.0930

Table C10. Run-10: results of XRD analysis (d_p > 425 μm).

#	t [sec]	area	fwhm	2 θ	d [Å]	area	fwhm	2 θ	d [Å]
		SILICON (111)				ALPHA (201)			
1	1731	883	0.0488	28.413	1866	2.026	0.0978	30.982	937
2	2043	917	0.0467	28.439	1950	9.133	0.1336	30.996	686
3	2258	864	0.0518	28.440	1758	15.619	0.1540	30.992	595
4	2538	845	0.0569	28.491	1601	22.24	0.1163	31.048	788
5	3000	828.6	0.0627	28.479	1452	33.36	0.1418	31.034	646
6	3600	731.2	0.0533	28.410	1708	42.09	0.1522	30.966	602
7	4800	632	0.1129	28.534	807	62.68	0.1700	31.093	539
8	6000	556.6	0.1034	28.507	881	94.02	0.1640	31.071	559
9	7430	449.2	0.0627	28.436	1452	131.54	0.1342	30.999	683
10	9000	340.8	0.0908	28.457	1003	159	0.1420	31.025	645
11	10800	225.4	0.0738	28.386	1234	170.59	0.1386	30.953	661
12	14400	141.7	0.0804	28.396	1132	192.57	0.1494	30.967	613
13	25200	97.31	0.1074	28.475	848	221.12	0.1599	31.047	573
14	43200	84.26	0.0873	28.429	1043	222	0.1489	31.003	615
15	72000	71.48	0.0987	28.474	923	225.3	0.1510	31.049	607

Table C10 (continued). Run-10: results of XRD analysis (d_p > 425 μm).

#	t [sec]	area	fwhm	2 θ	d [Å]	area	fwhm	2 θ	d [Å]
		ALPHA (102)				ALPHA (210)			
1	1731	1.631	0.0970	34.534	953	1.862	0.0814	35.309	1138
2	2043	9.039	0.1350	34.558	685	10.247	0.1634	35.325	567
3	2258	15.132	0.1357	34.564	681	17.679	0.1558	35.331	595
4	2538	23.19	0.1421	34.614	651	25.67	0.1513	35.381	612
5	3000	31.71	0.1387	34.604	667	34.45	0.1470	35.368	630
6	3600	40.19	0.1477	34.533	626	43.42	0.1528	35.303	606
7	4800	60.72	0.1789	34.660	517	63.44	0.1836	35.429	505
8	6000	87.52	0.1608	34.639	575	99.11	0.1551	35.407	597
9	7430	116.86	0.1379	34.567	670	123.45	0.1308	35.337	708
10	9000	142.13	0.1417	34.591	652	157.04	0.1522	35.361	609
11	10800	153.54	0.1409	34.522	656	159.01	0.1352	35.291	685
12	14400	172.76	0.1424	34.534	649	188	0.1453	35.304	638
13	25200	197.48	0.1698	34.616	545	218.53	0.1616	35.385	573
14	43200	199.94	0.1494	34.573	619	213.77	0.1483	35.341	625
15	72000	201.87	0.1571	34.616	589	223.54	0.1537	35.383	603

Table C10 (continued). Run-10: results of XRD analysis (d_p > 425 μm).

#	t [sec]	area	fwhm	2 θ	d [Å]	area	fwhm	2 θ	d [Å]
		BETA (101)				BETA (210)			
1	1731	0	0.2549	33.602	362	0	0.1580	35.969	587
2	2043	4.3738	0.8090	33.610	114	1.1578	0.0895	36.009	1037
3	2258	1.74	0.0868	33.674	1062	3.385	0.2210	36.018	420
4	2538	4.166	0.2090	33.726	441	3.36	0.1484	36.091	626
5	3000	5.718	0.2197	33.707	420	6.373	0.2998	36.057	310
6	3600	6.291	0.2197	33.633	420	6.022	0.2030	35.998	457
7	4800	8.912	0.2007	33.756	460	7.323	0.2305	36.126	403
8	6000	12	0.2183	33.744	423	10.534	0.1717	36.109	541
9	7430	16.337	0.2255	33.665	409	14.72	0.1858	36.041	500
10	9000	22.666	0.2341	33.690	394	20.413	0.2108	36.067	440
11	10800	25.835	0.2384	33.619	387	21.296	0.1737	35.998	534
12	14400	32.86	0.2311	33.629	399	30.113	0.2144	36.015	433
13	25200	41.67	0.2373	33.713	389	38.4	0.2459	36.100	378
14	43200	42.33	0.2280	33.670	404	36.97	0.1984	36.052	468
15	72000	42.85	0.2301	33.710	401	39.12	0.2061	36.097	450

Table C10 (continued). Run-10: results of XRD analysis (d_p > 425 μm).

#	t [sec]	W_α	W_β	W_{St}	W_α'	W_β'	X	X_α	X_β
1	1731	0.0125	0.0000	0.9875	1.0000	0.0000	0.0076	0.0076	0.0000
2	2043	0.0516	0.0096	0.9388	0.8435	0.1565	0.0377	0.0318	0.0059
3	2258	0.0900	0.0091	0.9010	0.9082	0.0918	0.0619	0.0563	0.0057
4	2538	0.1253	0.0125	0.8622	0.9094	0.0906	0.0876	0.0797	0.0079
5	3000	0.1781	0.0211	0.8009	0.8943	0.1057	0.1299	0.1162	0.0137
6	3600	0.2358	0.0225	0.7417	0.9130	0.0870	0.1730	0.1579	0.0150
7	4800	0.3436	0.0291	0.6273	0.9220	0.0780	0.2630	0.2425	0.0205
8	6000	0.4651	0.0363	0.4985	0.9275	0.0725	0.3766	0.3493	0.0273
9	7430	0.5876	0.0491	0.3633	0.9228	0.0772	0.5128	0.4732	0.0396
10	9000	0.6751	0.0629	0.2620	0.9148	0.0852	0.6285	0.5749	0.0536
11	10800	0.7481	0.0730	0.1790	0.9111	0.0889	0.7337	0.6685	0.0652
12	14400	0.8025	0.0906	0.1069	0.8985	0.1015	0.8338	0.7492	0.0846
13	25200	0.8304	0.1034	0.0662	0.8893	0.1107	0.8945	0.7954	0.0991
14	43200	0.8384	0.1040	0.0576	0.8897	0.1103	0.9076	0.8075	0.1001
15	72000	0.8459	0.1055	0.0486	0.8892	0.1108	0.9216	0.8195	0.1022

Table C11. Run-11: results of XRD analysis (d_p > 425 μm).

#	t [sec]	area	fwhm	2 θ	d [Å]	area	fwhm	2 θ	d [Å]
		SILICON (111)				ALPHA (201)			
1	1008	764	0.0476	28.351	1913	1.87	0.1462	30.915	626
2	1301	865	0.0535	28.503	1702	11.607	0.1179	31.062	777
3	1403	846	0.0600	28.512	1518	16.889	0.1715	31.065	534
4	1999	791.4	0.0599	28.420	1520	30.85	0.1274	30.979	719
5	2800	737.7	0.0953	28.502	956	51.29	0.1776	31.060	516
6	3600	608.7	0.0549	28.418	1659	79.03	0.1393	30.978	658
7	4500	443.2	0.0907	28.571	1004	96.71	0.1636	31.133	560
8	5400	387.1	0.1393	28.520	654	128.31	0.1943	31.087	472
9	6300	284.7	0.1037	28.579	878	133.07	0.1674	31.148	547
10	7200	246.3	0.0917	28.547	993	155.63	0.1588	31.116	577
11	10800	163.5	0.1014	28.472	898	200.59	0.1671	31.045	548
12	21600	127.79	0.0911	28.438	1000	208.27	0.1570	31.012	583
13	31200	113.49	0.0930	28.402	979	200.44	0.1594	30.977	575
14	43200	114	0.0773	28.430	1178	208.4	0.1346	31.002	681
		ALPHA (102)				ALPHA (210)			
1	1008	2.13	0.1219	34.485	758	1.953	0.0828	35.244	1119
2	1301	11.195	0.1545	34.626	598	13.371	0.1463	35.391	633
3	1403	15.18	0.1228	34.633	753	17.826	0.1400	35.407	662
4	1999	30.6	0.1513	34.548	611	33.34	0.1478	35.317	627
5	2800	48.76	0.1816	34.628	509	53.67	0.1873	35.397	495
6	3600	69.63	0.1325	34.546	698	76.41	0.1344	35.316	689
7	4500	90.92	0.1631	34.701	567	101.86	0.1574	35.470	589
8	5400	117.34	0.2018	34.653	458	135.95	0.1975	35.425	469
9	6300	125.52	0.1622	34.714	570	135.19	0.1818	35.484	510
10	7200	144.76	0.1670	34.681	554	159.31	0.1606	35.450	577
11	10800	181.14	0.1706	34.613	542	195.53	0.1571	35.381	590
12	21600	189.86	0.1543	34.581	599	201.25	0.1496	35.349	619
13	31200	180.33	0.1609	34.545	575	194.02	0.1545	35.313	600
14	43200	191.25	0.1441	34.572	642	205.3	0.1465	35.341	632

Table C11 (continued). Run-11: results of XRD analysis (d_p > 425 μm).

#	t [sec]	area	fwhm	2 θ	d [Å]	area	fwhm	2 θ	d [Å]
		BETA (101)				BETA (210)			
1	1008	0	***	***	***	0	***	***	***
2	1301	0	***	***	***	0	***	***	***
3	1403	2.4358	0.2181	33.742	423	3.4599	0.2755	36.062	337
4	1999	4.204	0.1728	33.651	534	4.086	0.2861	35.979	324
5	2800	6.753	0.2276	33.733	405	4.506	0.2695	36.113	344
6	3600	10.066	0.2285	33.645	404	8.868	0.1985	36.011	468
7	4500	13.139	0.2383	33.800	387	10.837	0.1748	36.164	531
8	5400	19.185	0.2950	33.758	313	17.518	0.2185	36.130	425
9	6300	23.083	0.2447	33.808	377	22.107	0.2532	36.189	367
10	7200	26.356	0.2022	33.772	456	21.447	0.1590	36.161	584
11	10800	42.85	0.2407	33.706	383	38.19	0.2225	36.093	417
12	21600	46.07	0.2449	33.675	377	38.64	0.1979	36.059	469
13	31200	44.76	0.2498	33.639	369	40.33	0.2173	36.025	427
14	43200	47.98	0.2255	33.664	409	40.88	0.1935	36.049	480
		W_α	W_β	W_{Si}	W_α'	W_β'	X	X_α	X_β
1	1008	0.0133	0.0000	0.9867	1.0000	0.0000	0.0081	0.0081	0.000
2	1301	0.0690	0.0000	0.9310	1.0000	0.0000	0.0426	0.0426	0.000
3	1403	0.0982	0.0113	0.8905	0.8964	0.1036	0.0688	0.0617	0.007
4	1999	0.1746	0.0146	0.8108	0.9226	0.0774	0.1229	0.1134	0.009
5	2800	0.2721	0.0194	0.7086	0.9336	0.0664	0.1981	0.1849	0.013
6	3600	0.4035	0.0338	0.5627	0.9226	0.0774	0.3182	0.2936	0.024
7	4500	0.5235	0.0421	0.4344	0.9255	0.0745	0.4389	0.4062	0.032
8	5400	0.6098	0.0572	0.3331	0.9143	0.0857	0.5460	0.4992	0.046
9	6300	0.6669	0.0748	0.2583	0.8992	0.1008	0.6329	0.5691	0.063
10	7200	0.7203	0.0733	0.2064	0.9077	0.0923	0.6978	0.6334	0.064
11	10800	0.7771	0.1082	0.1147	0.8778	0.1222	0.8226	0.7221	0.100
12	21600	0.7992	0.1120	0.0888	0.8771	0.1229	0.8604	0.7547	0.105
13	31200	0.8003	0.1177	0.0820	0.8718	0.1282	0.8705	0.7589	0.111
14	43200	0.8038	0.1165	0.0796	0.8734	0.1266	0.8741	0.7634	0.110

Table C12. Run-12: results of XRD analysis (d_p > 425 μm).

#	t [sec]	area	fwhm	2 θ	d [Å]	area	fwhm	2 θ	d [Å]
		SILICON (111)				ALPHA (201)			
1	825	806	0.0555	28.469	1641	1.788	0.1605	31.038	571
2	1411	685	0.0476	28.421	1913	19.96	0.1086	30.976	843
3	2000	657.2	0.0584	28.404	1559	33.96	0.1329	30.959	689
4	2600	641.1	0.0607	28.429	1500	49.86	0.1261	30.986	726
5	3252	574.3	0.0576	28.433	1581	69.38	0.1226	30.989	747
6	4071	437.5	0.0555	28.393	1641	88.04	0.1154	30.953	794
7	4990	376.9	0.0688	28.442	1324	119.33	0.1182	31.006	775
8	6175	232.7	0.0718	28.382	1268	130.49	0.1194	30.949	767
9	7200	194	0.0735	28.423	1239	159.95	0.1159	30.989	790
10	8400	141.9	0.0845	28.418	1078	169.41	0.1372	30.988	668
11	9600	111.4	0.0720	28.410	1265	177.75	0.1231	30.978	744
12	10800	96.96	0.0711	28.410	1281	183.8	0.1212	30.978	756
		ALPHA (102)				ALPHA (210)			
1	825	1.78	0.1007	34.603	918	2.296	0.0942	35.373	984
2	1411	20.09	0.1155	34.544	800	22.17	0.1155	35.315	802
3	2000	30.25	0.1238	34.527	747	33	0.1217	35.299	761
4	2600	45.73	0.1194	34.553	774	51.2	0.1258	35.323	736
5	3252	61.89	0.1161	34.558	796	65.47	0.1138	35.326	814
6	4071	75.94	0.1175	34.523	787	81.33	0.1250	35.292	741
7	4990	107.28	0.1230	34.579	752	117.87	0.1238	35.343	748
8	6175	120.56	0.1247	34.520	741	128.16	0.1169	35.288	792
9	7200	143.06	0.1207	34.561	766	157.66	0.1271	35.328	729
10	8400	153.61	0.1362	34.559	679	167.91	0.1353	35.328	685
11	9600	163.48	0.1268	34.548	729	175.01	0.1300	35.315	713
12	10800	160.59	0.1178	34.550	785	172.31	0.1216	35.317	762

Table C12 (continued). Run-12: results of XRD analysis (d_p > 425 μm).

#	t [sec]	area	fwhm	2 θ	d [Å]	area	fwhm	2 θ	d [Å]
		BETA (101)				BETA (210)			
1	825	0	****	****	****	0	****	****	****
2	1411	3.152	0.1689	33.623	546	3.977	0.1773	36.013	523
3	2000	4.091	0.2356	33.633	391	4.751	0.1786	35.983	520
4	2600	5.415	0.1156	33.652	798	5.115	0.1342	36.016	692
5	3252	8.978	0.1729	33.654	533	7.948	0.1785	36.031	520
6	4071	9.803	0.1493	33.610	618	9.259	0.1443	35.989	643
7	4990	16.335	0.2007	33.669	460	15.378	0.1844	36.052	503
8	6175	19.723	0.2050	33.613	450	17.184	0.1733	35.988	536
9	7200	23.395	0.1701	33.651	542	21.76	0.1729	36.037	537
10	8400	28.083	0.1986	33.649	464	26.992	0.2179	36.034	426
11	9600	29.74	0.1863	33.635	495	25.92	0.163	36.019	569
12	10800	30.76	0.1957	33.640	471	28.456	0.1935	36.027	480
		W_α	W_β	W_{Si}	W_α'	W_β'	X	X_α	X_β
1	825	0.0121	0.0000	0.9879	1.0000	0.0000	0.0073	0.0073	0.0000
2	1411	0.1366	0.0149	0.8485	0.9016	0.0984	0.0968	0.0873	0.0095
3	2000	0.2177	0.0197	0.7627	0.9171	0.0829	0.1575	0.1444	0.0131
4	2600	0.2943	0.0207	0.6851	0.9343	0.0657	0.2164	0.2022	0.0142
5	3252	0.3869	0.0333	0.5798	0.9208	0.0792	0.3032	0.2792	0.0240
6	4071	0.5055	0.0396	0.4548	0.9273	0.0727	0.4186	0.3881	0.0304
7	4990	0.6013	0.0548	0.3439	0.9165	0.0835	0.5340	0.4894	0.0446
8	6175	0.7048	0.0677	0.2276	0.9124	0.0876	0.6709	0.6121	0.0588
9	7200	0.7594	0.0738	0.1668	0.9115	0.0885	0.7500	0.6836	0.0664
10	8400	0.7921	0.0878	0.1201	0.9002	0.0998	0.8148	0.7335	0.0813
11	9600	0.8198	0.0872	0.0930	0.9038	0.0962	0.8541	0.7720	0.0821
12	10800	0.8260	0.0951	0.0789	0.8968	0.1032	0.8752	0.7849	0.0903

Table C13. Run-13: results of XRD analysis (d_p > 425 μm).

#	t [sec]	area	fwhm	2 θ	d [Å]	area	fwhm	2 θ	d [Å]
		SILICON (111)				ALPHA (201)			
1	3253	914	0.0604	28.439	1508	0.923	0.1310	31.006	699
2	3650	851	0.0473	28.411	1925	9.072	0.1323	30.969	692
3	4500	758.9	0.0675	28.389	1349	21.56	0.1533	30.944	597
4	5400	829	0.0511	28.468	1782	33.89	0.1422	31.021	644
5	6600	781	0.0558	28.475	1632	45.94	0.1259	31.030	728
6	8400	676.8	0.0575	28.422	1584	62.74	0.1329	30.981	689
7	9644	603.7	0.0600	28.408	1518	75.87	0.1348	30.965	679
8	10800	565.5	0.0582	28.424	1565	92.52	0.1253	30.983	731
9	12600	419.8	0.0585	28.359	1556	102.34	0.1192	30.921	768
10	14400	400.5	0.0725	28.423	1256	135.41	0.1309	30.988	700
11	16200	331.4	0.0676	28.407	1347	149.94	0.1274	30.972	719
12	21600	217.1	0.0693	28.431	1314	190	0.1226	30.999	747
13	44220	114.04	0.0807	28.437	1128	216.5	0.1375	31.007	666
14	57600	91.83	0.0790	28.408	1153	211.1	0.1368	30.980	670
15	86400	78.57	0.0803	28.415	1134	218.2	0.1387	30.991	660

Table C13 (continued). Run-13: results of XRD analysis (d_p > 425 μm)

#	t [sec]	area	fwhm	2 θ	d [Å]	area	fwhm	2 θ	d [Å]
		ALPHA (102)				ALPHA (210)			
1	3253	0.973	0.0574	34.561	1610	1.3741	0.2418	35.355	383
2	3650	9.14	0.1386	34.538	667	8.521	0.1287	35.302	720
3	4500	19.877	0.1372	34.515	674	23.3	0.1585	35.284	584
4	5400	30.06	0.1210	34.590	764	33.96	0.1338	35.358	692
5	6600	42.01	0.1291	34.602	716	46.14	0.1367	35.369	678
6	8400	59.52	0.1323	34.547	699	63.54	0.1298	35.317	714
7	9644	70.8	0.1289	34.536	717	76.14	0.1365	35.303	679
8	10800	84.45	0.1201	34.552	770	92.7	0.1348	35.322	687
9	12600	94.82	0.1428	34.489	647	100.41	0.1260	35.257	735
10	14400	123.26	0.1330	34.558	695	136.24	0.1342	35.325	690
11	16200	134.62	0.1213	34.543	762	147.47	0.1285	35.311	721
12	21600	173.57	0.1284	34.569	720	183.57	0.1266	35.337	732
13	44220	196.45	0.1416	34.575	653	212.7	0.1392	35.342	666
14	57600	191.85	0.1308	34.552	707	206.39	0.1371	35.318	676
15	86400	199.47	0.1390	34.562	665	214.3	0.1375	35.329	674

Table C13 (continued). Run-13: results of XRD analysis (d_p > 425 μm).

#	t [sec]	area	fwhm	2 θ	d [Å]	area	fwhm	2 θ	d [Å]
		BETA (101)				BETA (210)			
1	3253	0	****	****	****	0	****	****	****
2	3650	1.8292	0.1953	33.595	472	0.9111	0.1503	36.003	618
3	4500	3.662	0.2165	33.618	426	3.227	0.2853	35.975	325
4	5400	5.418	0.2118	33.706	435	6.22	0.2415	36.065	384
5	6600	7.24	0.1861	33.705	496	6.617	0.1914	36.068	485
6	8400	9.162	0.1712	33.638	539	8.221	0.2102	36.025	442
7	9644	10.043	0.2169	33.631	425	9.301	0.1975	36.007	470
8	10800	12.733	0.1690	33.648	546	9.754	0.1424	36.026	652
9	12600	13.286	0.1932	33.582	477	12.885	0.1737	35.967	534
10	14400	19.745	0.1861	33.646	496	19.35	0.2104	36.031	441
11	16200	21.707	0.1796	33.630	513	20.53	0.1803	36.015	515
12	21600	32.02	0.1955	33.667	472	29.41	0.1961	36.044	473
13	44220	40.76	0.2110	33.663	437	37.07	0.1943	36.053	478
14	57600	41.38	0.2178	33.642	423	37.94	0.2037	36.029	456
15	86400	42.49	0.1815	33.653	508	40.24	0.1918	36.035	484

Table C13 (continued). Run-13: results of XRD analysis (d_p > 425 μm).

#	t [sec]	W_α	W_β	W_{SI}	W_α'	W_β'	X	X_α	X_β
1	3253	0.0055	0.0000	0.9945	1.0000	0.0000	0.0033	0.0033	0.0000
2	3650	0.0553	0.0056	0.9392	0.9088	0.0912	0.0375	0.0340	0.0034
3	4500	0.1338	0.0138	0.8524	0.9064	0.0936	0.0942	0.0854	0.0088
4	5400	0.1803	0.0212	0.7985	0.8948	0.1052	0.1316	0.1178	0.0139
5	6600	0.2392	0.0243	0.7364	0.9077	0.0923	0.1769	0.1606	0.0163
6	8400	0.3285	0.0300	0.6415	0.9163	0.0837	0.2513	0.2302	0.0210
7	9644	0.3959	0.0337	0.5704	0.9215	0.0785	0.3115	0.2870	0.0244
8	10800	0.4569	0.0375	0.5056	0.9241	0.0759	0.3700	0.3419	0.0281
9	12600	0.5466	0.0474	0.4060	0.9202	0.0798	0.4677	0.4304	0.0373
10	14400	0.6124	0.0597	0.3279	0.9112	0.0888	0.5517	0.5027	0.0490
11	16200	0.6680	0.0647	0.2673	0.9117	0.0883	0.6221	0.5672	0.0549
12	21600	0.7586	0.0844	0.1569	0.8999	0.1001	0.7634	0.6869	0.0764
13	44220	0.8207	0.1010	0.0783	0.8904	0.1096	0.8761	0.7801	0.0960
14	57600	0.8281	0.1067	0.0652	0.8858	0.1142	0.8959	0.7936	0.1023
15	86400	0.8371	0.1083	0.0546	0.8855	0.1145	0.9123	0.8078	0.1045

Table C14. Run-14: results of XRD analysis (d_p > 425 μm).

#	t [sec]	area	fwhm	2 θ	d [Å]	area	fwhm	2 θ	d [Å]
		SILICON (111)				ALPHA (201)			
1	2968	852	0.0481	28.397	1893	0.0000	****	****	****
2	3600	839	0.0477	28.421	1909	10.907	0.1674	30.974	547
3	4502	709	0.0482	28.370	1889	23.1	0.1371	30.926	668
4	5400	823	0.0562	28.474	1620	36.38	0.1379	31.031	664
5	6600	666.6	0.0631	28.377	1443	38.24	0.1539	30.936	595
6	8400	595.4	0.0519	28.368	1754	50.12	0.1298	30.926	706
7	9600	676.4	0.0536	28.439	1699	65.46	0.1369	30.966	669
8	10800	585.4	0.0571	28.400	1595	69.88	0.1289	30.960	711
9	12600	516.8	0.0575	28.379	1583	78.25	0.1267	30.939	723
10	14400	482.9	0.0549	28.393	1658	96.77	0.1209	30.954	758
11	16200	457.4	0.0591	28.414	1541	112.43	0.1281	30.976	715
12	18000	366.6	0.0589	28.355	1546	112.17	0.1240	30.918	739
13	21600	353.9	0.0617	28.424	1476	144.61	0.1232	30.987	743
14	32400	198.8	0.0696	28.380	1308	169.71	0.1357	30.947	675
15	43200	132	0.0702	28.382	1297	189.1	0.1270	30.950	721
16	72000	63.84	0.0801	28.377	1137	210.4	0.1241	30.950	738
17	86400	53.38	0.0805	28.370	1131	204.5	0.1231	30.945	744

Table C14(continued). Run-14: results of XRD analysis (d_p > 425 μm).

#	t [sec]	area	fwhm	2 θ	d [Å]	area	fwhm	2 θ	d [Å]
		ALPHA (102)				ALPHA (210)			
1	2968	0	****	****	****	0	****	****	****
2	3600	11.479	0.1325	34.542	698	10.477	0.1716	35.310	540
3	4502	21.68	0.1371	34.497	674	25.514	0.1752	35.266	529
4	5400	34.38	0.1437	34.592	643	38.2	0.1547	35.364	599
5	6600	35.57	0.1384	34.501	668	39.03	0.1471	35.273	630
6	8400	46.54	0.1348	34.494	686	50.94	0.1358	35.127	682
7	9600	58.26	0.1245	34.562	743	64.02	0.1327	35.334	698
8	10800	65.55	0.1269	34.527	728	70.66	0.1314	35.295	705
9	12600	70.75	0.1210	34.506	764	79	0.1364	35.276	679
10	14400	83.38	0.1153	34.522	802	93.46	0.1246	35.291	743
11	16200	100.85	0.1244	34.544	743	110.41	0.1104	35.616	840
12	18000	103.66	0.1328	34.485	696	109.1	0.1247	35.254	743
13	21600	131.33	0.1225	34.558	755	143.46	0.1256	35.237	737
14	32400	156.35	0.1291	34.515	716	161.55	0.1222	35.284	758
15	43200	171.57	0.1256	34.519	736	185.49	0.1293	35.286	716
16	72000	189.08	0.1301	34.518	710	202.1	0.1309	35.287	708
17	86400	186.78	0.1278	34.514	723	199.58	0.1299	35.281	713

Table C14 (continued). Run-14: results of XRD analysis (d_p > 425 μm).

#	t [sec]	area	fwhm	2 θ	d [Å]	area	fwhm	2 θ	d [Å]
		BETA (101)				BETA (210)			
1	2968	0	****	****	****	0	****	****	****
2	3600	2.6143	0.2886	33.626	320	0.618	0.0227	36.024	4089
3	4502	3.77	0.1696	33.605	544	3.502	0.2883	35.957	322
4	5400	6.344	0.2913	33.698	317	5.295	0.1378	36.067	674
5	6600	5.917	0.2110	33.601	437	5.446	0.1932	35.971	480
6	8400	6.053	0.1103	33.589	836	7.877	0.2045	35.958	454
7	9600	9.674	0.1828	33.662	504	9.666	0.2161	36.015	430
8	10800	9.46	0.1410	33.628	654	9.433	0.1990	35.993	466
9	12600	10.411	0.1554	33.598	593	10.43	0.2010	35.985	462
10	14400	13.562	0.2022	33.620	456	10.8	0.1354	36.000	685
11	16200	14.94	0.1846	33.636	500	13.258	0.1873	36.023	496
12	18000	13.52	0.1616	33.574	571	12.896	0.1674	35.958	554
13	21600	18.812	0.1730	33.651	533	16.18	0.1529	36.030	607
14	32400	23.977	0.1927	33.611	479	20.734	0.1666	35.993	557
15	43200	28.27	0.1848	33.610	499	24.455	0.1718	35.998	540
16	72000	31.27	0.1625	33.612	567	27.91	0.1532	35.998	606
17	86400	32.3	0.1683	33.609	548	26.68	0.1425	35.996	651

Table C14 (continued). Run-14: results of XRD analysis (d_p > 425 μm).

#	t [sec]	W_α	W_β	W_{SI}	W_α'	W_β'	X	X_α	X_β
1	2968	0.0000	0.0000	1.0000	0.6072	0.3928	0.0000	0.0000	0.0000
2	3600	0.0666	0.0063	0.9271	0.9130	0.0870	0.0451	0.0412	0.0039
3	4502	0.1502	0.0150	0.8348	0.9093	0.0907	0.1062	0.0966	0.0096
4	5400	0.1923	0.0200	0.7877	0.9060	0.0940	0.1393	0.1262	0.0131
5	6600	0.2350	0.0232	0.7418	0.9103	0.0897	0.1729	0.1574	0.0155
6	8400	0.3083	0.0285	0.6632	0.9154	0.0846	0.2337	0.2140	0.0198
7	9600	0.3363	0.0344	0.6292	0.9072	0.0928	0.2614	0.2371	0.0243
8	10800	0.3837	0.0344	0.5819	0.9176	0.0824	0.3014	0.2766	0.0248
9	12600	0.4375	0.0394	0.5231	0.9174	0.0826	0.3538	0.3246	0.0292
10	14400	0.5018	0.0447	0.4534	0.9182	0.0818	0.4199	0.3856	0.0344
11	16200	0.5486	0.0474	0.4041	0.9205	0.0795	0.4697	0.4324	0.0373
12	18000	0.5981	0.0480	0.3539	0.9256	0.0744	0.5230	0.4841	0.0389
13	21600	0.6555	0.0540	0.2905	0.9239	0.0761	0.5947	0.5494	0.0453
14	32400	0.7674	0.0698	0.1628	0.9166	0.0834	0.7555	0.6925	0.0630
15	43200	0.8184	0.0782	0.1034	0.9128	0.0872	0.8389	0.7657	0.0732
16	72000	0.8674	0.0849	0.0477	0.9108	0.0892	0.9231	0.8408	0.0823
17	86400	0.8726	0.0862	0.0412	0.9101	0.0899	0.9332	0.8493	0.0839

Table C15. Run-15: results of XRD analysis (d_p > 425 μm).

#	t [sec]	area	fwhm	2 θ	d [Å]	area	fwhm	2 θ	d [Å]
		SILICON (111)				ALPHA (201)			
1	2951	827	0.0479	28.394	1901	1.675	0.1457	30.960	629
2	3600	788	0.0467	28.401	1950	13.007	0.1641	30.956	558
3	4500	677	0.0480	28.358	1897	22.13	0.1269	30.915	722
4	5400	674.2	0.0510	28.372	1785	31.19	0.1295	30.928	707
5	6600	687.3	0.0512	28.395	1778	39.31	0.1379	30.949	664
6	8400	666.5	0.0510	28.408	1785	53.54	0.1285	30.964	713
7	10800	668	0.0650	28.485	1401	71.69	0.1495	31.043	613
8	12600	608.6	0.0527	28.437	1728	79.84	0.1314	30.996	697
9	14400	548.1	0.0553	28.415	1647	86.21	0.1254	30.974	730
10	16200	473.3	0.0533	28.370	1708	89.09	0.1271	30.929	721
11	18000	485.5	0.0601	28.421	1515	105.77	0.1279	30.980	716
12	19800	480.9	0.0660	28.421	1380	116.43	0.1328	30.983	690
13	25200	318.9	0.0725	28.381	1256	135	0.1368	30.946	670
14	36000	250.7	0.0661	28.411	1378	164.88	0.1185	30.976	773
15	46800	194.6	0.0754	28.427	1208	189.77	0.1390	30.995	659
16	72000	101.71	0.0730	28.407	1247	204.9	0.1272	30.977	720
17	86400	78.46	0.0769	28.392	1184	205.5	0.1286	30.964	712

Table C15 (continued). Run-15: results of XRD analysis (d_p > 425 μm).

#	t [sec]	area	fwhm	2 θ	d [Å]	area	fwhm	2 θ	d [Å]
		ALPHA (102)				ALPHA (210)			
1	2951	2.404	0.1026	34.517	901	1.596	0.0451	35.299	2054
2	3600	13.648	0.1468	34.530	630	15.49	0.1626	35.301	570
3	4500	23.56	0.1545	34.482	598	24.52	0.1483	35.254	625
4	5400	28.89	0.1338	34.498	691	31.68	0.1417	35.271	654
5	6600	37.32	0.1466	34.518	631	40.14	0.1393	35.293	665
6	8400	48.99	0.1501	34.535	616	53	0.1300	35.301	713
7	10800	67.7	0.1565	34.612	591	69.91	0.1497	35.381	619
8	12600	74.27	0.1375	34.565	672	79.57	0.1335	35.334	694
9	14400	79.71	0.1310	34.542	706	85.44	0.1306	35.310	709
10	16200	84.12	0.1347	34.497	686	89.5	0.1301	35.266	712
11	18000	96.43	0.1373	34.547	673	106.81	0.1405	35.318	659
12	19800	107.39	0.1293	34.552	715	117.44	0.1404	35.320	660
13	25200	127.28	0.1404	34.515	658	137.29	0.1348	35.281	687
14	36000	154.8	0.1322	34.545	699	163.41	0.1278	35.314	725
15	46800	173.31	0.1380	34.562	670	188.19	0.1332	35.331	695
16	72000	184.12	0.1236	34.547	748	200.6	0.1296	35.313	715
17	86400	191.89	0.1363	34.534	678	200.97	0.1327	35.301	698

Table C15 (continued). Run-15: results of XRD analysis (d_p > 425 μm).

#	t [sec]	area	fwhm	2 θ	d [Å]	area	fwhm	2 θ	d [Å]
		BETA (101)				BETA (210)			
1	2951	0	****	****	****	0	****	****	****
2	3600	2.1734	0.1721	33.620	536	1.3078	0.1863	36.008	498
3	4500	3.927	0.2172	33.581	424	4.487	0.2635	35.933	352
4	5400	4.546	0.1340	33.592	688	3.053	0.1102	35.971	842
5	6600	5.598	0.1867	33.606	494	6.656	0.2556	35.983	363
6	8400	7.698	0.1783	33.624	517	7.02	0.1396	36.007	665
7	10800	9.649	0.1709	33.704	540	8.657	0.1384	36.077	671
8	12600	11.803	0.2215	33.662	416	10.441	0.1806	36.038	514
9	14400	12.478	0.1905	33.640	484	10.742	0.1686	36.016	551
10	16200	12.795	0.1905	33.593	484	11.562	0.1980	35.969	469
11	18000	14.653	0.1947	33.644	474	13.473	0.1936	36.025	479
12	19800	15.631	0.1763	33.651	523	14.096	0.1749	36.031	531
13	25200	17.89	0.2075	33.613	444	15.87	0.1564	35.990	593
14	36000	22.881	0.1687	33.638	547	21.527	0.1792	36.022	518
15	46800	28.52	0.1830	33.656	504	25.049	0.1724	36.042	538
16	72000	29.88	0.1515	33.638	609	25.94	0.1399	36.031	663
17	86400	33.36	0.1983	33.626	465	27.89	0.1671	36.009	555

Table C15 (continued). Run-15: results of XRD analysis (d_p > 425 μm).

#	t [sec]	W_α	W_β	W_{SI}	W_α'	W_β'	X	X_α	X_β
1	2951	0.0111	0.0000	0.9889	1.0000	0.0000	0.0067	0.0067	0.0000
2	3600	0.0830	0.0064	0.9106	0.9282	0.0718	0.0557	0.0517	0.0040
3	4500	0.1503	0.0170	0.8327	0.8983	0.1017	0.1077	0.0968	0.0110
4	5400	0.2002	0.0163	0.7835	0.9249	0.0751	0.1423	0.1316	0.0107
5	6600	0.2343	0.0240	0.7417	0.9071	0.0929	0.1730	0.1569	0.0161
6	8400	0.2987	0.0279	0.6734	0.9146	0.0854	0.2256	0.2063	0.0193
7	10800	0.3606	0.0310	0.6084	0.9208	0.0792	0.2788	0.2567	0.0221
8	12600	0.4042	0.0378	0.5579	0.9145	0.0855	0.3224	0.2949	0.0276
9	14400	0.4460	0.0406	0.5134	0.9166	0.0834	0.3627	0.3325	0.0302
10	16200	0.4872	0.0442	0.4686	0.9168	0.0832	0.4051	0.3714	0.0337
11	18000	0.5207	0.0466	0.4327	0.9178	0.0822	0.4405	0.4043	0.0362
12	19800	0.5454	0.0467	0.4079	0.9212	0.0788	0.4658	0.4291	0.0367
13	25200	0.6621	0.0547	0.2832	0.9237	0.0763	0.6032	0.5572	0.0460
14	36000	0.7323	0.0661	0.2016	0.9172	0.0828	0.7040	0.6457	0.0583
15	46800	0.7803	0.0748	0.1449	0.9125	0.0875	0.7800	0.7117	0.0682
16	72000	0.8448	0.0793	0.0759	0.9142	0.0858	0.8797	0.8042	0.0755
17	86400	0.8547	0.0862	0.0591	0.9084	0.0916	0.9053	0.8224	0.0830

Table C16. Run-16: results of XRD analysis (d_p > 425 μm).

#	t [sec]	area	fwhm	2 θ	d [Å]	area	fwhm	2 θ	d [Å]
		SILICON (111)				ALPHA (201)			
1	900	622.7	0.0635	28.371	1434	20.65	0.1343	30.932	682
2	2000	513.4	0.0592	28.363	1538	43.12	0.1193	30.921	768
3	4067	298.7	0.0725	28.339	1256	97.99	0.1260	30.905	727
4	5400	282.7	0.1058	28.434	861	136.95	0.1437	31.001	637
5	7200	179	0.0726	28.381	1254	148.5	0.1157	30.951	792
6	10800	88.9	0.0918	28.310	992	146.05	0.1330	30.884	689
7	14400	52.62	0.1061	28.243	858	124.44	0.1361	30.820	673
8	18000	44.72	0.0871	28.250	1045	126.74	0.1385	30.828	661
9	21600	63.84	0.0904	28.415	1007	189.79	0.1249	30.990	733
10	28800	52.71	0.0837	28.403	1088	188.3	0.1272	30.980	720
11	36000	28.67	0.0986	28.269	923	140.71	0.1343	30.851	682
12	43200	26.32	0.0981	28.268	928	141.34	0.1318	30.848	695
13	64800	19.33	0.0890	28.382	1023	181.65	0.1259	30.960	728
14	86400	12.486	0.0827	28.378	1101	184.13	0.1245	30.953	736
		ALPHA (102)				ALPHA (210)			
1	900	19.346	0.1288	34.492	718	22.35	0.1403	35.268	660
2	2000	39.71	0.1248	34.486	741	42.86	0.1214	35.257	763
3	4067	91.76	0.1252	34.474	738	96.33	0.1172	35.243	790
4	5400	123.41	0.1571	34.567	588	133.07	0.1439	35.336	644
5	7200	133.67	0.1187	34.520	779	145.43	0.1227	35.288	755
6	10800	134.68	0.1439	34.452	642	149	0.1365	35.223	678
7	14400	120.88	0.1582	34.388	584	131.84	0.1514	35.160	612
8	18000	118.03	0.1390	34.394	665	131.76	0.1363	35.164	679
9	21600	168.96	0.1247	34.557	741	190.42	0.1361	35.325	681
10	28800	169.57	0.1329	34.548	696	188.05	0.1334	35.315	694
11	36000	128.43	0.1316	34.418	702	147.14	0.1460	35.186	634
12	43200	133.33	0.1380	34.418	670	147.77	0.1475	35.186	628
13	64800	166.63	0.1256	34.528	736	175.33	0.1246	35.295	743
14	86400	170.73	0.1287	34.521	718	182.16	0.1271	35.289	729

Table C16 (continued). Run-16: results of XRD analysis (d_p > 425 μm).

#	t [sec]	area	fwhm	2 θ	d [Å]	area	fwhm	2 θ	d [Å]
		BETA (101)				BETA (210)			
1	900	3.0416	0.2549	33.602	362	2.49	0.1580	35.969	587
2	2000	5.091	0.2066	33.574	446	6.619	0.2715	35.952	342
3	4067	11.978	0.2102	33.571	439	8.586	0.1327	35.959	699
4	5400	15.545	0.2101	33.660	439	14.743	0.2120	36.047	438
5	7200	18.821	0.2010	33.613	459	16.419	0.1887	35.994	492
6	10800	18.728	0.1869	33.544	493	17.741	0.1856	35.934	500
7	14400	17.413	0.1764	33.480	523	13.979	0.2284	35.871	406
8	18000	19.684	0.2381	33.487	387	13.856	0.2548	35.877	364
9	21600	28.071	0.1901	33.648	485	24.956	0.2145	36.037	433
10	28800	27.955	0.2129	33.640	433	25.771	0.1997	36.030	465
11	36000	21.788	0.1839	33.506	501	16.893	0.2629	35.896	353
12	43200	23.946	0.2201	33.508	419	19.889	0.2295	35.901	404
13	64800	29.82	0.2162	33.619	427	27.103	0.2027	36.011	458
14	86400	33.08	0.2002	33.614	461	28.917	0.2115	36.001	439
		W_α	W_β	W_{Si}	W_α'	W_β'	X	X_α	X_β
1	900	0.1528	0.0131	0.8341	0.9210	0.0790	0.1067	0.0983	0.0084
2	2000	0.3079	0.0283	0.6638	0.9160	0.0840	0.2332	0.2136	0.0196
3	4067	0.6163	0.0436	0.3401	0.9339	0.0661	0.5381	0.5026	0.0356
4	5400	0.6896	0.0527	0.2577	0.9290	0.0710	0.6337	0.5887	0.0450
5	7200	0.7693	0.0628	0.1679	0.9245	0.0755	0.7485	0.6920	0.0565
6	10800	0.8380	0.0697	0.0924	0.9232	0.0768	0.8551	0.7895	0.0657
7	14400	0.8644	0.0695	0.0662	0.9256	0.0744	0.8945	0.8279	0.0665
8	18000	0.8690	0.0755	0.0555	0.9201	0.0799	0.9109	0.8380	0.0728
9	21600	0.8648	0.0826	0.0527	0.9129	0.0871	0.9153	0.8355	0.0798
10	28800	0.8712	0.0847	0.0442	0.9114	0.0886	0.9286	0.8463	0.0823
11	36000	0.8868	0.0805	0.0327	0.9167	0.0833	0.9467	0.8679	0.0788
12	43200	0.8814	0.0889	0.0297	0.9084	0.0916	0.9515	0.8643	0.0872
13	64800	0.8873	0.0956	0.0171	0.9028	0.0972	0.9719	0.8774	0.0945
14	86400	0.8881	0.1010	0.0109	0.8979	0.1021	0.9820	0.8817	0.1002

Table C17. Run-17: results of XRD analysis (d_p > 425 μm).

#	t [sec]	area	fwhm	2 θ	d [Å]	area	fwhm	2 θ	d [Å]
		SILICON (111)				ALPHA (201)			
1	620	794	0.0482	28.456	1889	4.931	0.1831	31.019	500
2	1243	674	0.0467	28.385	1950	13.418	0.1274	30.941	719
3	1901	570.1	0.0532	28.398	1711	46.03	0.1245	30.954	736
4	2671	480.2	0.0559	28.420	1629	81.56	0.1309	30.980	700
5	3536	340.8	0.0661	28.474	1378	99.39	0.1246	31.033	735
6	4780	250.7	0.0693	28.411	1314	114.94	0.1347	30.977	680
7	6670	138.4	0.0855	28.369	1065	121.06	0.1383	30.941	662
8	9570	117.4	0.0752	28.419	1211	144.64	0.1479	30.992	619
9	15000	104.72	0.0896	28.480	1016	141.28	0.1364	31.050	672
10	23100	86.53	0.0767	28.358	1187	127.24	0.1374	30.933	667
		ALPHA (102)				ALPHA (210)			
1	620	4.837	0.1264	34.578	731	6.257	0.1188	35.351	780
2	1243	12.956	0.1425	34.510	649	15.429	0.1531	35.277	605
3	1901	40.24	0.1263	34.524	732	47.6	0.1352	35.294	685
4	2671	72.45	0.1294	34.551	714	76.41	0.1280	35.320	724
5	3536	83.08	0.1385	34.605	668	94.4	0.1366	35.377	678
6	4780	97.58	0.1363	34.548	678	109.94	0.1422	35.318	651
7	6670	108.53	0.1385	34.513	667	115.06	0.1464	35.281	633
8	9570	132.87	0.1532	34.556	603	132.4	0.1520	35.328	609
9	15000	133.39	0.1438	34.619	643	134.01	0.1408	35.476	658
10	23100	118.43	0.1427	34.505	648	122.11	0.1342	35.270	690

Table C17 (continued). Run-17: results of XRD analysis (d_p > 425 μm).

#	t [sec]	area	fwhm	2 θ	d [Å]	area	fwhm	2 θ	d [Å]
		BETA (101)				BETA (210)			
1	620	0.425	0.0398	33.607	2317	0.756	0.3664	36.015	253
2	1243	2.1049	0.1824	33.593	506	1.1521	0.1856	36.008	500
3	1901	6.083	0.2135	33.616	432	4.225	0.1200	35.983	773
4	2671	12.154	0.2320	33.645	397	11.124	0.2256	36.020	411
5	3536	16.895	0.2344	33.714	393	12.082	0.1469	36.074	632
6	4780	22.513	0.2430	33.642	379	20.942	0.2291	36.020	405
7	6670	29.12	0.2394	33.609	385	25.785	0.2209	35.988	420
8	9570	34.64	0.2452	33.656	376	29.43	0.1875	36.040	495
9	15000	37.02	0.2097	33.718	440	32.46	0.2111	36.102	440
10	23100	33.69	0.2297	33.597	401	31.192	0.2179	35.982	426
		W_α	W_β	W_{si}	W_α'	W_β'	X	X_α	X_β
1	620	0.0331	0.0023	0.9646	0.9356	0.0644	0.0215	0.0202	0.0014
2	1243	0.0983	0.0073	0.8944	0.9309	0.0691	0.0662	0.0617	0.0046
3	1901	0.3013	0.0229	0.6758	0.9294	0.0706	0.2237	0.2079	0.0158
4	2671	0.4614	0.0467	0.4919	0.9081	0.0919	0.3829	0.3477	0.0352
5	3536	0.5792	0.0612	0.3596	0.9045	0.0955	0.5168	0.4674	0.0494
6	4780	0.6534	0.0885	0.2580	0.8807	0.1193	0.6333	0.5577	0.0756
7	6670	0.7321	0.1163	0.1515	0.8629	0.1371	0.7708	0.6651	0.1057
8	9570	0.7673	0.1199	0.1128	0.8649	0.1351	0.8253	0.7138	0.1115
9	15000	0.7679	0.1291	0.1031	0.8561	0.1439	0.8394	0.7186	0.1208
10	23100	0.7706	0.1345	0.0949	0.8514	0.1486	0.8514	0.7249	0.1265

Table C18. Run-18: results of XRD analysis (d_p > 425 μm and d_p < 355 μm).

#	t [sec]	area	fwhm	2 θ	d [Å]	area	fwhm	2 θ	d [Å]
d_p > 425 μm		SILICON (111)				ALPHA (201)			
1	1800	776	0.0517	28.420	1761	0.98	0.0807	30.980	1135
2	3600	639.6	0.0476	28.360	1913	10.607	0.1601	30.924	572
3	5400	546.1	0.0490	28.365	1858	36.74	0.2030	30.922	451
4	7200	517	0.0507	28.377	1796	53.54	0.2064	30.936	444
5	10800	404.6	0.0557	28.375	1635	81.42	0.1973	30.938	464
6	14400	332	0.0635	28.369	1434	97.3	0.1857	30.933	493
7	21600	244.5	0.0669	28.350	1361	106.85	0.1831	30.918	500
8	28800	241.4	0.0733	28.378	1242	121.18	0.1908	30.948	480
9	36000	231.2	0.0735	28.380	1239	122.98	0.1957	30.949	468
10	43200	222.1	0.0711	28.377	1281	125.2	0.1994	30.945	459
11	57600	232.9	0.0786	28.403	1158	132.27	0.1814	30.973	505
12	72000	208.1	0.0697	28.378	1306	127.27	0.1979	30.948	463
13	86400	194.6	0.0751	28.363	1212	124.78	0.1911	30.933	479
d_p < 355 μm									
2	3600	690	0.0496	28.388	1836	10.221	0.1831	30.944	500
3	5400	565.2	0.0645	28.372	1412	34.75	0.2083	30.932	440
4	7200	509.9	0.0503	28.382	1810	53.43	0.2203	30.941	416
5	10800	456.7	0.0634	28.414	1436	80.98	0.2072	30.976	442
6	14400	398.9	0.0630	28.425	1445	105.27	0.2033	30.987	451
7	21600	265.7	0.0679	28.371	1341	111.66	0.2008	30.938	456
8	28800	270.1	0.0689	28.413	1322	125.81	0.1995	30.978	459
9	36000	267.6	0.0704	28.437	1293	132.37	0.1823	31.003	502
10	43200	249.8	0.0712	28.421	1279	133.08	0.2031	30.988	451
13	86400	259.6	0.0942	28.528	967	131.42	0.1983	30.967	462

Table C18 (continued). Run-18: results of XRD analysis (d_p > 425 μm and d_p < 355 μm).

#	t [sec]	area	fwhm	2 θ	d [Å]	area	fwhm	2 θ	d [Å]
d_p > 425 μm		ALPHA (102)				ALPHA (210)			
1	1800	3.379	0.2929	34.435	316	1.348	0.0837	35.302	1107
2	3600	9.462	0.1376	34.487	672	12.306	0.2483	35.266	373
3	5400	33.36	0.2130	34.492	434	39.54	0.2246	35.269	412
4	7200	49.72	0.2029	34.505	456	52.89	0.2204	35.278	420
5	10800	73.1	0.1825	34.507	506	80.68	0.1979	35.276	468
6	14400	89.94	0.1966	34.503	470	95.69	0.1896	35.273	489
7	21600	101.95	0.1870	34.488	494	111.76	0.1930	35.258	480
8	28800	113.4	0.1873	34.519	493	121.71	0.1949	35.289	475
9	36000	113.33	0.1958	34.518	472	123.95	0.1914	35.287	484
10	43200	117.14	0.1883	34.516	491	124.79	0.1931	35.286	480
11	57600	119.08	0.1987	34.542	465	132.87	0.1954	35.312	474
12	72000	117.77	0.1833	34.517	504	129.67	0.1975	35.286	469
13	86400	112.74	0.1763	34.502	524	125.57	0.1918	35.274	483
d_p < 355 μm									
2	3600	10.278	0.2544	34.505	363	12.625	0.2063	35.294	449
3	5400	32.38	0.2112	34.498	438	37.15	0.2253	35.277	411
4	7200	49.7	0.2057	34.512	449	52.98	0.2025	35.283	457
5	10800	76.29	0.2136	34.544	433	85.06	0.2127	35.315	436
6	14400	96.4	0.1930	34.556	479	104.73	0.1963	35.329	472
7	21600	102.97	0.1909	34.508	484	113.43	0.2033	35.279	456
8	28800	116.28	0.1914	34.551	483	129.91	0.2085	35.320	444
9	36000	121.1	0.1965	34.575	470	132.47	0.2169	35.344	427
10	43200	120.4	0.2095	34.558	441	131.83	0.1934	35.328	479
13	86400	120.49	0.1967	34.536	470	132.91	0.2077	35.306	446

Table C18 (continued). Run-18: results of XRD analysis (d_p > 425 μm and d_p < 355 μm).

#	t [sec]	area	fwhm	2 θ	d [Å]	area	fwhm	2 θ	d [Å]
d_p > 425 μm			BETA	(101)			BETA	(210)	
1	1800	0.235	0.0122	33.573	7557	2.4682	0.3297	36.187	282
2	3600	1.7626	0.1764	33.596	523	0.8565	0.2345	35.984	396
3	5400	4.05	0.1411	33.607	653	4.501	0.2224	35.974	417
4	7200	7.8	0.2288	33.613	403	9.76	0.3888	35.960	239
5	10800	13.341	0.2736	33.604	337	10.193	0.2923	35.981	318
6	14400	19.472	0.2696	33.599	342	17.973	0.3156	35.968	294
7	21600	26.384	0.2667	33.582	346	24.529	0.2766	35.963	336
8	28800	34.789	0.2840	33.612	325	30.675	0.2711	36.001	342
9	36000	36.123	0.2699	33.614	342	31.49	0.2584	35.999	359
10	43200	35.908	0.2745	33.611	336	32.142	0.2670	35.998	348
11	57600	40.05	0.2658	33.634	347	36.835	0.2687	36.023	345
12	72000	39.79	0.2776	33.609	332	36.279	0.2658	35.995	349
13	86400	38.3	0.2660	33.601	347	32.156	0.2201	35.980	422
d_p < 355 μm									
2	3600	0.8912	0.1065	33.681	866	1.5225	0.3077	35.943	302
3	5400	5.337	0.3024	33.605	305	4.255	0.3233	35.945	287
4	7200	6.707	0.1909	33.609	483	5.372	0.2684	35.985	346
5	10800	12.35	0.2538	33.642	363	9.826	0.1963	36.012	473
6	14400	20.126	0.2932	33.658	315	18.546	0.2917	36.031	318
7	21600	26.772	0.2677	33.600	344	25.793	0.2759	35.976	336
8	28800	35.764	0.2761	33.650	334	31.051	0.2681	36.027	346
9	36000	37.013	0.2592	33.672	356	33.79	0.2654	36.052	350
10	43200	39.48	0.2655	33.651	347	36.047	0.2805	36.030	331
13	86400	41.69	0.2750	33.633	335	38.384	0.2841	36.013	327

Table C18 (continued). Run-18: results of XRD analysis (d_p > 425 μm and d_p < 355 μm).

#	t [sec]	W_α	W_β	W_{Si}	W_α'	W_β'	X	X_α	X_β
d_p > 425 μm									
1	1800	0.0069	0.0026	0.9905	0.7299	0.2701	0.0057	0.0042	0.0015
2	3600	0.0834	0.0065	0.9101	0.9278	0.0722	0.0560	0.0519	0.0040
3	5400	0.2655	0.0201	0.7144	0.9295	0.0705	0.1936	0.1800	0.0137
4	7200	0.3498	0.0387	0.6115	0.9003	0.0997	0.2762	0.2486	0.0275
5	10800	0.5003	0.0495	0.4502	0.9099	0.0901	0.4232	0.3850	0.0381
6	14400	0.5720	0.0747	0.3534	0.8846	0.1154	0.5236	0.4631	0.0604
7	21600	0.6376	0.0983	0.2642	0.8664	0.1336	0.6259	0.5423	0.0836
8	28800	0.6490	0.1169	0.2341	0.8473	0.1527	0.6627	0.5616	0.1012
9	36000	0.6558	0.1209	0.2232	0.8443	0.1557	0.6763	0.5711	0.1053
10	43200	0.6653	0.1211	0.2137	0.8460	0.1540	0.6885	0.5825	0.1060
11	57600	0.6595	0.1302	0.2103	0.8351	0.1649	0.6929	0.5786	0.1142
12	72000	0.6689	0.1330	0.1980	0.8341	0.1659	0.7086	0.5911	0.1176
13	86400	0.6786	0.1298	0.1916	0.8394	0.1606	0.7170	0.6019	0.1151
d_p < 355 μm									
2	3600	0.0752	0.0051	0.9196	0.9362	0.0638	0.0499	0.0467	0.0032
3	5400	0.2479	0.0221	0.7300	0.9181	0.0819	0.1818	0.1669	0.0149
4	7200	0.3566	0.0271	0.6162	0.9293	0.0707	0.2722	0.2530	0.0193
5	10800	0.4739	0.0421	0.4839	0.9183	0.0817	0.3904	0.3585	0.0319
6	14400	0.5523	0.0687	0.3790	0.8894	0.1106	0.4960	0.4412	0.0549
7	21600	0.6297	0.0990	0.2713	0.8642	0.1358	0.6173	0.5335	0.0838
8	28800	0.6393	0.1122	0.2485	0.8506	0.1494	0.6449	0.5486	0.0963
9	36000	0.6465	0.1168	0.2367	0.8470	0.1530	0.6595	0.5586	0.1009
10	43200	0.6521	0.1263	0.2216	0.8377	0.1623	0.6784	0.5683	0.1101
13	86400	0.6402	0.1309	0.2290	0.8303	0.1697	0.6692	0.5556	0.1136

Table C19. Run-19: results of XRD analysis (d_p > 425 μm).

#	t [sec]	area	fwhm	2 θ	d [Å]	area	fwhm	2 θ	d [Å]
		SILICON (111)				ALPHA (201)			
1	5400	592.4	0.0495	28.340	1839	14.217	0.1953	30.899	469
2	7200	488.2	0.0536	28.318	1698	29.811	0.2050	30.878	447
3	10800	540.9	0.0531	28.397	1715	56.75	0.2000	30.957	458
4	14400	500.5	0.0533	28.427	1708	80.36	0.2051	30.984	447
5	18000	362.8	0.0550	28.355	1655	84.88	0.2121	30.918	432
6	21600	353.7	0.0588	28.386	1548	103.96	0.1961	30.949	467
7	28800	245.3	0.0749	28.329	1215	109.71	0.1973	30.896	464
8	36000	211.9	0.0624	28.356	1459	127.79	0.1739	30.922	527
9	43200	188.4	0.0688	28.380	1323	147.08	0.1936	30.947	473
10	50400	147.4	0.0690	28.365	1319	148.2	0.1902	30.933	482
11	61200	121.4	0.0707	28.349	1288	149.47	0.1884	30.916	486
12	72000	110.9	0.0702	28.364	1297	160.55	0.1903	30.934	481
13	86400	100.32	0.0756	28.386	1204	171.66	0.1785	30.958	513
		ALPHA (102)				ALPHA (210)			
1	5400	14.774	0.2200	34.465	420	14.794	0.2084	35.243	444
2	7200	29.216	0.2090	34.450	442	34.03	0.2351	35.222	394
3	10800	52.75	0.1948	34.524	475	56.82	0.1990	35.296	465
4	14400	74.97	0.1910	34.554	484	78.46	0.2155	35.326	430
5	18000	78.05	0.1968	34.485	470	87.12	0.1985	35.259	467
6	21600	95.76	0.1963	34.518	471	105.69	0.1918	35.289	483
7	28800	102.56	0.2055	34.466	450	112.33	0.2024	35.235	458
8	36000	121.74	0.1877	34.493	492	131.68	0.1808	35.264	512
9	43200	136.46	0.1856	34.519	498	149.17	0.1894	35.287	489
10	50400	132.86	0.1730	34.503	534	147.76	0.1760	35.272	526
11	61200	137.37	0.1807	34.487	511	150.27	0.1838	35.259	504
12	72000	149.21	0.1888	34.506	490	158.86	0.1899	35.274	488
13	86400	158.68	0.1786	34.530	518	172.84	0.1898	35.3	488

Table C19 (continued). Run-19: results of XRD analysis (d_p > 425 μm).

#	t [sec]	area	fwhm	2 θ	d [Å]	area	fwhm	2 θ	d [Å]
		BETA (101)				BETA (210)			
1	5400	1.106	0.2139	33.564	431	0.8665	0.1128	35.956	823
2	7200	4.291	0.3633	33.557	254	2.96	0.2398	35.928	387
3	10800	7.73	0.2389	33.633	386	6.953	0.2057	35.99	451
4	14400	9.429	0.2118	33.671	435	13.248	0.3443	36.028	270
5	18000	11.507	0.2522	33.592	366	8.013	0.1709	35.947	543
6	21600	12.944	0.2476	33.617	372	12.529	0.2488	35.983	373
7	28800	14.167	0.2077	33.555	444	12.155	0.2028	35.941	458
8	36000	18.54	0.2397	33.596	385	14.907	0.1948	35.975	476
9	43200	22.97	0.2523	33.610	365	17.582	0.1984	35.998	468
10	50400	22.309	0.2293	33.595	402	19.478	0.2066	35.981	449
11	61200	20.632	0.2567	33.579	359	20.779	0.2538	35.969	366
12	72000	26.038	0.2583	33.603	357	26.349	0.2695	35.978	344
13	86400	28.463	0.2529	33.624	365	25.536	0.2226	36.012	417
		W_α	W_β	W_{SI}	W_α'	W_β'	X	X_α	X_β
1	5400	0.1164	0.0050	0.8785	0.9586	0.0414	0.0767	0.0735	0.0032
2	7200	0.2476	0.0184	0.7341	0.9309	0.0691	0.1787	0.1664	0.0123
3	10800	0.3556	0.0308	0.6136	0.9202	0.0798	0.2744	0.2525	0.0219
4	14400	0.4498	0.0430	0.5072	0.9127	0.0873	0.3685	0.3363	0.0322
5	18000	0.5404	0.0413	0.4182	0.9290	0.0710	0.4552	0.4228	0.0323
6	21600	0.5890	0.0482	0.3628	0.9244	0.0756	0.5133	0.4745	0.0388
7	28800	0.6738	0.0534	0.2728	0.9266	0.0734	0.6156	0.5704	0.0452
8	36000	0.7217	0.0616	0.2167	0.9213	0.0787	0.6847	0.6308	0.0539
9	43200	0.7554	0.0694	0.1752	0.9159	0.0841	0.7387	0.6766	0.0621
10	50400	0.7834	0.0755	0.1411	0.9121	0.0879	0.7852	0.7162	0.0690
11	61200	0.8063	0.0751	0.1186	0.9148	0.0852	0.8170	0.7474	0.0696
12	72000	0.8097	0.0891	0.1013	0.9009	0.0991	0.8420	0.7586	0.0835
13	86400	0.8256	0.0870	0.0874	0.9047	0.0953	0.8625	0.7803	0.0822

Table C20. Run-20: results of XRD analysis (d_p > 425 μm and d_p < 355 μm).

#	t [sec]	area	fwhm	2 θ	d [Å]	area	fwhm	2 θ	d [Å]
d_p > 425 μm		SILICON (111)				ALPHA (201)			
1	536	536	596.6	0.0550	28.373	1655	22.36	0.1275	30.92
2	1136	1136	498.9	0.0558	28.362	1632	44.2	0.1156	30.91
3	1736	1736	417.4	0.0552	28.375	1649	74.64	0.1140	30.93
4	2530	2530	276.5	0.0608	28.359	1497	105.5	0.1154	30.92
5	3760	3760	192.2	0.0717	28.414	1270	148.22	0.1214	30.98
6	5400	5400	142.9	0.0793	28.397	1148	160.54	0.1336	30.96
7	7200	7200	111.78	0.0771	28.366	1181	158.64	0.1246	30.93
8	10800	10800	111.84	0.0786	28.396	1158	173.05	0.1314	30.97
9	14400	14400	87.99	0.0768	28.321	1185	146.53	0.1255	30.89
10	21600	21600	56.85	0.0853	28.219	1067	114.24	0.1366	30.79
11	28800	28800	59.46	0.1004	28.236	907	121.87	0.1459	30.81
12	36000	36000	68.25	0.0863	28.297	1055	150.8	0.1382	30.87
13	43200	43200	64.59	0.1053	28.307	865	152.67	0.1577	30.88
14	67260	67260	45.2	0.0873	28.286	1043	147.81	0.1316	30.86
15	76920	76920	44.71	0.0811	28.339	1123	174.84	0.1280	30.91
16	86400	86400	40.5	0.0977	28.324	932	172.92	0.1403	30.89
d_p < 355 μm									
1	536	536	564.7	0.0562	28.369	1620	20.12	0.1467	30.92
2	1136	1136	468.7	0.0526	28.354	1731	40.78	0.1164	30.91
3	1736	1736	356.8	0.0616	28.336	1478	65.76	0.1205	30.89
4	2530	2530	235.2	0.0960	28.303	948	92.22	0.1455	30.87
5	3760	3760	190.7	0.0879	28.350	1036	120.71	0.1367	30.91
7	7200	7200	108.2	0.0846	28.383	1076	152.41	0.1358	30.95
11	28800	28800	73.43	0.0735	28.361	1239	151.53	0.1248	30.93
14	67260	67260	37.24	0.0921	28.295	988	142.32	0.1447	30.87
16	86400	86400	37.83	0.0801	28.436	1137	194.8	0.1268	31.01

Table C20 (continued). Run-20: results of XRD analysis (d_p > 425 μm and d_p < 355 μm).

#	t [sec]	area	fwhm	2 θ	d [Å]	area	fwhm	2 θ	d [Å]
d_p > 425 μm		ALPHA (102)				ALPHA (210)			
1	536	21.373	0.1454	34.493	636	24.38	0.1483	35.267	625
2	1136	41.14	0.1226	34.488	754	44.86	0.1289	35.255	719
3	1736	69.4	0.1212	34.504	763	76.8	0.1232	35.274	752
4	2530	95.71	0.1146	34.493	807	104.5	0.1187	35.261	780
5	3760	132.05	0.1189	34.550	777	147.02	0.1299	35.317	713
6	5400	147.89	0.1316	34.537	702	161.18	0.1324	35.304	700
7	7200	144.69	0.1323	34.509	699	157.28	0.1314	35.277	705
8	10800	157.27	0.1335	34.538	692	163.74	0.1272	35.304	728
9	14400	132.28	0.1229	34.460	752	152.32	0.1353	35.228	684
10	21600	110.24	0.1387	34.461	666	117.67	0.1334	35.131	694
11	28800	116.71	0.1496	34.379	618	131.46	0.1495	35.151	619
12	36000	139.02	0.1346	34.442	687	154.5	0.1432	35.211	647
13	43200	143.4	0.1553	34.451	595	156.2	0.1513	35.219	612
14	67260	139.88	0.1318	34.431	701	151.44	0.1344	35.201	689
15	76920	158.52	0.1293	34.482	715	170.1	0.1259	35.251	736
16	86400	160.98	0.1377	34.465	671	174.16	0.1365	35.233	678
d_p < 355 μm									
1	536	17.366	0.1190	34.494	777	20.889	0.1513	35.256	612
2	1136	39.71	0.1472	34.477	628	44.56	0.1454	35.250	637
3	1736	62.42	0.1269	34.462	728	68.9	0.1258	35.235	736
4	2530	87.07	0.1455	34.440	635	93.98	0.1388	35.210	667
5	3760	111.85	0.1388	34.489	666	122.08	0.1371	35.256	676
7	7200	138.99	0.1356	34.523	682	151.1	0.1355	35.293	684
11	28800	139.55	0.1288	34.504	718	149.55	0.1281	35.272	723
14	67260	134.43	0.1426	34.441	648	142.1	0.1347	35.208	688
16	86400	176.47	0.1311	34.580	705	191.44	0.1326	35.349	699

Table C20 (continued). Run-20: results of XRD analysis (d_p > 425 μm and d_p < 355 μm).

#	t [sec]	area	fwhm	2 θ	d [Å]	area	fwhm	2 θ	d [Å]
d_p > 425 μm		BETA (101)				BETA (210)			
1	536	2.3192	0.2127	33.578	433	2.0697	0.1696	35.963	547
2	1136	5.328	0.2018	33.586	457	4.005	0.1608	35.979	577
3	1736	8.042	0.1834	33.590	503	7.102	0.1852	35.981	501
4	2530	9.947	0.1526	33.584	604	9.198	0.1323	35.970	701
5	3760	19.07	0.1976	33.644	467	17.991	0.1986	36.033	467
6	5400	23.199	0.1762	33.628	523	20.393	0.1755	36.015	529
7	7200	24.125	0.2211	33.603	417	20.107	0.1568	35.992	592
8	10800	25.771	0.1909	33.630	483	25.771	0.1909	36.017	486
9	14400	22.166	0.1771	33.547	521	21.38	0.1828	35.944	508
10	21600	17.136	0.1767	33.456	522	15.898	0.2339	35.850	397
11	28800	18.49	0.2041	33.470	452	18.207	0.2325	35.857	399
12	36000	23.602	0.2304	33.531	400	20.839	0.2243	35.922	414
13	43200	24.414	0.2002	33.542	460	23.467	0.2294	35.927	405
14	67260	25.164	0.1926	33.520	479	22.636	0.1941	35.914	478
15	76920	28.731	0.2037	33.575	453	26.42	0.1727	35.962	537
16	86400	31.22	0.1975	33.554	467	25.62	0.2251	35.943	412
d_p < 355 μm									
1	536	1.2495	0.2801	33.603	329	1.059	0.2658	35.948	349
2	1136	4.505	0.2314	33.567	398	4.03	0.2420	35.947	383
3	1736	6.971	0.1770	33.553	521	6.297	0.2644	35.925	351
4	2530	10.012	0.1994	33.531	462	10.215	0.2291	35.913	405
5	3760	15.97	0.1988	33.580	464	15.24	0.1844	35.962	503
7	7200	24.881	0.2233	33.616	413	22.061	0.2121	36.007	438
11	28800	22.981	0.1634	33.593	564	20.526	0.1545	35.982	601
14	67260	25.147	0.2016	33.531	457	22.88	0.2126	35.920	436
16	86400	35.88	0.2008	33.678	459	29.64	0.1693	36.059	548

Table C20 (continued). Run-20: results of XRD analysis (d_p > 425 μm and d_p < 355 μm).

#	t [sec]	W_α	W_β	W_{St}	W_α'	W_β'	X	X_α	X_β
d_p > 425 μm									
1	536	0.1697	0.0105	0.8198	0.9416	0.0584	0.1166	0.1098	0.0068
2	1136	0.3211	0.0225	0.6563	0.9344	0.0656	0.2393	0.2236	0.0157
3	1736	0.4809	0.0322	0.4869	0.9372	0.0628	0.3876	0.3633	0.0243
4	2530	0.6509	0.0403	0.3089	0.9417	0.0583	0.5734	0.5400	0.0334
5	3760	0.7572	0.0651	0.1778	0.9209	0.0791	0.7353	0.6771	0.0582
6	5400	0.7985	0.0729	0.1287	0.9164	0.0836	0.8026	0.7355	0.0671
7	7200	0.8181	0.0775	0.1044	0.9134	0.0866	0.8375	0.7650	0.0725
8	10800	0.8191	0.0851	0.0958	0.9059	0.0941	0.8500	0.7700	0.0800
9	14400	0.8280	0.0820	0.0900	0.9099	0.0901	0.8586	0.7812	0.0773
10	21600	0.8447	0.0792	0.0761	0.9143	0.0857	0.8794	0.8040	0.0754
11	28800	0.8446	0.0808	0.0746	0.9127	0.0873	0.8816	0.8047	0.0770
12	36000	0.8475	0.0830	0.0695	0.9108	0.0892	0.8895	0.8101	0.0794
13	43200	0.8475	0.0876	0.0649	0.9063	0.0937	0.8964	0.8124	0.0840
14	67260	0.8609	0.0914	0.0477	0.9040	0.0960	0.9231	0.8345	0.0886
15	76920	0.8659	0.0940	0.0401	0.9021	0.0979	0.9350	0.8434	0.0916
16	86400	0.8680	0.0952	0.0368	0.9011	0.0989	0.9402	0.8472	0.0930
d_p < 355 μm									
1	536	0.1634	0.0064	0.8302	0.9624	0.0376	0.1094	0.1053	0.0041
2	1136	0.3178	0.0208	0.6614	0.9385	0.0615	0.2352	0.2207	0.0145
3	1736	0.4883	0.0319	0.4797	0.9386	0.0614	0.3944	0.3702	0.0242
4	2530	0.6519	0.0471	0.3010	0.9326	0.0674	0.5824	0.5431	0.0393
5	3760	0.7287	0.0629	0.2084	0.9205	0.0795	0.6952	0.6400	0.0552
7	7200	0.8109	0.0849	0.1042	0.9052	0.0948	0.8377	0.7583	0.0794
11	28800	0.8438	0.0822	0.0740	0.9113	0.0887	0.8825	0.8042	0.0783
14	67260	0.8623	0.0969	0.0409	0.8990	0.1010	0.9338	0.8395	0.0943
16	86400	0.8693	0.1002	0.0306	0.8967	0.1033	0.9501	0.8520	0.0982

Table C21. Run-21: results of XRD analysis (d_p > 425 μm).

#	t [sec]	area	fwhm	2 θ	d [Å]	area	fwhm	2 θ	d [Å]
		SILICON (111)				ALPHA (201)			
1	2556	587.4	0.0551	28.325	1652	8.199	0.1793	30.876	511
2	3619	517	0.0513	28.308	1775	20.842	0.1592	30.867	575
3	5447	447	0.0585	28.317	1556	42.27	0.2061	30.878	444
4	7200	488.4	0.0640	28.386	1423	69.57	0.1813	30.951	505
5	8400	263.3	0.0658	28.323	1384	95.47	0.1647	30.891	556
6	9600	120.6	0.0717	28.315	1270	127.69	0.1623	30.888	564
7	10240	53.04	0.0827	28.263	1101	124.19	0.1769	30.838	518
8	10796	37.61	0.0789	28.325	1154	149.76	0.1556	30.900	589
9	11402	23.41	0.0832	28.321	1094	134	0.1638	30.899	559
		ALPHA (102)				ALPHA (210)			
1	2556	7.029	0.1556	34.452	594	8.628	0.1829	35.221	506
2	3619	20.456	0.1724	34.441	536	20.018	0.1391	35.217	666
3	5447	39.07	0.2134	34.443	433	45.71	0.1963	35.220	472
4	7200	66.26	0.1786	34.519	518	72.38	0.1908	35.290	485
5	8400	88.79	0.1732	34.459	534	100.25	0.1847	35.228	501
6	9600	118.71	0.1819	34.457	508	133.46	0.1861	35.227	498
7	10240	117.25	0.1617	34.411	571	129.24	0.1765	35.180	525
8	10796	138.15	0.1823	34.470	507	152.4	0.1657	35.238	559
9	11402	123.22	0.1659	34.469	557	135.64	0.1639	35.237	565

Table C21 (continued). Run-21: results of XRD analysis (d_p > 425 μm).

#	t [sec]	area	fwhm	2 θ	d [Å]	area	fwhm	2 θ	d [Å]
		BETA (101)				BETA (210)			
1	2556	1.0542	0.3802	33.504	242	0.6175	0.0802	35.899	1157
2	3619	2.275	0.1200	33.512	768	2.3771	0.3817	35.861	243
3	5447	4.034	0.1169	33.546	789	5.009	0.2484	35.924	374
4	7200	11.599	0.2507	33.609	368	11.661	0.2230	35.982	416
5	8400	20.728	0.2257	33.552	408	19.412	0.2458	35.942	378
6	9600	41.34	0.2174	33.552	424	38.16	0.2098	35.939	442
7	10240	44.97	0.1899	33.500	485	44.67	0.2048	35.893	453
8	10796	58.6	0.1958	33.560	471	54.23	0.1868	35.945	497
9	11402	49.95	0.1702	33.554	542	48.57	0.1875	35.946	495
		W_α	W_β	W_{SI}	W_α'	W_β'	X	X_α	X_β
1	2556	0.0712	0.0049	0.9239	0.9354	0.0646	0.0472	0.0441	0.0030
2	3619	0.1797	0.0134	0.8070	0.9308	0.0692	0.1256	0.1169	0.0087
3	5447	0.3352	0.0231	0.6417	0.9354	0.0646	0.2511	0.2349	0.0162
4	7200	0.4202	0.0456	0.5342	0.9021	0.0979	0.3437	0.3101	0.0337
5	8400	0.6110	0.0839	0.3051	0.8792	0.1208	0.5777	0.5079	0.0698
6	9600	0.7273	0.1483	0.1244	0.8306	0.1694	0.8087	0.6717	0.1370
7	10240	0.7618	0.1793	0.0589	0.8095	0.1905	0.9056	0.7331	0.1725
8	10796	0.7712	0.1938	0.0351	0.7992	0.2008	0.9429	0.7536	0.1893
9	11402	0.7825	0.1927	0.0248	0.8024	0.1976	0.9595	0.7699	0.1896

Table C22. Run-22: results of XRD analysis (d_p > 425 μm).

#	t [sec]	area	fwhm	2 θ	d [Å]	area	fwhm	2 θ	d [Å]
		SILICON (111)				ALPHA (201)			
1	630	452.3	0.0648	28.255	1405	21.49	0.1269	30.811	722
2	1800	183.6	0.0697	28.279	1306	103.26	0.1202	30.847	762
3	2991	100.4	0.0782	28.367	1164	162.5	0.1227	30.938	746
4	3302	63.15	0.0843	28.279	1080	140.56	0.1257	30.851	728
5	3633	51.57	0.0832	28.282	1094	141.9	0.1192	30.856	768
6	4003	37.83	0.0763	28.259	1193	136.3	0.1259	30.834	727
7	4621	34.69	0.0797	28.291	1142	157.34	0.1251	30.873	732
8	5601	26.72	0.0767	28.326	1187	169.01	0.1199	30.899	764
9	7766	14.384	0.1102	28.307	826	164.04	0.1308	30.887	700
10	8400	10.384	0.1089	28.286	836	151.03	0.1186	30.867	772
		ALPHA (102)				ALPHA (210)			
1	630	20.67	0.1268	34.379	729	23.16	0.1319	35.150	702
2	1800	96.85	0.1214	34.415	761	104.71	0.1235	35.185	750
3	2991	147.8	0.1238	34.505	747	156.62	0.1224	35.274	757
4	3302	130.66	0.1269	34.420	728	142.48	0.1267	35.190	731
5	3633	133.75	0.1275	34.425	725	146.89	0.1274	35.194	727
6	4003	128.72	0.1337	34.403	691	138.39	0.1215	35.174	762
7	4621	144.95	0.1249	34.441	740	160.4	0.1326	35.211	698
8	5601	155.48	0.1197	34.467	772	164.79	0.1195	35.236	775
9	7766	152.76	0.1364	34.456	678	167.39	0.1363	35.225	679
10	8400	143.32	0.1306	34.437	708	154.82	0.1229	35.206	754

Table C22 (continued). Run-22: results of XRD analysis (d_p > 425 μm).

#	t [sec]	area	fwhm	2 θ	d [Å]	area	fwhm	2 θ	d [Å]
		BETA (101)				BETA (210)			
1	630	1.8865	0.2309	33.470	399	2.7208	0.1810	35.830	513
2	1800	20.694	0.1896	33.511	486	19.552	0.1992	35.898	466
3	2991	35.38	0.1802	33.596	512	33.29	0.1703	35.989	545
4	3302	33.88	0.1785	33.509	516	31.72	0.1736	35.902	534
5	3633	34.45	0.1691	33.515	545	30.86	0.1697	35.906	547
6	4003	33.32	0.1751	33.490	526	31.03	0.1755	35.886	529
7	4621	39.08	0.1853	33.531	498	36.68	0.1941	35.925	478
8	5601	40.8	0.1860	33.554	496	37.52	0.1896	35.950	489
9	7766	42.07	0.1770	33.546	521	38.26	0.1924	35.940	482
10	8400	36.11	0.1439	33.528	641	36.57	0.1745	35.892	532
		W_α	W_β	W_{SI}	W_α'	W_β'	X	X_α	X_β
1	630	0.2050	0.0139	0.7811	0.9363	0.0637	0.1441	0.1349	0.0092
2	1800	0.6891	0.0890	0.2219	0.8856	0.1144	0.6781	0.6005	0.0776
3	2991	0.7950	0.1160	0.0889	0.8726	0.1274	0.8602	0.7506	0.1096
4	3302	0.8086	0.1256	0.0658	0.8655	0.1345	0.8951	0.7747	0.1204
5	3633	0.8221	0.1238	0.0541	0.8691	0.1309	0.9131	0.7936	0.1195
6	4003	0.8291	0.1292	0.0417	0.8651	0.1349	0.9325	0.8067	0.1257
7	4621	0.8330	0.1337	0.0333	0.8617	0.1383	0.9458	0.8150	0.1308
8	5601	0.8426	0.1333	0.0241	0.8634	0.1366	0.9605	0.8293	0.1312
9	7766	0.8487	0.1378	0.0135	0.8603	0.1397	0.9778	0.8412	0.1366
10	8400	0.8546	0.1348	0.0106	0.8638	0.1362	0.9824	0.8486	0.1338

Table C23. Run-23: results of XRD analysis (d_p > 425 μm).

#	t [sec]	area	fwhm	2 θ	d [Å]	area	fwhm	2 θ	d [Å]
		SILICON (111)				ALPHA (201)			
1	1060	633.7	0.0664	28.434	1371	45.24	0.1172	30.987	782
2	1815	506.9	0.0525	28.408	1734	70.89	0.1095	30.963	836
3	2700	419.1	0.0611	28.447	1490	106.65	0.1037	31.008	883
4	3396	178.5	0.0678	28.435	1343	168.4	0.1069	31.005	857
5	3976	96.61	0.1145	28.469	795	178.16	0.1445	31.041	634
6	4355	79.52	0.0960	28.466	949	164.88	0.1334	31.038	687
7	4705	61.54	0.0723	28.489	1260	161.23	0.1282	31.056	715
8	5087	52.45	0.0715	28.426	1274	189.3	0.1160	30.999	790
9	5978	38.7	0.0717	28.377	1270	181.3	0.1126	30.951	813
10	7295	26.74	0.0800	28.500	1138	174.9	0.1049	31.076	873
11	9605	14.88	0.0812	28.398	1121	178.4	0.1058	30.974	866
12	11700	11.166	0.0918	28.400	992	173.4	0.1076	30.974	851
		ALPHA (102)				ALPHA (210)			
1	1060	35.07	0.1390	34.555	665	44.17	0.1148	35.326	807
2	1815	52.53	0.1133	34.533	816	57.47	0.1059	35.300	875
3	2700	87.05	0.1052	34.579	879	92.97	0.1140	35.342	813
4	3396	136.07	0.1054	34.566	877	142.86	0.1185	35.349	782
5	3976	138.97	0.1675	34.618	552	155.15	0.1447	35.378	640
6	4355	148.17	0.1320	34.606	700	169	0.1263	35.373	734
7	4705	166.16	0.1120	34.630	826	180.7	0.1171	35.394	791
8	5087	153.99	0.1247	34.565	741	162.53	0.1216	35.335	762
9	5978	141.51	0.0992	34.520	932	162.21	0.1153	35.289	803
10	7295	161.02	0.1184	34.645	781	180.74	0.1201	35.413	772
11	9605	163.44	0.1131	34.544	817	179.7	0.1145	35.311	809
12	11700	166.06	0.1147	34.544	806	179.4	0.1157	35.311	801

Table C23 (continued). Run-23: results of XRD analysis (d_p > 425 μm).

#	t [sec]	area	fwhm	2 θ	d [Å]	area	fwhm	2 θ	d [Å]
		BETA (101)				BETA (210)			
1	1060	6.163	0.1888	33.650	488	3.408	0.1061	36.036	875
2	1815	9.092	0.2046	33.625	451	6.786	0.1897	36.010	489
3	2700	9.987	0.2400	33.654	384	11.113	0.1467	36.046	633
4	3396	31.99	0.1452	33.661	635	25.74	0.1357	36.039	684
5	3976	34.49	0.1736	33.707	531	31.18	0.1662	36.089	559
6	4355	37.87	0.1592	33.698	579	37.43	0.1661	36.084	559
7	4705	38.15	0.1463	33.720	630	31.13	0.1244	36.106	746
8	5087	43.36	0.1597	33.660	577	30.56	0.1328	36.046	699
9	5978	36.27	0.1646	33.610	560	37.88	0.1465	35.998	634
10	7295	40.02	0.1415	33.735	652	39.16	0.1489	36.120	624
11	9605	42.59	0.1418	33.637	650	40.53	0.1452	36.023	639
12	11700	40.02	0.1265	33.637	729	41.24	0.1548	36.022	600
		W_α	W_β	W_{Si}	W_α'	W_β'	X	X_α	X_β
1	1060	0.2767	0.0216	0.7017	0.9275	0.0725	0.2034	0.1886	0.0147
2	1815	0.4187	0.0391	0.5421	0.9146	0.0854	0.3365	0.3078	0.0287
3	2700	0.5595	0.0424	0.3981	0.9295	0.0705	0.4759	0.4424	0.0335
4	3396	0.7542	0.1010	0.1448	0.8819	0.1181	0.7801	0.6880	0.0921
5	3976	0.8047	0.1163	0.0790	0.8738	0.1262	0.8750	0.7646	0.1104
6	4355	0.8058	0.1238	0.0704	0.8668	0.1332	0.8881	0.7698	0.1182
7	4705	0.8345	0.1078	0.0577	0.8856	0.1144	0.9075	0.8037	0.1039
8	5087	0.8325	0.1258	0.0418	0.8687	0.1313	0.9323	0.8100	0.1224
9	5978	0.8357	0.1320	0.0323	0.8636	0.1364	0.9474	0.8181	0.1292
10	7295	0.8492	0.1273	0.0235	0.8696	0.1304	0.9615	0.8361	0.1253
11	9605	0.8534	0.1337	0.0129	0.8645	0.1355	0.9787	0.8461	0.1326
12	11700	0.8592	0.1308	0.0100	0.8679	0.1321	0.9834	0.8535	0.1299

Table C24. Run-24: results of XRD analysis (d_p > 425 μm).

#	t [sec]	area	fwhm	2 θ	d [Å]	area	fwhm	2 θ	d [Å]
		SILICON (111)				ALPHA (201)			
1	9000	547.7	0.0541	28.423	1683	64.1	0.1359	30.978	674
2	10800	489.3	0.0534	28.439	1705	83.79	0.1199	30.995	764
3	12600	397.7	0.0585	28.419	1557	103.88	0.1201	30.982	763
4	16200	253.5	0.0653	28.401	1394	131.08	0.1283	30.965	714
5	19800	204.9	0.0734	28.448	1241	160.07	0.1271	31.016	721
6	23400	158	0.0712	28.405	1279	152.04	0.1221	30.973	750
7	29100	150.4	0.0779	28.410	1169	161.19	0.1325	30.979	691
8	43200	148	0.0717	28.416	1270	163.19	0.1287	30.985	712
		ALPHA (102)				ALPHA (210)			
1	9000	58.73	0.1287	34.546	718	62.76	0.1296	35.316	715
2	10800	75.43	0.1223	34.563	756	80.49	0.1216	35.334	762
3	12600	92.71	0.1268	34.549	729	104	0.1355	35.319	684
4	16200	140.14	0.1262	34.541	732	149.84	0.1343	35.310	690
5	19800	138.32	0.1282	34.585	721	154.36	0.1325	35.355	699
6	23400	120.36	0.1295	34.534	714	128.21	0.1321	35.303	701
7	29100	129.9	0.1433	34.548	645	142.98	0.1354	35.316	684
8	43200	134.67	0.1241	34.556	745	150.01	0.1346	35.323	688

Table C24 (continued). Run-24: results of XRD analysis (d_p > 425 μm).

#	t [sec]	area	fwhm	2 θ	d [Å]	area	fwhm	2 θ	d [Å]
		BETA (101)				BETA (210)			
1	9000	8.932	0.1506	33.649	612	7.164	0.1324	36.028	701
2	10800	10.415	0.1321	33.657	698	9.055	0.1447	36.040	641
3	12600	13.737	0.2120	33.644	435	12.299	0.1744	36.024	532
4	16200	22.586	0.2173	33.631	424	22.084	0.2212	36.011	420
5	19800	31.32	0.1888	33.684	488	29.857	0.2161	36.059	430
6	23400	35.22	0.2078	33.638	444	30.895	0.2081	36.019	446
7	29100	36.12	0.1889	33.644	488	29.49	0.1916	36.025	484
8	43200	35.77	0.2054	33.654	449	30.9	0.1960	36.038	474
		W_α	W_β	W_{Si}	W_α'	W_β'	X	X_α	X_β
1	9000	0.3798	0.0326	0.5876	0.9210	0.0790	0.2965	0.2731	0.0234
2	10800	0.4677	0.0378	0.4945	0.9252	0.0748	0.3804	0.3520	0.0284
3	12600	0.5622	0.0481	0.3897	0.9211	0.0789	0.4847	0.4465	0.0382
4	16200	0.6897	0.0687	0.2415	0.9094	0.0906	0.6535	0.5943	0.0592
5	19800	0.7315	0.0989	0.1695	0.8809	0.1191	0.7463	0.6574	0.0889
6	23400	0.7352	0.1265	0.1383	0.8532	0.1468	0.7891	0.6732	0.1159
7	29100	0.7550	0.1174	0.1276	0.8654	0.1346	0.8042	0.6960	0.1083
8	43200	0.7600	0.1152	0.1248	0.8684	0.1316	0.8081	0.7018	0.1063

APPENDIX D.
DERIVATION OF THE RELATIONSHIP DESCRIBING THE CHANGE IN THE SURFACE AREA OF THE UNREACTED SOLID REACTANT VERSUS THE OVERALL CONVERSION OF SOLID: CASE OF A SIZE DISTRIBUTION OF SPHERICAL GRAINS IN A POROUS PELLET

Given the size distribution of spherical grains in the reacting porous pellet as the two-dimensional array of a length M containing the range of grains with a mean initial radius $R_{m,0}$ and its mass, i.e. volume, fraction w_m, the relative change in the surface area of the unreacted solid, S, with respect to the initial surface area of the solid, S_0, can be related to the overall conversion of the solid, X, as follows.

If the number of grains having the initial radius $R_{m,0}$ is designated N_m, then one may express the initial volume, $V_{m,0}$, occupied by these grains as

$$V_{m,0} = w_m V_0 = \frac{4}{3} \pi N_m R_{m,0}^3 \qquad \text{(D-1)}$$

or

$$\frac{N_m}{V_0} = \frac{3}{4} \frac{w_m}{\pi} \frac{1}{R_{m,0}^3} \qquad \text{(D-2)}$$

If the time dependent total surface area of the unreacted grains and the corresponding radius of the grains from the range m are designated as $S = S(t)$ and $R_m = R_m(t)$, respectively, then

$$S = \sum_{m=1}^{M} N_m S_m = \sum_{m=1}^{M} N_m 4 \pi R_m^2 \quad \text{(D-3)}$$

and

$$\frac{S}{V_0} = \sum_{m=1}^{M} \frac{N_m}{V_0} S_m = 3 \sum_{m=1}^{M} w_m \frac{R_m^2}{R_{m,0}^3} \quad \text{(D-4)}$$

Since the grains are spherical, the conversion of the each size range m, $X_m=X_m(t)$, may be expressed as

$$X_m = 1 - \left(\frac{R_m}{R_{m,0}} \right)^3 \quad \text{(D-5)}$$

which gives

$$R_m = R_{m,0} \left(1 - X_m\right)^{\frac{1}{3}} \quad \text{(D-6)}$$

Substituting Equation D-6 into Equation D-4, one may write

$$\frac{S}{V_0} = 3 \sum_{m=1}^{M} \frac{w_m}{R_{m,0}} \left(1 - X_m\right)^{\frac{2}{3}} \quad \text{(D-7)}$$

Since

$$\frac{S_0}{V_0} = 3 \sum_{m=1}^{M} \frac{w_m}{R_{m,0}} \quad \text{(D-8)}$$

it follows that

$$\frac{S}{S_0} = \frac{\sum_{m=1}^{M} \frac{w_m}{R_{m,0}} \left(1 - X_m\right)^{\frac{2}{3}}}{\sum_{m=1}^{M} \frac{w_m}{R_{m,0}}} \qquad \text{(D-9)}$$

$$X = \sum_{m=1}^{M} w_m X_m$$

For a given reaction mechanism, i.e. knowing the dependence

$$X_m = X_m\left(R_{m,0}\right) \qquad \text{(D-10)}$$

Equations D-9 and D-10 can be used to relate the total surface area of the unreacted solid grains with the overall conversion of the solid. For example, in case of a process proceeding according to the shrinking core model, for the case of ash diffusion control the implicit form of Equation D-10 is given by Equations 45 and 46 ($x \leftarrow X_m$), while an analogous equation for the case of a first order reaction control is (Levenspiel, 1993)

$$1 - \left(1 - X_m\right)^{\frac{1}{3}} = \frac{\rho_B}{b\, k_s\, C_{A_g}} R_{m,0}$$

with k_s being an apparent reaction constant [m/s] and C_{A_g} bulk gas concentration of the gaseous reactant.